Eastern Michigan University
DigitalCommons@EMU

Master's Theses and Doctoral Dissertations

Master's Theses, and Doctoral Dissertations, and Graduate Capstone Projects

6-2011

Plasma processing of poly(ethylene terephthalate) (PET) in an oxygen decoupled plasma source

Russell L. Rhoton

Follow this and additional works at: http://commons.emich.edu/theses

Part of the Engineering Science and Materials Commons

Recommended Citation
Rhoton, Russell L., "Plasma processing of poly(ethylene terephthalate) (PET) in an oxygen decoupled plasma source" (2011). *Master's Theses and Doctoral Dissertations*. 330.
http://commons.emich.edu/theses/330

This Open Access Dissertation is brought to you for free and open access by the Master's Theses, and Doctoral Dissertations, and Graduate Capstone Projects at DigitalCommons@EMU. It has been accepted for inclusion in Master's Theses and Doctoral Dissertations by an authorized administrator of DigitalCommons@EMU. For more information, please contact lib-ir@emich.edu.

Plasma Processing of Poly(ethylene terephthalate) (PET) in an Oxygen Decoupled Plasma Source

by

Russell L. Rhoton

Dissertation

Submitted to the College of Technology

Eastern Michigan University

In partial fulfillment for the degree of

DOCTOR OF PHILOSOPHY

Dissertation Committee:

Mary L. Brake, Ph.D., Chair

Mohammad Bari, Ph.D.

James A. Carroll, Ph.D.

Erik Lokensgard, Ph.D.

June 2011

Ypsilanti, Michigan

© Russell L. Rhoton 2011

All Rights Reserved

Abstract

Plasma Processing of Poly(ethylene terepthalate) (PET) in an Oxygen Decoupled Plasma Source

In a novel use of a decoupled plasma system (DPS), polymer samples were exposed to an energetic oxygen discharge in order to modify the local surface properties of poly(ethylene terepthalate) (PET) samples. Samples were placed at differing distances (13 cm and 20 cm) from the center of the discharge coil to assess the change in interaction between the sample and the DPS discharge resulting from an increase in sample distance from the center of the discharge coil. Radio frequency discharge generated at 13.56 MHz was used to modify the surface of 200 mm samples. The discharge was generated in a pure oxygen atmosphere at varying pressures of 100, 300, 500, and 1000 mtorr at applied power levels of 250, 500, 750, and 1000 watts.

Optical emission spectroscopy (OES), used as a diagnostic tool, allowed non-invasive monitoring of spectra enabling the characterization of the interaction between the oxygen discharge and the samples during processing. Spectra were acquired between 250 nm and 900 nm. The spectra showed increased overall intensity related to the increase in power. Additionally, the spectra showed a decrease in intensity at pressures above 300 mtorr attributable to increased recombination of oxygen. Increased intensities of CO, OH and atomic OI, andH_α, as well as a continuum attributed to chemiluminescent recombination of CO^+, were also seen as applied power levels increased.

Surface energy (γ) of the PET samples was monitored using the sessile drop method equating the change in the contact angle to the degree of change in the surface energy of the sample as a result of processing. The samples showed a reduction in contact angle of

48 degrees, indicating a change from the initial hydrophobic (78°) to an average value of 30° after processing. Additionally, visible changes were seen in the samples ranging from a light roughening of the surfaces at lower applied power levels to distortion and melting of the samples at applied power levels of 750 and 1000 watts.

Table of Contents

Abstract ii

List of Figures vi

List of Tables xvii

List of Appendices xviii

Chapter

1. Introduction 1

    1.1 Glow Discharges 1

    1.2 Use of Plastics 1

    1.3 Secondary Processing 2

2. Literature Review 5

    2.1 Overview 5

    2.2 Polymers 8

    2.3 Plasma processing of plastics 10

    2.4 Summary 14

3. Experimental Design 16

    3.1 Introduction 16

    3.2 Experimental Design 17

    3.3 RF Power system 20

    3.4 Decoupled Plasma Source (DPS) 29

3.5 Optical Diagnostics 35

3.6 Material Diagnostics 39

3.7 Summary 44

4. Experimental Results 46

4.1 Preliminary Work 46

4.1.1 Optical Emission Spectroscopy 47

4.1.2 Surface Modification Results 49

4.2 DPS Results 20 cm from coil center (**Far**) 50

4.2.1 Optical Emission Spectroscopy 51

4.2.2 Surface Modification Results for DPS (**Far**) 64

4.3 DPS Results 13 cm from coil center (**Near**) 71

4.3.1 Comparison of DPS experiment--(**Near**) and (**Far**) 91

4.4 Summary 96

5. Conclusions 98

5.1 Conclusions 98

5.2 Further Work 100

Bibliography 103

Appendices 119

List of Figures

Figure

2.1 Condensation reaction between terepthalic acid ($C_6H_4(COOH)_2$) and ethylene glycol ($C_2H_6O_2$) showing H_2O byproduct. 9

2.2 poly(ethylene terepthalate) monomer 9

2.3 Polymer chain formed by addition polymerization reaction 10

3.1 EMU processing chamber showing the capacitive glow discharge.(CCP) 17

3.2 Experimental layout of the capacitive discharge system (CCP). 18

3.3 Advanced Energy Navigator 7013-L90 (L90) matching network showing (a) operating power input and I/O network connections. (b) Schematic diagram showing matching network components. 19

3.4 Lumped impedance of a capacitive discharge showing resistive and reactive components of the complex impedance.[27] 21

3.5 Case 1 and 2 matching networks illustrating the arrangements of reactance used with (3.5) and (3.6) to calculate components required for impedance match.[109,110] 23

3.6 Schematic of matching network showing calculated values substituted into original two-node network. 25

3.7 Navigator L90 tuning range showing chamber impedance (Z_D) of capacitively coupled discharge (circle) located on, a) a plot of tuning range showing real versus imaginary axes and, b) tunable range plotted on admittance Smith Chart. Blank charts are taken from Navigator L-90 Manual.[122] 26

3.8 Smith chart showing a) Normalized complex impedance value of processing chamber (Z_D), b) Cancellation of initial capacitive reactance, c) Cancellation of remaining reactance and adjustment of resistance to $50 + j0\Omega$. Chart plotted using LLSmith software application.[122] 28

3.9 Experimental layout of the decoupled plasma source system (DPS). . . 29

3.10 Internal construction of inductive top plate assembly. Note the cooling connections to the inductor and the copper straps used to deliver RF power. 30

3.11 Sample placement in DPS reactor at a distance of 13 cm from the center of the coil. 31

3.12 Sample placement in DPS reactor at a distance of 20 cm from the center of the coil. 31

3.13 Design and integration of the water cooling manifold consisted of: a) Design and fabrication of an additional manifold. b) Modification of the water cooling system to direct cooling water through manifold and inductive coil. 32

3.14 Placement of optical fiber bundle in DPS System 33

3.15 Navigator L-90 tuning range showing chamber impedance (Z_D) of inductive DPS discharge (circle) located on, a) Chart of real versus imaginary axes and, b) Tunable range plotted on admittance Smith Chart. Blank charts are taken from Navigator L-90 Manual.[125] 34

3.16 Schematic of L-90 matching unit showing: a) Matching network as supplied for use with a capacitive system and, b) Matching network as modified for use with the inductive DPS system. 35
3.17 Diagram of the Acton 2300i monochromator (Czerny-Turner Style) showing grating turret, PMT at output slit, and field lens assembly used with the Eastern Michigan University chamber. 36
3.18 Showing setup for wavelength alignment 38
3.19 Relative irradiance calibration used a NIST traceable tungsten ribbon lamp imaged on to the entrance slit of the monochromator. 39
3.20 Initial material testing and sample creation, a) ASTM inspection test, b) Samples cut from the as-received material. 41
3.21 Sessile drop showing relationship between contact angle and surface energies γ_{GL}, γ_{SL}, and γ_{GS}. 42
3.22 Results of the FTA-200 DCA used in tensiometer mode showing measured interfacial tension value of 72.89 for sample of deionized water test fluid. 43
3.23 Initial material testing and sample creation, a) 39-point DCA sample examination, b) 9-point sample examination. 44
4.1 Spectrum of (**Cap**) discharge before introduction of sample in an O_2 process atmosphere at a pressure of 100 mtorr and an applied power of 250 watts. 47
4.2 Spectrum of (**Cap**) discharge acquired during the first two minutes of processing at a pressure of 100 mtorr and an applied power of 500 watts. 48
4.3 Monitored intensity of $(3p^5P - 3s^5S)$ transition of OI at 778 nm shown for the first 60 seconds of processing in the capacitive discharge (**Cap**) at a pressure of 100 mtorr and an applied power of 500 watts. 49

4.4 a) Untreated PET sample shows a large contact angle indicating low surface energy b) Treated PET sample shows a significant reduction in the contact angle 50

4.5 A comparison of averaged contact angle of untreated samples (84°) to samples after processing at four listed pressure and power combinations. 51

4.6 Spectrum of DPS (**Far**) discharge before introduction of sample in an O_2 and Ar process atmosphere at a pressure of 100 mtorr and an applied power of 250 watts. 53

4.7 Intensity of the OH ($A^2\Sigma^+ - X^2\Pi$) band for two experimental configurations as a function of wavelength. The solid line shows the results for the inductive DPS (**Far**) discharge and the dashed line shows the results for the capacitive (**Cap**) discharge under the same conditions; a pressure of 500 mtorr and an applied power of 250 watts. 54

4.8 Comparison of intensity at the OI transitions at 778 nm and at 844 nm. The dashed lines show the intensities of the capacitive (**Cap**) and the solid line shows the intensity of the inductive DPS (**Far**) discharge. . . 55

4.9 Intensity of the OH ($A^2\Sigma^+ - X^2\Pi$) transition as a function of processing time in the inductive DPS (**Far**) system showing the average of all three trials. The discharge conditions were a pressure of 100 mtorr and 250 watts of applied power. 56

4.10 Comparison of intensity and wavelength shows a non-significant increase in the intensity of the OH ($A^2\Sigma^+ - X^2\Pi$) transition at 313 nm and the CO ($b^3\Sigma - a^1\Pi$) transition at 315 nm for a pressure of 100 mT and a power level of 250 W. 57

4.11 Comparison of intensity versus wavelength shows an increase in the intensity of the OH ($A^2\Sigma^+ - X^2\Pi$) transition at 313 nm as well as a similar increase in the CO ($b^3\Sigma - a^1\Pi$) transition at 315 nm for a pressure of 100 mtorr and a power level of 500 watts 58
4.12 Comparison of intensity and wavelength shows an increase in the intensity of the OH ($A^2\Sigma^+ - X^2\Pi$) transition at 313 nm as well as a similar increase in the CO ($b^3\Sigma - a^1\Pi$) transition at 315 nm for a pressure of 100 mtorr and a power level of 250 watts. 59
4.13 Intensity of the OI ($3p^5P - 3s^5S^0$) transition at 778 nm and the OI ($3p^3P3s^3S^0$) transition at 844 nm showing the change in intensity for a processing time of 10 minutes at a pressure of 100 mtorr and an applied power of 250 watts. 60
4.14 Averaged intensity of the OI ($3p^5P - 3s^5S^0$) transition at 778 nm showing variations between sample groups processed for varying time periods at a pressure of 100 mtorr and an input power of 250 watts. 61
4.15 Intensity as a function of time of the OI transitions at 778 nm (solid), 844 nm (dashed), and the OH bandhead at 309 nm (dotted) for the 150 second sample period at a pressure of 300 mtorr and an applied power of 500 watts. 62
4.16 Boltzmann plot of $ln\frac{I_{ki}\lambda_{ki}}{g_k A_{ki}}$ versus E_k for a sample processed for 2 minutes at a pressure of 100 mtorr and an applied power of 500 watts. 64
4.17 Calibration of the DCA system showing: a) Tensiometer verification of interfacial tension value of deionized water drop. b) Sapphire standard used for sessile drop characterization. 65

4.18 PET material samples showing: a) Untreated PET sample shows a large contact angle (> 75°) indicating low surface energy. b) Sample treated at a pressure of 500 mtorr and an applied power of 500 watts for 16 minutes shows a ≈ 80% decrease in contact angle (> 13°) showing an increase in surface energy after treatment. 65

4.19 Comparison of initial characterization values showing (◊) 39-point characterization of sample, (○) 9-point characterization of sample, (▲) ASTM characterization of sample, and (− −) calculated average of all initial CCA values. 66

4.20 Comparison of average contact angle of an unprocessed sample (78°) to contact angles of sample after processing at four pressure and power combinations. 67

4.21 Contact angles across sample (200 mm). Observe the large contact angle values at the edges of the sample due to shading of the sample edge by the outer ring of the substrate holder. 68

4.22 Comparison of contact angle versus processing time for samples processed at a pressure of 100 mtorr and applied power levels of 250 and 500 watts. 70

4.23 Intensity versus wavelength of an O_2 discharge at 100 mtorr and 250 watts applied power with no sample. 72

4.24 A close up of intensity versus wavelength of the spectrum shown in Figure 4.23. 73

4.25 Intensity as a function of wavelength at a pressure of 100 mtorr at applied powers of 250 (blue), 500 (green), 750 (orange), and 1000 (red) watts. . 74

4.26 Intensity as a function of wavelength at a pressure of 300 mtorr at applied powers of 250 (blue), 500 (green), 750 (orange), and 1000 (red) watts. . 75

4.27 Intensity as a function of wavelength at a pressure of 500 mtorr at applied powers of 250 (blue), 500 (green), 750 (orange), and 1000 (red) watts. . 76

4.28 Intensity as a function of wavelength at a pressure of 1000 mtorr at applied powers of 250 (blue), 500 (green), 750 (orange), and 1000 (red) watts. 77

4.29 Comparison of intensity versus wavelength shows increased activity at 309 nm (OH), as well as at 395 nm (OI), 410 nm (H_γ), 437 nm (CO), and 616 nm (OI) visible after introduction of sample which was processed at a pressure of 100 mtorr and at applied power levels as shown. 78

4.30 Comparison of intensity versus wavelength shows greatly increased activity at 309 nm (OH), as well as at 395 nm (OI), 410 nm (H_γ), 437 nm (CO), and 616 nm (OI) visible after introduction of sample to the processing system. Sample was processed at a pressure of 300 mtorr and applied power levels as shown. 79

4.31 Intensity as a function of wavelength at a pressure of 100 mtorr shows the OH ($A^2\Sigma^+ - X^2\Pi$) transition at 309 nm as well as the CO ($b^3\Sigma - a^1\Pi$) bandhead at 315 nm at applied powers of 250 (blue), 500 (green), 750 (orange), and 1000 (red) watts. 81

4.32 Intensity as a function of wavelength at a pressure of 300 mtorr shows the OH ($A^2\Sigma^+ - X^2\Pi$) transition at 309 nm as well as the CO ($b^3\Sigma - a^1\Pi$) bandhead at 315 nm at applied powers of 250 (blue), 500 (green), 750 (orange), and 1000 (red) watts. 82

4.33 Intensity as a function of wavelength at a pressure of 100 mtorr shows the OH ($A^2\Sigma^+ - X^2\Pi$) transition at 309 nm as well as the CO ($b^3\Sigma - a^1\Pi$) bandhead at 315 nm at applied powers of 250 (blue), 500 (green), 750 (orange), and 1000 (red) watts. 83

4.34 Intensity as a function of wavelength at a pressure of 100 mtorr shows the OH ($A^2\Sigma^+ - X^2\Pi$) transition at 309 nm as well as the CO ($b^3\Sigma - a^1\Pi$) bandhead at 315 nm at applied powers of 250 (blue), 500 (green), 750 (orange), and 1000 (red) watts. 84

4.35 Intensity of OI versus pressure plotted for applied powers of 250, 500, 750 and 1000 watts. 86

4.36 Intensity of the ($2s - 3p$) H_α transition at 656 nm for four pressures: a) 100, b) 300, c) 500, and d) 1000 mtorr. 87

4.37 Samples after processing in the inductive DPS (**Near**) at a pressure of 300 mtorr and applied power levels of a) 250, b) 500, c) 750 d) 1000 watts. 89

4.38 Intensities as a function of time of: a) the OH bandhead at 309 nm, b) the OI transition at 778 nm, and c) the H_α line at 656 nm for a pressure of 100 mtorr and an applied power of 250 watts. 90

4.39 Comparison of spectra acquired at a distance of 20 cm from the center of the coil (black) and at a distance of 13 cm from the center of the coil (red) respectively at a pressure of 100 mtorr and an applied power of 500 watts. 92

4.40 Intensity as a function of wavelength for processing discharges at a distance of 20 cm (red) and a distance of 13 cm (black) from the center of the coil at a pressure of 300 mtorr and an applied power of 500 watts. 94

4.41 Spectra at a distance of 20 cm (black) and 13 cm (red) from the center of the coil at a pressure of 100 mtorr and an applied power of 500 watts. 95

4.42 Comparison of OES data showing the H_α transition at 656 nm data taken at the (**Near**) sample position (black) and the (**Far**) sample position (red) for an applied power of 500 watts at a pressure of 100 mtorr. . . 96

4.43 Overlapping bandheads of CO and continuum attributed to chemiluminescence during recombination of CO and O showing the (**Near**) sample position (red) and the (**Far**) sample position (black) at a pressure of 100 mtorr and an applied power of 500 watts. 97
A.1 Contact angle values acquired across the diameter of a sample processed for 2 minutes at 100 mtorr in an $O_2 + Ar$ atmosphere at an applied power of 250 Watts. 121
A.2 Contact angle values acquired across the diameter of a sample processed for 2 minutes at 100 mtorr in an $O_2 + Ar$ atmosphere at an applied power of 500 Watts. 122
A.3 Contact angle values acquired across the diameter of a sample processed for 6 minutes at 100 mtorr in an $O_2 + Ar$ atmosphere at an applied power of 250 Watts. 123
A.4 Contact angle values acquired across the diameter of a sample processed for 10 minutes at 100 mtorr in an $O_2 + Ar$ atmosphere at an applied power of 250 Watts. 124
A.5 Contact angle values acquired across the diameter of a sample processed for 10 minutes at 100 mtorr in an $O_2 + Ar$ atmosphere at an applied power of 500 Watts. 125
A.6 Contact angle values acquired across the diameter of a sample processed for 16 minutes at 100 mtorr in an $O_2 + Ar$ atmosphere at an applied power of 250 Watts. 126
A.7 Contact angle values acquired across the diameter of a sample processed for 16 minutes at 100 mtorr in an $O_2 + Ar$ atmosphere at an applied power of 500 Watts. 127

B.1 Initial characterization test liquid (deionized water) shows an interfacial tension of 72.89 dynes/cm. This value is in good agreement with published values. 129
B.2 Initial characterization of video system using vendor-supplied Sapphire calibration standard (90°± 0.10) 130
B.3 Contact angle value acquired across the diameter of a sample processed for 2 minutes at 400 mtorr in an $O_2 + Ar$ atmosphere at an applied power of 250 Watts, Sample 1. 131
B.4 Contact angle value acquired across the diameter of a sample processed for 2 minutes at 400 mtorr in an $O_2 + Ar$ atmosphere at an applied power of 250 Watts, Sample 2 132
B.5 Contact angle value acquired across the diameter of a sample processed for 2 minutes at 400 mtorr in an $O_2 + Ar$ atmosphere at an applied power of 250 Watts, Sample 3 133
B.6 Contact angle value acquired across the diameter of a sample processed for 2 minutes at 400 mtorr in an $O_2 + Ar$ atmosphere at an applied power of 250 Watts, Sample 4 134
B.7 Contact angle value acquired across the diameter of a sample processed for 2 minutes at 400 mtorr in an $O_2 + Ar$ atmosphere at an applied power of 250 Watts, Sample 5 135
B.8 Contact angle value acquired across the diameter of a sample processed for 2 minutes at 400 mtorr in an $O_2 + Ar$ atmosphere at an applied power of 250 Watts, Sample 6 136
B.9 Contact angle value acquired across the diameter of a sample processed for 2 minutes at 400 mtorr in an $O_2 + Ar$ atmosphere at an applied power of 250 Watts, Sample 7 137

B.10 Contact angle value acquired across the diameter of a sample processed for 2 minutes at 400 mtorr in an $O_2 + Ar$ atmosphere at an applied power of 250 Watts, Sample 8 138

B.11 Contact angle value acquired across the diameter of a sample processed for 2 minutes at 400 mtorr in an $O_2 + Ar$ atmosphere at an applied power of 250 Watts, Sample 9 139

C.1 Intensity as a function of wavelength of a sample processed for 2 minutes at a pressure of 100 mtorr and an applied power of 250 watts. 141

C.2 Intensity as a function of wavelength of a sample processed for 2 minutes at a pressure of 100 mtorr and an applied power of 500 watts. 142

C.3 Intensity as a function of wavelength of a sample processed for 6 minutes at a pressure of 100 mtorr and an applied power of 250 watts. 143

C.4 Intensity as a function of wavelength of a sample processed for 2 minutes at a pressure of 100 mtorr and an applied power of 500 watts. 144

C.5 Intensity as a function of wavelength of a sample processed for 10 minutes at a pressure of 100 mtorr and an applied power of 250 watts. 145

C.6 Intensity as a function of wavelength of a sample processed for 10 minutes at a pressure of 100 mtorr and an applied power of 500 watts. 146

C.7 Intensity as a function of wavelength of a sample processed for 16 minutes at a pressure of 100 mtorr and an applied power of 250 watts. 147

C.8 Intensity as a function of wavelength of a sample processed for 16 minutes at a pressure of 100 mtorr and an applied power of 500 watts. 148

D.1 Intensity as a function of wavelength of samples processed for 2 minutes at a pressure of 100 mtorr and an applied power of 250, 500, 750 1000 Watts as shown. 150

D.2 Intensity as a function of wavelength of samples processed for 2 minutes at a pressure of 300 mtorr and an applied power of 250, 500, 750 1000 Watts as shown. 151
D.3 Intensity as a function of wavelength of samples processed for 2 minutes at a pressure of 500 mtorr and an applied power of 250, 500, 750 1000 Watts as shown. 152
D.4 Intensity as a function of wavelength of samples processed for 2 minutes at a pressure of 1000 mtorr and an applied power of 250, 500, 750 1000 Watts as shown. 153

List of Tables

Table

2.1 Non-thermal plasma discharges used in materials processing. 6

3.1 Comparison of component values used to calculate the complex conjugate (Z^*_D) of the discharge impedance Z_D using both analytic and graphical (Smith chart) methods. 27

3.2 Comparison of impedance values between the planar electrode discharge and the DPS coil discharge showing the change in the reactive component of the impedance from capacitive to inductive. 33

3.3 Surface tension values of ASSTM-D2578 testing pens 40

4.1 Comparison of experimental parameters between previous work and current experiments. 46

4.2 Table of emission lines monitored during processing in the DPS (**Far**) configuration. 52

4.3 Emission lines of argon used in the calculation of discharge temperature. 63

4.4 Comparison of contact angle versus processing pressure. 69

4.5 Emission lines monitored during experiment three. Note that argon gas was not used in this experimental series. 80

4.6 Bandheads of the CO ($B^1\Sigma^+ - A^1\Pi$) Ångstrom system as cited in [174] . 93

List of Appendices

Appendix

A. Contact Angle Plots 120

B. Contact Angle Pictures 128

C. Spectra of Runs in Inductive Decoupled Plasma System (DPS)(**20.0 cm**) 140

D. Spectra of Runs in Inductive Decoupled Plasma System (DPS)(**13.0 cm**) 149

E. ASTM-2855 Test Protocols and Equipment 154

Chapter 1

Introduction

1.1 Glow Discharges

The use of a glow discharge to modify engineering materials in manufacturing processes is not new. The ability of glow discharges to modify the chemical qualities of a sample surface is well known.[1,2] Industrial processes have used glow discharges and related treatments (flames and corona discharges) as methods for secondary processing of sheet and other forms of plastics for many years.[3,4] Wider application of glow discharges include adhesion enhancement through surface modification,[1,5,6] sterilization of sealed packages,[7,8] processing of metals,[9] boundary layer flow control,[10] and reforming of methane (CH_4) gas.[11] Consumer and automotive-related products are manufactured using batch processing of plastic parts in glow discharges as a means of enhancing the adhesion of paint and printed decoration.[12–14]

1.2 Use of Plastics

The development of new engineered polymer materials has allowed major changes in the design and manufacture of consumer products. The ability of plastics to be molded into shapes and finishes never before available has led to the utilization of these materials in an increasingly wider number of devices and products ranging from plastic blow-molded automobile parts (bumper supports and covers) to grocery bags and containers for liquids and creams; plastic artifacts have become ubiquitous. Each of these

product examples, as well as others, requires, or benefits from, secondary processing to enhance or modify the material qualities, to cleaning the product after manufacturing.

Glow discharges are able to perform these modifications through the interaction of energetic electrons, neutrals, and ions with the surface atoms and molecules of plastic products. Functionalization of the surface, i.e., leaving remains of the process gas and fragments of the sputtered plastic attached to the surface, as well as increasing the roughness of the surface through sputtering or etching away the plastic surface, are the most often used methods of enhancing the ability of adhesives, printing, painting, and other decoration to adhere to the modified surfaces.[1,5,6] Discharges are additionally used for cleaning mold release and other contaminants from molded parts as well as the sterilization, by inactivation of bacteria, of sealed and unsealed packages.[7,8] Surface enhancement technology has advanced from early techniques involving flame treatment and abrasive blasting, although adequate to create changes in the macro structure of processed materials, to glow discharge processes able to modify the micro structure of materials.[15–17]

1.3 Secondary Processing

Low pressure glow discharges are able to modify material properties at the atomic and molecular level. Exposure of the material surface to active species in the process atmosphere allow interaction between the process and material at an atomic level. Functionalization of the material surface permits controlled local tailoring of the chemical properties of the surface without modifying the bulk properties of the part. The control of energetic particle interaction with the material surface by controlling input power, pressure, and process atmosphere enables these processing methods to act with a degree of control not available with more traditional methods. Perhaps most important is the ability to modify materials with minimal heat addition to the process. Traditional, non plasma, secondary processes add significant amounts of heat to the workpiece,[18] creating

the need for heat control and protection schemes not required by glow discharge processing. An investigation into the ability of processes and tools developed for use in the semiconductor industry, where production quality and quantity are equally important, re-purposed for use in modification of polymer products, would bring an increased knowledge of surface processing of plastics.

This dissertation examines the question: can an inductive decoupled plasma discharge (DPS) processing system process poly(ethylene terepthalate) (PET) polymer samples in a more efficient manner that can justify or recommend the use of the DPS style of system as a production processing system for the modification of polymer surface qualities? Others researchers have studied the behavior of PET exposed to a glow discharge in both capacitive[19–21] and inductive[2,22,23] RF discharges but the use of an inductive DPS system specifically for the modification of the surface qualities of PET polymer has not been widely studied. The differences between these systems will be discussed in Chapter 2.

This research study is organized as follows. Chapter 2 presents a survey of published research literature, industry white papers, patents, and presentations organized by the major types of glow discharges currently used for materials processing in industry: capacitive discharge, dielectric barrier discharge, and inductive discharges. Comparison and examination of these various processing methods will provide accepted diagnostic methods and procedures as possible candidates for use in this work. Examination of the data collection techniques used by other researchers will enable the frugal choice of setpoints and procedures. The results of other studies will enable the contextual placement of this work within the wider scope of related research.

Chapter 3 outlines the experimental design used in this study. A description of the chamber, vacuum system, radio frequency (RF) power supply, matching of the loads for maximum power delivery, and modifications to the chamber will be discussed. The major diagnostics such as material diagnostics and optical emission spectroscopy (OES) will

also be presented.

Chapter 4 presents the data gathered during the processing steps. The data will be organized to first present a summary of preliminary work that led to the present study, a comparison of the changes found based on the use of inductive discharge processing, and an enumeration of new findings.

Chapter 5 consists of the experimental results compared to previous studies and summarizes the conclusions reached as a consequence of the research. Future work possibilities will also be discussed.

The appendices present supporting data and collections of data too large for inclusion in the body of the study. Appendix A contains contact angle plots showing the measured contact angles of the treated samples plotted with reference to the average value derived in Chapter 3. Appendix B contains video stills of the interface between the sample surface and the test fluid used to calculate the sessile drop contact angle testing results. Appendix C contains optical emission spectra for each of the processing runs using the inductive decoupled plasma system (DPS) acquired with the sample 20 cm distant from the center of the discharge (**Far**). Appendix D contains optical emission spectra for each of the processing runs (**Near**) using the inductive decoupled plasma system (DPS) acquired with the sample 13 cm from the center of the discharge. Finally, Appendix E contains the text of the ASTM-2855 Testing standard as well as data sheets for the testing pens used for initial characterization of polymer materials at incoming inspection (Chapter 4).

Chapter 2

Literature Review

2.1 Overview

The semiconductor industry introduced capacitively coupled discharges into the manufacturing processes of integrated circuits in the 1960s because previous methods using wet chemicals like HF did not give the desired result. The use of capacitive discharges for processing was the mainstay of the semiconductor industry from the mid-1970s to the late 1990s. Ongoing research targeted the improvement of special manufacturing processes for the etching of silicon devices as well as development of more efficient processing tools.[24,25] In the 1990s, inductively coupled plasma discharge (ICP) systems were scaled up to manufacturing size to ameliorate problems that developed with capacitive systems, in particular the non-uniformity of processing that resulted as the electrodes were made larger in order to process the larger wafer size introduced to increase production output.[26,27] ICP systems showed a processing advantage over capacitive systems due to the increase in density and uniformity of the discharge, a widely studied topic.[24,26–29] ICP systems from the LAM 9400 planar system (1992) and the Applied Materials Omega series inductive solenoid system (1993) were widely adopted as the primary styles of processing system used by semiconductor manufacturers.[26,28] The increased density and uniformity of these discharges suited them for uses in other manufacturing processes formerly served by the less dense capacitive discharges.[26,28] Divisions in processing discharges emerged, shown in Table 2.1, each serving to fill a

broad processing need. Note that T_e stands for electron temperature and T_i stands for ion and atom temperature; T_i is always much less than T_e in these types of discharge.

Table 2.1: Non-thermal plasma discharges used in materials processing.

Discharge type	Pressure	Electron Density(cm^{-3})	T_e (eV)	T_e to T_i
Inductive	1 mtorr - 2 torr	$10^{11} - 10^{13}$	$0.1 - 5$	$T_i << T_e$
Decoupled Plasma Source	1 mtorr - 2 torr	$10^{13} - 10^{14}$	$0.1 - 5$	$T_i << T_e$
Capacitive	1 mtorr - 2 torr	$10^{8} - 10^{10}$	$0.1 - 5$	$T_i << T_e$
Dielectric Barrier	≈ 760 torr	$10^{14} - 10^{15}$	$0.1 - 5$	$T_i << T_e$

Most discharges used in surface modification are produced using a radio frequency (RF) generator at 13.56 MHz although additional frequencies are sometimes used for special applications.[27,30] The two main types of RF processing discharges (Table 2.1) are capacitive and inductive systems. Capacitively coupled discharges transfer the energy carried by RF fields to a gaseous system where a small population of electrons (due to their small mass and relatively large charge) gain enough energy to escape the hold of the atom (ionize) and randomly excite nearby atoms/electrons as they move toward the positive electrode. Once enough of the population is ionized, a cascade of electrons and ions are produced and breakdown is achieved.[31] The discharge begins to glow, while showing a decrease in electrical resistance due to the increase in the number of created ions and electrons; the glow and decrease in electrical resistance of the system is an indication of a plasma state. The degree of ionization of these types of discharges is extremely small, approximately $\frac{1}{10{,}000}$ of total atoms are ionized. Any RF discharge operating at a frequency above 1 MHz will create a sheath area between the bulk plasma and the power electrodes (anode and cathode). The sheath accelerates the electrons and ions increasing collisions with the materials to be processed. The basic mechanisms of plasma discharges have been widely discussed by Chen,[30] Lieberman and Lichtenberg,[27] and others.[32–34]

Inductively coupled discharges transfer energy from the RF generator to the discharge through the interaction between the changing field of the RF coil and the

electrons of the process gas in the chamber. The combination of the coil and the discharge act as a transformer with the physical coil serving as the primary winding and the plasma as a single turn secondary winding[26,35] interacting according to Faraday's law: $\vec{\nabla} x \vec{\mathbf{E}} = -\frac{\delta \vec{\mathbf{B}}}{\delta t}$ where the magnetic flux generated by the time-varying current in the coil induces a varying electrical field in the discharge that accelerates the electrons and sustains the discharge as described by Keller,[26] Godyak,[35] Hopwood,[28] and others.[27,33,36]

The decoupled plasma discharge is a refinement of the inductively coupled discharge in that the electron density is controlled by a high frequency rf source applied to the inductive coil, as described above, while control of the ion energy is separated (decoupled) from the inductive source and driven by lower frequency rf energy applied to the chuck or substrate holder. Separation of electron density from ion energy allows for independent control of both the electron density and the ion energy.[27,33,37]

Non-thermal processing discharges generate lower electron densities ($< 10^{15} cm^{-3}$) at processing (electron) temperatures of 0.1 to 5.0 eV, at much lower pressures (less than 2 torr), and with a power input of 10 to 1000 watts, substantially less than the requirements for a thermal plasma.[15,38,39] Electron temperatures (T_e) are much greater than the ion temperatures (T_i), resulting in a discharge that is not in thermal equilibrium ($T_i << T_e$). Low pressure discharges are used for materials processing as a gentle method for modification of sensitive materials; however, the reduced pressure required by these processes (1 mtorr - 2 torr) limits their use to materials that are able to withstand processing in a vacuum.[26] Large or bulky units requiring surface modification before painting or removal of mold release from molded plastic parts (automobile bumpers, plastic tanks or tubs) as well as high-value items (integrated circuit dies/wafers) that require the removal of photolithographic masks or cleaning between process steps are often batch processed using these non-thermal discharges.[19,40–42]

Many of these secondary processes employ dielectric barrier discharges. The dielectric barrier discharge plasma (DBD) is formed between parallel, dielectric covered

surfaces at atmospheric pressure (760 torr) if sufficient energy is supplied to maintain the process. DBD is a low temperature, high density plasma and is attractive for use in treatment processes where the process product cannot survive exposure to vacuum or where processing in a vacuum would be impractical. DBD is often used in the treatment of dielectric sheet goods (plastic films, paper goods, and fabrics) as it is well adapted to inclusion in the manufacturing process as an in-line processing step.[43–49] Although researchers[50] have also examined the ability of this process to inactivate both *E. coli* bacterium on surfaces and *P. phosphoreum, L. sakei and L. monocytogenes* in sealed containers to increase shelf life in packaged seafood, the bulk of DBD research examined here is concerned with surface modification of polymer materials.[46,48,51–53]

2.2 Polymers

Polymers, such as poly(ethylene terepthalate), polyester, polyurethane, polycarbonate, and polyamide (nylon), are all products of condensation polymerization reactions. In condensation polymerization the reaction between multiple molecular compounds create the required monomer. Poly(ethylene terepthalate) (PET), is the result of the condensation polymerization of terepthalic acid ($C_6H_4(COOH)_2$) and ethylene glycol ($C_2H_6O_2$). The reaction of the alcohol and the acid serves to join the two into a monomer (n) of PET as shown in Figure 2.1. In this reaction, a molecule of water (H_2O) is squeezed out, leaving an available acid (HO) and alcohol (OH) molecule on either end of the polymer chain available for further reaction. Unlike some condensation reactions,[3] the PET reaction begins with a condensation reaction that creates the monomer, shown in Figure 2.2, followed by an additive reaction that joins and lengthens the polymer chains until all of the reactive material is consumed.

In a thermo plastic polymer, the molecular chains, shown in Figure 2.2, lie side by side without any connection between the individual strands; these polymers can be formed and reformed after an addition of energy raises the temperature above the glass

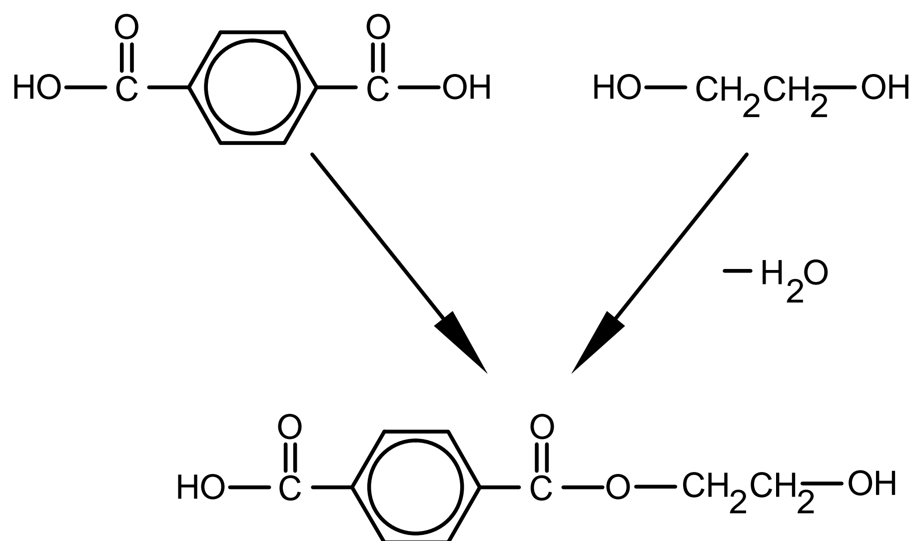

Figure 2.1: Condensation reaction between terepthalic acid ($C_6H_4(COOH)_2$) and ethylene glycol ($C_2H_6O_2$) showing H_2O byproduct.

transition temperature (T_g), which allows the polymer strands to move and slide freely over one another. In a thermoset polymer, curing is brought about by the action of a catalyzing agent (heat or chemical) that causes reactions at active sites cross-linking the polymer strands into a three-dimensional structure. Cross-linking of polymer strands

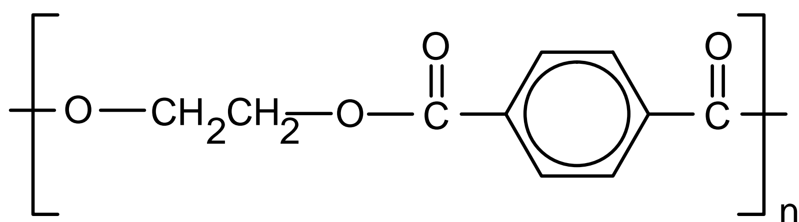

Figure 2.2: poly(ethylene terepthalate) monomer

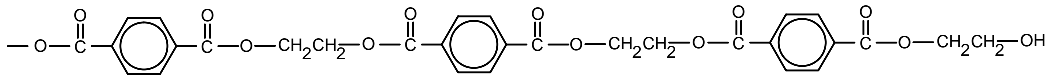

Figure 2.3: Polymer chain formed by addition polymerization reaction

creates larger molecules with higher weight and a transition temperature (T_g) generally above the temperature required to cause chemical decomposition of the polymer. Thermoset plastics, as a rule, are not able to be reformed (by the application of heat) in the same manner as thermoplastics and are generally recycled by grinding and reuse as filler in reformulated compounds,[38] although other methods of recycling such as pyrolysis using fluidized bed reactors[54] and glycosis (depolymerization) to recover the original bis(hydroxyethyl) terephthalate (BHET) monomer for re-polymerization[55] are current topics of research.[15,38,39,56]

2.3 Plasma processing of plastics

The increased use of plasmas for processes not solely engaged with the preparation for or creation of features on silicon wafers[57,58] signaled a beginning of the expansion of plasma processing into other areas of the semiconductor manufacturing process and ultimately into the processing of materials other than semiconductors.[15,16,24,34,59] United States patents filed in the 1980s by Polak of UOP[60] and Heinecke of Standard Telephone & Cables[61] show the early use of a discharge for the secondary processing of plastics products. Prior to this time (1969), a patent filed by Keane and Lough of E. I. du Pont de Nemours[62] detailed chemical washes and flame treatments used to prepare the surface of plastic items for metal plating. Increased use of discharges for the processing of polymers is evidenced by numerous papers and articles discussing the use of inductive plasmas in materials processing in the late 1980s and early 1990s.[24,28,63–65] Berins,[3] in the Plastics Engineering Handbook of The Society of Plastics Engineers, discusses finishing processes common in the early 1990s. Secondary processing of polymers was

common practice but used abrasives for some surface conditioning and plasma processing was only mentioned as an item of minor interest. The Polak patent of 1982[60] accomplished the same levels of surface preparation described by Berins,[3] using a plasma discharge, illustrating the possibility of replacing older methods of surface modification with the use of plasma discharges. By the end of the 1990s, plasma discharges were being used in numerous materials processes including the modification of surfaces of polymer materials.[16,39,47,61,63,66–71] In two succeeding editions of the textbook Manufacturing Engineering and Technology, Kalpakjian and Schmid[18,72] survey the processes used by the manufacturing industry. It is significant to note that between the 5th (2006) and 6th (2010) edition, the chapter on micromachining and fabrication of microelectric devices was expanded to include discussions of plasma etching and other energetic discharge enhanced advanced processes. This addition to a general educational text indicates the growing importance discharge processes hold as basic methods to be used by engineers and technologists trained today.

Plasma discharges are used for many purposes, but here we are concerned with the uses of these systems for processing of polymers and other materials, specifically poly(ethyleneterepthalate) (PET), with the goal of local modification of material properties. Local modification of surface qualities of polymers is of interest to secondary processes such as printing,[73–75] adhesive bonding,[1,68,76] painting[17,77] and coating of plastics[71,78,79] while PET, as discussed in Section 2.2, and is widely used in many products created or finished using these processes.

An experimental chamber and RF generators were donated to Eastern Michigan University by Advanced Energy, Inc., of Colorado and Applied Materials, Inc., of California. The equipment was modified in order to investigate changes in the surface energy of poly(ethylene terepthalate) (PET) polymer samples, as representative of materials used in many secondary processed artifacts, processed in a low electron density non-thermal discharge. Initially configured as a capacitively coupled system, the

operation of the chamber configuration and results of processing diagnostics were reported in earlier works[20,21] and are briefly reviewed in Chapter 4. A description of the experimental configurations examined in this dissertation will be discussed in Chapter 3.

The original design intent of the donated plasma chamber system was as a prototype of the Applied Materials *Centura*® photomask etch system, a decoupled plasma system (DPS), developed for etching of features smaller than 0.13 μm into silicon based wafers used in semiconductor manufacture.[37] The primary use of this configuration, however, was the removal (ashing) of photoresist coatings by exposure to a dense, energetic oxygen discharge,[80] a common use in the semiconductor industry for systems of this type.[26,33,81–84] Huang et al.[37] characterized the performance of two similar systems over time (1 month of industrial use) and reported that the DPS chamber (original configuration) showed stable and reproducible results for commercially significant etching processes such as etch rate, selectivity, and uniformity. Ma et al.,[85] in investigations of another similar system, also reported increased density and stable performance over processing times investigated. Cunge et al.[86] reported a density of $10^{13} cm^{-3}$ at a temperature of 3 eV and pressure of 10 mtorr while using both a LAM system and an Applied Materials DPS system comparable to the original configuration of the system donated to Eastern Michigan University.

The restoration of the processing chamber to the original DPS configuration was undertaken in order to increase the density of the processing discharge beyond the densities achievable with the capacitive non-thermal discharge configuration used for previous investigations.[20,21] Preliminary experiments with this system showed that modification of the surface of a poly(ethylene terepthalate) (PET) sample processed in an capacitive oxygen discharge[20,21] at varying pressures and times resulted in an overall reduction of the contact angle of the sample$(40 - 50\%)$, indicating an increase in the wettability of the polymer sample, thus enabling easier subsequent processing. Similar results using a capacitive system were reported by Vassallo et al.,[87] Ignaki et al.,[88] and

others.[4,89,90] Vujovsevic et al.[91] and Vesel et al.,[92] however, reported a larger decrease in the contact angle ($\approx 60 - 70\%$) of samples processed in an inductive post glow discharge having a density of $10^{13} cm^{-3}$,[84] much larger than in the previous work.

Non-thermal capacitive and inductive discharges are widely used as methods for secondary processing of polymer and other materials. While many studies investigate the uses of both capacitive and inductive discharges as a preparation step used to increase surface energy before printing, painting, coating, or gluing, the use of a DPS system for the modification of polymer surfaces has not been found in the literature. Although researchers have examined the behavior of the DPS discharge with regard to production etching of SiO_2,[86,93] including damage caused to etched devices as a result of charge build-up during processing[85,94] and extended investigations of a similar domed inductive discharge by Tuszewski and others[95–100] examining stability and behavior of DPS discharges generated primarily in an Ar/SF_6 process atmosphere, none have studied plasma surface modification. Other than a discussion of the prototype system being used as a photoresist removal tool,[80] a process related to polymer modification, no prior investigations have examined the use of a DPS system specifically to modify the surface qualities of polymeric materials. The increased electron density ($10^{13} cm^{-3}$) reported and confirmed by Cunge et al.,[86] as well as the uniformity of discharge and increased etch rate achievable by the DPS style of commercial processing tool as reported by Huang et al.,[37] and Ma et al.,[85] indicate the possibility of using a decoupled plasma discharge (DPS), with a more uniform, higher density discharge than capacitive and RF discharges, for secondary processing of appropriate materials. It is proposed that the exposure of polymer PET samples to the increased density and uniformity of the DPS discharge will lead to increased etch rates across the sample surface, resulting in reduced processing time and more uniform treatment, which would be advantageous in industrial applications generally associated with plasma processing of polymers.

2.4 Summary

The use of plasma discharges to modify polymers and other materials is widespread across industry today. Originally developed as process tools for device production in the semiconductor industry, improvement and extension of the special properties of these discharges have enabled the creation of smaller feature sizes, allowed the minimization of damage to the substrates, and enabled increased output. Research into uses beyond semiconductor processing has led to improved methods of processing glass,[101] metal, and ceramic[70] materials as well as additional advanced procedures for processing of polymers.[17,102,103]

The polymer of interest in this dissertation is a polymer formed by condensation polymerization of terepthalic acid ($C_6H_4(COOH)_2$) and ethylene glycol ($C_2H_6O_2$); poly(ethylene terepthalate) (PET). PET is widely used in consumer goods such as polyester yarn or fabric, electronics (electrical insulation and dielectric in capacitors), and printed materials usually of short life duration although the biaxially stabilized form of the polymer is often used for archival storage of physical engineering documentation and other general plastic uses. The biaxially stabilized form of PET (Mylar film) was used in the experiments reported here.

Certain methods and approaches have become standard or associated with certain areas of secondary processing of plastics. The increased capability of these processes to modify polymer surfaces as a result of the increased electron density of the discharges has found many applications in materials processing. Capacitive discharges with their lower electron density and low temperatures are still used for material processing as described by Vassallo et al.[19] and others,[4,89] while inductive discharges with their higher density and low electron temperatures are able to apply a high electron density discharge to the material surface for modification of more sensitive materials. The dielectric barrier discharge (DBD) is widely used in the commercial processing of sheet goods (fabrics, paper, and plastics) as described by Borcia et al.[51,104,105] and others,[43–49] as well as

sterilization.[50] Secondary processing of polymers using plasma procedures and equipment originally developed for the semiconductor industry shows that the use of energetic discharges has grown beyond the limited uses mentioned by Berins[3] to encompass a wide range of processing requirements including both DC and AC (RF) driven discharges as well as varying process pressures ranging from low pressure to multiple atmospheric pressures depending on the "robustness" of the materials to be processed.

Previous investigations in agreement with other researchers have shown that an energetic capacitive discharge can modify the surface of a polymer sample by functionalization of the surface and by physical etching the surface of amorphous poly(ethylene terepthalate) (PET) samples. The application of the inductive DPS discharge to the processing of PET samples will show, for the first time, the increased ability of the discharge to modify the surface of polymer samples due to the increased electron density of the discharge.

Chapter 3

Experimental Design

3.1 Introduction

Three sets of experiments were conducted to investigate the effect of an energetic plasma discharge on poly(ethylene terepthalate) (PET) sample surfaces. The first involved an RF capacitively coupled discharge (CCP), and the second and third, an inductively coupled RF system known as a decoupled plasma system (DPS). The main diagnostic used during processing was optical emission spectroscopy.

In the first experiment, the polymer samples were placed on the powered electrode of the CCP and exposed to the oxygen discharge at a fixed pressure, gas flow, power, and time intervals. In the second experiment, the polymer samples were placed on the isolated electrode of the DPS and exposed to the oxygen discharge at fixed pressure, gas flow, power, and time intervals at a distance of 20 cm from the center of the coil. In the third experiment, the polymer samples were again placed on the isolated electrode of the ICP and exposed to the oxygen discharge at fixed pressure, gas flow, power, and time intervals at a distance of 13 cm from the center of the coil. After treatment, in all experiments, the treated samples were removed from the chamber and examined for changes to the surface. Optical measurements of contact angle and surface energy as well as visual inspection were used to determine the degree of change in the surface of the samples after processing. Note that the discharge produced in the coil extended all the way to the grounded electrode.

3.2 Experimental Design

The EMU capacitive discharge processing system, shown in Figure 3.1, consisted of a rectangular machined aluminum main chamber, 40 cm by 20 cm by 18 cm, with access ports for KF bulkhead fittings on 3 sides, two removable top plates with additional access ports, and a transparent loading/unloading door in the front side of the chamber. A hard-anodized black coating serves to protect the aluminum chamber from damage as well as create an insulating surface coating. Process gases were fed into the reactor

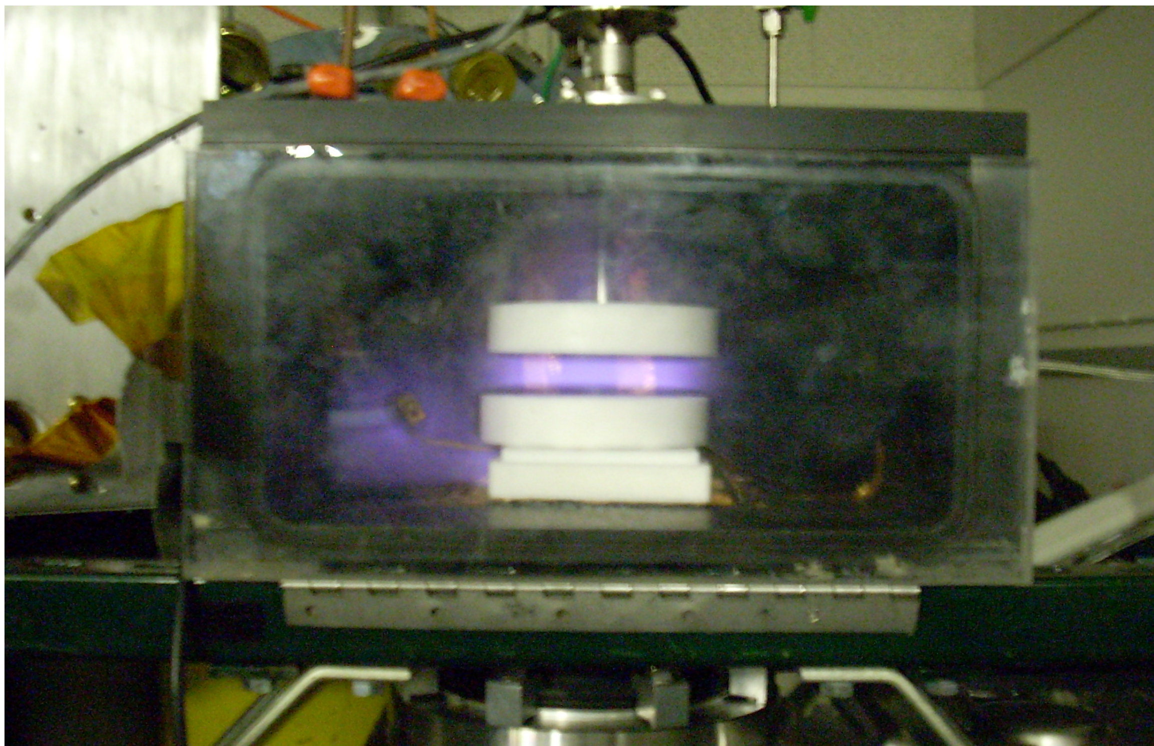

Figure 3.1: EMU processing chamber showing the capacitive glow discharge.(CCP)

through a manifold system consisting of the process gas supply (gas bottle), MKS mass flow controller modules controlled by an MKS Model 305 gas controller, and an MKS PDR-2000 baratron pressure sensor fed into the top of the process chamber through an additional in-line shut-off valve as shown in the system schematic in Figure 3.2. Closed-loop feedback from the baratron gauge allowed the MKS 305 controller to maintain the set point pressure in the process chamber to regulate the gas flow volume. A

Lesker Model PDR-900 pirani gauge and a Varian P-CC2C pressure gauge in the chamber were monitored by separate controllers. The system vacuum was generated by a Varian Model D70V Turbo pump backed by a Varian Model MKX roughing pump in the foreline. A pneumatically controlled VAT Model 64 gate valve allowed the process chamber to operate in either a closed (static pressure/stirred tank) regime or in a throttled flow mode. An additional Lesker 925C pirani gauge monitored the foreline pressure.

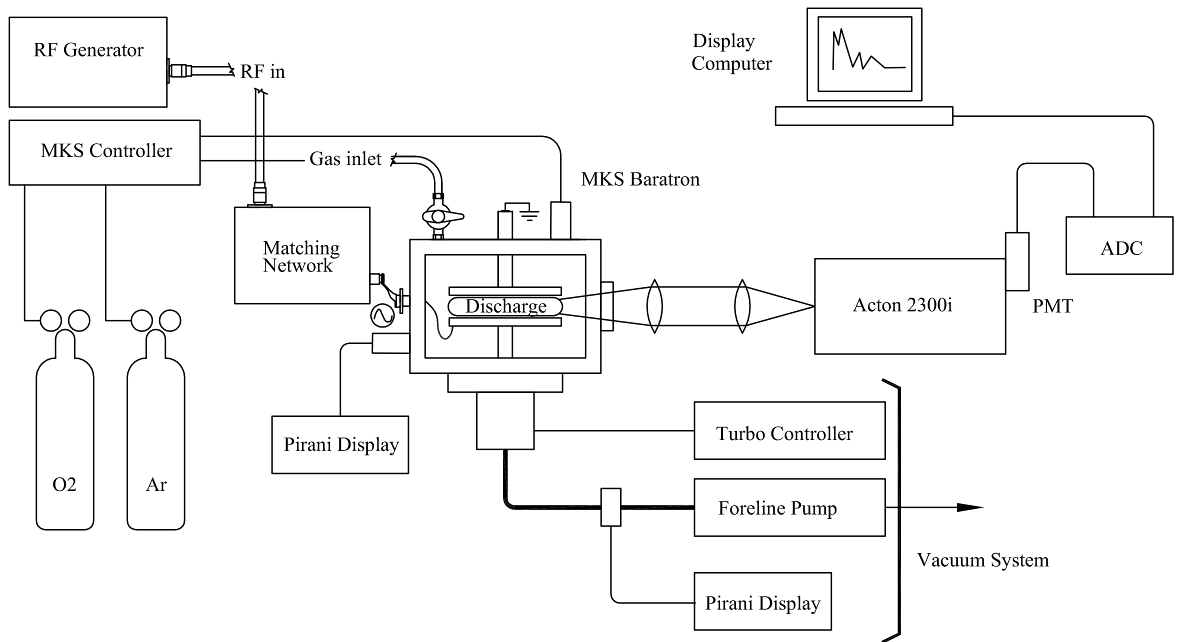

Figure 3.2: Experimental layout of the capacitive discharge system (CCP).

Radio frequency (RF) energy was supplied by a 5kW, water-cooled ENI Genesis RF Generator, model GHW-50, operating at a fixed frequency of 13.56 MHz. This style of generator is widely used in RF discharge research because of its similarity to those used in industrial processing systems.[106] The output of the GHW-50 was an RF wave of a fixed frequency (13.56 MHz) with a variable power output between zero and 3000 watts. The generator system presented a 50 ohm impedance at the output. The matching network, shown in Figure 3.3, is an Advanced Energy Navigator 7013-L90 (L90). The L90 matching unit is an L-type match consisting of a series (C1) and shunt (C2) variable vacuum capacitor, a fixed value high power inductor (L1), and required interface and

control hardware.

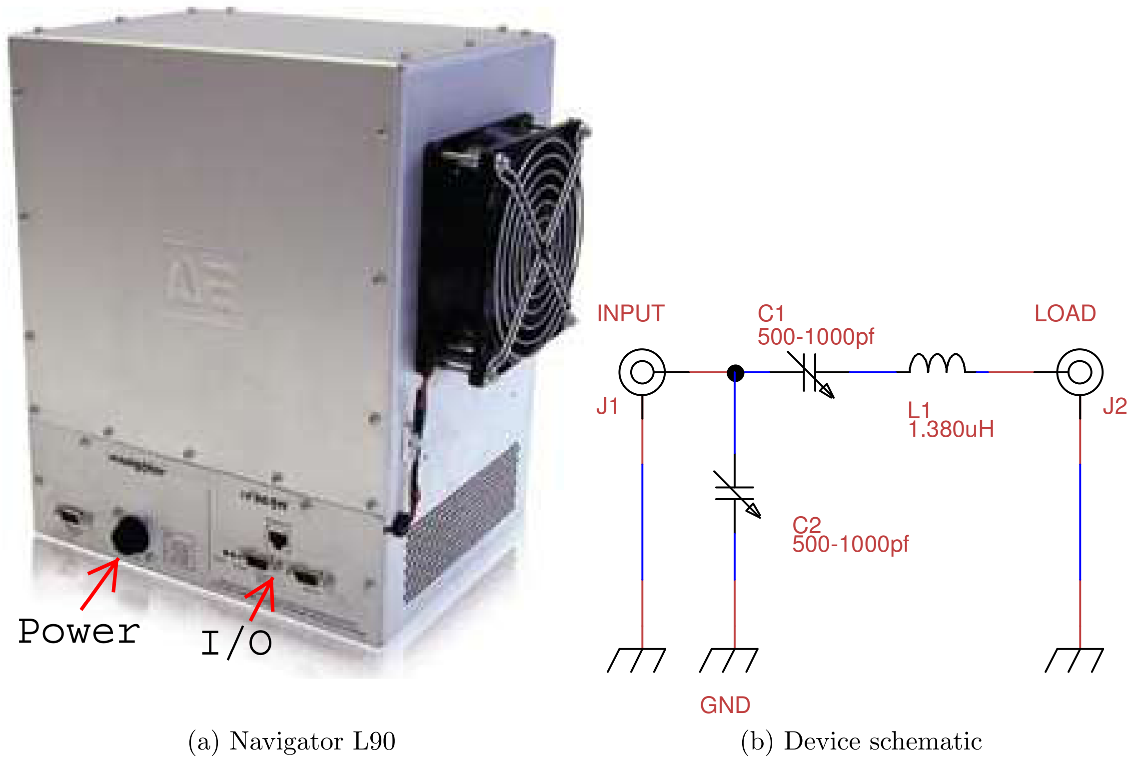

(a) Navigator L90

(b) Device schematic

Figure 3.3: Advanced Energy Navigator 7013-L90 (L90) matching network showing (a) operating power input and I/O network connections. (b) Schematic diagram showing matching network components.

The matching unit was connected to the chamber electrode/coil using 2.0-inch wide flat copper strap to take advantage of the skin effect of RF at higher frequencies and to introduce as little stray reactance as possible.[107,108] The Navigator unit was operated in automatic matching mode but can also be configured to allow on-line manual adjustments of the process in real time, using the supplied Virtual Front Panel (VFP) proprietary software. Many components of the experimental apparatus shown in Figure 3.2 were donated by Applied Materials of San Jose, CA, and Advanced Energy Industries, Inc., of Fort Collins, CO.

3.3 RF Power system

A plasma processing system, used in a production setting, functions best or most efficiently when as large a portion as possible of the generated power is delivered to the load, i.e. discharge chamber. The maximum power theorem can be applied to ensure the transfer of maximum power to the processing chamber. It is described by Orfanidis, Pozar, and others[109–113] as the matching of the generator impedance Z_G to the complex conjugate (${Z^*}_D$) of the discharge impedance Z_D where the resistive portions are equal and the reactive portions are equal in magnitude but of opposite sign, as shown in Equations (3.1) and (3.2).

$$Z_S = {Z^*}_D \tag{3.1}$$

$$Z_S = R \pm jX = {Z^*}_D = R \pm jX$$

where:

Z_S = Impedance of the source

${Z^*}_D$ = Impedance of the discharge (complex conjugate)

Power not delivered to the load is converted into heating losses, which can degrade components in the system and cause unexpected processing results. Once a match between the generator and the load is achieved, the maximum power theorem (3.1) is satisfied and the power from the generator can be efficiently used by the processing chamber.

The impedance of an AC circuit is determined by the relationship between resistance, reactance, and frequency.[111,114] Impedance, a complex quantity, consists of two components, one resistive and one reactive, as shown in equation 3.2

$$Z = R \pm jX \tag{3.2}$$

where R is the resistive portion and is real resistance that does not change with frequency, j is the imaginary operator, and X is the reactance, or that portion associated with inductance or capacitance and changes with the frequency. In order to match the impedance from the source, Z_S, to the impedance of the process discharge, Z_D, combinations of resistances and reactances are selected to cancel the difference in impedance between the two. The impedance of the chamber can be described as a lumped complex impedance consisting of resistive (R_D) and reactive (jX_D) elements (3.2) as shown in Figure 3.4.[27,115–118]

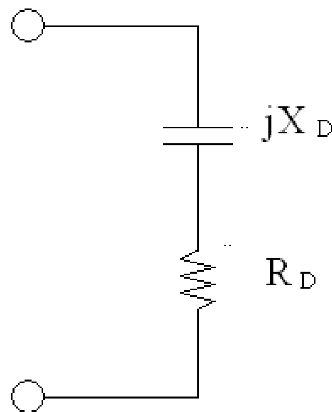

Figure 3.4: Lumped impedance of a capacitive discharge showing resistive and reactive components of the complex impedance.[27]

The initial impedance of the discharge is high since the unlit capacitive chamber is both an open circuit, with infinite resistance (R_D), as well as a completely reactive (jX_D) load. An initial impedance of a chamber of this type, neglecting stray capacitance, can be calculated by finding the reactance of the chamber using (3.3) and (3.4). The expected *capacitive* reactance, X_C, of the Eastern Michigan University chamber

calculated from the standard definition found in References[111,114,119] was:

$$
\begin{aligned}
X_C &= \frac{1}{2\pi f C} \qquad (3.3)\\
&= \frac{1}{2\pi \times 13.56 \text{ MHz} \times 3.5 \times 10^{-12} \text{ F}}\\
&= 298.5\ \Omega
\end{aligned}
$$

when:

$$
\begin{aligned}
C &= \epsilon_r \epsilon_0 \frac{A}{d} \qquad (3.4)\\
&= 1 \times 8.854 \times 10^{-12} \text{ F/m} \times \frac{0.01\ m^2}{0.0254 \text{ m}}\\
&= 3.5 \times 10^{-12} \text{ F}
\end{aligned}
$$

where:

f = generator frequency, Hz

C = capacitance in farads, F

A = area of overlap of the two plates measured in square meters (0.01) m^2.

ϵ_r = dielectric constant of the material between the plates (1.00059 for air),

ϵ_o = permittivity of free space $\epsilon_o = 8.854x10^{-12}F/m$

d = separation between the plates, measured in meters (1.0 inch=0.0254 m)

Equation (3.3) yields the reactive component of the chamber impedance of 298.5 ohms. In this example, the impedance is completely capacitive. The resistive portion will be extremely high (open circuit) until breakdown is achieved. Once the discharge is ignited, the matching network serves to balance the complex conjugate to the changing parameters of the plasma.

As an analytic example, an initial load impedance of $Z_D = 10 - j30\ \Omega$, reported by Ritchey[107] and Advanced Energy[120] as a reasonable beginning estimate for the impedance of a capacitive discharge, can be matched by using one of the methods

outlined by Pozar,[110] Orfanidis,[109] and others.[36,116,121] The two possible arrangements of components in a two-node matching network are shown in Figure 3.5. Case 1 shows the shunt component of the network nearest the load impedance, and Case 2 shows the series component nearest the discharge impedance. Case 1 is used if the $R_D > Z_G$, and Case 2 is used if $R_D < Z_G$. Since $Z_G = R_D \pm jX_D$ (from the generator) and is equal to $50 \pm j0$, while Z_D is equal to $10 \pm j30$, (10 Ω) is smaller than (50 Ω), so Case 2 applies.

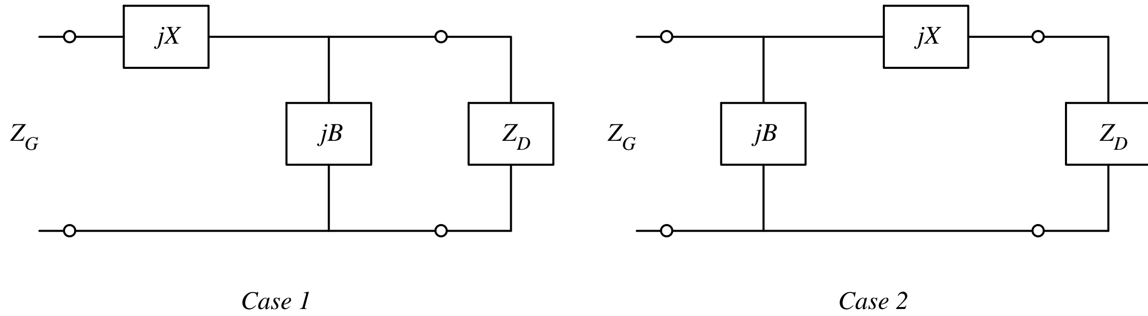

Figure 3.5: Case 1 and 2 matching networks illustrating the arrangements of reactance used with (3.5) and (3.6) to calculate components required for impedance match.[109,110]

This method of calculating the complex conjugate ($Z^*{}_D$) of the discharge impedance Z_D involves a simple relation of X_D, R_D, Z_G, and the calculated value for the susceptance (B) as shown in Equation 3.5 and 3.6 from Orfanidis[109] where:

$$B = X_D \pm \frac{\sqrt{R_D/Z_G}\sqrt{R_D^2 + X_D^2 - Z_G R_D}}{R_D^2 + X_D^2} \tag{3.5}$$

$$= 1.383\ S$$

and

$$X = \frac{1}{B} + \frac{X_D Z_G}{R_D} - \frac{Z_G}{B R_D} \tag{3.6}$$

where:

X_D= reactive component of the discharge (30 Ω)

R_D= resistive component of the discharge (assumed 50 Ω)

B=Susceptance (Siemens)

Z_G= generator impedance (50 Ω)

Once the susceptance (B) and reactance (X) are found, the values of the physical components required to represent (jB) and (jX), required to match the target impedance, can be calculated using Equations 3.7 and 3.8.[114]

Calculations (3.7) and (3.8) yield physical component values for both the shunt inductor (L) and for the series capacitor (C) required to match the generator impedance Z_G to the target discharge impedance, Z_D.

$$C = \frac{1}{2\pi f jX} \tag{3.7}$$
$$= 324.7 \text{ pF}$$

$$L = 2\pi f jB \tag{3.8}$$
$$= 293.2 \text{ nH}$$

where:

jX=capacitive reactance

jB=inductive reactance

f=13.56 MHz

Substituting these values back into the Case 2 diagram, re-drawn in Figure 3.6, shows the physical components and values required to match $Z_G = 50 + j0\ \Omega$ to $Z_D = 10 - j30\ \Omega$ and fulfill the requirements for maximum power transfer (3.1). This analytic approach, however, is suited only to a single-point, fixed impedance.[109,110]

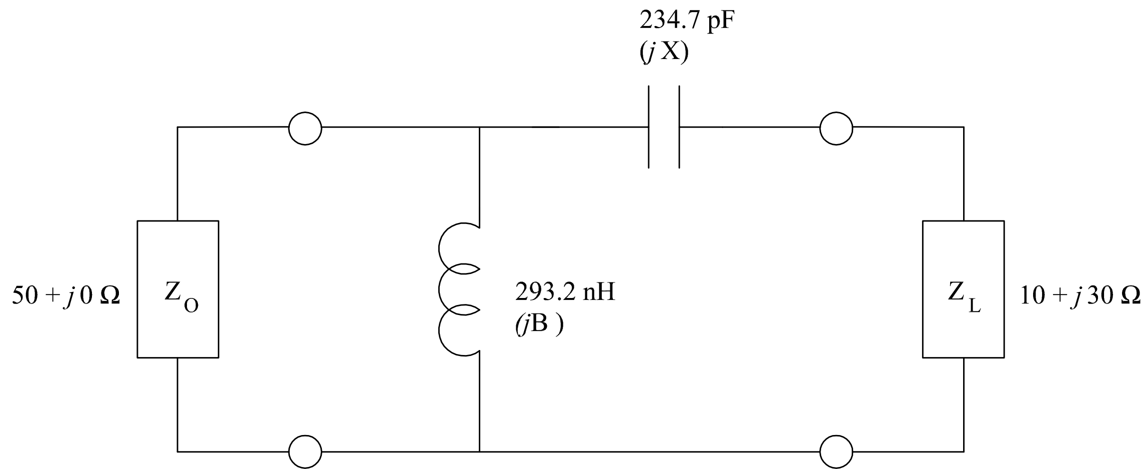

Figure 3.6: Schematic of matching network showing calculated values substituted into original two-node network.

Matching a changing process requires a more robust solution. A properly configured variable matching network uses continuously variable capacitive and inductive reactances, within component limits, to discover the complex conjugate ($Z^*{}_D$) of the discharge impedance Z_D based on feedback from the process, as the discharge parameters change during processing. This automated approach, as implemented in the L90 matching network, greatly extends the capabilities of the match beyond the single point matching discussed earlier (page 24). The use of an automated approach enables the unit to find a successive number of possible matches that fall anywhere within the area bounded by the minimum and maximum values of the reactive components. The initial measured impedance value ($10 - j30\ \Omega$) of the discharge (Z_D) is shown plotted in Figure 3.7a, as a plot of real versus imaginary components of the discharge impedance Z_D (page 24). The same impedance value is shown in Figure 3.7b plotted on an admittance Smith Chart outlining the same limits of the automatically tuned reactances.[120] The location on the charts of the impedance value within the limits of the matching area indicated the ability of the L90 unit to create a complex conjugate required to enable the unity match of the

chamber and the generator. The difference in hardware realization and control, and the extension of the tuning range due to the addition of variable reactances, enhances the ability of the network to match the load to the source although the method is fundamentally the same as discussed in (3.5) and (3.6).

The Smith Chart, although developed in the 1930s, is a tool that is still appropriate for use in RF plasma processing. Use of the chart allows a quick determination of a starting point about which the match can be adjusted as the process conditions change. The availability of Smith chart application software allows the wider use of this tool. The application used in this experiment was LLSmith software.[122] The Smith chart is a graphical format tool constructed to enable the relation of impedance, admittance, reactance, and resistance. The Smith chart consists of circles of constant resistance (R_D) and circles of constant reactance (X_D) that enable the manipulation of the same quantities used in the earlier analytic solution, but allow a graphical interaction with

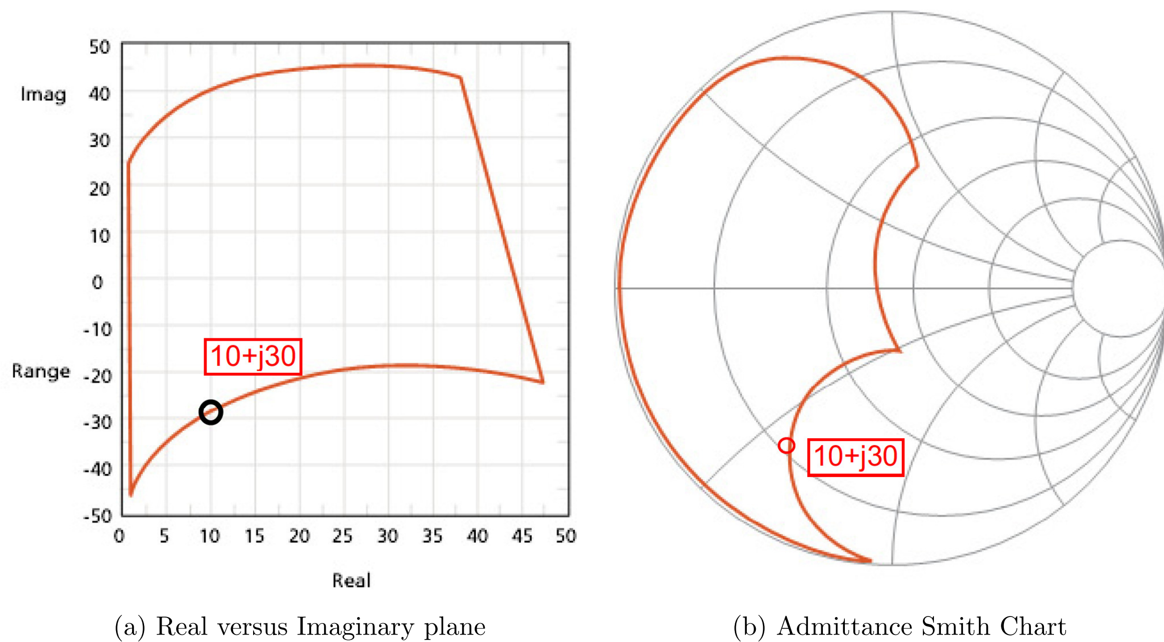

(a) Real versus Imaginary plane

(b) Admittance Smith Chart

Figure 3.7: Navigator L90 tuning range showing chamber impedance (Z_D) of capacitively coupled discharge (circle) located on, a) a plot of tuning range showing real versus imaginary axes and, b) tunable range plotted on admittance Smith Chart. Blank charts are taken from Navigator L-90 Manual.[122]

these quantities to show "real-time" modification of the matching parameters.[113,123] Plotting the complex impedance (from page 23) as shown in Figure 3.8 at point a locates the load impedance on the chart. Working from the load (Z_D) toward the generator (Z_G), the addition of a shunt inductance moves the inductance point clockwise along the constant reactance circle, above the r-axis to the intersection of the +j20 admittance circle at point b. The addition of a series capacitive reactance moves the point clockwise along the 50 Ω constant resistance circle to the generator match point, 50+j0 Ω at point c. A comparison of the final component values required to create the complex conjugate (${Z^*}_D$) of the discharge impedance Z_D using the analytical and Smith chart methods is shown in Table 3.1. Physical component values required to match the discharge impedance Z_D, calculated by using the Smith chart application and comparable values calculated using the analytic method, (3.7) and (3.8), were found to be in good agreement. The addition of the Smith chart as a processing tool allows the examination of additional solutions to the matching problem.

Table 3.1: Comparison of component values used to calculate the complex conjugate (${Z^*}_D$) of the discharge impedance Z_D using both analytic and graphical (Smith chart) methods.

	Generator			Load			Reactance	
	Z_G	R_G	X_G	Z_D	R_D	X_D	Capacitive	Inductive
Analytic	50+j0	50	0	10-j30	10	-30	324.74 pF	293.21 nH
Smith	50+j0	50	0	10-j30	10	-30	324.73 pF	293.81 nH

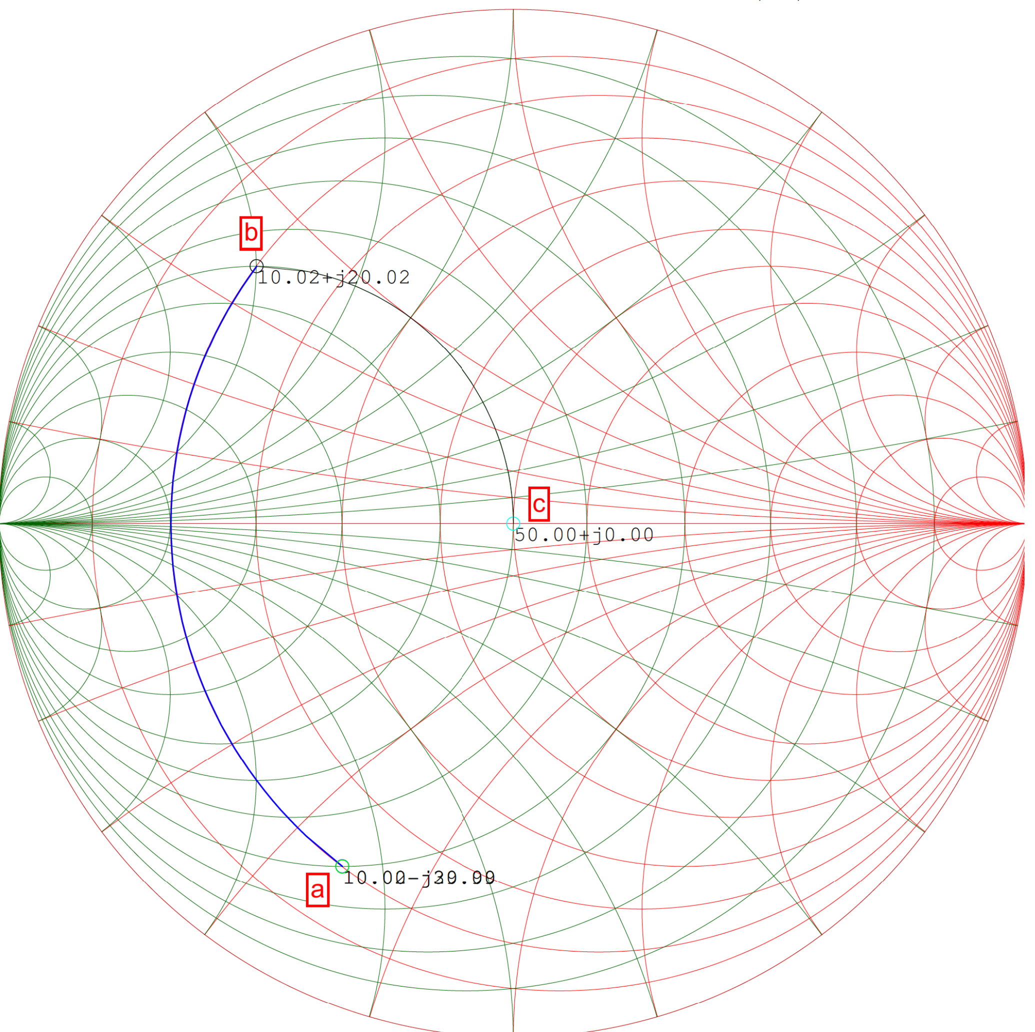

Figure 3.8: Smith chart showing a) Normalized complex impedance value of processing chamber (Z_D), b) Cancellation of initial capacitive reactance, c) Cancellation of remaining reactance and adjustment of resistance to $50 + j0\Omega$. Chart plotted using LLSmith software application.[122]

3.4 Decoupled Plasma Source (DPS)

In order to provide plasma with a higher electron density (10^{12} cm^{-3} vs. 10^{10} cm^{-3}) for improved sample processing, the Eastern Michigan University system was modified to change the process reactor from a capacitively coupled plasma discharge (CCP) system to a decoupled plasma source (DPS) system. These changes, although related to work by Miller et al.[124] and in a design reminiscent of the early LAM Systems ICP process tools,[26] originated as an in-house experimental chamber built by Advanced Energy for the removal of pattern photo resist from silicon wafers,[80] also known as ashing.

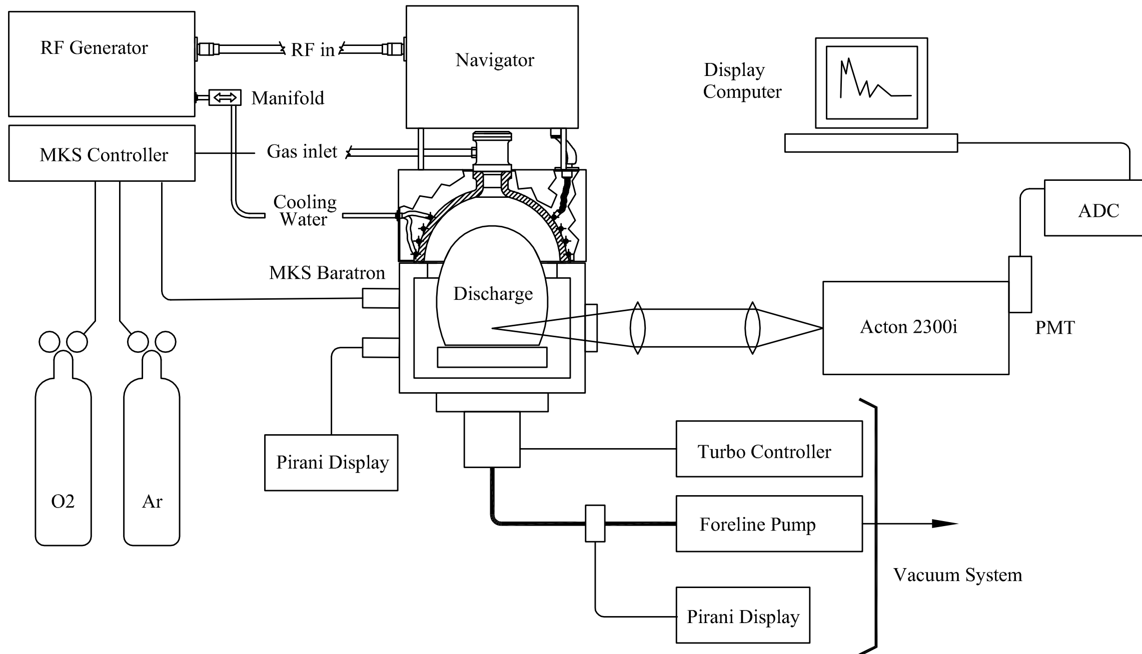

Figure 3.9: Experimental layout of the decoupled plasma source system (DPS).

The top electrode used in the DPS assembly (Figures 3.9, 3.11, and 3.12) consists of a bell jar (9.0 inches in diameter by 4.5 inches high) with a four-turn coil wound around the outside of the dome, comparable to the Applied Materials Omega series inductive solenoid system,[26] and includes a process gas inlet upstream of the coil and direct attachment of the matching network to the support structure. The coil was fabricated of 0.25 inch diameter copper tubing supported equally around the dielectric dome with

fabricated delrin supports. The ends of the coil were connected to bulkhead mounted coolant fittings in the supporting framework. Modifications to the power distribution system included the mounting of a 2-inch wide silver plated copper power inlet strap on the supporting structure.

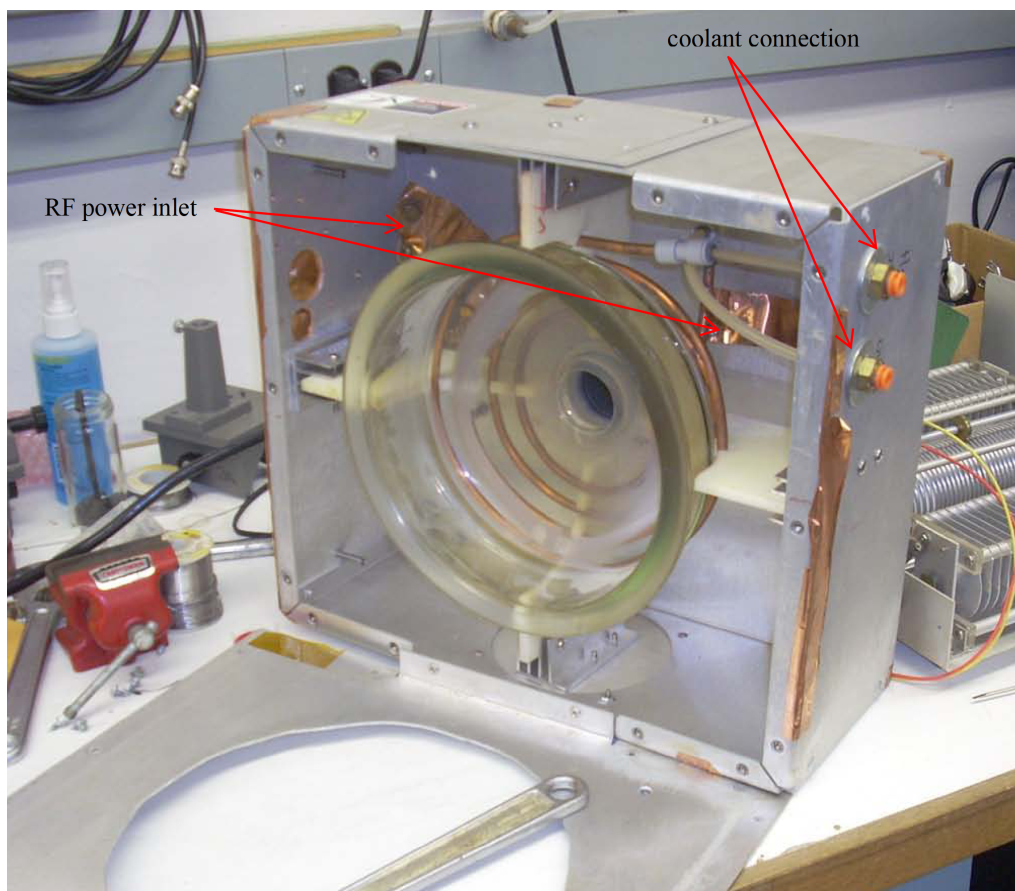

Figure 3.10: Internal construction of inductive top plate assembly. Note the cooling connections to the inductor and the copper straps used to deliver RF power.

Samples to be processed were placed on the isolated electrode at differing distances from the center of the discharge as shown in Figures 3.11 and 3.12. Samples processed in the setup shown in Figure 3.11 were placed in the bulk discharge, 13 cm from the center of the coil, while samples processed in the setup shown in Figure 3.12 were placed at a location, 20 cm from the center of the coil. Design and integration of the water cooling manifold consisted of opening the water cooling system previously used to cool the ENI RF generator and inserting an additional manifold, shown in Figure 3.13a, to direct a

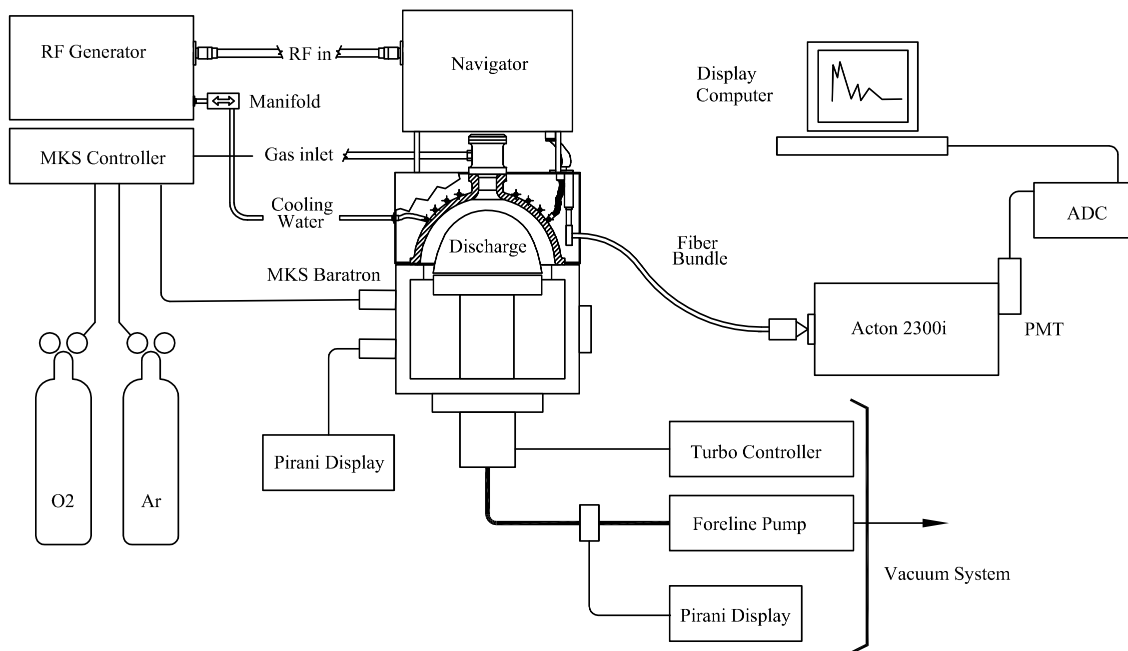

Figure 3.11: Sample placement in DPS reactor at a distance of 13 cm from the center of the coil.

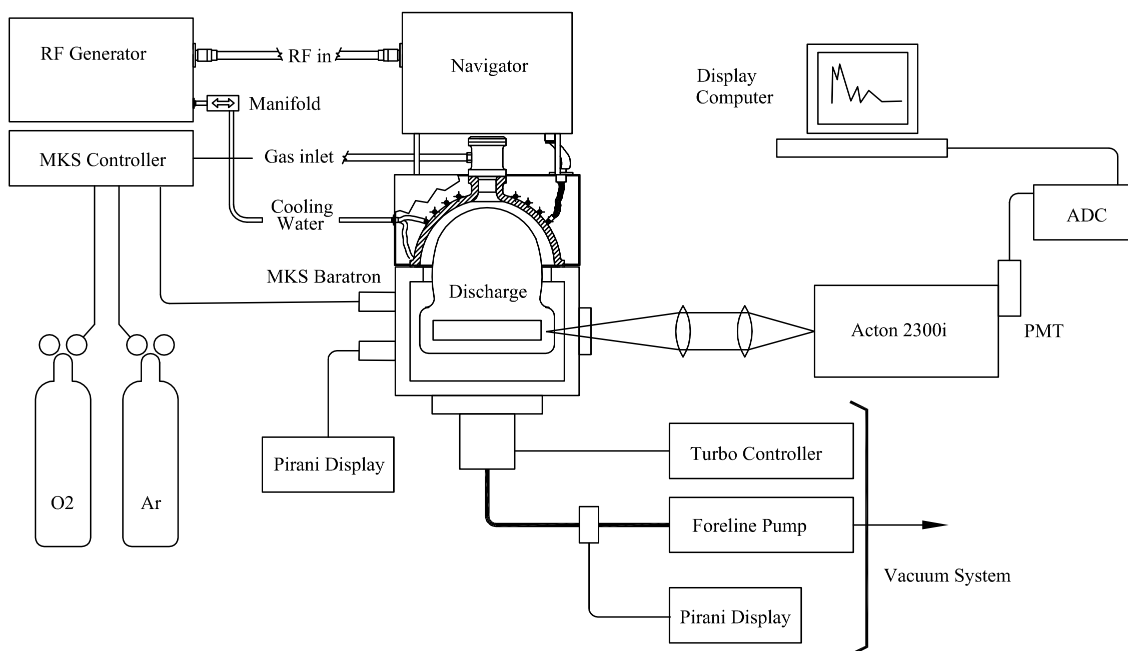

Figure 3.12: Sample placement in DPS reactor at a distance of 20 cm from the center of the coil.

portion of the cooling water through the newly added inductive coil and back into the bulk flow of cooling water, as shown in Figure 3.13b.

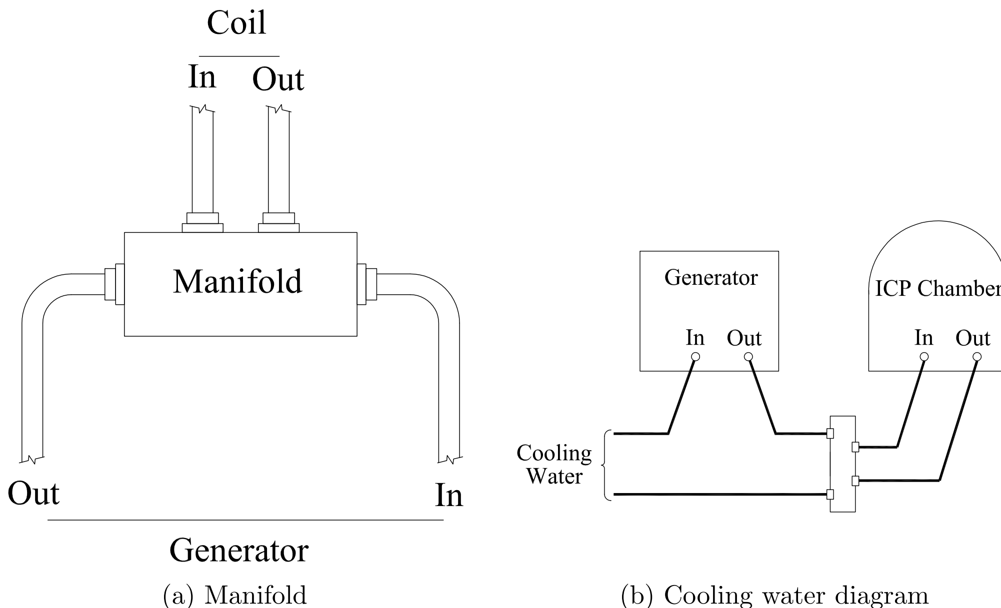

(a) Manifold

(b) Cooling water diagram

Figure 3.13: Design and integration of the water cooling manifold consisted of: a) Design and fabrication of an additional manifold. b) Modification of the water cooling system to direct cooling water through manifold and inductive coil.

The system configuration allowed no direct optical access to the densest part of the discharge, the center of the coil. An optical fiber bundle was placed in the line of sight of the dense discharge by fabricating a ferrule mounting fixture that was attached to the bell jar supporting structure. This optical line of sight was used to monitor the samples using optical emission spectroscopy (OES) during processing of the poly(ethylene terepthalate) (PET) samples. Location and attachment of the ferrule is shown in Figure 3.14.

Modification of the Navigator L-90 matching unit was required to compensate for the increase in inductive reactance of the system created by the addition of the discharge coil. Comparison of the capacitive chamber starting impedance (Z_D) to the initial measured impedance of the inductive DPS chamber, shown in Table 3.2, illustrates the change in system impedance from capacitive to inductive ($-j$ to $+j$), and an increase in system inductive reactance due to the addition of the coil used for generation of the

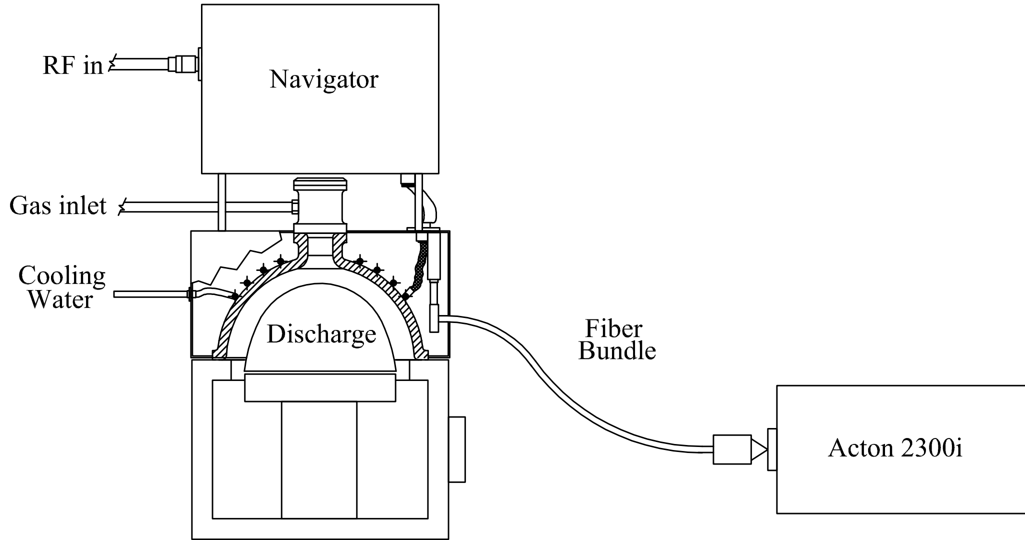

Figure 3.14: Placement of optical fiber bundle in DPS System

discharge. The change in system impedance, from capacitive to inductive, was consistent with behavior found by Miller et al.[124]

Table 3.2: Comparison of impedance values between the planar electrode discharge and the DPS coil discharge showing the change in the reactive component of the impedance from capacitive to inductive.

chamber configuration	Z_D (ohms)	R	X	Z_D mode
planar electrode	$10 - j30$	10	$-j30$	capacitive
DPS coil	$10 + j50$	10	$+j50$	inductive

A plot of the inductive DPS system impedance (Z_D), shown in Figures 3.15a and b, illustrates the change in system impedance in a graphical format. The measured initial impedance value ($10 + j50\ \Omega$) of the DPS discharge (Z_D) is shown in Figure 3.15a, as a point on the chart of real versus imaginary components of the discharge impedance Z_D (page 24) that lie within the limits of the matching components used in the L-90 matching unit. The impedance value is also shown in Figure 3.15b as a point on an admittance Smith Chart outlining the same limits of the possible reactances that can be

automatically tuned.[120] The value of the new impedance (Z_D) is not within the boundaries of the matchable area as outlined by the Navigator specifications[125] and therefore cannot be matched by the L90 match unit in the present configuration.

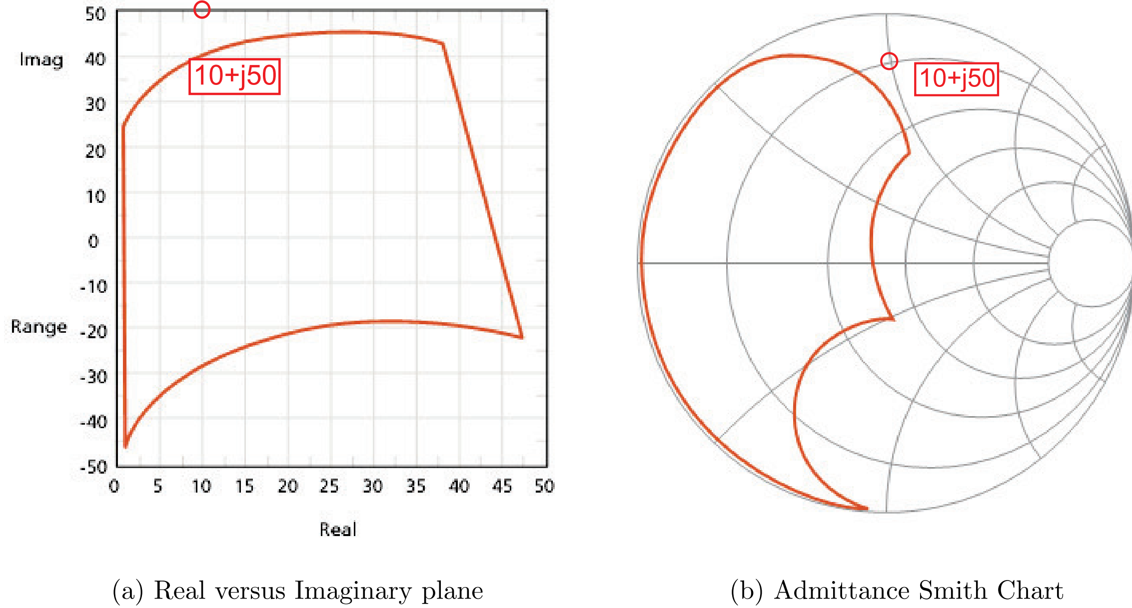

(a) Real versus Imaginary plane

(b) Admittance Smith Chart

Figure 3.15: Navigator L-90 tuning range showing chamber impedance (Z_D) of inductive DPS discharge (circle) located on, a) Chart of real versus imaginary axes and, b) Tunable range plotted on admittance Smith Chart. Blank charts are taken from Navigator L-90 Manual.[125]

The required reduction of system inductance was accomplished by removing the standard inductor, as discussed in reference,[124] and replacing it with a 1-inch wide silver-plated copper strap. The electrical change to the matching network is shown in Figure 3.16. After completion of the chamber modifications, the DPS system was prepared for a preliminary test processing run. The system was evacuated using the vacuum management and sensor systems used previously and shown in Figure 3.2, to a chamber pressure of 1.0 x 10^{-5} torr to establish the system base pressure. Oxygen gas was streamed at 20-50 sccm and system pressure was raised from 3.0 x 10^{-3} torr and maintained at 1.0 x 10^{-1} torr. A forward power of 250 watts was applied to the chamber by the generator (ENI), and a reflected power of 0 watts was measured by the power

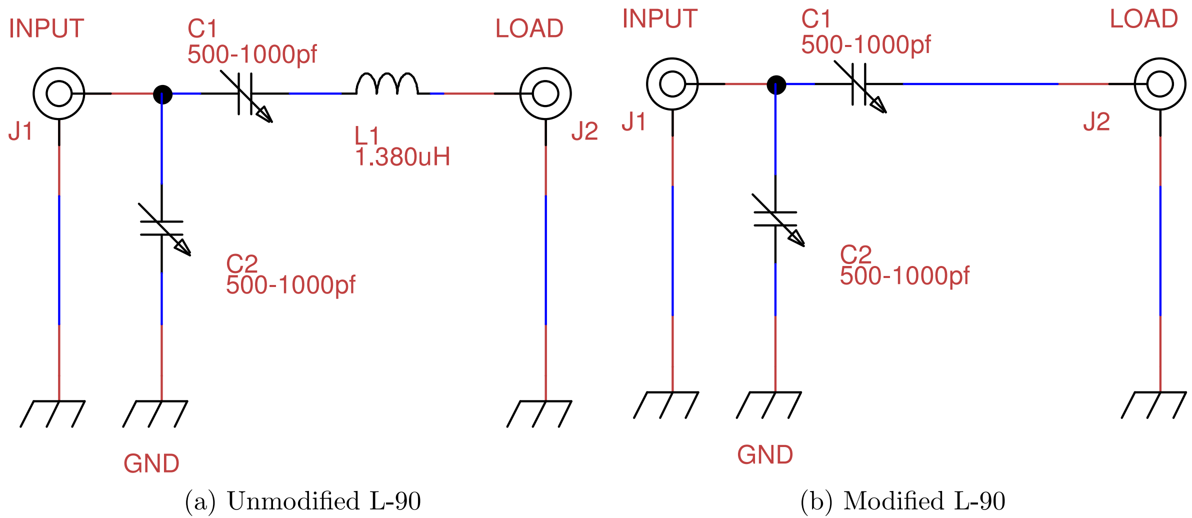

Figure 3.16: Schematic of L-90 matching unit showing: a) Matching network as supplied for use with a capacitive system and, b) Matching network as modified for use with the inductive DPS system.

metering display in the generator, indicating an ideal match which remained stable throughout the remainder of testing. System behaviors after the modifications were consistent with those found by Miller et al.[124]

3.5 Optical Diagnostics

Optical emission spectroscopy (OES) was used to monitor and identify atomic and molecular species generated during processing. OES is a non-invasive method of monitoring changes in the discharge during processing and can give real-time information regarding the species generated during processing.[27,126] The species seen can also give insights into the type of reaction between the discharge and the sample. The appearance of atomic hydrogen (H_α) at 656 nm indicated that the plastic was being broken down by interaction with the discharge, freeing the hydrogen bound in the PET molecules. If sputtering occurred, free carbon atoms would be released and observed in the discharge; they were not. Two optical assemblies were required; a collimating field lens assembly using a pair of 50 mm diameter, f/9 quartz lenses with a 14 inch focal length was

constructed to image light from the center of the discharge onto the entrance slit of the spectrometer as shown in Figure 3.11 while optical fiber was used to acquire light from the center of the discharge and carry it to an Oriel 77612 collimator assembly that imaged the light onto the entrance slit of the spectrometer, as shown in Figure 3.12. The spectrometer was an Acton model 2300i, a Czerny-Turner configuration instrument with an integrated photomultiplier tube (PMT) detector both supplied by Princeton Instruments. The focal length of the 2300i is 300 mm and had a f/D ratio of f/4. The

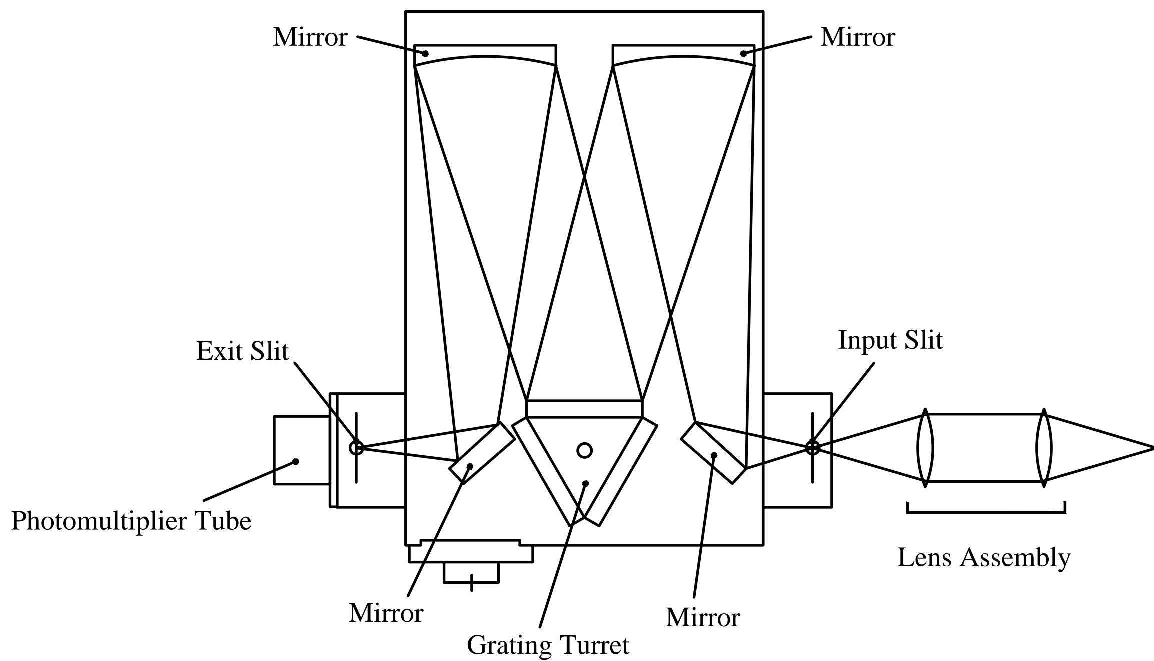

Figure 3.17: Diagram of the Acton 2300i monochromator (Czerny-Turner Style) showing grating turret, PMT at output slit, and field lens assembly used with the Eastern Michigan University chamber.

spectroscopic/optical configuration was sufficient to allow resolution of spectral features as small as 0.7 nm, as measured from an isolated Ar line in a wavelength calibration lamp. The resolution is defined to be the full width at half-maximum of an isolated line.[127] Initial spectral scans were taken using the method outlined by Selwyn,[126] i.e., an initial scan of the area of interest using a low rule number grating and increasing by repetition to the highest ruling available in order to see finer and finer features.

Real-time acquisition and display of spectral data was carried out using the supplied SpectraSense^{TM} software. The software allowed the control of several parameters such as integration time, PMT voltage, dark current subtraction, and timing of multiple scans. The optical signal-to-noise ratio was determined by varying the input and output slit width, sample integration time, and PMT voltage. Both the input and output slit widths were set at 20 μm x 4.0 mm. The integration time was adjusted to optimize the signal to noise ratio (largest number of counts that would not saturate the PMT detector) and was finalized at 100 μs. The PMT voltage was set to 975 volts and was not changed throughout the experiments. A background spectrum was automatically acquired before each scan and used for dark current subtraction, allowing automatic removal of temperature dependent and electronic noise generated in the PMT. The SpectraSense^{TM} software also allowed off line display and processing of acquired spectra. Spectral line identification was carried out using Spectrum Analyzer software.[128] This software allowed the comparison of the acquired spectra to the NIST[129] spectral information databases.

Calibration and alignment of the optical system was required prior to the acquisition of spectral data. Alignment of the optical path through the monochrometer assures that the maximum signal can be acquired from the low light level of the oxygen discharge for spectral characterization. Initial calibration of the scanning mechanism minimized mechanical uncertainty in the wavelength scanning mechanism of the monochrometer to ensure accurate identification of species produced by the discharge. Relative calibration of intensity takes into account the individual wavelength responses of the items that make up the optical system, such as the lenses, monochromator, quartz window, and PMT, and allows the calculation of the *system* response as a function of wavelength ($R(\lambda)$). The wavelength calibration gave an accurate comparison of intensities at different wavelengths.

Alignment of the optical path was accomplished using a modification of the method described by Sainz and Coleman.[130] A low power Helium-Neon laser was set at the optical

center (XZ-axis) of the input slit of the monochromator. The beam was reflected through the optical path of the monochromator (mirror 1, mirror 2, grating, mirror 3, mirror 4) onto the exit slit at the center of the optical path. The vertical (Z-axis) alignment was confirmed by measurement of the beam height above the common base plane at the entrance and exit slit of the instrument. The components in the optical assembly were adjusted into the optical centerline in the same manner as the initial alignment of the monochromator. After alignment, the PMT was attached to the monochromator output, the process chamber replaced, and the quartz access window centered on the optical axis.

Calibration of the instrument wavelength scale for accuracy across the spectrum was accomplished by scanning across the range of the instrument using a calibration lamp as the source. The output of a Hg(Ar) calibration lamp (Newport 6035) was imaged onto the slit of the spectrometer as shown in Figure 3.18. Comparison of the peak wavelengths scanned by the instrument versus published spectral peak data[129,131] allowed the calculation of a wavelength correction factor ($\Delta\lambda$) that was applied in the instrument scan control software for correction[132,133] of any inaccuracies in the scanning mechanism. A tungsten spectral irradiance standard manufactured and calibrated by Optronics

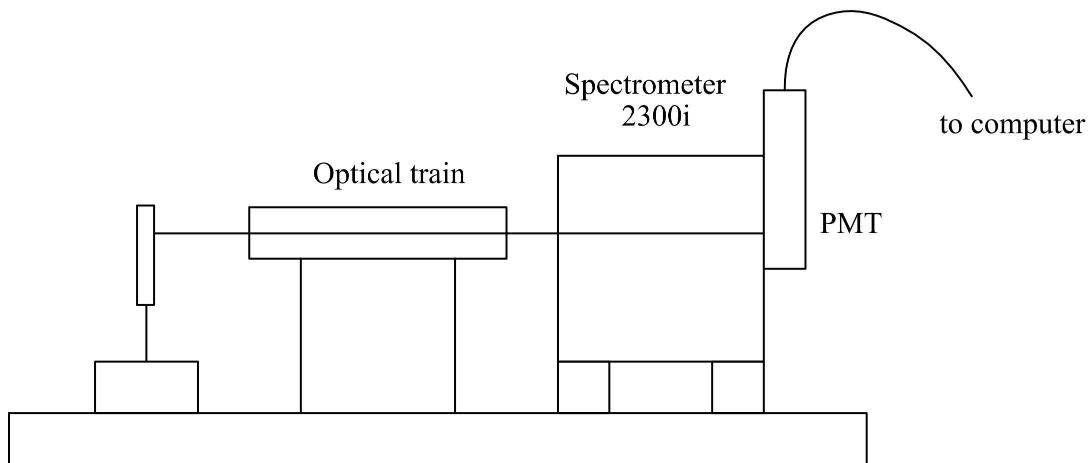

Figure 3.18: Showing setup for wavelength alignment

Labs,[134] scanned over a range of 250 nm to 900 nm, was used to determine the wavelength response of the system as shown in Figure 3.19. The measured intensity, $I(\lambda)$,

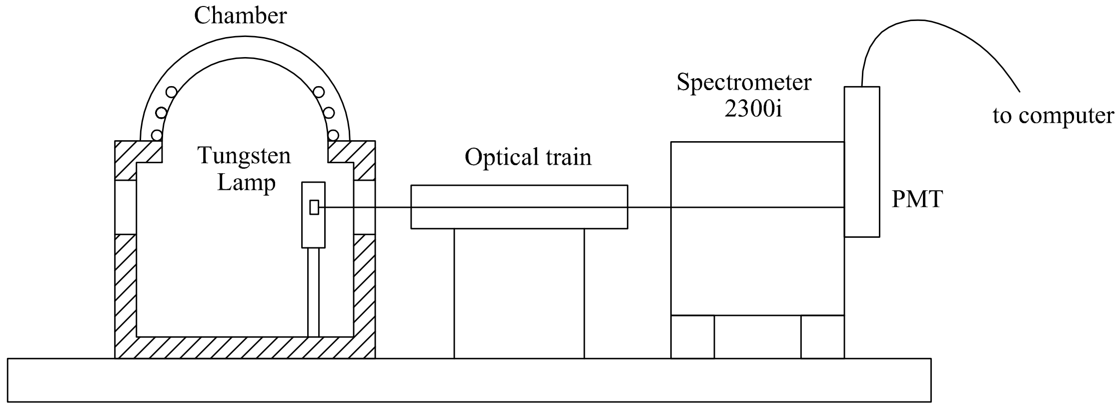

Figure 3.19: Relative irradiance calibration used a NIST traceable tungsten ribbon lamp imaged on to the entrance slit of the monochromator.

was related to the tungsten calibration data, $I_\omega(I\lambda)$, as shown in equation (3.9), yielding an intensity correction factor, as a function of wavelength ($R(\lambda)$) for the instrument and optical path.[132,133,135]

$$R(\lambda) = \frac{I(\lambda)}{I_\omega(I\lambda)} \tag{3.9}$$

3.6 Material Diagnostics

Initial characterization of the full data set measured the surface energy (γ) and contact angle (θ) of the sample material using two methods. The sample material tested was poly(ethylene terephalate) (PET) film, 0.005 inches thick, supplied in a 36.0-inch wide roll, purchased from McMaster-Carr. The first testing method used was the Standard Test Method for Wetting Tension of Polyethylene and Polypropylene Films, ASTM-D2578,[136] which is intended for use in a factory metrology setting to give an "order-of-magnitude" indication of the wetting tension value of the material surface and is generally used in industry for inspection of new or incoming sheet polymer materials. The ASTM-D2578 procedure outlines a protocol for comparing the surface tension of a test liquid, a mixture of formamide ($HCONH_2$) and ethyl cellosolve

($CH_3CH_2OCH_2CH_2OH$), to the wetting tension of a material sample in order to ascertain the surface energy of the incoming material sample. The ASTM standard specifies the method for testing the sample at several points across the width of the sheet in order to determine the average surface energy of the material and is shown in schematic form in Figure 3.23a. A complete description of the procedure and a copy of the standard is included in Appendix E. The ASTM-D2578 method specifies the use of freshly mixed reagent-grade solutions for testing but also allows the use of commercially prepared solutions.[136] The solutions used for these tests were purchased from UV Process Supply, Inc., and consisted of 6 pens, each covering a range of surface energies as shown in Table 3.3. The surface tension values were certified by the vendor and were guaranteed to be stable for the duration of the testing.

Table 3.3: Surface tension values of ASSTM-D2578 testing pens

	Test Liquid Series					
Tube	1	2	3	4	5	6
Dynes/cm	20-30	30-40	40-50	50-55	55-60	60-65

After initial inspection using the ASTM standard method, 200 mm diameter sample coupons of the PET material were cut from the roll of sample material, as shown in Figure 3.23b, as supplied by the vendor. The test coupons produced were washed with isopropyl alcohol, rinsed with deionized water, and wiped dry with a lint-free wipe. After preparation the sample coupons were stored in an air-tight container until exposed to the processing discharge.

The second testing method compared the relationship between the contact angle of a sessile drop of test liquid, deionized water, (DI) and the surface of the material sample to indicate a change in surface condition of the sample.[137] A dynamic contact angle (DCA) video goniometer Model FTA-200, supplied by First Ten Angstroms, was used to measure contact angles for sample characterization and was also used for characterization of samples in the preliminary study. The DCA method was more time-consuming than

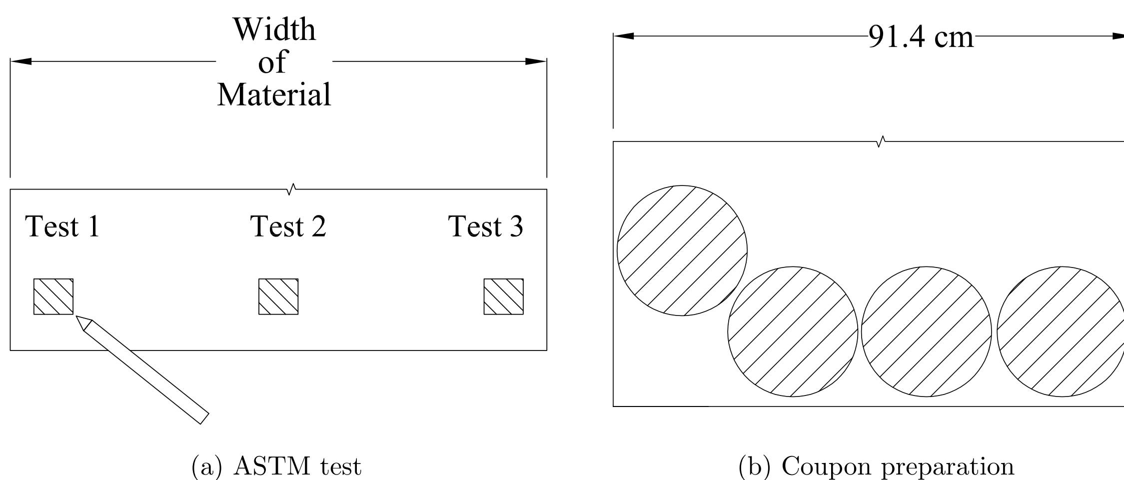

(a) ASTM test (b) Coupon preparation

Figure 3.20: Initial material testing and sample creation, a) ASTM inspection test, b) Samples cut from the as-received material.

the ASTM test; however, the greater resolution of the measured data made possible by the use of the DCA gave additional insights into the relationship between the discharge and the sample surface. All tests were conducted at standard laboratory controlled temperature, pressure, and humidity.

The sessile drop method of surface energy measurement is a widely used[5,19,105,138,139] method of surface energy measurement that uses Young's equation and the contact angle formed between the drop and material surface to calculate the surface energy of a material sample. The contact angle value alone is widely used as a quick relative measure of comparison of the relative wettability of one surface with respect to another or in order to quantify the change in wettability of a surface after treatment.[5,138,140] Contact angle is only one component of the surface energy of a material. Surface energy is the relation of three force components, γ_{GL}, γ_{SL}, and γ_{GS}, shown in equation 3.10 and Figure 3.21. Young's theorem, shown in Equation 3.10, says that the force on the gas-liquid side of the equation (γ_{GL}) is related to the difference between the surface energy of the gas-solid (γ_{GS}) and the solid-liquid (γ_{SL}) interfaces at some equilibrium angle (θ). A large contact angle indicates a hydrophobic material condition, and a small contact angle

indicates a hydrophyllic material condition. When the surface tension of the test liquid equals the wetting tension of the sample, the equilibrium angle will be zero; at that point $\cos\theta = 1$ and the liquid is said to have wetted the solid surface.[137]

$$\gamma_{\mathrm{GL}} \cos\theta = \gamma_{GS} - \gamma_{SL} \tag{3.10}$$

Where:

θ = angle of contact of the edge of the drop with the solid surface

$\gamma_G L$ = surface energy of the gas - liquid interface

γ_{GS} = surface energy of the gas - solid interface

γ_{SL} = surface energy of the solid - liquid interface.

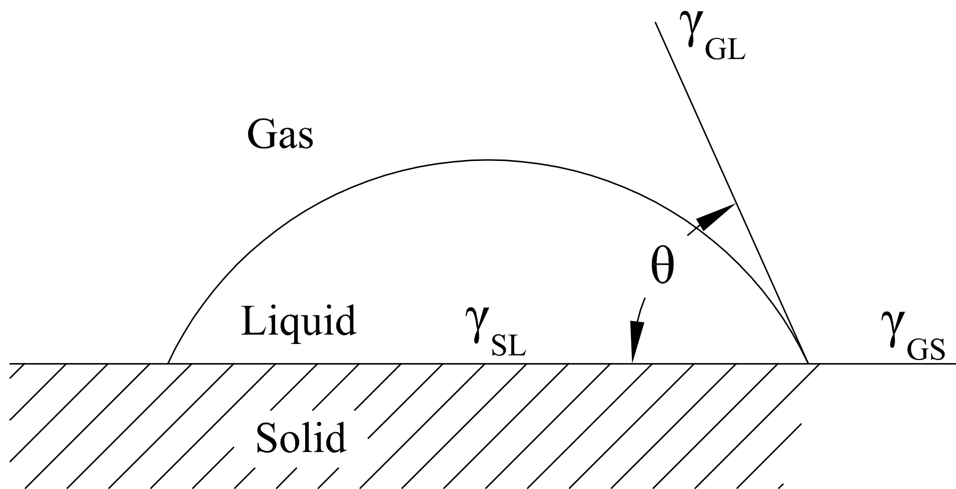

Figure 3.21: Sessile drop showing relationship between contact angle and surface energies γ_{GL}, γ_{SL}, and γ_{GS}.

The DCA goniometer was calibrated using the optical tensiometer function of the FTA-200. Measurement of surface tension of a known test fluid, shown in Figure 3.22, consisted of dispensing a quantity of deionized water such that the drop is large enough to be affected by gravity (about 14 μl) and calculating the surface tension of the droplet using Young-Laplace relation as shown in equation 3.11 to compare the change in the

radius of the drop about the centerline of the pendant drop.[141]

$$\Delta p = \gamma \left(\frac{1}{R_1} + \frac{1}{R_2} \right) \tag{3.11}$$

where:

Δp = pressure difference between the phases (liquid-air)

γ = the interfacial tension

R_1 and R_2 = radii of the curved surfaces.

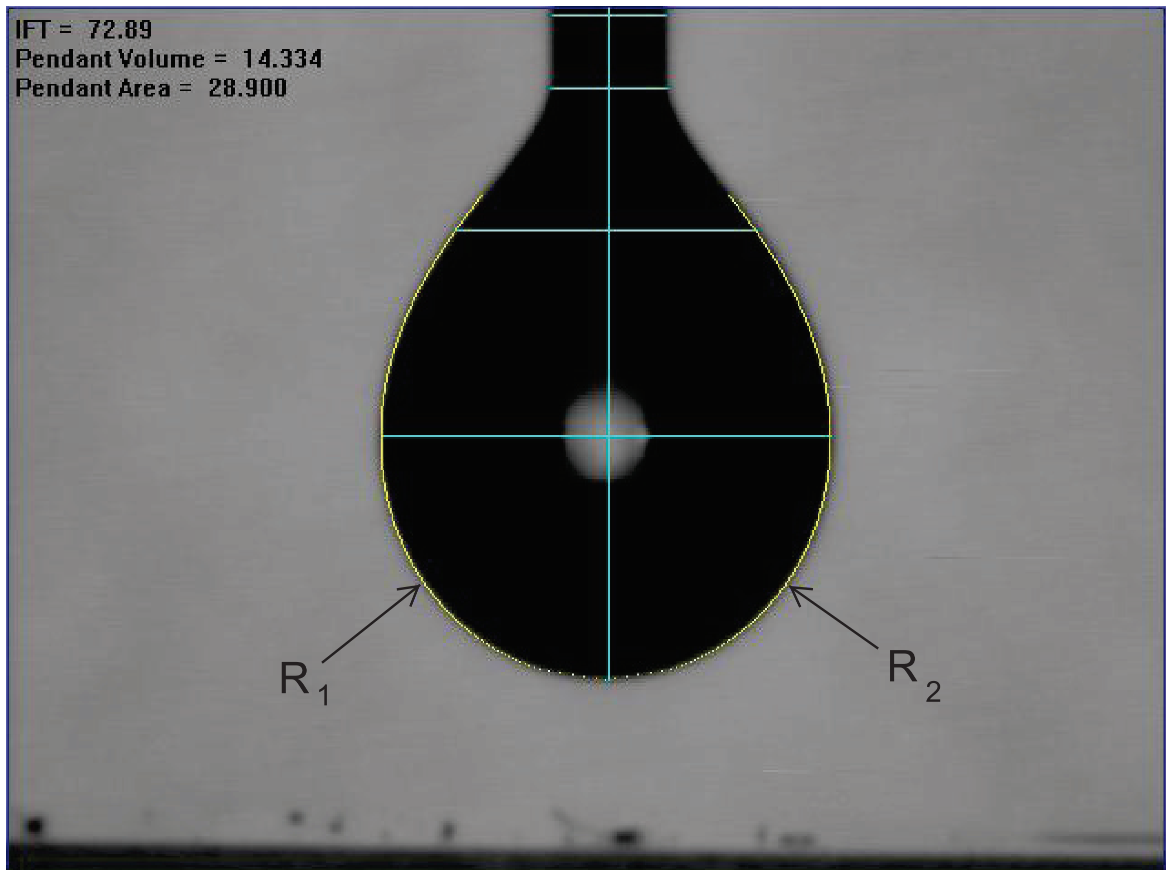

Figure 3.22: Results of the FTA-200 DCA used in tensiometer mode showing measured interfacial tension value of 72.89 for sample of deionized water test fluid.

A randomly chosen prepared sample was subjected to an initial characterization that consisted of two series of contact angle measurement using the FTA-200 measuring system (DCA). The first sample characterization consisted of a series of contact angle measurements taken at 5 mm intervals along the centerline of the sample, as shown in Figure 3.23a. The second sample characterization consisted of nine samples taken at 25 mm intervals along the centerline of the sample, as shown in Figure 3.23b. These datasets were used to set the baseline average contact angle value of the samples prior to treatment. Comparison of the average values of both methods is discussed in Chapter 4.

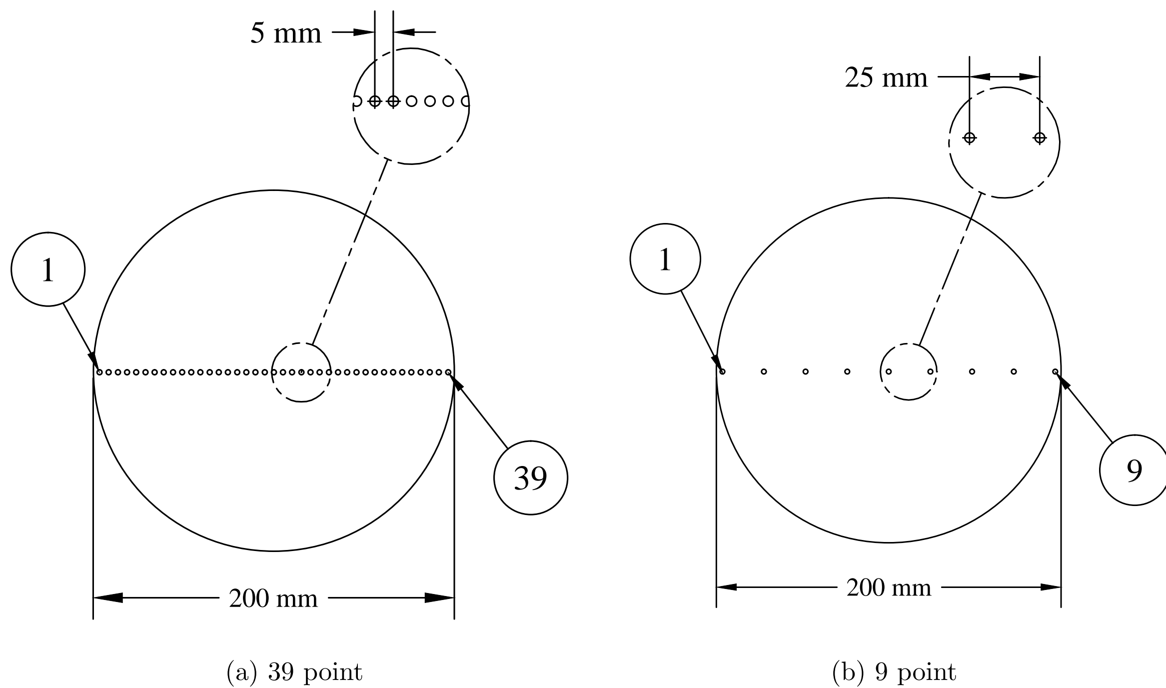

(a) 39 point

(b) 9 point

Figure 3.23: Initial material testing and sample creation, a) 39-point DCA sample examination, b) 9-point sample examination.

3.7 Summary

Experiments were conducted to investigate the effect of an energetic plasma discharge on poly(ethyleneterepthalate) (PET) sample surfaces. The first involved an RF capacitively coupled plasma discharge (CCP) and the second and third, an inductive RF decoupled plasma system (DPS). The plasma discharge was monitored by optical

emission spectroscopy (OES) in the visible spectrum. Prior to processing, all major systems were calibrated and aligned as described in sections 3.5 and 3.6. After calibration, a random material sample was characterized using visual inspection, ASTM test protocols, and optical measurements of contact angle and surface energy to establish a baseline condition of the material to be examined.

In the first sets of experiments, the polymer samples were placed on the powered electrode of the CCP and exposed to the oxygen discharge at a fixed pressure, gas flow, power, and time intervals. In the second sets of experiments, the polymer samples were placed on the isolated electrode of the DPS and exposed to the oxygen discharge at fixed pressure, gas flow, power, and time intervals at a distance of 20 cm from the center of the coil. In the third sets of experiments, the polymer samples were again placed on the isolated electrode of the ICP and exposed to the oxygen discharge at fixed pressure, gas flow, power, and time intervals at a distance of 13 cm from the center of the coil. After treatment, in all experiments, the treated samples were removed from the chamber and examined for changes to the surface. Optical measurements of contact angle and surface energy as well as visual inspection were used to determine the degree of change in the surface of the samples after processing.

Chapter 4

Experimental Results

4.1 Preliminary Work

The work discussed in Chapter 2 enabled the refinement of the experimental protocols used in this experiment. The preliminary work[20] used set pressures and power levels to examine the modification of the surface of poly(ethyleneterepthalate) (PET) samples in a capacitively coupled discharge (**Cap**). The similarities and differences between the experimental parameters used in the previous (**Cap**) experiment and those used in the current inductive decoupled plasma system (**DPS**) experiments are summarized in Table 4.1 for comparison.

Table 4.1: Comparison of experimental parameters between previous work and current experiments.

Experiment	Cap	DPS Far	DPS Near
Distance from center	6 cm	20 cm	13 cm
Discharge type	capacitive	inductive (DPS)	inductive (DPS)
Sample material	PET	PET	PET
Sample area	300 mm^2	600 mm^2	600 mm^2
Sample thickness	0.1 mm	0.1 mm	0.1 mm
Pressure (mtorr)	100, 500	300, 1000	100, 300, 500, 1000
Process atmosphere	O_2	O_2+Ar	O_2
Process Time (min)	2, 6, 10, 16	2, 6, 10, 16	2
Discharge density[27]	$\approx 10^9 cm^{-1}$	$\approx 10^{11} cm^{-1}$	$\approx 10^{13} cm^{-1}$
Applied power (watts)	250, 500	250, 500	250, 500, 750, 1000

Sample preparation, cleaning, and preliminary characterization, described in Chapter 3, were unchanged between all sets of experiments. The main analysis steps are

discussed in the same order in each experiment **(Cap), (DPS) Far, (DPS) Near** in order to provide comparison. Results of each experiment will be compared and summarized in succeeding sections.

4.1.1 Optical Emission Spectroscopy

Optical Emission Spectroscopy (OES) was used to monitor spectral changes during processing in the capacitive discharge (**Cap**). An OES spectrum acquired during the initial characterization of the chamber, using oxygen as a process gas, at a pressure of 100 mtorr and an applied power of 250 watts, shows the initial state of the process system before the introduction of the sample and is shown in Figure 4.1. The discharge

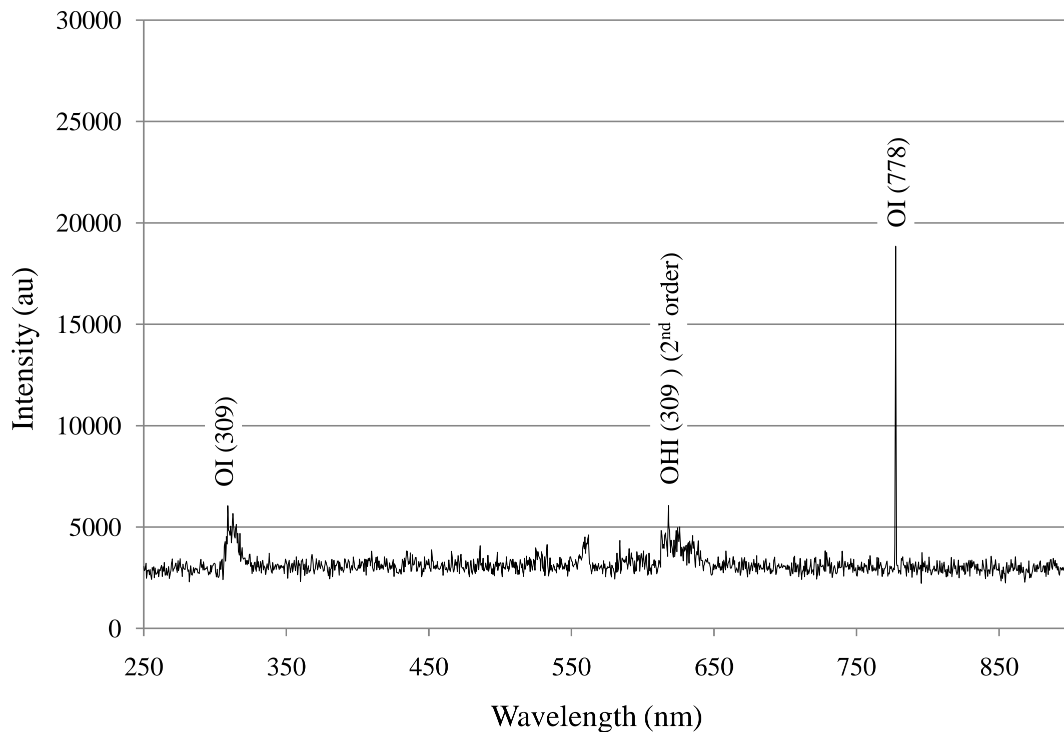

Figure 4.1: Spectrum of (**Cap**) discharge before introduction of sample in an O_2 process atmosphere at a pressure of 100 mtorr and an applied power of 250 watts.

initially showed a large peak at the $(3p^5P - 3s^5S)$ transition of oxygen at 778 nm, indicating the presence of neutral oxygen (OI). An occasional secondary peak was also seen at 844 nm (OI) but since oxygen discharges are generally dim and the 778 nm line is

the most prominent of the oxygen lines,[124,129] the line at 844 nm was used only as a secondary indicator of oxygen atom activity. The spectrum showed no indications of any other atomic species or of O_2 molecular emission sometimes seen at 762 nm. The low intensity ($A^2\Sigma^+ - X^2\Pi$) OH bandhead at 309 nm, generally attributed to the existence of residual water vapor in the system,[142–144] and a second order peak at 618 nm were also observed. No other molecular lines were observed. Spectral intensity levels and composition changed significantly during sample processing, as shown in Figure 4.2. The appearance of several atomic species (H_α, H_γ, OI) were noted during processing. A significant decrease in the intensity of the neutral oxygen line at 778 nm was also observed. A significant increase in the bandheads of molecular species (CO_2, CO, H_2) were also seen, in addition to a significant increase in the ($A^2\Sigma^+ - X^2\Pi$) bandhead of OH at 309 nm, indicating the presence of more free hydrogen.

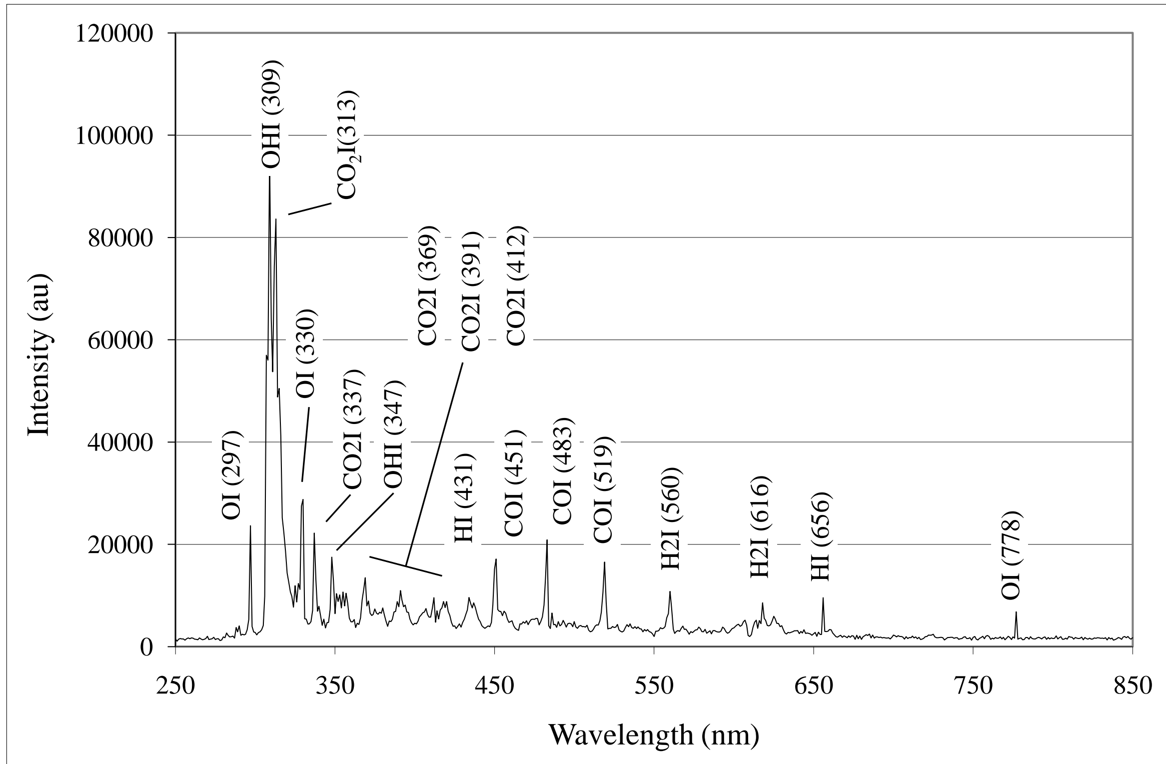

Figure 4.2: Spectrum of (**Cap**) discharge acquired during the first two minutes of processing at a pressure of 100 mtorr and an applied power of 500 watts.

In addition, the intensity of the $(3p^5P - 3s^5S)$ line of OI at 778 nm, shown in Figure 4.3, was monitored over time. Although many researchers reported significant changes in intensity and species makeup in the initial 60 seconds of processing, [2,7,19,43,81,91,92,145,146] no significant changes in intensity were seen during the first 60 seconds of processing.

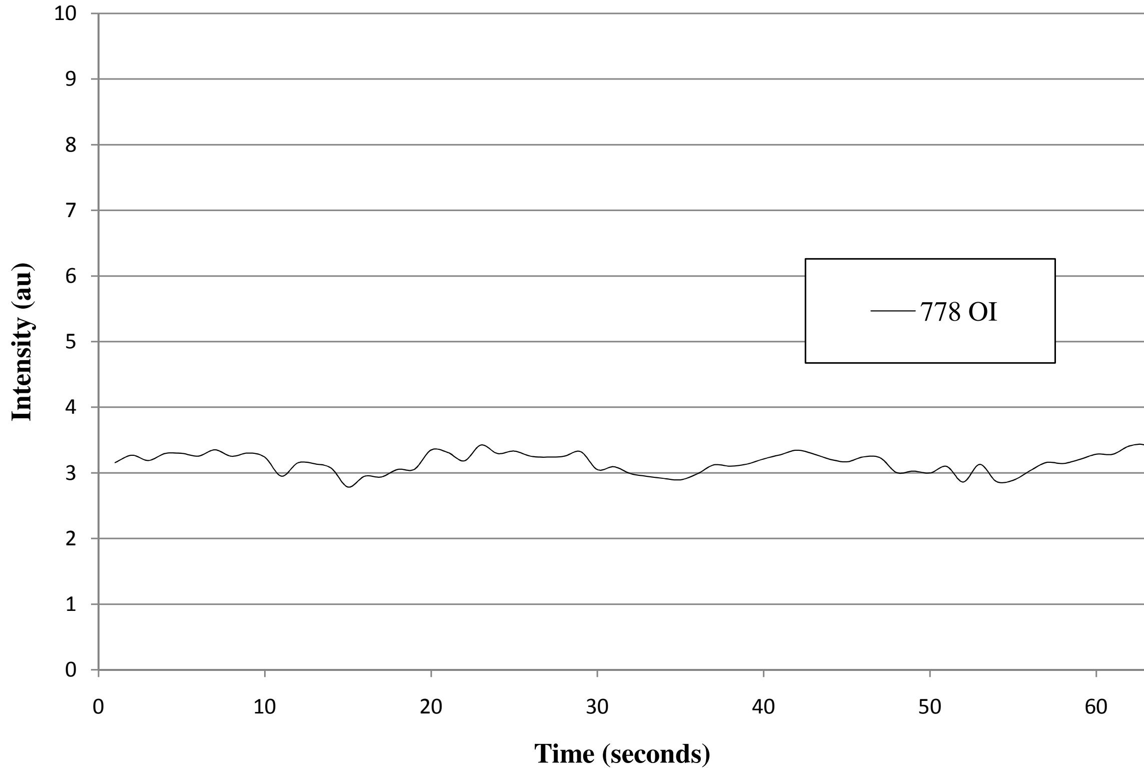

Figure 4.3: Monitored intensity of $(3p^5P - 3s^5S)$ transition of OI at 778 nm shown for the first 60 seconds of processing in the capacitive discharge (**Cap**) at a pressure of 100 mtorr and an applied power of 500 watts.

4.1.2 Surface Modification Results

Video capture images of the sample/water interface were used with the FTA200 proprietary software to calculate the contact angle of the sessile drop. The images also served to visibly illustrate the changes in surface wettability of the samples. The initial condition of the cleaned but untreated sample is shown in Figure 4.4. Figure 4.4a showed a large contact angle (84°), indicating low surface energy and a hydrophobic initial

condition, while Figure 4.4b reveals a change in the contact angle (50°) after exposure of the sample to an oxygen discharge at a pressure of 100 mtorr and an applied power of 500 watts for 16 minutes. Subsequent data and images taken at each of the pressure and power combinations confirmed a consistent decrease in the contact angle of each sample group as a result of processing. A plotted comparison of the change in contact angle

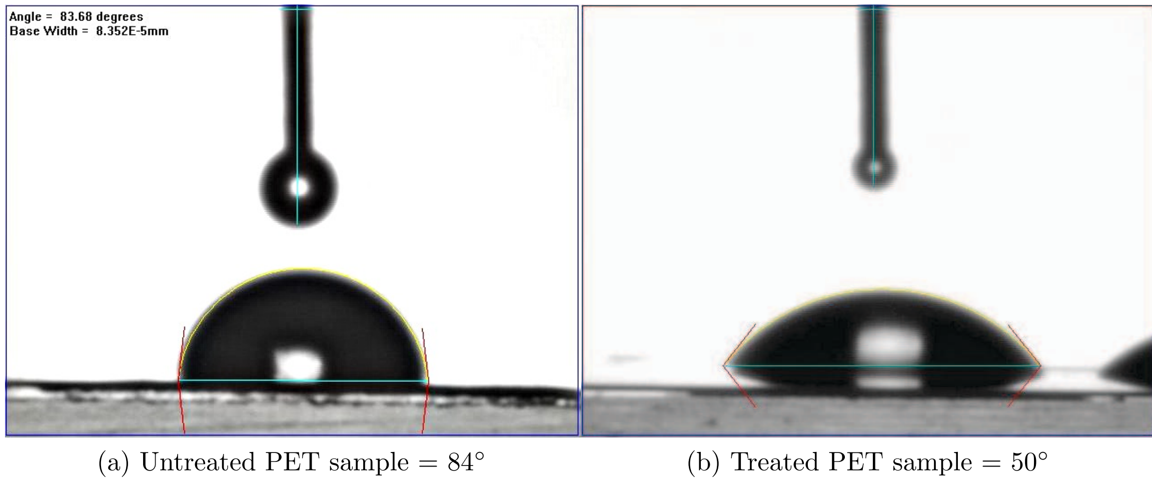

(a) Untreated PET sample = 84°   (b) Treated PET sample = 50°

Figure 4.4: a) Untreated PET sample shows a large contact angle indicating low surface energy b) Treated PET sample shows a significant reduction in the contact angle

values for selected pressure and power combinations is shown in Figure 4.5. The initial deionized (DI) water contact angle averaged 84° and decreased to a low of 45° over the period of treatment, around 16 minutes. Each data point in Figure 4.5 represents the average of three measurements taken across the surface of each sample. The average contact angles exhibited a significant decrease when compared to the untreated state and a reduction in contact angle of greater than half overall.

4.2 DPS Results 20 cm from coil center (Far)

The DPS (**Far**) experiments consisted of prepared samples placed at a distance of 20 cm from the center of the coil and monitored using the quartz lens optic system described in Figure 3.12 on page 31. The dielectric plasma system (DPS) data show characteristics similar to the preliminary (**Cap**) data series in terms of atomic and

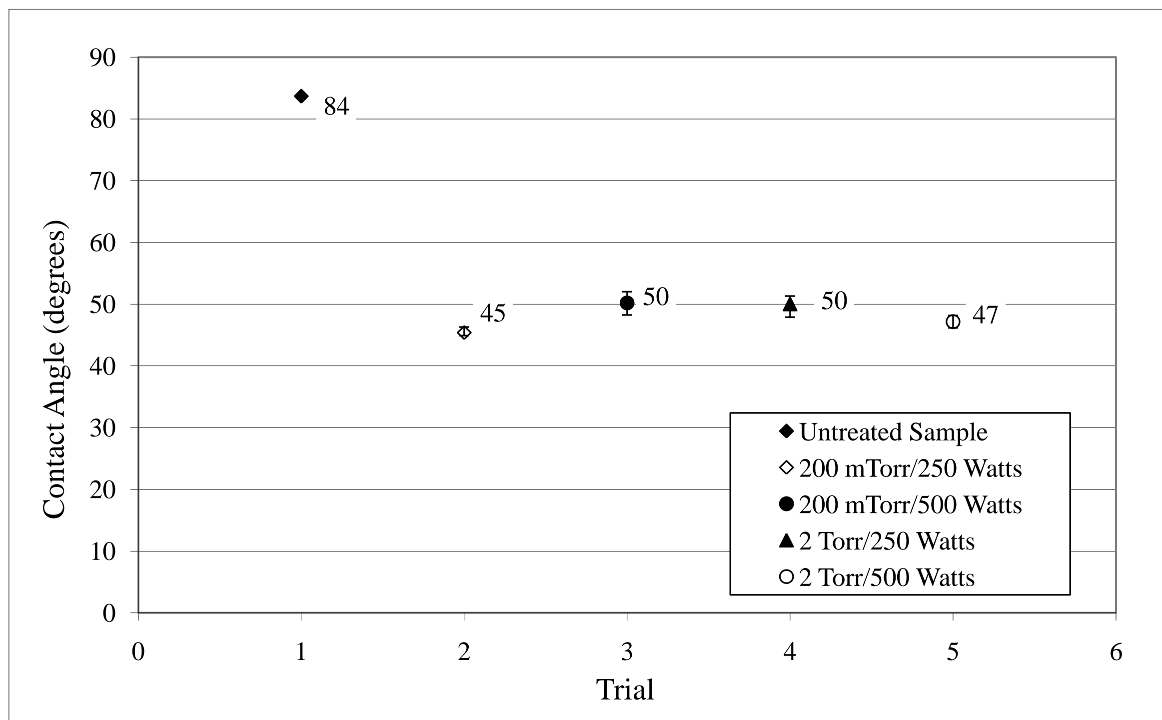

Figure 4.5: A comparison of averaged contact angle of untreated samples (84°) to samples after processing at four listed pressure and power combinations.

molecular species observed and modification of the sample surface. In addition to monitoring the OH ($A^2\Sigma^+ - X^2\Pi$) and OI ($3p^5P - 3s^5S^0$) transition emission intensities during processing, the introduction of Ar gas (approximately 2%) was used in an attempt to obtain electronic temperature data using methods as described in Greim,[147] Lochte-Holtgreven,[148] and Thorne et al.[149] Atomic (OI, ArI, and H) and neutral molecular lines (OH, CO_2, and CO) were detected as in the earlier work. No lines of N_2, which would indicate a chamber air leak, were seen. An increase in the degree of modification of the sample surface was seen, however. This increased modification was based upon the greater decrease in contact angle (CA) values.

4.2.1 Optical Emission Spectroscopy

Optical emission spectroscopy (OES) was used to monitor spectral changes during processing of samples in the inductive discharge. The acquired spectra showed significant

changes over the treatment period.

Spectral lines monitored for this study are shown in Table 4.2. The monitoring of the same group of lines monitored in the earlier work allowed a direct comparison of spectral data relative to the type of discharge.

Table 4.2: Table of emission lines monitored during processing in the DPS (**Far**) configuration.

Species	λ (nm)	Vibrational Transition	Band
OI	778		$(3p^5P - 3s^5S^0)$
	844		$(3p^3P - 3s^5S^0)$
OH	306	(0,0)	$(A^2\Sigma^+ - X^2\Pi)$
	307	(0,0)	
	308	(0,0)	
	309	(0,0)	
	313	(1,1)	
CO	283	(0,0)	$(b^3\Sigma - a^1\Pi)$
	297	(0,1)	
	313	(0,2)	
	331	(0,3)	
	349	(0,4)	
CO	451	(0,0)	$(B^1\Sigma - A^1\Pi)$
	484	(0,1)	
	519	(0,2)	
	561	(0,3)	
	608	(0,4)	
CH	431	(0,0)	$(A^2\Delta - X^2\Pi)$
CI	801		$(2s^22P(^2P^\circ)3p - 2s^22P(^2P^\circ)4d)$
H_α	656		$(2s - 3p)$
H_β	489		$(2s - 3p)$
Ar	697		$(3s^23P^5(^2P^\circ_{3/2})4p - 3s^2P^5(^2P^\circ_{1/2})4d)$
	707		$(3s^23P^5(^2P^\circ_{3/2})4p - 3s^2P^5(^2P^\circ_{1/2})6s)$
	715		$(3s^23P^5(^2P^\circ_{3/2})4p - 3s^2P^5(^2P^\circ_{1/2})4p)$
	727		$(3s^23P^5(^2P^\circ_{3/2})4s - 3s^2P^5(^2P^\circ_{1/2})4p)$
	738		$(3s^23P^5(^2P^\circ_{3/2})4s - 3s^2P^5(^2P^\circ_{1/2})4p)$
	772		$(3s^23P^5(^2P^\circ_{3/2})4p - 3s^2P^5(^2P^\circ_{1/2})4p)$

An OES spectrum of the O_2/Ar plasma taken during the the initial characterization of the inductive discharge chamber is shown in Figure 4.6. The acquired spectrum shows the initial state of the process system after cracking of the process gas (O_2) but before the addition of the sample. The ($A^2\Sigma^+ - X^2\Pi$) OH bandhead at 309 nm (and second order at 618 nm) is again seen in the initial reference spectrum; however, the appearance of this molecular species may be accounted for in this instance not solely as residual water vapor in the chamber[142] but as polymerized residue of previous sample material not removed by the oxygen discharge treatment (ashing) used to clean the chamber prior to beginning the current series of tests. The ($3p^5P - 3s^5S^0$) transition of OI at 778 nm seen in earlier spectra is reduced by half in this spectrum and is dominated by the more prominent Ar lines (618 nm, and 750 nm) added to the process gas to facilitate measurement of electronic temperature.

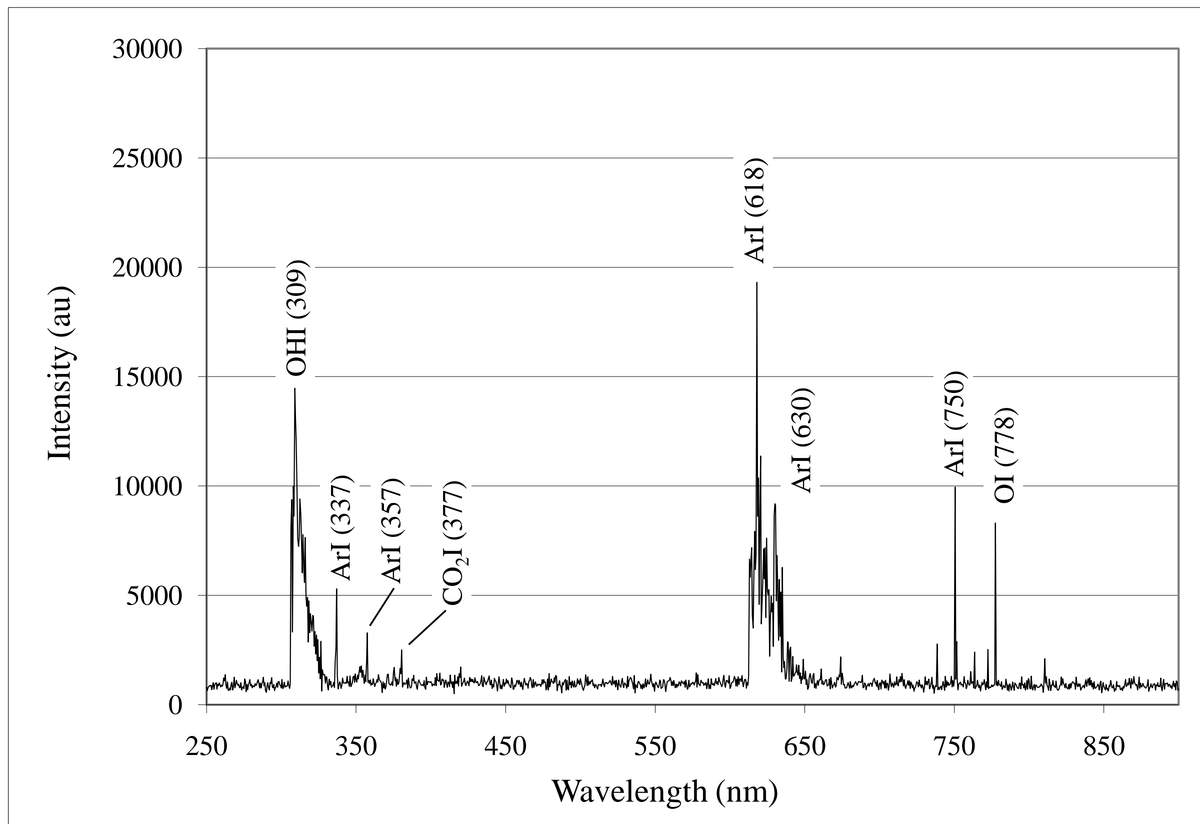

Figure 4.6: Spectrum of DPS (**Far**) discharge before introduction of sample in an O_2 and Ar process atmosphere at a pressure of 100 mtorr and an applied power of 250 watts.

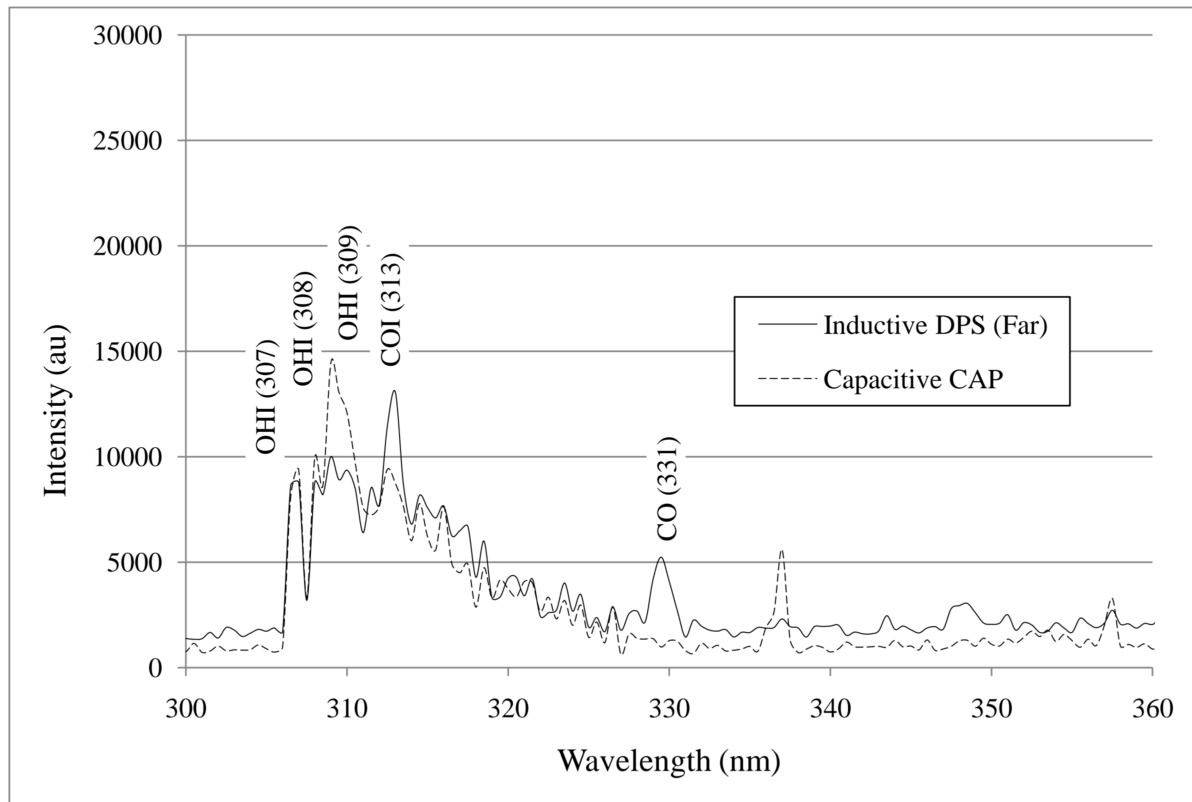

Figure 4.7: Intensity of the OH ($A^2\Sigma^+ - X^2\Pi$) band for two experimental configurations as a function of wavelength. The solid line shows the results for the inductive DPS (**Far**) discharge and the dashed line shows the results for the capacitive (**Cap**) discharge under the same conditions; a pressure of 500 mtorr and an applied power of 250 watts.

The OH bandhead ($A^2\Sigma^+ - X^2\Pi$) is again seen after the beginning of processing and, although visible in the earlier capacitive spectra (**Cap**), is seen with increased intensity using the inductive (**DPS**) system. The change appears to slightly enhance the ability to see some of the rotational structures of the of OH band at 309 nm[144] and also enhances the visibility of the CO bandhead at 313 (0,2) as shown in Figure 4.7. A view of the OI lines at 778 and 844 nm shows an increase in intensity that parallels the change from a capacitive (**Cap**) to an inductive (**DPS**) discharge as shown in Figure 4.8. A general increase in spectral intensity was also seen. The OH ($A^2\Sigma^+ - X^2\Pi$) transition at 309 nm has also been seen by other researchers as well as a relationship between the OH transition at 309 nm and the OI line at 778 nm. Krstulović et al.[2] and Cvelbar et al.,[81] reported that the intensity of the ($A^2\Sigma^+ - X^2\Pi$) transition of OH at 309 nm increased

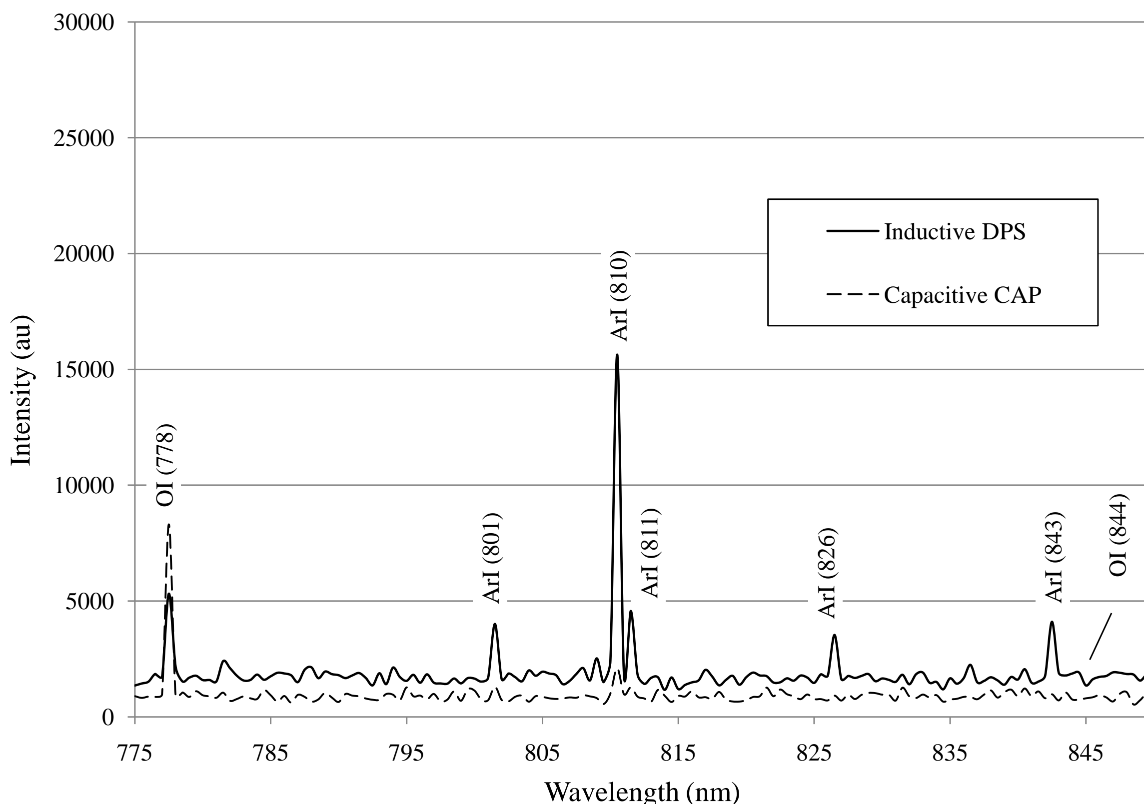

Figure 4.8: Comparison of intensity at the OI transitions at 778 nm and at 844 nm. The dashed lines show the intensities of the capacitive (**Cap**) and the solid line shows the intensity of the inductive DPS (**Far**) discharge.

while the intensity of the OI transition at 778 nm decreased during the first 50 seconds of processing, but after 140 seconds the intensity of OH declined and the intensity of the OI line increased. Individual sample runs showed a fairly wide variation in spectral intensities between runs of equal processing time, but a plot of averaged intensity seen in each of the series, as shown in Figure 4.9, showed an insignificant change in intensity at the 309 transition for all series run at 100 mtorr and 250 watts input power, regardless of processing time.

Changes in the intensity of OH ($A^2\Sigma^+ - X^2\Pi$) transition at 309 nm were investigated by many of the other researchers[92,150–153] examining the reaction of PET polymer in energetic discharges. All reported changes in the intensity of the OH ($A^2\Sigma^+ - X^2\Pi$) transition at 309 nm that paralleled applied power levels for samples

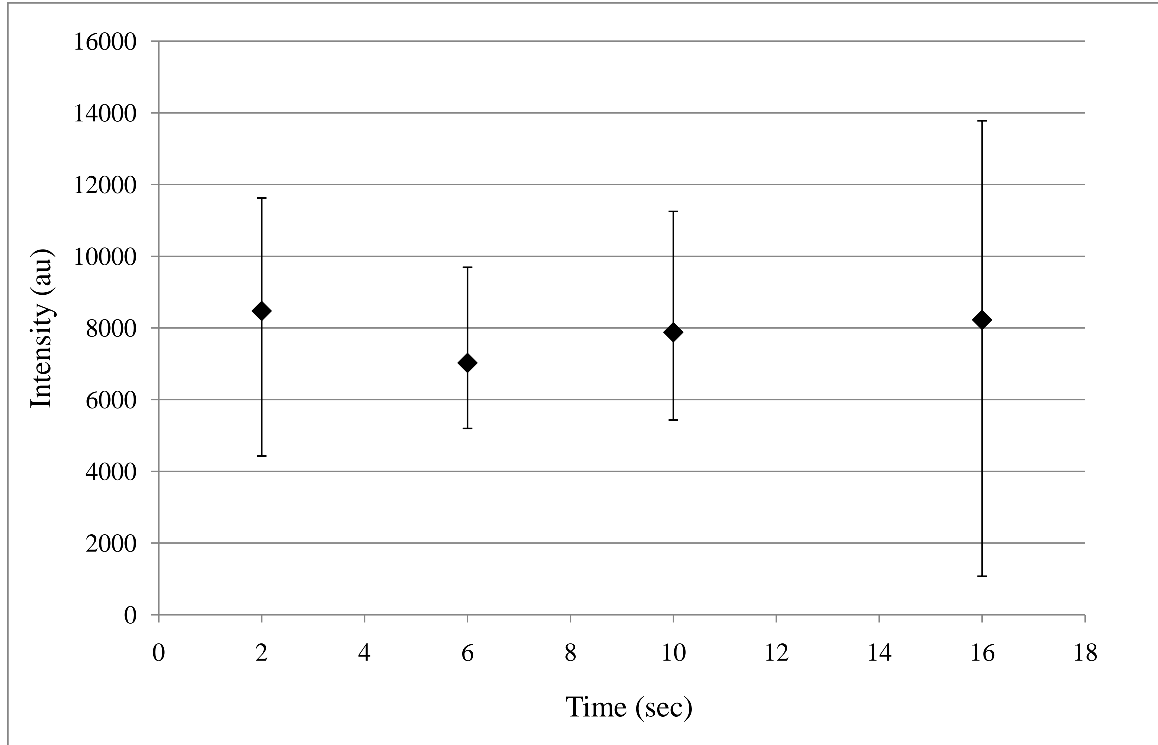

Figure 4.9: Intensity of the OH ($A^2\Sigma^+ - X^2\Pi$) transition as a function of processing time in the inductive DPS (**Far**) system showing the average of all three trials. The discharge conditions were a pressure of 100 mtorr and 250 watts of applied power.

processed at fixed processing pressures. The greatest change in spectral intensities of the OH line were reported in the first few seconds of exposure to all of the discharges.[2,19,92] Most[2,19,92,138] reported an end to visible changes in the intensity of the OH lines approaching 2 minutes of processing in the discharge, and no significant changes were seen to extend beyond about 2 minutes from the beginning of treatment.[2,19,92,138] Changes in the intensity of the OH and CO bandheads in the range of 305 to 323 nm are shown in Figures 4.10 through 4.12. This series showed only a slight increase in intensity despite the expected increase in intensity due to the increase in power from 250 watts to 500 watts. A small increase in intensity over processing time was also seen by comparing multiple spectra taken *during* the longer processing runs. The time required for the scanning mechanism to make a complete scan from 250 nm to 900 nm allowed for two scans, one taken from 0-3.5 minutes and the second taken from 4.0-7.5 minutes. The

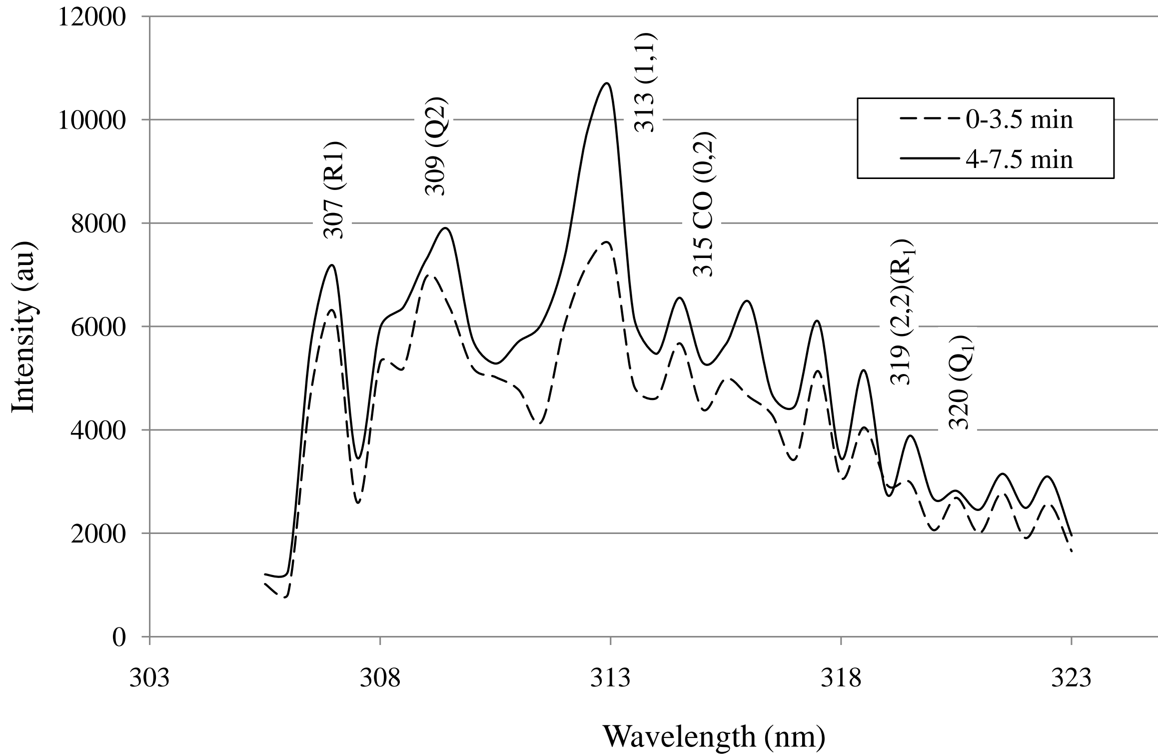

Figure 4.10: Comparison of intensity and wavelength shows a non-significant increase in the intensity of the OH ($A^2\Sigma^+ - X^2\Pi$) transition at 313 nm and the CO ($b^3\Sigma - a^1\Pi$) transition at 315 nm for a pressure of 100 mT and a power level of 250 W.

spectral scan shown in Figure 4.10 shows an increase in the intensity of the OH (1,1) transition at 313 nm as well a slight increases in the CO transition at 315 nm for a pressure of 100 mtorr and an applied power level of 250 watts. There was not much difference between the scans as expected and discussed earlier. The spectra, shown in Figure 4.11, also showed a consistency in intensity even with an increase in power from 250 to 500 watts while maintaining the process pressure (100 mtorr). While these increases are not significant, they may indicate the sample has reached a kind of equilibrium. Chan et al.[152] and Morra et al.[154] postulated a two-stage process to explain this behavior also seen in the spectral results of treatment of a PTFE sample in an oxygen discharge. The processing showed an initial stage consisting of an increase in "...products formed by interaction with the surface" and a second phase (beginning about 15 minutes after the start of the process) where the OES process monitoring reverted to

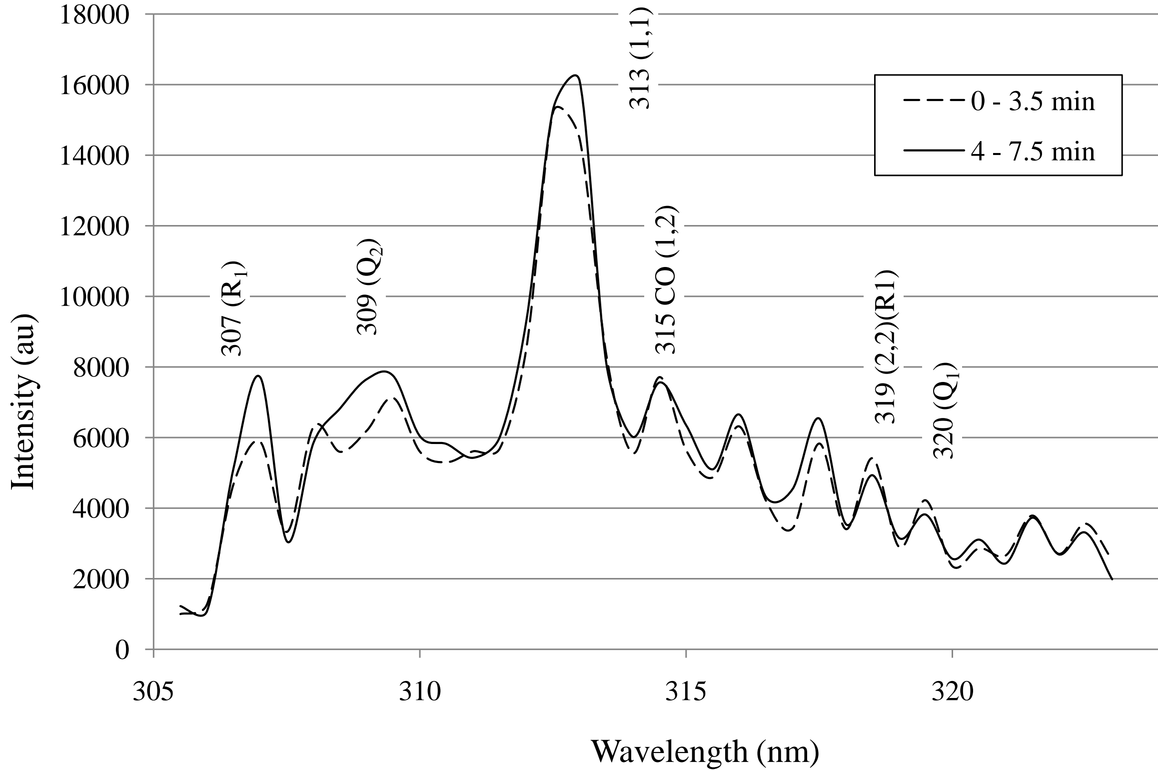

Figure 4.11: Comparison of intensity versus wavelength shows an increase in the intensity of the OH ($A^2\Sigma^+ - X^2\Pi$) transition at 313 nm as well as a similar increase in the CO ($b^3\Sigma - a^1\Pi$) transition at 315 nm for a pressure of 100 mtorr and a power level of 500 watts

"a PTFE-like" spectrum, indicating the beginning of what the researchers[152,154] called the etching phase of sample exposure. The description of the processing of PTFE samples substantially agrees with the findings of this set of experiments, i.e., initially high intensities of OH and CO were seen concurrent with a reduction in the intensities of OI corresponding to a combining of oxygen with species removed from the sample surface to generate the OH and CO species seen. As processing continued, a recovery of OI intensities with a decrease in the intensities of OH and CO were seen at extended processing times corresponding to a decrease in the combination of oxygen and other species seen in the earlier phase and a change to the mechanism called etching by Chan et al.[152] and Morra et al.[154] This behavior was also seen by other experimenters,[2,81] who also reported processing dominated by surface modification during the early period of the

exposure (increased OH and CO emissions) with a change to etching (decreased OH and CO emissions) during the later portion of the exposure. The use of the term *etching* by Chan et al.[152] and Morra et al.[154] is more properly described as sputtering of the surface of the sample, i.e., a process where the impact of heavy particles (usually ions) with the surface of the sample removes atoms from the surface by repeated impact transfer of energy until some atoms of the material escape the material surface.[27] This mechanism would more properly account for the reversion of the process to "a PTFE-like" spectrum described.[152,154] The set of spectra shown in Figure 4.12 consisted of four spectra acquired sequentially during a processing period of 16 minutes at a pressure of 100 mtorr and a applied power of 250 watts. The spectra showed an increase in the intensity of both OH and CO, although the most activity was seen at the OH ($A^2\Sigma^+ - X^2\Pi$) transition at 313 nm which showed a very slight increase throughout the processing period.

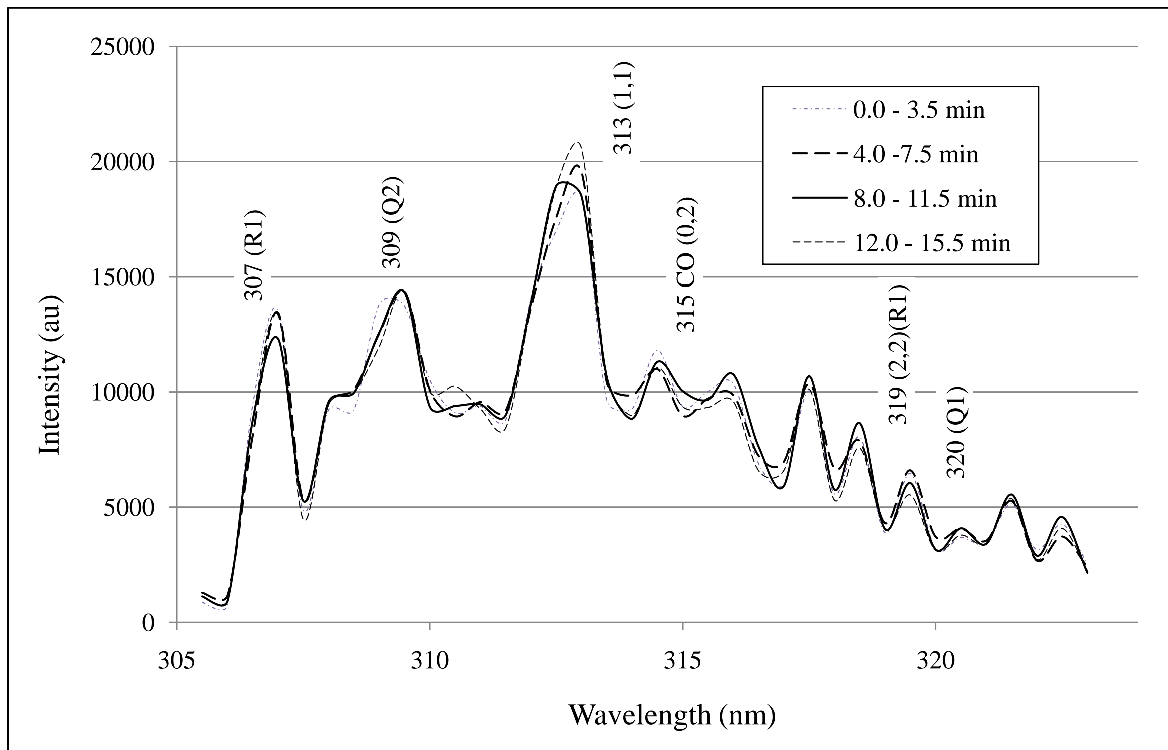

Figure 4.12: Comparison of intensity and wavelength shows an increase in the intensity of the OH ($A^2\Sigma^+ - X^2\Pi$) transition at 313 nm as well as a similar increase in the CO ($b^3\Sigma - a^1\Pi$) transition at 315 nm for a pressure of 100 mtorr and a power level of 250 watts.

The most prominent line of the CO band was the ($b^3\Sigma - a^1\Pi$) transition at 315 nm. Again, clearly there is a mechanism that approximates chemical equilibrium. (Note the spectra were very similar). Initial intensity of the OI ($3p^5P - 3s^5S^0$) transition at 778 nm, shown in Figure 4.13, is reduced when compared to the intensity seen in the initial state of the inductive chamber (**Near**) before any processing has occurred. The OI ($3p^3P3s^3S^0$) transition at 844 nm is reduced to the level of the background. During the

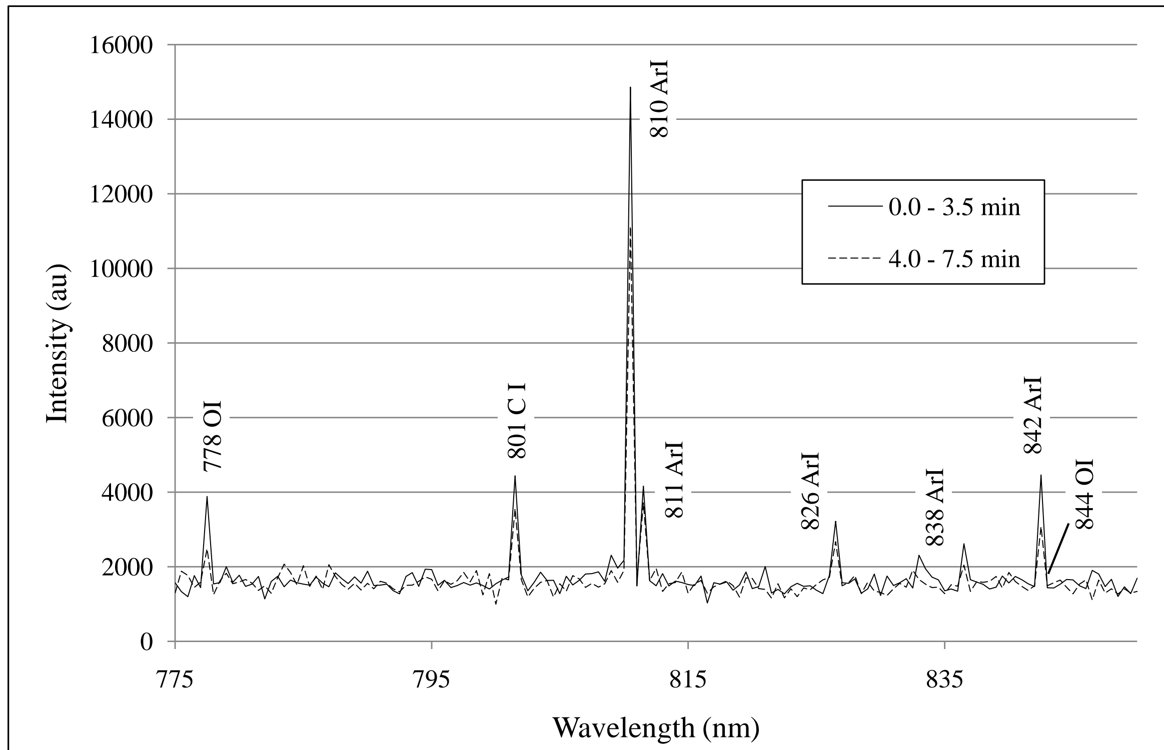

Figure 4.13: Intensity of the OI ($3p^5P{-}3s^5S^0$) transition at 778 nm and the OI ($3p^3P3s^3S^0$) transition at 844 nm showing the change in intensity for a processing time of 10 minutes at a pressure of 100 mtorr and an applied power of 250 watts.

processing, however, the OI levels deceased slightly (778 nm), as shown in Figure 4.13, and although some variation from the shortest to the longest time period was seen, the average level intensity at particular time intervals, shown in Figure 4.14, showed a constant intensity, within error. The variations in the OI intensities are in keeping with results seen during processing by Krstulović et al.[2] and Cvelbar et al.,[81] although the current experimental setup was slightly different. The behavior of the OI intensities also

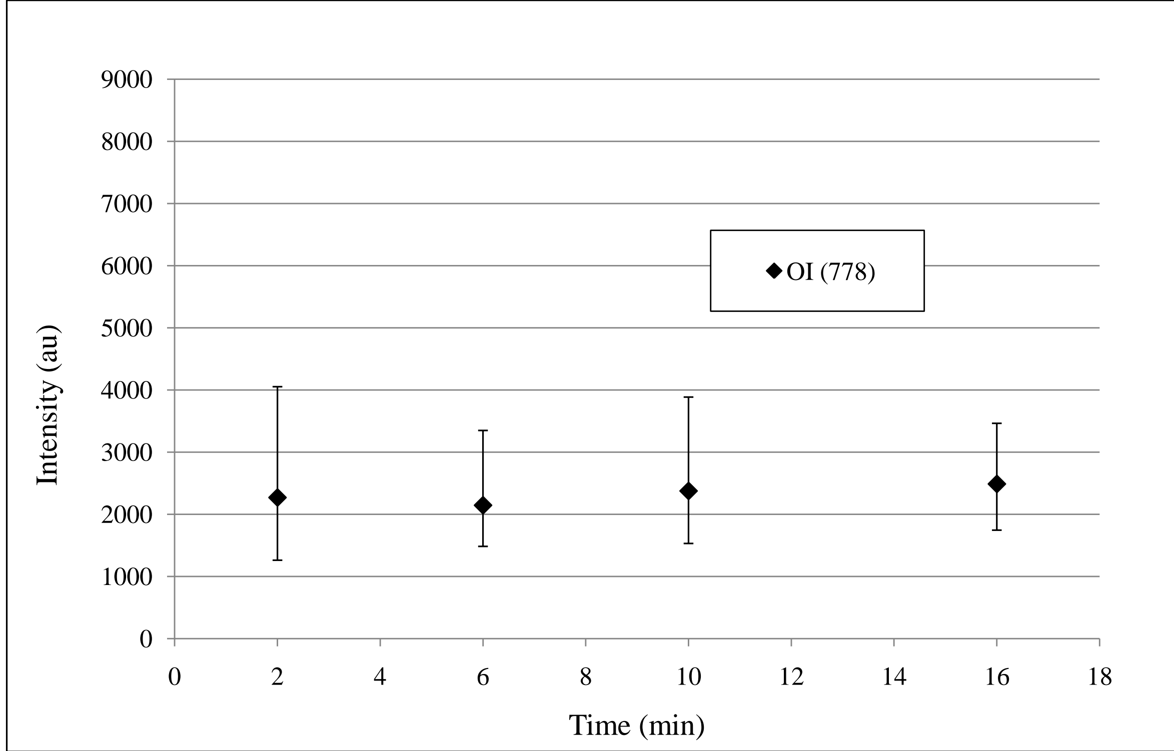

Figure 4.14: Averaged intensity of the OI ($3p^5P - 3s^5S^0$) transition at 778 nm showing variations between sample groups processed for varying time periods at a pressure of 100 mtorr and an input power of 250 watts.

corresponded to the findings of Chan et al.[152] and Morra et al.,[154] further suggesting the initial period of processing primarily consisted of surface modification, as indicated by the increase in intensity of OH and CO transitions, while increased processing time showed an increase in the etching or sputtering of the sample indicated by a corresponding decrease in OH and CO intensities and a slight increase in the intensity of the ($3p^5P - 3s^5S^0$) transition of OI at 778 nm.

The ($A^2\Sigma^+ - X^2\Pi$) bandhead of OH at 309, as well as the ($3p^5P - 3s^5S^0$) and ($3p^3P - 3s^5S^0$) transitions of OI at 778 and 844 nm, were also monitored over time. No significant change was seen over the initial 150 seconds of processing. But in examining the first 10 seconds, shown in Figure 4.15, an initial increase in OI was observed followed by a subsequent decline. The OH bandhead at 309 shows an initial increase (0 to 12 arbitrary units of intensity) which was maintained throughout the sampling period.

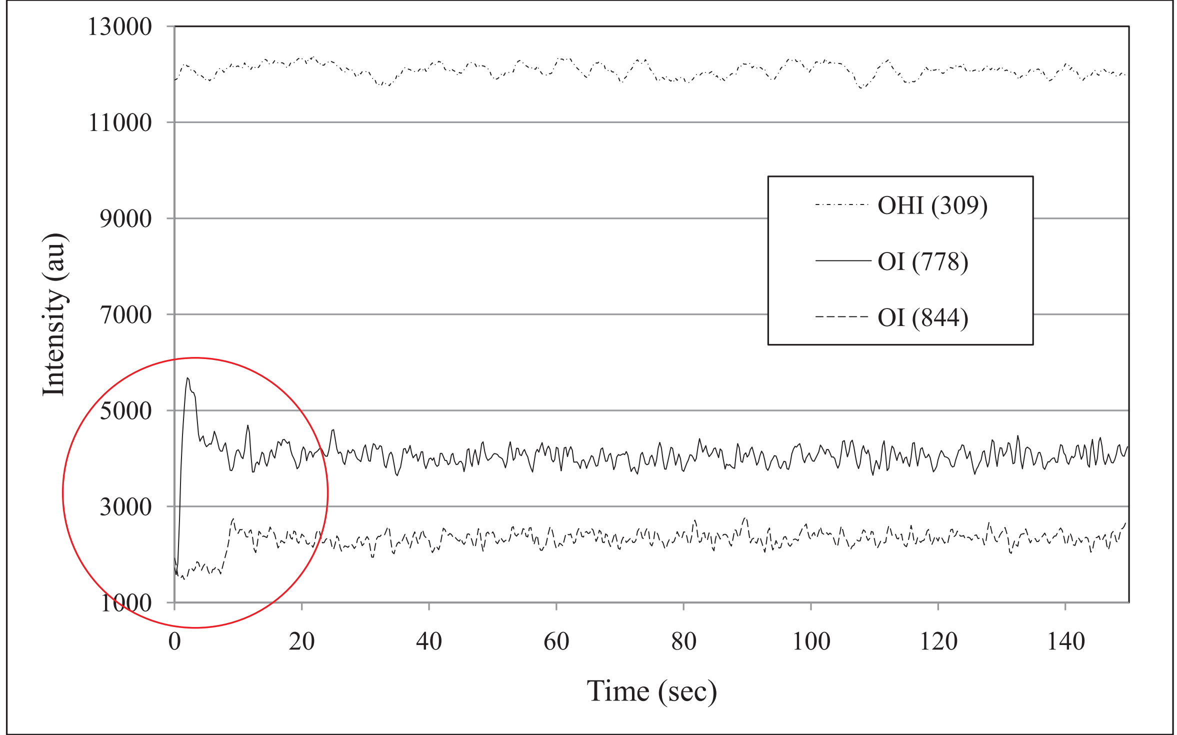

Figure 4.15: Intensity as a function of time of the OI transitions at 778 nm (solid), 844 nm (dashed), and the OH bandhead at 309 nm (dotted) for the 150 second sample period at a pressure of 300 mtorr and an applied power of 500 watts.

In the second series of experiments, DPS (**Far**), argon gas (2%) was added to the process atmosphere to enable the calculation of the electronic temperature, T, of the discharge using the Boltzmann plot method described in Griem[147] and Thorne et al.[149] and as used by many other researchers.[155–159] If the discharge is in Local Thermodynamic Equilibrium (LTE) the temperature can be estimated using the Boltzmann distribution to find the population of the excited state by comparing relative intensities of spectral lines from the same element or ionization stage using Equation (4.1),[147]

$$ln\left(\frac{I_{ki}\lambda_{ki}}{g_k A_{ki}}\right) = ln\left(\frac{hcN_0L}{4\pi Z}\right) - \frac{E_k}{k_B T} \tag{4.1}$$

where I_{ki} is the relative intensity of the emission lines, λ_{ki} is the relative wavelength, g_k is the statistical weight of the upper transition level, A_{ki} is the transition probability, E_m is the upper level energy, k_B is the Boltzmann constant, h is Planck's constant, c is

velocity of light, N is the total population density of the element, Z is the partition function, and T is the temperature. For a discharge in LTE, a plot of the results of $ln\frac{I_{ki}\lambda_{ki}}{g_k A_{ki}}$ versus E_k will be a straight line with a slope of $1/kT$. T, the inverse of the slope of the line, was calculated for the second series of experiments, DPS (**Far**) using the argon lines shown in Table 4.3.

Table 4.3: Emission lines of argon used in the calculation of discharge temperature.

Species	λ (nm)	Transition	Band
Ar	697		$(3s^2 3P^5(^2P^\circ_{3/2})4p - 3s^2P^5(^2P^\circ_{1/2})4d)$
	707		$(3s^2 3P^5(^2P^\circ_{3/2})4p - 3s^2P^5(^2P^\circ_{1/2})6s)$
	715		$(3s^2 3P^5(^2P^\circ_{3/2})4p - 3s^2P^5(^2P^\circ_{1/2})4p)$
	727		$(3s^2 3P^5(^2P^\circ_{3/2})4s - 3s^2P^5(^2P^\circ_{1/2})4p)$
	738		$(3s^2 3P^5(^2P^\circ_{3/2})4s - 3s^2P^5(^2P^\circ_{1/2})4p)$
	772		$(3s^2 3P^5(^2P^\circ_{3/2})4p - 3s^2P^5(^2P^\circ_{1/2})4p)$

A typical Boltzmann plot of the temperature of the discharge during a processing run is shown in Figure 4.16. The linear fit shown produced a T_e of 0.07 eV but had an average correlation coefficient (R^2) of 0.68 likely caused by the wide variation in points at the upper end of the E_k axis. After lengthy trials of measuring neutral argon emission lines and correcting for wavelength sensitivity of the optical equipment, reliable Boltzmann plots were never obtained.

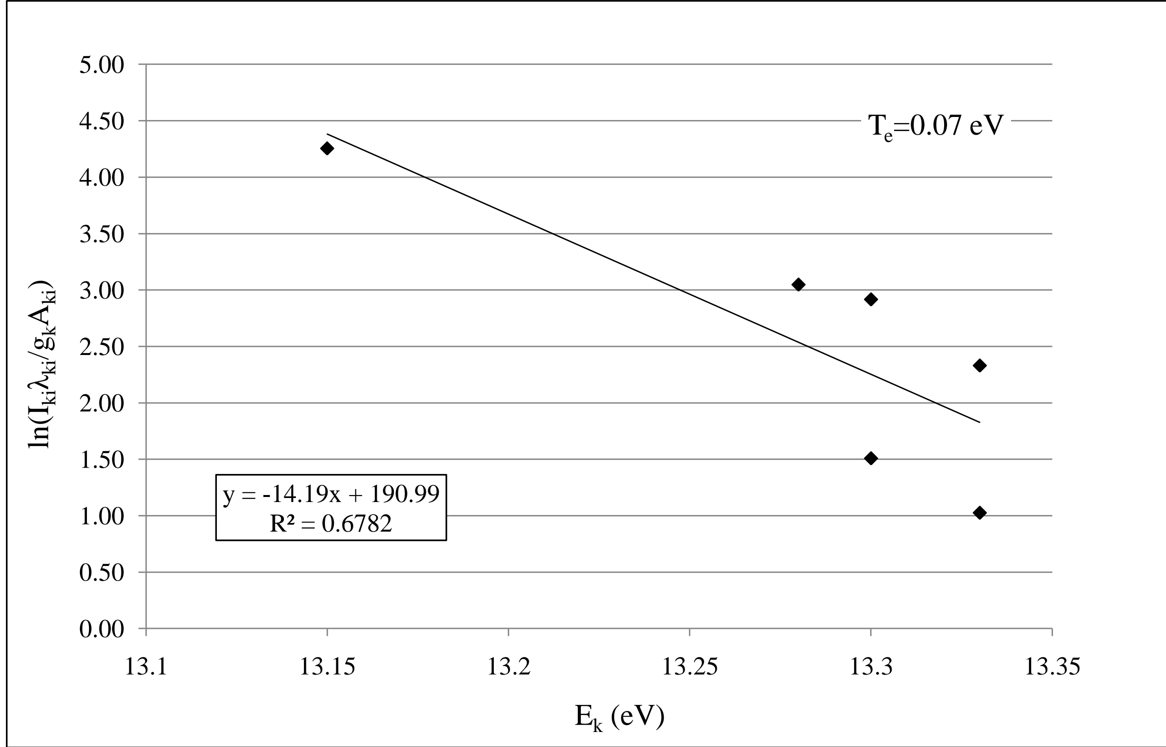

Figure 4.16: Boltzmann plot of $ln\frac{I_{ki}\lambda_{ki}}{g_k A_{ki}}$ versus E_k for a sample processed for 2 minutes at a pressure of 100 mtorr and an applied power of 500 watts.

4.2.2 Surface modification results for DPS (Far)

Calibration of the video goniometer system (DCA) is described in Section 3.6. Initial measurement of the interfacial tension (IFT) of the deionized water test fluid used the average of three samples, shown in Figure 4.17b, and was found to be 72.8±0.1 dynes/cm, which is in good agreement with published values.[137,160] Initial calibration of the video/software subsystem using the average of three samples of the manufacturer supplied standard, shown in Figure 4.17b, shows an average contact angle of 90.1±0.1°. Inspection of the test samples to characterize the changes in the surface before and after exposure to the discharge used the DCA to calculate and record the contact angle (CA) of the test liquid on the surface of the sample. The initial condition of a cleaned but untreated sample is shown in Figure 4.18. Figure 4.18a showed a large contact angle (78°) indicating low surface energy and a hydrophobic initial condition. After treatment in the discharge

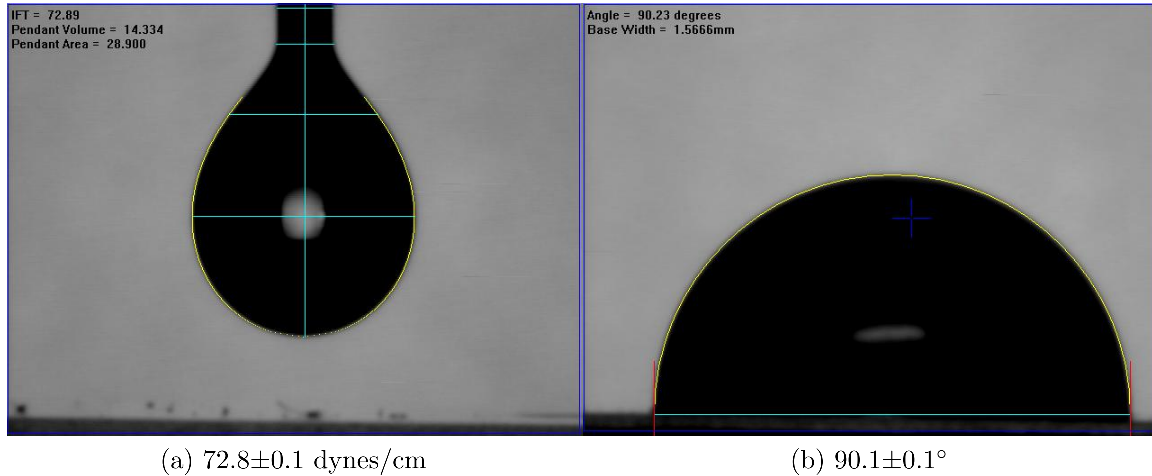

(a) 72.8±0.1 dynes/cm (b) 90.1±0.1°

Figure 4.17: Calibration of the DCA system showing: a) Tensiometer verification of interfacial tension value of deionized water drop. b) Sapphire standard used for sessile drop characterization.

for 16 minutes at a pressure of 500 mtorr and a 500 watt applied power, Figure 4.18b, the sample showed a significant decrease in the measured contact angle (10°) indicating an increase in surface energy and a more hydrophyllic condition after processing. Subsequent

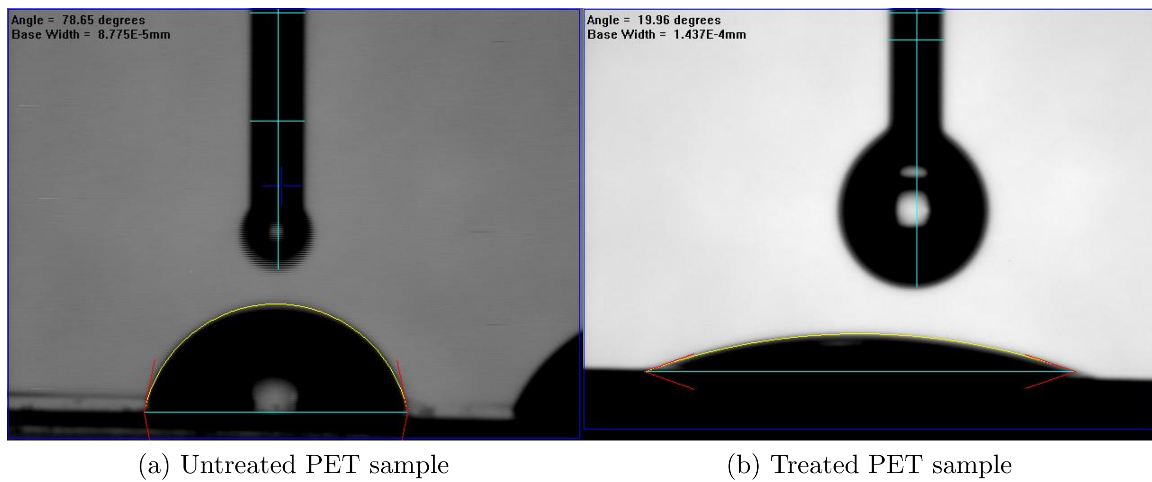

(a) Untreated PET sample (b) Treated PET sample

Figure 4.18: PET material samples showing: a) Untreated PET sample shows a large contact angle ($> 75°$) indicating low surface energy. b) Sample treated at a pressure of 500 mtorr and an applied power of 500 watts for 16 minutes shows a $\approx 80\%$ decrease in contact angle ($> 13°$) showing an increase in surface energy after treatment.

images taken at each pressure and power combination confirmed a consistent decrease in the contact angle of each sample group as a result of exposure to the discharge and can be

found in Appendix B. A comparison of initial characterization baseline data results are shown in Figure 4.19. The initial CA of the sample material as found by the ASTM test was measured to be $76° \pm 1°$. When compared to the data from the initial characterization using the DCA, the additional resolution of the instrument, not surprisingly, indicates a less uniform CA across the surface than indicated by the ASTM test. The measured results of the 39-point test yielded a CA value for the untreated samples that varies between 58° and 68° as shown in Figure 4.19. The 9-point series tests showed measured CA values between 74° and 77°. The averages of these baseline values give the untreated material value, 72°, used for all other calculations of change in contact angle and surface condition.

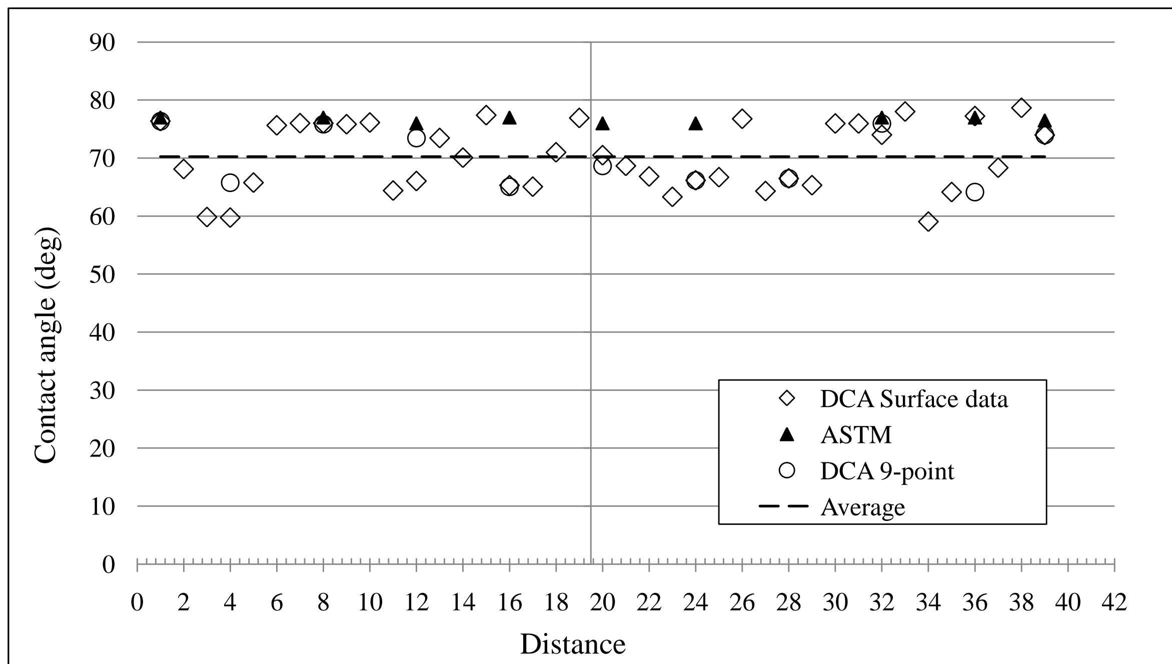

Figure 4.19: Comparison of initial characterization values showing (◊) 39-point characterization of sample, (○) 9-point characterization of sample, (▲) ASTM characterization of sample, and (– –) calculated average of all initial CCA values.

Consistent with findings of the previous study, shown in Figure 4.5 (page 51), an overall lowering of the contact angle was seen in all series of tests. In this (**Far**) study, however, the average contact angle decreased from an initial high value of 78° to a low of 30°. A comparison of average final contact angles to starting condition is shown in Figure 4.20.

Decrease in contact angle as a result of treatment in an energetic discharge was reported by Deshmukh and Bhat,[5] who reported a decrease in contact angle from 76° to 38° over a 15 minute processing time in a similar inductive discharge. Thurston et al.[138] saw a decrease in contact angle from 102° to 88° for a polyethylene sample processed in an atmospheric pressure discharge, while Vassallo et al.[19] saw a decrease in contact angle to a low value of 10° from an average 72° at a processing power of 200 watts; all of these results are in good agreement with current experimental findings.

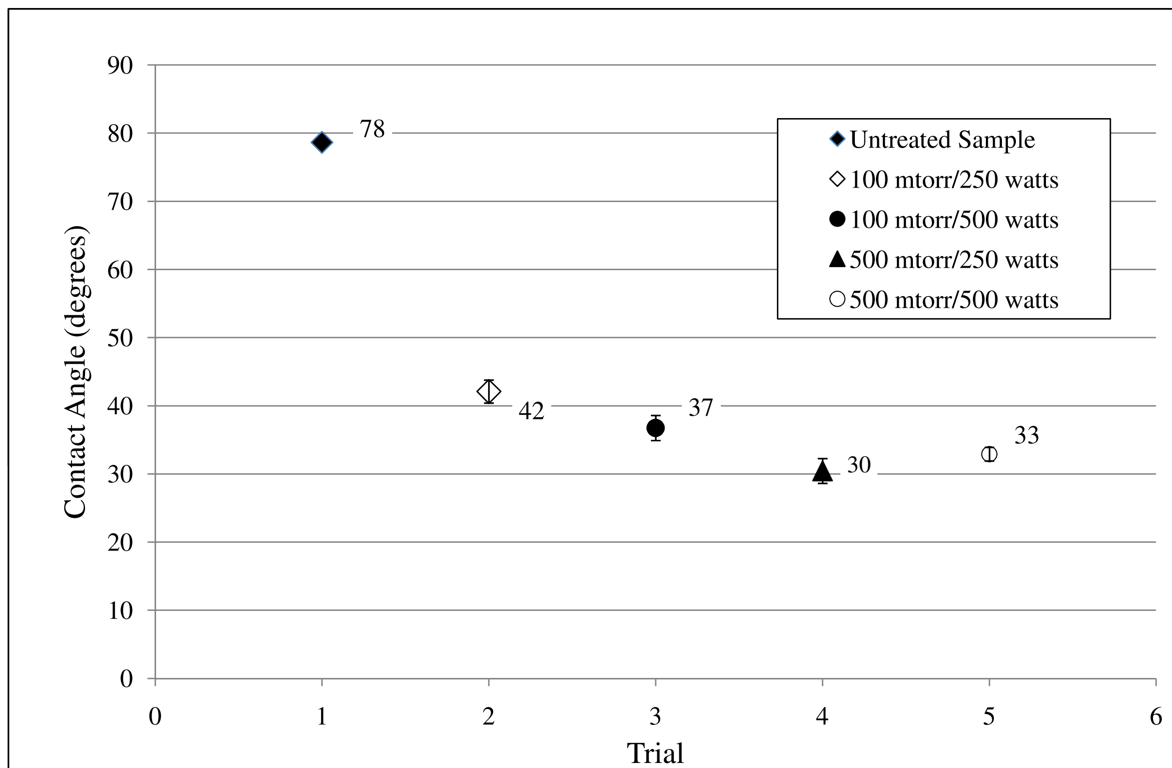

Figure 4.20: Comparison of average contact angle of an unprocessed sample (78°) to contact angles of sample after processing at four pressure and power combinations.

An anomaly was occasionally seen, as shown in Figure 4.21, showing an increased contact angle near the edges of the sample after processing. This departure from the trend of reduction of contact angle after exposure to the discharge can be attributed to a "shading-effect" caused, in this case, by the focus ring enclosing the sample on the system electrode; the ring acts as an additional surface bending the sheath away from the sample edge causing a "shadow" to be cast at the edge of the discharge. The disturbance in the sheath interferes with the mechanisms (chain-scission/activation and sputtering) responsible for the surface modification and etching of the sample.

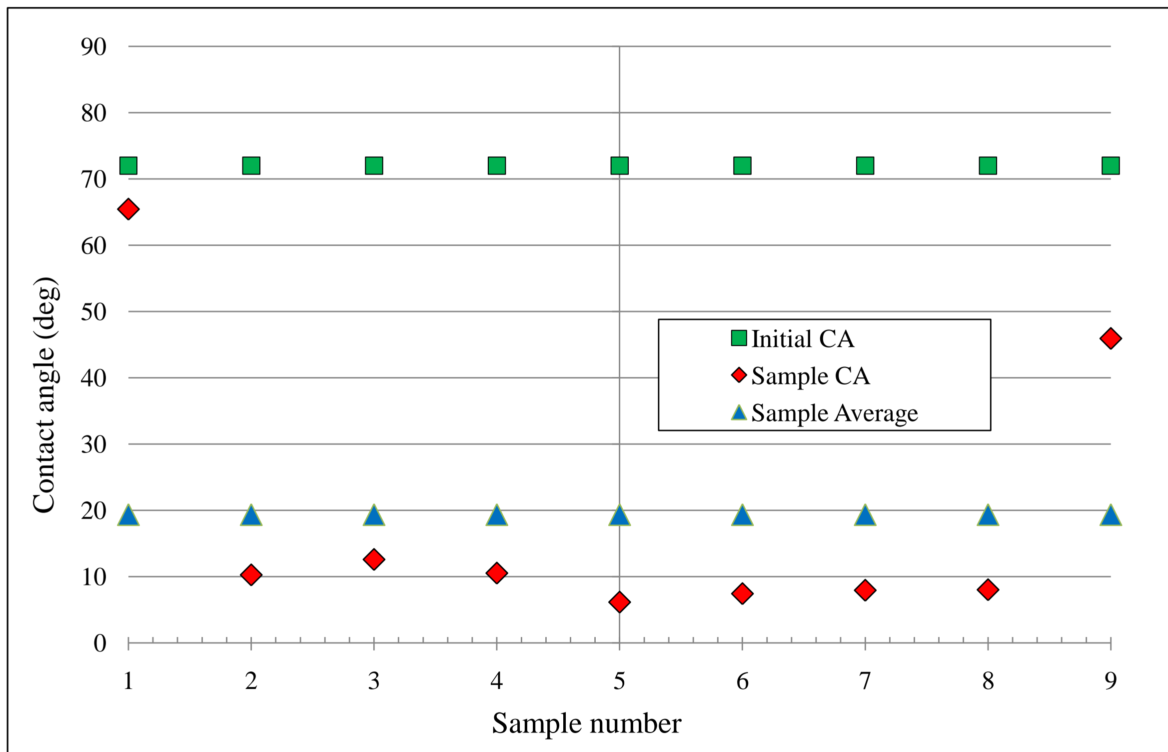

Figure 4.21: Contact angles across sample (200 mm). Observe the large contact angle values at the edges of the sample due to shading of the sample edge by the outer ring of the substrate holder.

Shading and uneven etching at the edges is also seen in the processing of silicon wafers for semiconductor devices where it is a cause of device failure and contributes to increased costs. It is a widely studied problem[42,161] but beyond the scope of this work.

After processing, the samples also showed, in Table 4.4, a difference in final contact angle when processed under different pressures. Although each group of samples showed a decrease in contact angle after processing in the oxygen/argon atmosphere, the group processed at 500 mtorr showed a slightly greater decrease in contact angle than did the samples processed at 100 mtorr.

Table 4.4: Comparison of contact angle versus processing pressure.

	Low Pressure (100 mtorr)	High Pressure (500 mtorr)
Initial CA	72°	72°
Final CA	39°	35°

Reduction in contact angle as a function of processing pressure was also seen by other researchers;[162–164] the resulting changes varied between a decrease of 53%, (76° ⇒ 42°) seen by Deshmukh and Bhat[165] (150 mtorr) to an 85% (90° ⇒ 15°) reduction in contact angle seen by Roth et al.,[162] when PET samples were processed at atmospheric pressure in a dielectric barrier discharge. Table 4.4 shows the change in average contact angle values after treatment in the discharge in the first series of samples. Both series show a reduction in contact angle (72° ⇒ 39° and 72° ⇒ 35°) indicating a slight increase in the effectiveness of the modification of the surface of the samples.

A comparison of averaged contact angle to treatment time for each of the sample groups processed at 100 mtorr is shown in Figure 4.22. Each series shows a reduction in contact angle (starting from the untreated sample angle of 72°) of the samples at each of the time markers. Samples exposed to the discharge for 2 minutes showed the least change in contact angle, while samples processed for 6 and 10 minutes at both power levels show a comparable decrease in contact angle. The samples processed for 16 minutes showed an uncharacteristic increase in average contact angle for the samples processed at 250 watts contrary to the trend of reduction in contact angle seen in the samples processed at 500 watts. This local increase can be attributed to uneven processing due to contamination of one of the samples. Decreases in contact angle

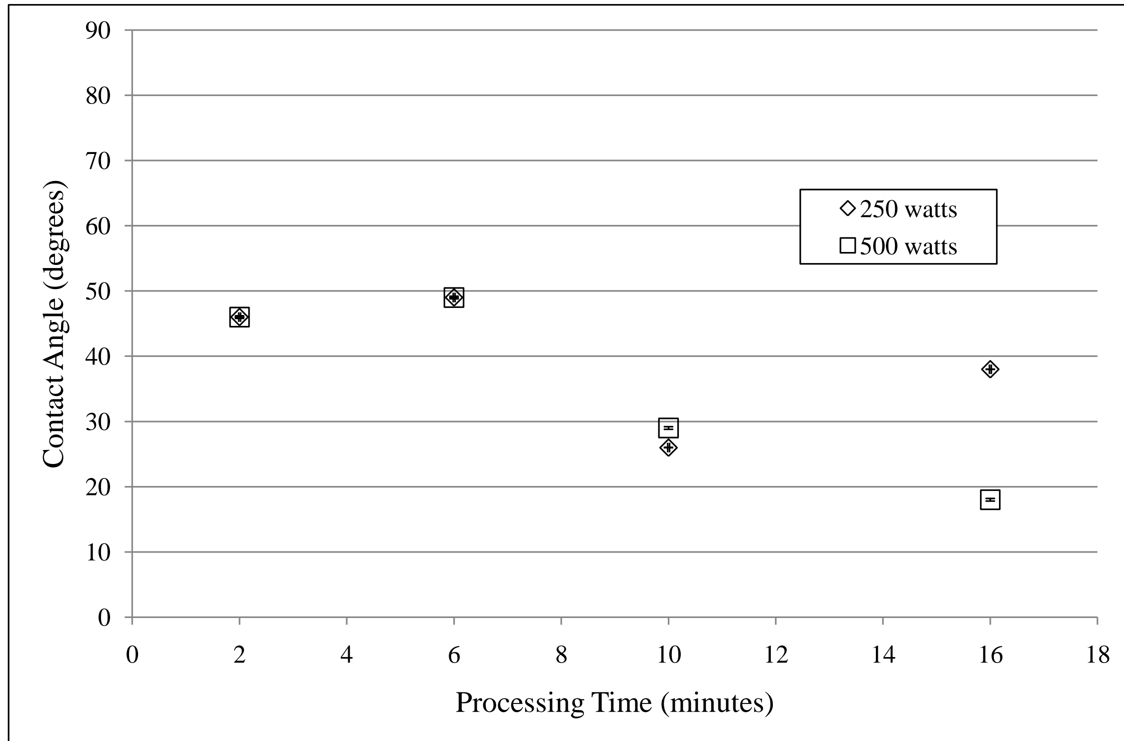

Figure 4.22: Comparison of contact angle versus processing time for samples processed at a pressure of 100 mtorr and applied power levels of 250 and 500 watts.

consistent with an increase in processing time or power were also seen by other researchers[5,43,163,164] and showed close agreement with these results.

Change in contact angle, which is often equated with a change in wettability of material surfaces, as a result of exposure to an energetic discharge is reported by many researchers[2,12,166,167] as due to the build- up of molecular fragments initially freed from the sample, or generated by breakdown of process gases, on the surface of the sample (activation) in the initial portion of processing. After longer exposure to the discharge, however, the mechanism responsible for surface modification changes as described (page 62) by Chan et al.[152] and Morra et al.,[154] and is seen as increased surface roughness attributed to sputtering of the sample surface. The increase in processing time appears to increase the degree of modification of samples processed at 250 and 500 watts applied power.

The difference between values reported in the literature and the behavior observed

in this experiment can be attributed, in large part, to the difference in the plasma geometry of the experimental layout used in this research. Other researchers[2,81,84,145,168] used a quartz cylinder surrounded by the inductive coil producing a reported discharge density of 10^{16} cm^{-3} and an electron temperature of 5-6 eV.[2,81] The discharge was monitored using OES with an optical fiber and CCD spectrometer along the long axis, or most dense portion, of the discharge. The DPS (**Far**) experiment produced a much larger plasma volume than the quartz tube used by others.[2,81,84,145,168] The density of the DPS inductive discharge was estimated to be on the order of 10^{10} cm^{-3},[27] substantially less than the discharges of other researchers.[19] Sample sizes also differed greatly. Vassallo et al.,[19] Cvelbar et al.,[81] and Krstulović et al.[2] used samples of unknown areas, but certainly no larger than 30 mm in diameter or about 700 mm^2 by 0.02 mm thickness versus a sample of 30,000 mm^2 in area by 0.1 mm thickness used in these experiments.

4.3 DPS Results 13 cm from center of coil (Near)

The DPS **Near** experiments consisted of prepared samples placed at a distance of 13 cm from the center of the coil; the samples were closer to the center of the coil and were exposed to the denser portion of the plasma compared to the (**Far**) samples. All interactions between the samples and the discharge were monitored using a quartz fiber optic system described in Figure 3.11 (page 31). As with previous experimental series, an OES spectrum of the O_2 discharge was acquired during the initial characterization of the processing chamber and is shown in Figure 4.23. The spectrum shows the initial state of the processing system using an O_2 discharge without the sample. The $(A^2\Sigma^+ - X^2\Pi)$ bandhead of OH at 309 nm is seen in the reference spectrum and can again be attributed, in part, to residual water vapor in the chamber[142–144] but also to polymerized residue of previous sample material not removed by the oxygen discharge treatment (ashing) used to clean the chamber prior to beginning each series of tests.

The placement of the sample closer to the center of the coil appeared to increase the

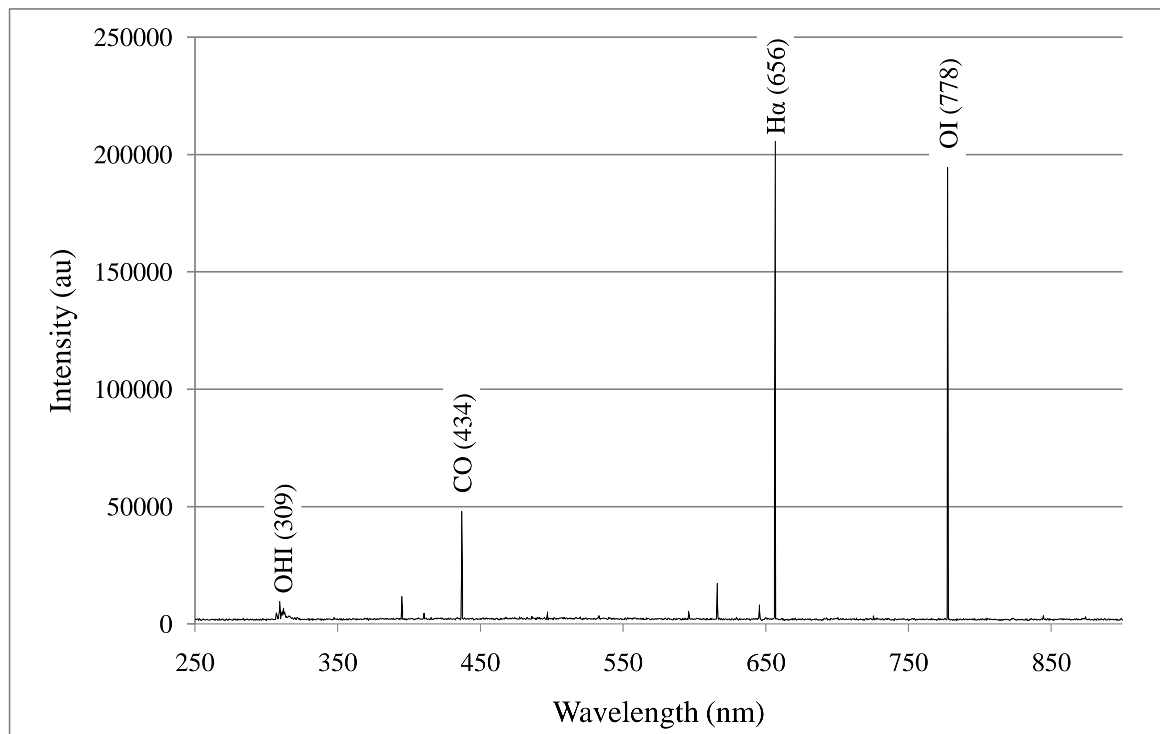

Figure 4.23: Intensity versus wavelength of an O_2 discharge at 100 mtorr and 250 watts applied power with no sample.

overall intensity of spectral information acquired even before the addition of samples to the chamber. The appearance of the H_α line at 656 nm in addition to the significant increase in spectral intensity of the OI line at 788 nm were the major changes seen in DPS (**Near**) when compared to the spectrum seen in DPS (**Far**) (Figure 4.6 page 53).

A close-up of the spectrum shown in Figure 4.24 (meaning the peaks of H_α [656 nm] and OI [778 nm] were not seen) allowed a better view of spectral activity during the processing session. An increase in overall emission intensities and significant increases in the intensities of certain atomic and molecular species either seen at a much reduced intensity or completely unreported in the earlier experimental series were also observed.

The appearance of the OH transition at 309 nm as well as the bandhead of CO at 434 nm indicate a reaction taking place even during this initial calibration discharge as the components of both OH and CO could not come from the supplied O_2 process gas. Oxygen free radicals may be interacting with polymers coating the chamber from

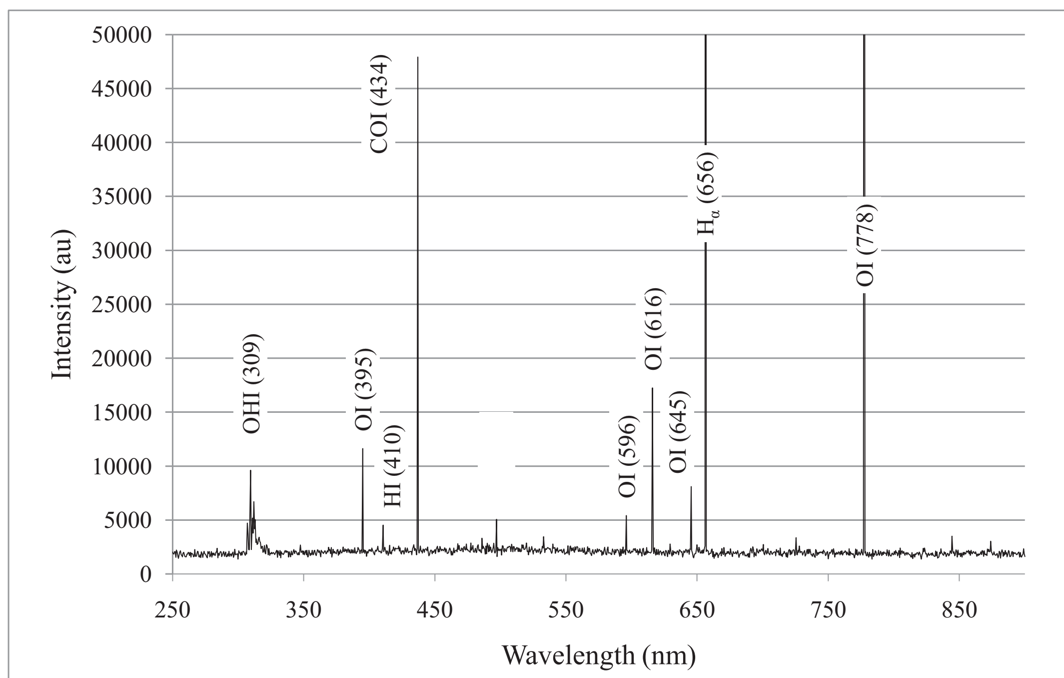

Figure 4.24: A close up of intensity versus wavelength of the spectrum shown in Figure 4.23.

previous runs. The appearance of the OI lines at 395, 596, 616, and 645 nm show the expected appearance of neutral oxygen species but at a much higher intensity than seen in either of the previous experiments.

After the introduction of samples into the processing chamber, a comparison of applied power level versus pressure, Figures 4.25–4.28, showed significant changes in the spectral intensity of several of the monitored atomic and molecular species. The ($A^2\Sigma^+ - X^2\Pi$) bandhead of OH at 309 nm as well as the H_α transition (2s-3p) at 656 nm, and the ($3p^5P - 3s^5S^0$) and ($3p^3P3s^3S^0$) OI transitions at 778 and 844 nm paralleled the increase in applied power for process pressures of 100 and 300 mtorr (Figure 4.25 and 4.26). A slight decrease in intensity of all species (except OH) was seen at 500 mtorr (Figure 4.27), while a significant decrease in the intensity of all species was seen after process pressure was increased to 1000 mtorr as shown in (Figure 4.28). The H_α transition (2s-3p) at 656 nm was also monitored by Vesel et al.,[92] Gupta et al.,[150] and others[151–153] and was the most active of the monitored atomic species while the ($A^2\Sigma^+ - X^2\Pi$) transition of OH at 309 nm was overall the most active molecular species monitored.

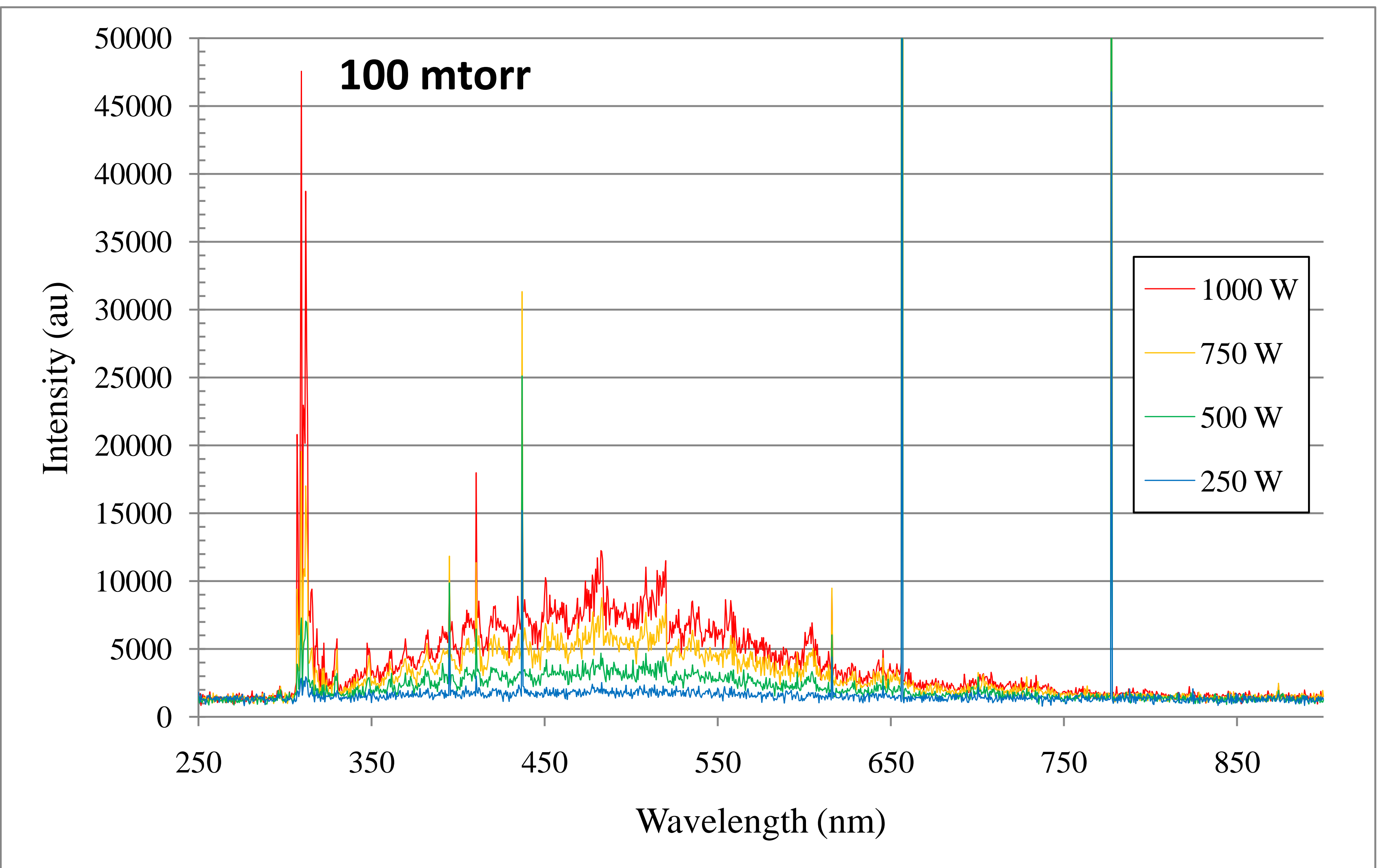

Figure 4.25: Intensity as a function of wavelength at a pressure of 100 mtorr at applied powers of 250 (blue), 500 (green), 750 (orange), and 1000 (red) watts.

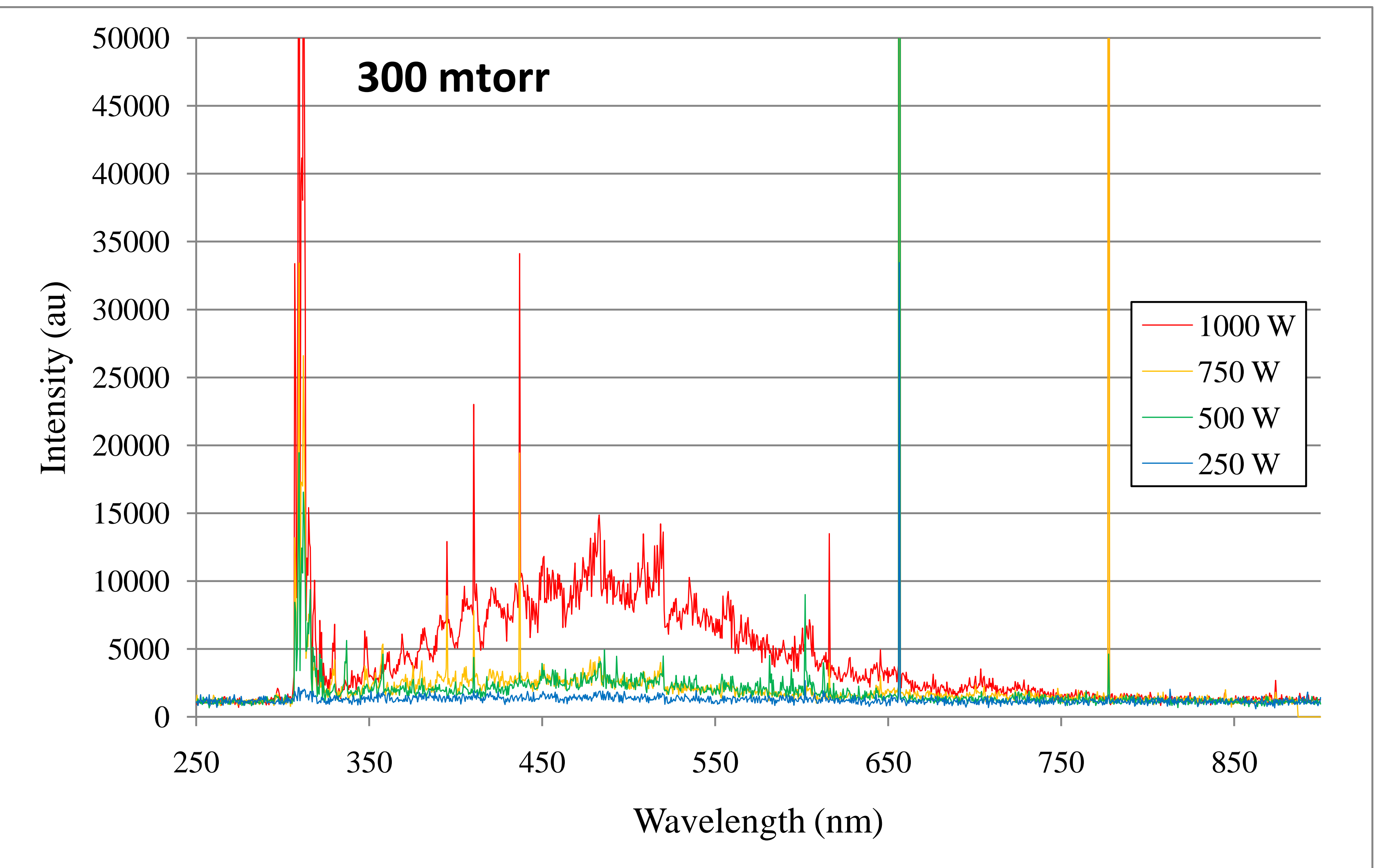

Figure 4.26: Intensity as a function of wavelength at a pressure of 300 mtorr at applied powers of 250 (blue), 500 (green), 750 (orange), and 1000 (red) watts.

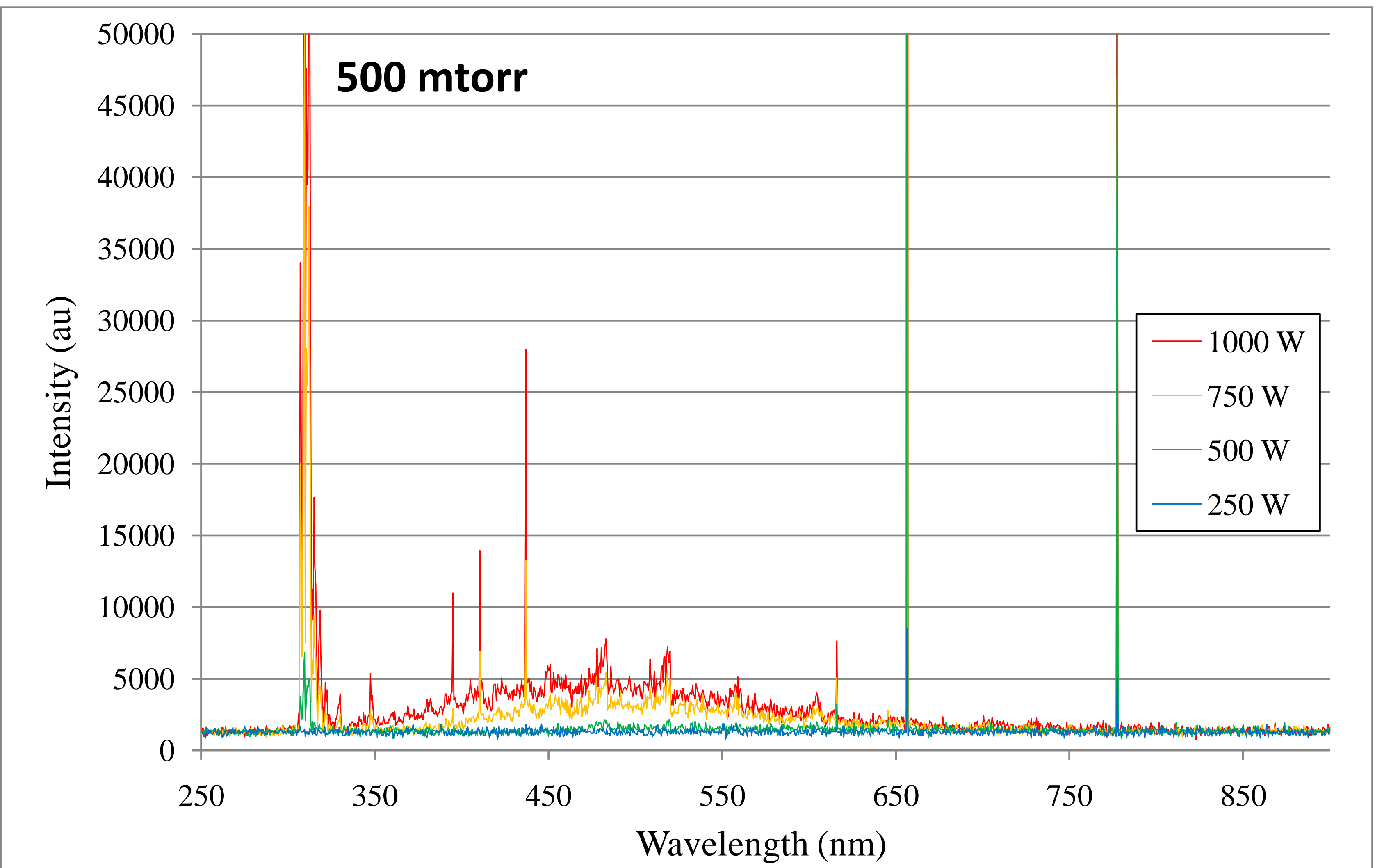

Figure 4.27: Intensity as a function of wavelength at a pressure of 500 mtorr at applied powers of 250 (blue), 500 (green), 750 (orange), and 1000 (red) watts.

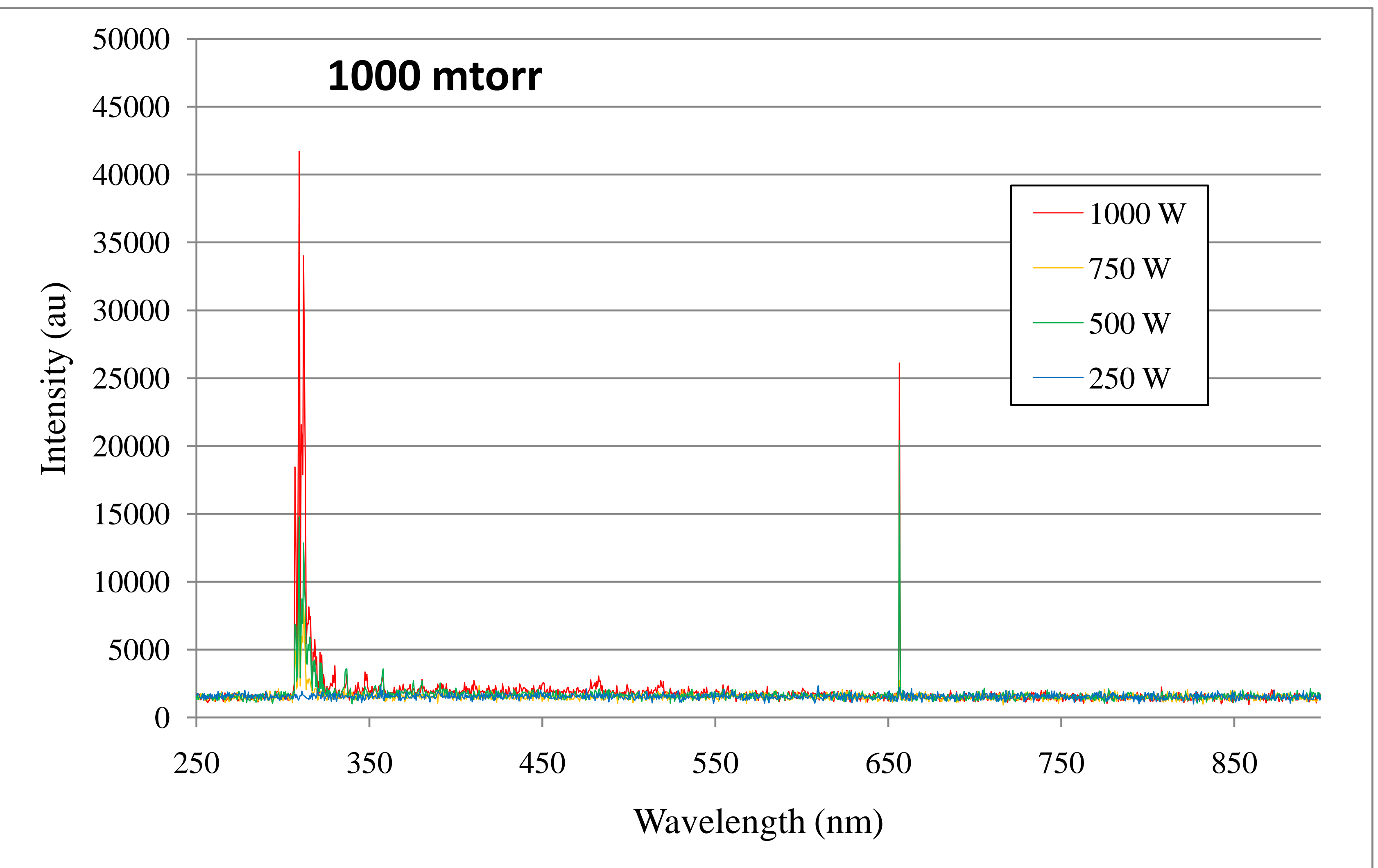

Figure 4.28: Intensity as a function of wavelength at a pressure of 1000 mtorr at applied powers of 250 (blue), 500 (green), 750 (orange), and 1000 (red) watts.

Examples of narrowing the area of interest to exclude the large intensity lines of H_α at 656 and OI at 778 nm, which tended to saturate the detection system, allowing a closer examination of the atomic and molecular species not easily visible in complete spectra are shown in Figures 4.29 and 4.30. The appearance of peaks, shown in Figure 4.29, at 395 (OI), and 410 (H_γ), were not seen in either (**Cap**) or (**Far**) experiments, while the ($A^2\Sigma^+ - X^2\Pi$) bandhead of OH at 309 nm and ($B^1\Sigma - A^1\Pi$) bandhead of CO at 437 nm were seen in the earlier experiments. Activity around the monitored transitions (Table 4.5) showed increased spectral intensities at 309 (OH), 395 (OI), 410 (H_γ), 437 (CO), and 656 nm H_α as well as an increase in the intensity of a continuum, seen from about 300–700 nm, with its midpoint around 500 nm that increased approximately linearly with each increase in applied power.

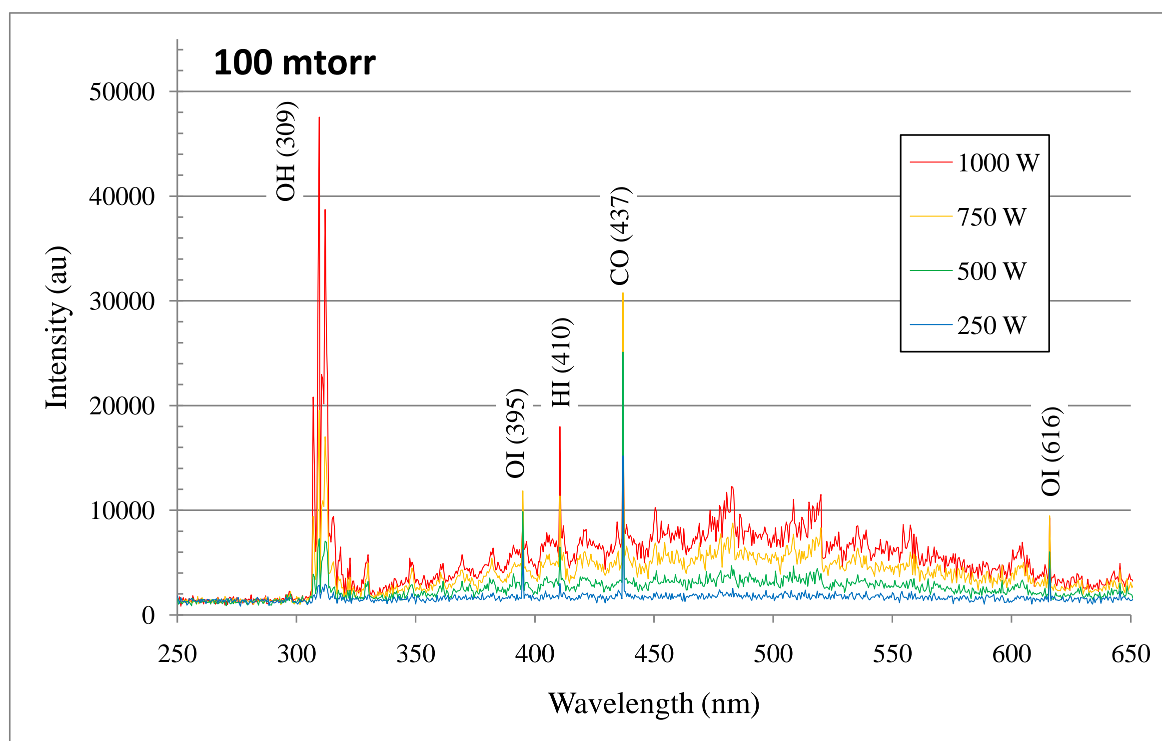

Figure 4.29: Comparison of intensity versus wavelength shows increased activity at 309 nm (OH), as well as at 395 nm (OI), 410 nm (H_γ), 437 nm (CO), and 616 nm (OI) visible after introduction of sample which was processed at a pressure of 100 mtorr and at applied power levels as shown.

The spectrum acquired at a processing pressure of 300 mtorr, shown in Figure 4.30, showed an increase (77 percent) in the intensity of the $(A^2\Sigma^+ - X^2\Pi)$ bandhead of OH at 309 nm, with less significant increases in the lines at 395 nm (OI), 410 nm (H_γ), 437 nm (CO), and 616 nm (OI) as well as an overall decrease in the intensity of the continuum seen at a pressure of 100 mtorr. The continuum maintained the intensity seen at 100 mtorr only at an applied power of 1000 watts.

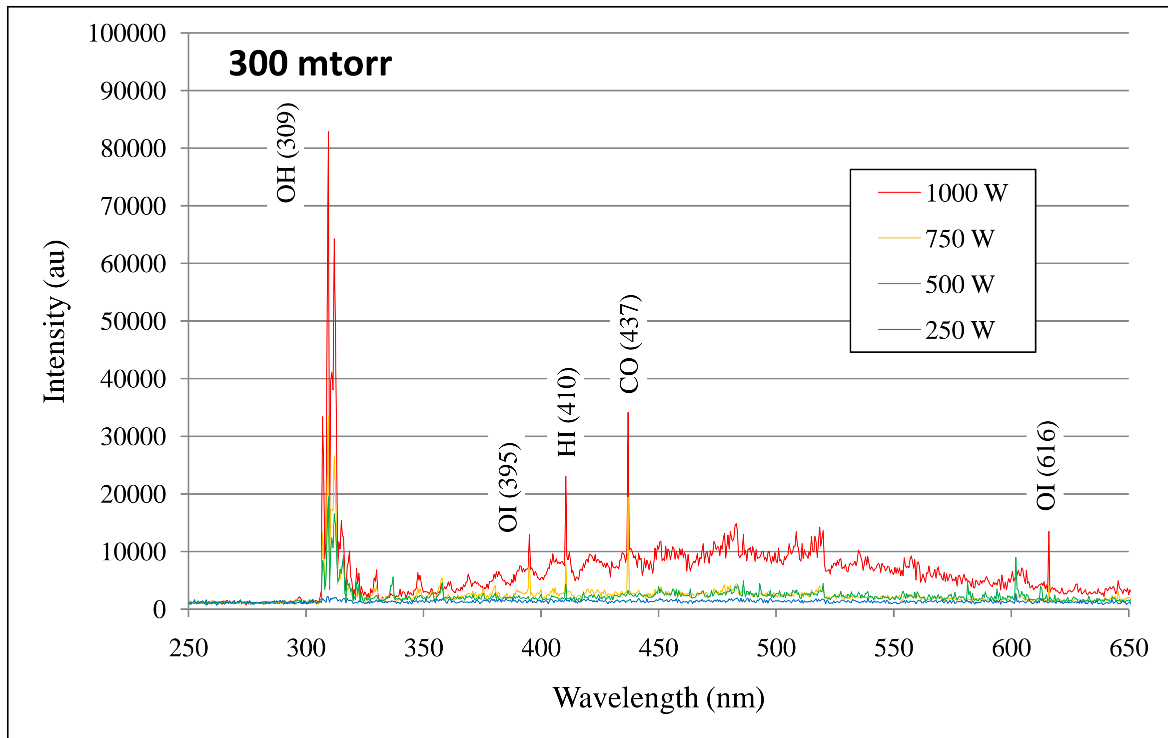

Figure 4.30: Comparison of intensity versus wavelength shows greatly increased activity at 309 nm (OH), as well as at 395 nm (OI), 410 nm (H_γ), 437 nm (CO), and 616 nm (OI) visible after introduction of sample to the processing system. Sample was processed at a pressure of 300 mtorr and applied power levels as shown.

Examining the same base group of lines monitored in the preliminary works allowed a direct comparison of spectral data relative to both the type of discharge used as well as the distance from the center of the coil. Spectral lines monitored for this experiment are shown in Table 4.5. Changes in intensity levels of the OH and CO molecular bandheads between 304 and 324 nm are shown in Figures 4.31–4.34. Contrary to the results found

in both previous experimental series, this series (**Near**) showed a significant increase in the intensity of all monitored species in what appeared to be a direct relationship to the level of applied power.

Table 4.5: Emission lines monitored during experiment three. Note that argon gas was not used in this experimental series.

Species	λ (nm)	Vibrational Transition	Band
OI	395		
	778		$(3p^5P - 3s^5S^0)$
	844		$(3p^3P - 3s^5S^0)$
OH	307	(0,0)	$(A^2\Sigma^+ - X^2\Pi)$
	309	(0,0)	
	313	(1,1)	
	319	(2,2)	
	320	(2,2)	
CO	283	(0,0)	$(b^3\Sigma - a^1\Pi)$
	297	(0,1)	
	313	(0,2)	
	331	(0,3)	
	349	(0,4)	
CO	451	(0,0)	$(B^1\Sigma - A^1\Pi)$
	484	(0,1)	
	519	(0,2)	
	561	(0,3)	
	608	(0,4)	
H_α	656		$(2s - 3p)$
H_β	489		$(2s - 3p)$
H_γ	434		$(2s - 3p)$
H_δ	410		$(2s - 3p)$

In Figure 4.31, the bandhead at 309 nm showed a steady increase in intensity at a fixed pressure of 100 mtorr while the applied power level was increased from 250 watts to a maximum value of 1000 watts. The $(A^2\Sigma^+ - X^2\Pi)$ bandhead at 309 nm, seen in Figure 4.32, showed a significant increase in intensity at a pressure of 300 mtorr as applied power was increased from 250 watts to a maximum value of 1000 watts. The spectra acquired at a pressure of 500 mtorr showed, in Figure 4.33, only a non-significant increase in intensity that appeared to be related to the increase in the applied power

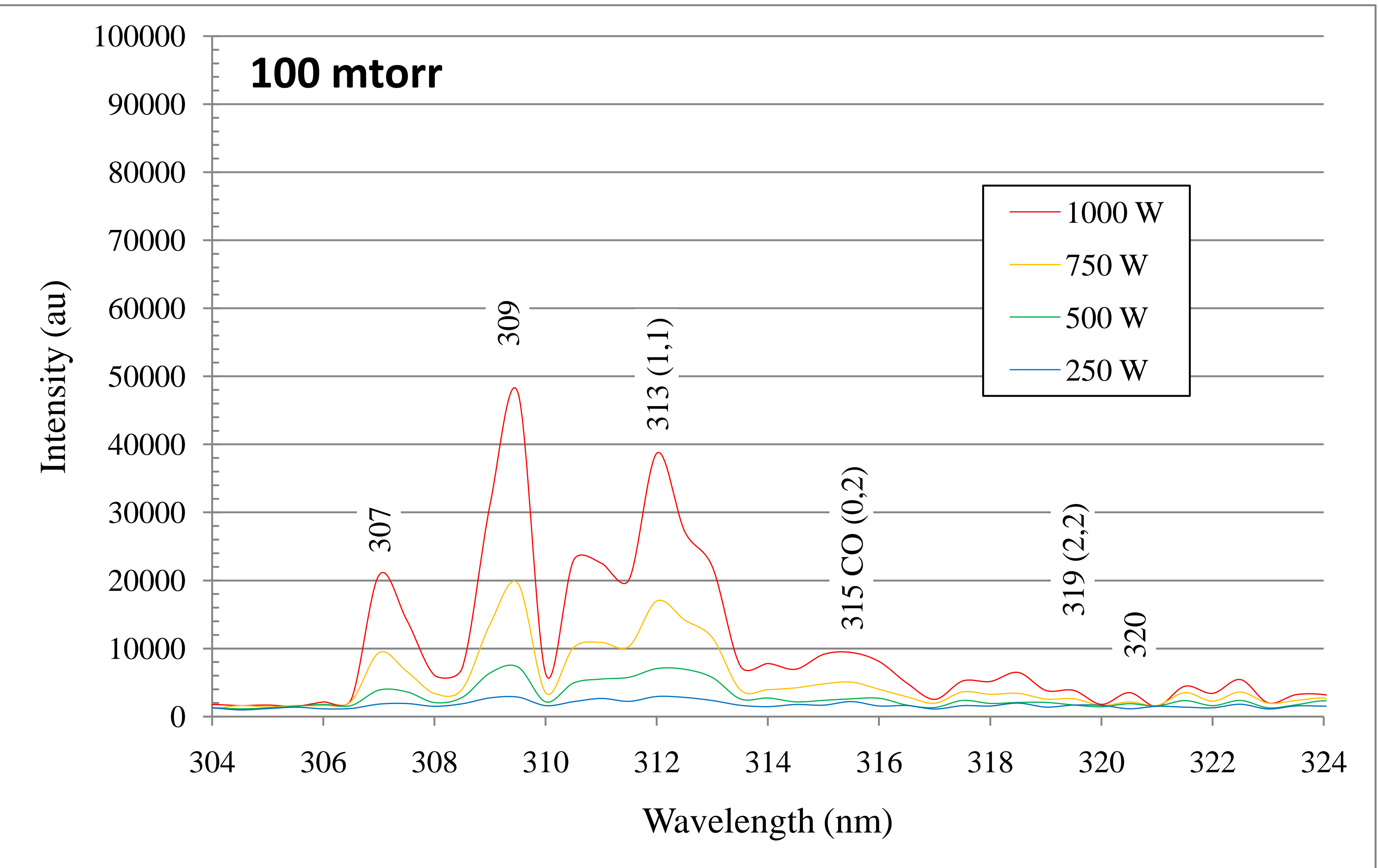

Figure 4.31: Intensity as a function of wavelength at a pressure of 100 mtorr shows the OH ($A^2\Sigma^+ - X^2\Pi$) transition at 309 nm as well as the CO ($b^3\Sigma - a^1\Pi$) bandhead at 315 nm at applied powers of 250 (blue), 500 (green), 750 (orange), and 1000 (red) watts.

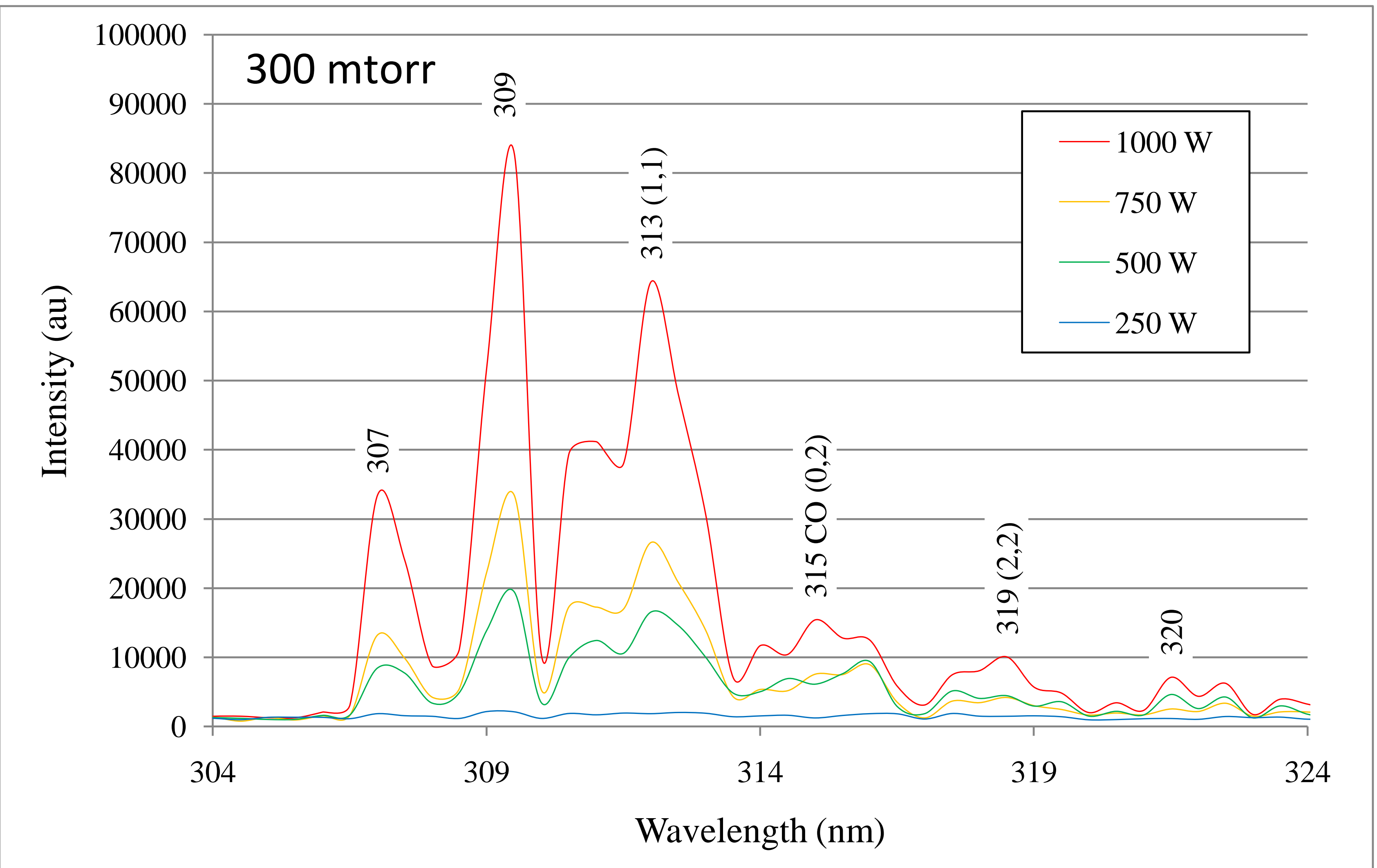

Figure 4.32: Intensity as a function of wavelength at a pressure of 300 mtorr shows the OH ($A^2\Sigma^+ - X^2\Pi$) transition at 309 nm as well as the CO ($b^3\Sigma - a^1\Pi$) bandhead at 315 nm at applied powers of 250 (blue), 500 (green), 750 (orange), and 1000 (red) watts.

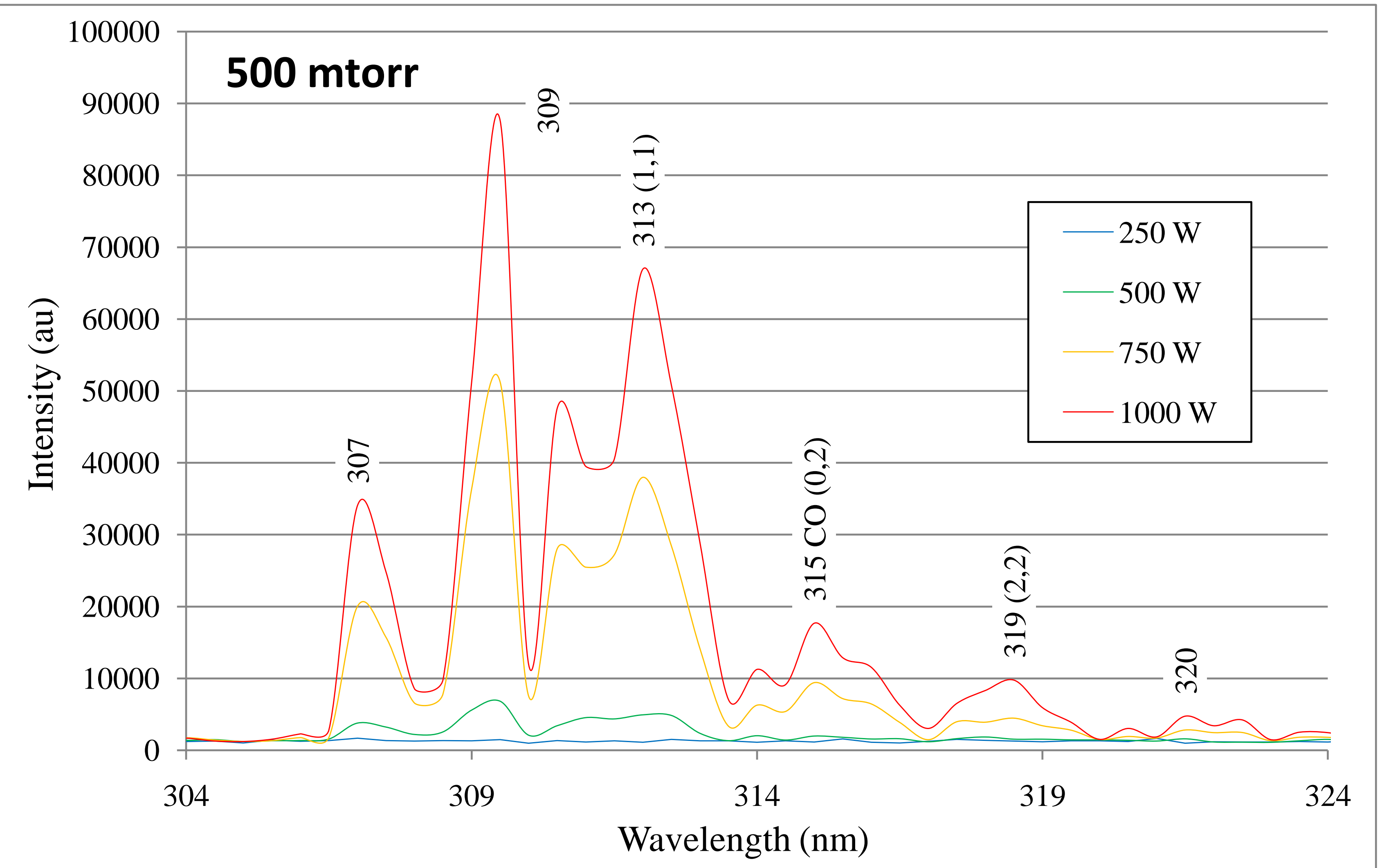

Figure 4.33: Intensity as a function of wavelength at a pressure of 100 mtorr shows the OH ($A^2\Sigma^+ - X^2\Pi$) transition at 309 nm as well as the CO ($b^3\Sigma - a^1\Pi$) bandhead at 315 nm at applied powers of 250 (blue), 500 (green), 750 (orange), and 1000 (red) watts.

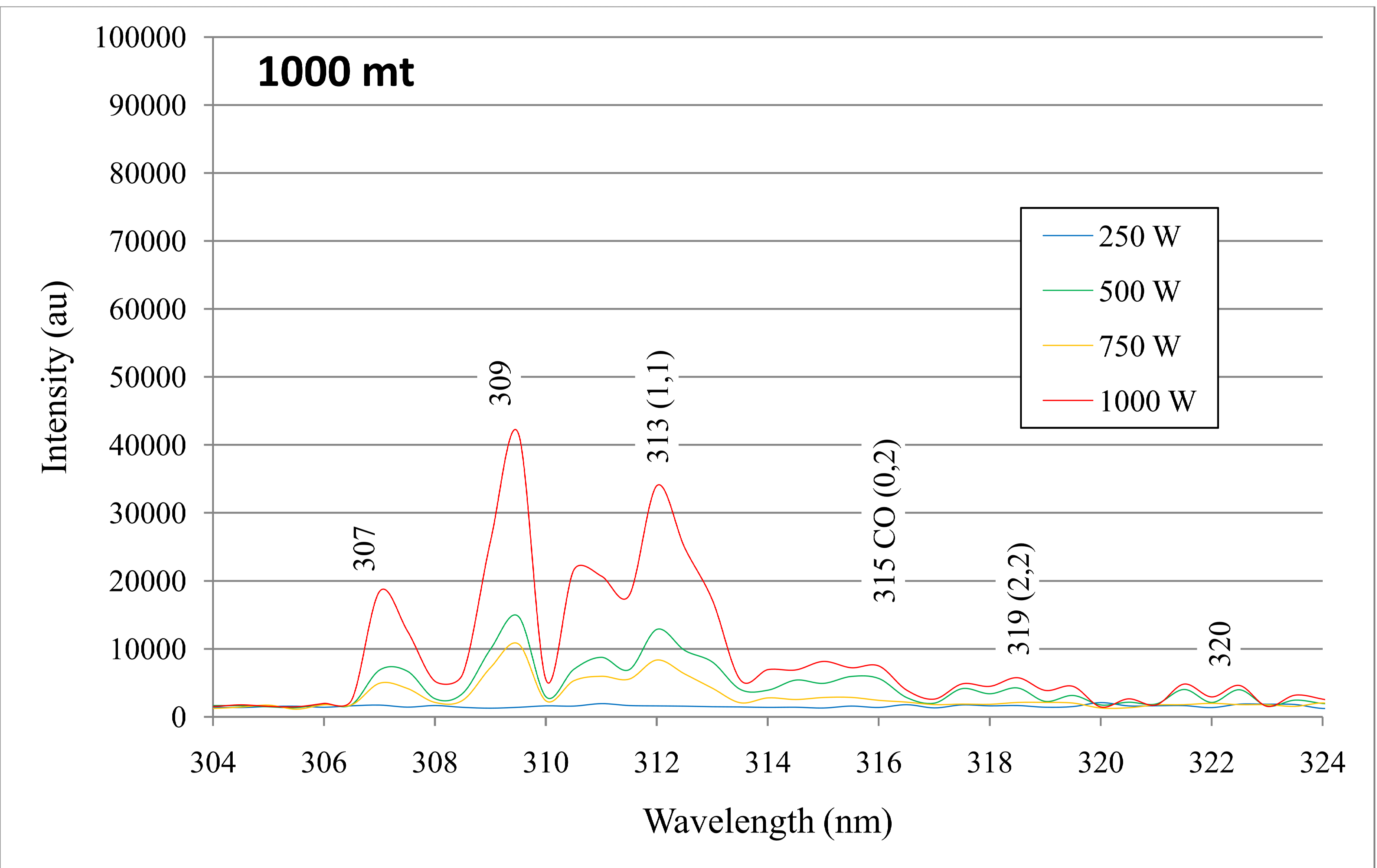

Figure 4.34: Intensity as a function of wavelength at a pressure of 100 mtorr shows the OH ($A^2\Sigma^+ - X^2\Pi$) transition at 309 nm as well as the CO ($b^3\Sigma - a^1\Pi$) bandhead at 315 nm at applied powers of 250 (blue), 500 (green), 750 (orange), and 1000 (red) watts.

level. The sample processed at 1000 mtorr, and shown in Figure 4.34, showed a significant overall decrease in intensity to a level lower than the spectrum acquired at 100 mtorr for all applied power levels. Note that each spectrum changed in intensity but not composition.

Chan et al.[152] and Morra et al.[154] reported that after an initial increase in "combination products" resulting from the interaction of the sample with the process gas (O_2), the sample might reach an equilibrium state after the completion of functionalization of the sample surface, causing the OES spectral information to revert to a more sample-like spectrum indicating the end of functionalization and the beginning of an etch-cycle where sample material is removed by further exposure to the discharge. This explanation seemed a good fit when applied to samples in the (**Far**) experiment as they were processed for long periods of time. However, the samples in the (**Near**) experiment were processed for a much shorter period and do not show the same behavior but do show ever-increasing intensities linked with increased power. Cvelbar et al.[81] mention changes in spectral intensity related to pressure that parallel these findings, specifically that at pressures corresponding to those used in the (**Near**) experiment the decrease in spectral activity can be linked not only to an increase in activity that follows an increase in power but an additional relationship that shows a decrease in activity that follows the increase in pressure.

Intensities of the ($3p^5P - 3s^5S^0$) transition of OI at 778 nm, shown in Figure 4.35, showed a significant increase as the pressure was raised to 300 mtorr for applied power levels of 750 and 1000 watts. An increase of the pressure to a value of 500 mtorr, however, produced a significant decline in intensity for power levels above 500 watts with an increase in intensity for only the applied power level of 500 and 250 watts. All levels of applied power showed a significant reduction in intensity at the final pressure of 1000 mtorr.

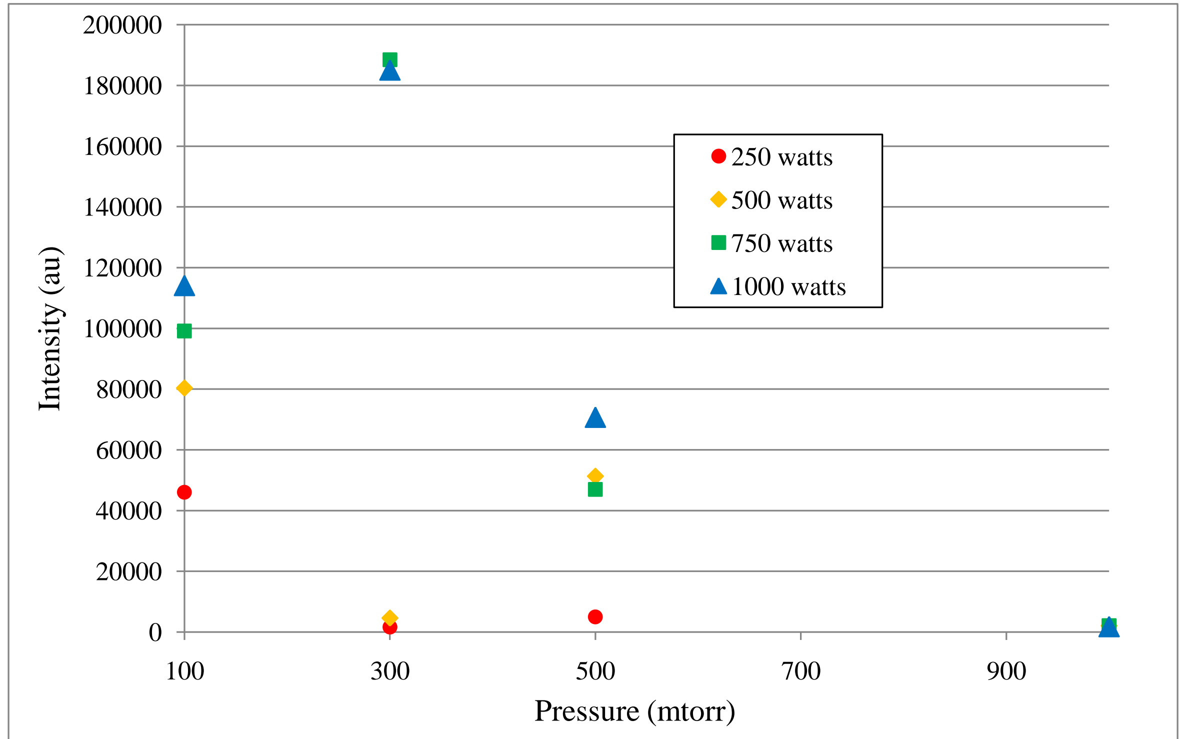

Figure 4.35: Intensity of OI versus pressure plotted for applied powers of 250, 500, 750 and 1000 watts.

The $(2s-3p)$ transition of H_α at 656 nm was not seen in the (**Far**) experiments and was only occasionally seen in the (**Cap**) and only then at relatively low intensity levels. The increase in intensity with respect to the increase in applied power is shown in Figure 4.36. Each of the pressure setpoints showed an increase in intensity of the H_α line at 656 nm, consistent with the increase in the level of applied power. The spectral intensity increased in relation to applied power level at 100 mtorr, increased significantly at 300 mtorr for applied power levels above 250 watts, returned to near-initial levels at 500 mtorr, but decreased significantly as the pressure is increased to 1000 mtorr.

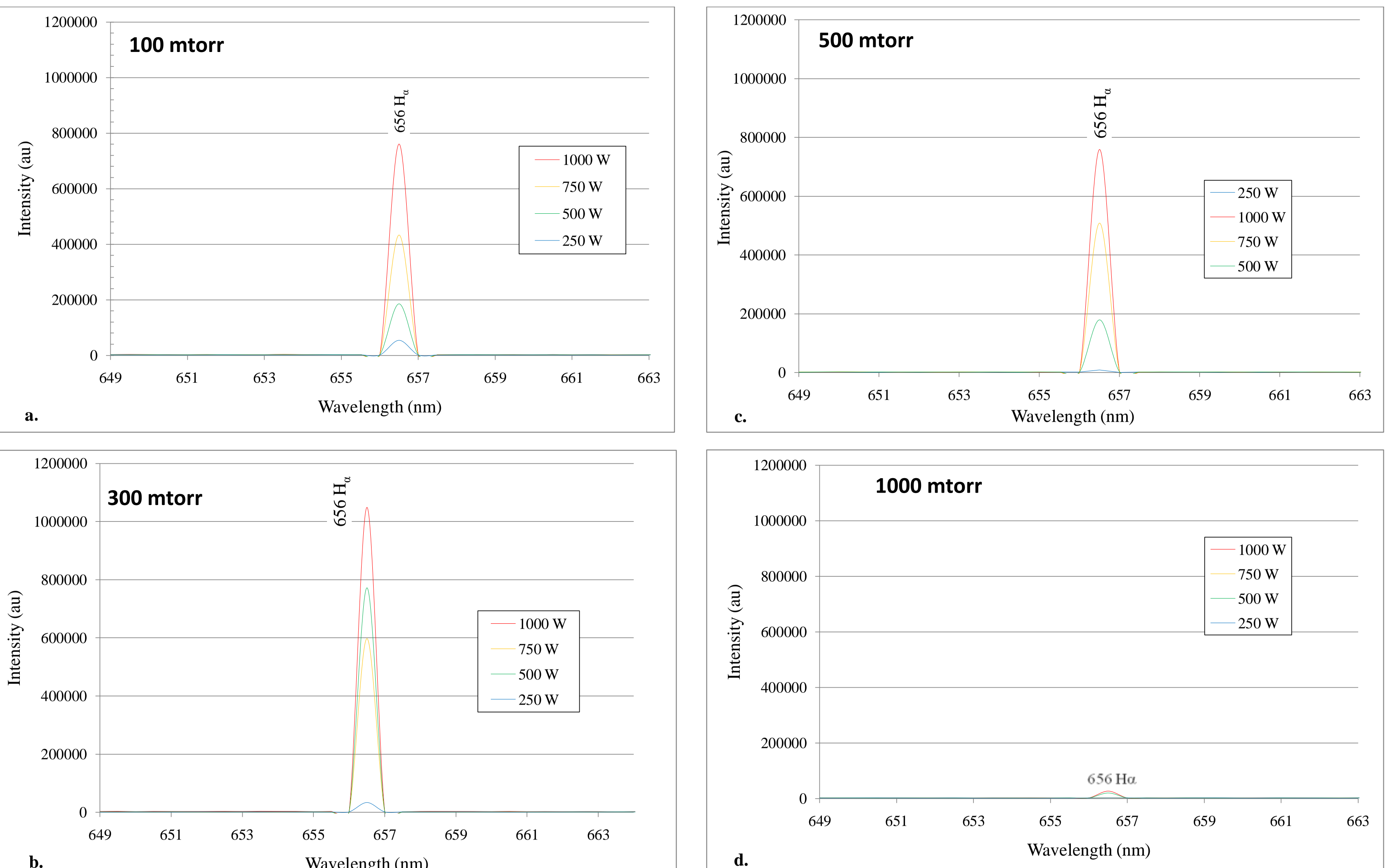

Figure 4.36: Intensity of the $(2s - 3p)$ H_α transition at 656 nm for four pressures: a) 100, b) 300, c) 500, and d) 1000 mtorr.

The decrease in both overall spectral intensity (Figure 4.28) as well as the decrease in the intensities of OI (Figure 4.35) and H_α (Figure 4.36) seen as processing pressure was increased can be explained as the result of two and three body recombination. At low pressures, the number of free OI atoms increases with the increase in pressure, from 100 mtorr to 300 mtorr, since there are more O_2 atoms available for dissociation:[66,142]

$$e + O_2 \Rightarrow O + O + e \tag{4.2}$$

but at higher pressures, 500 mtorr and 1000 mtorr, two body (4.3) and three body (4.4) recombination, where M is a third body, appears to scavenge the free oxygen:[66,142]

$$O + O \Rightarrow O_2 + h\nu \tag{4.3}$$

$$O + O + M \Rightarrow O_2 + M \tag{4.4}$$

An investigation into the dissociation and recombination of oxygen is discussed by Eilasson and Koegelschatz.[66] A more thorough treatment of these mechanisms would require construction of a detailed model of the chemical kinetics, which is outside the scope of this work.

Visual examination of processed samples, shown in Figure 4.37, showed modification of the sample surface consistent with results reported in both the (**Near**) and the (**Cap**) experiments, i.e., applied power levels of 250 or 500 watts (Figure 4.37a and b) resulted in both visible (dulling) and structural (roughening) changes in the sample at levels reported by Deshmukh and Shetty[165] and others.[2,20,164] Some moderate to severe heat damage (clouding and melting) was seen after exposure of the samples to applied power levels of 750 watts, Figure 4.37c, while at 1000 watts of applied power, Figure 4.37d, significant damage to the sample was seen.

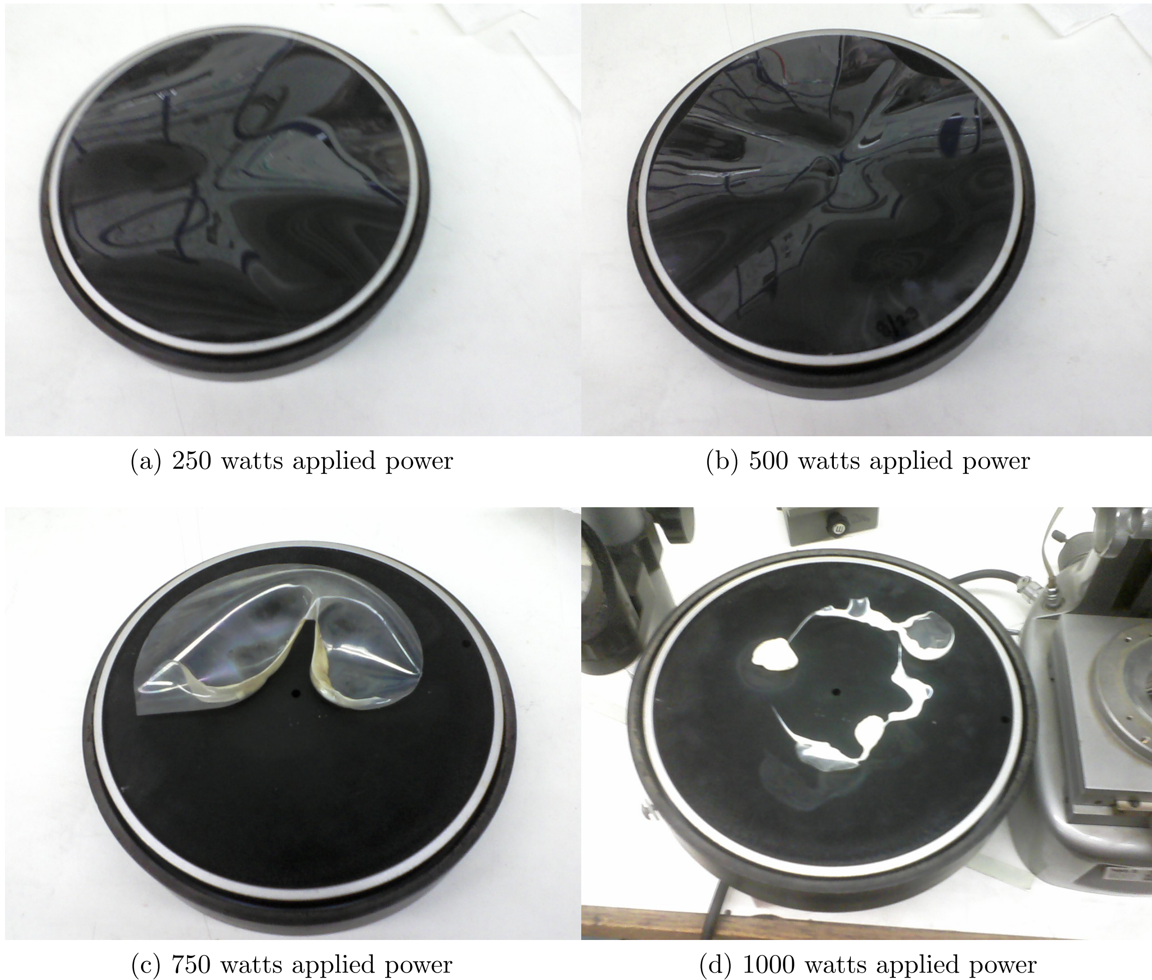
(a) 250 watts applied power
(b) 500 watts applied power
(c) 750 watts applied power
(d) 1000 watts applied power

Figure 4.37: Samples after processing in the inductive DPS (**Near**) at a pressure of 300 mtorr and applied power levels of a) 250, b) 500, c) 750 d) 1000 watts.

Few researchers concerned with the modification of PET surface characteristics exposed samples to the discharge to the point of destruction. Krstulović et al.,[2] however, in the examination of a PET sample, monitored the physical changes in a sample exposed to the discharge and reported an inverse relation in the intensity levels of the oxygen transition ($3p^5P - 3s^5S^0$) at 778 nm and the OH ($A^2\Sigma^+ - X^2\Pi$) transition at 309 nm as the sample began to oxidize. Comparison of intensity over time of the transitions of OI ($3p^5P - 3s^5S^0$) at 778 nm, OH ($A^2\Sigma^+ - X^2\Pi$) at 309 nm, and H_α ($2s - 3p$) at 656 nm in both DPS systems, shown in Figure 4.38, showed minor, but not significant, levels of the activity reported by Krstulović et al.[2] While all of the spectra

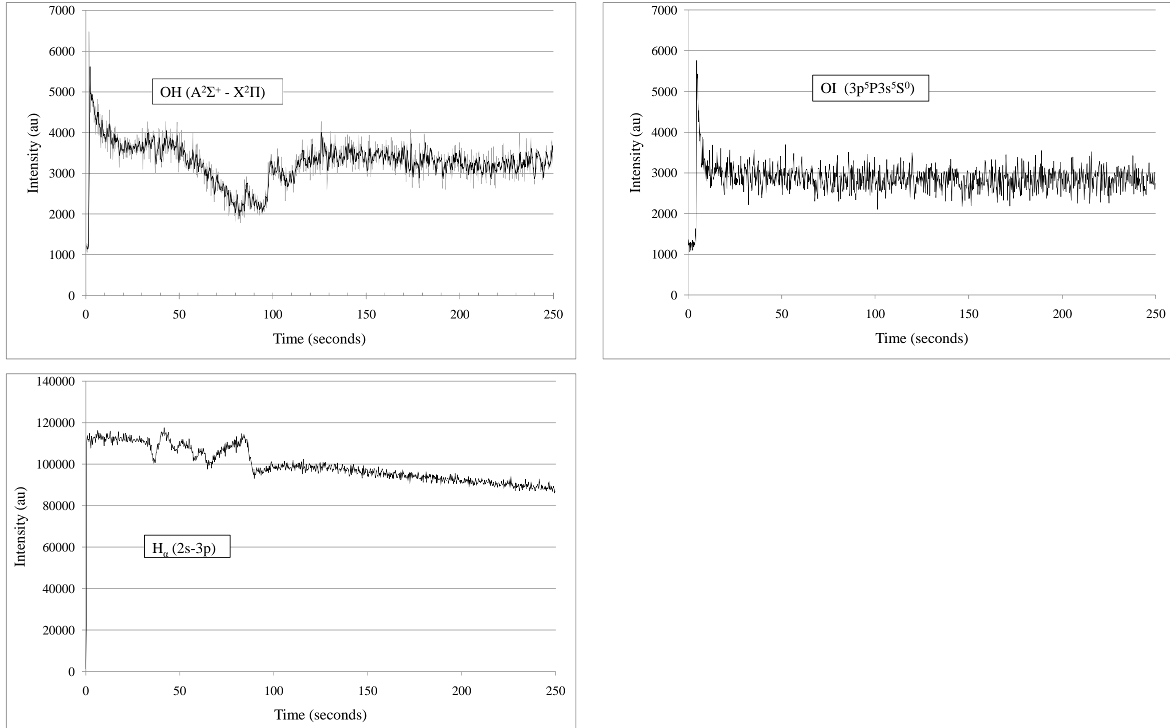

Figure 4.38: Intensities as a function of time of: a) the OH bandhead at 309 nm, b) the OI transition at 778 nm, and c) the H_α line at 656 nm for a pressure of 100 mtorr and an applied power of 250 watts.

show an initial increase in intensity indicating the reaction of the sample to the initiation of the discharge, the spectra of OI at 788 nm shows a decrease by half in the initial seconds of the discharge followed by an extended period of no significant change while the OH bandhead at 309 nm shows a decrease in intensity at about t=90 seconds as the H_α line at 656 shows an initial decline in intensity (although less steep then OI) but showing a local peak intensity at about t=90 seconds as well. The time beyond about 100 seconds until the end of the monitored period show no significant change in intensities. Although the process chamber included provision for cooling the sample stage, no external sample cooling was used in any of the experiments.

4.3.1 Comparison of DPS experiment—(Near) and (Far)

A comparison of spectra acquired from samples placed in the discharge at different distances from the center of the coil is seen in Figure 4.39. The sample placed at 13 cm (**Near**) from the center showed an increase in intensity of both atomic and molecular species when compared to the sample placed at 20 cm (**Far**) from the coil center. The increase appeared to be directly related to the distance of the sample from the center of the coil. The ($A^2\Sigma^+ - X^2\Pi$) bandhead of OH, seen at 309 nm, is visible in both spectra and appears to show only insignificant variation. The ($3p^5P - 3s^5S^0$) transition of OI at 395 and the ($2s - 3p$) transition of H_γ at 410 were not seen in the (**Far**) spectrum (although H_γ at 410 might be hidden by the line of ArI at 420 nm; H_β and H_δ were occasionally seen). Strong lines of the the CO Ångstrom system, listed in Table 4.6, page 93, and the ($B^1\Sigma^+ - A^2\Pi$) bandhead of CO are seen in the (**Near**) spectra but except for the transition at 439 nm, appear to be partially masked by the increase in the continuum centered at about 425 nm. Increased intensity of the spectrum seen just above the CO line at 607 nm was only seen in the initial (**Far**) sample and was considered to be a second order line of the OH bandhead at 309 nm.[126,142] Lines of argon clustered around 750 nm indicate trace gas[147,149,169] added to the process atmosphere during the (**Far**) series in an attempt to monitor the temperature of the discharge using the Boltzmann plot method but were obviously absent in the (**Near**) series because argon was not present.

The CO line at 439 nm, the H_α line at 656 nm, and the OI line at 778 nm showed the greatest increase in intensity as a result of the reduction in distance to the center of the coil undoubtedly due to the increase in electron density in the center of the discharge. After the beginning of processing, the comparison of spectra over the monitored transitions listed earlier (Table 4.5) and in Table 4.6 (beginning Figure 4.31) are shown beginning with Figure 4.40. A minor increase in spectral intensity of the OH transitions at 309 and 313 nm when the sample was 13 cm (**Near**) distant from the center of the

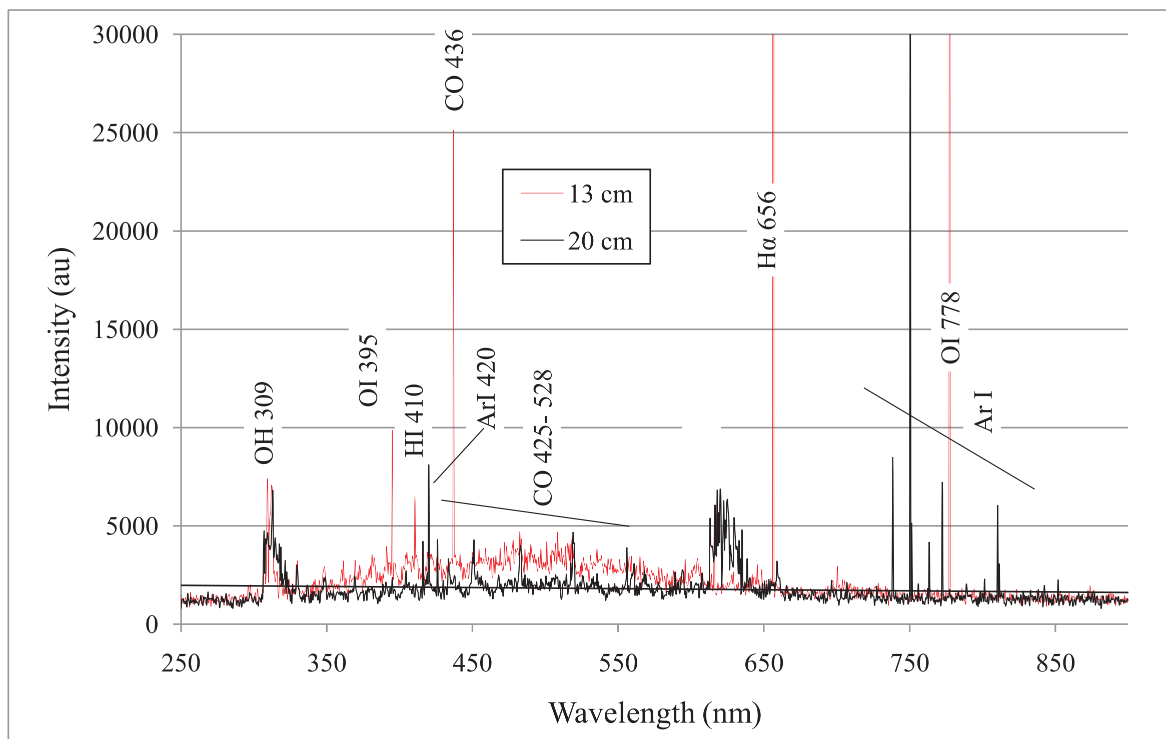

Figure 4.39: Comparison of spectra acquired at a distance of 20 cm from the center of the coil (black) and at a distance of 13 cm from the center of the coil (red) respectively at a pressure of 100 mtorr and an applied power of 500 watts.

coil and an actual decrease in intensity of the CO lines above about 314 nm was seen for the sample placed at 20 cm (**Far**) distant from the center of the coil.

The $A^2\Sigma^+ - X^2\Pi$ bandhead of OH at 309 nm, as expected, was seen with increased intensity in the (**Near**) as compared to the intensities found in the (**Far**) samples. In addition to the overall increase in intensity, the change in location of the samples with respect to the center of the coil appeared to enhance the ability to see some of the rotational structures of the of OH band at 309 nm[144] and also enhanced the visibility of the CO bandhead at 315 nm (0,2) as shown in Figure 4.40.

Table 4.6: Bandheads of the CO ($B^1\Sigma^+ - A^1\Pi$) Ångstrom system as cited in [174]

λ_H	Intensity	v'-v"	Reference
413	7	1-1	Schmid & Gerö
439	8	0-1	Schmid & Gerö
451	10	0-0	Schmid & Gerö
470	2	1-2	Birge
484	10	0-1	Schmid & Gerö
502	1	0-3	Birge
520	10	0-2	Johnson & Asundi
540	2	1-4	Birge
561	10	0-3	Johnson & Asundi
582	2	1-5	Birge
608	9	0-4	Johnson & Asundi
630	2	1-6	Birge
662	7	0-5	Johnson & Asundi

A comparison of the ($3p^5P - 3s^5S^0$) transition of OI at 778 nm and the ($3p^5P3s^3S^0$) transition at 844 nm is shown in Figure 4.41. The variation in intensities of the OI line at 778 nm were seen during the (**Near**) series (Figure 4.35) appeared to show sensitivity to both power and pressure of the discharge. In comparison to the spectra from the (**Far**) sample, the spectra acquired at the (**Near**) sample position showed a significant increase in intensity of the OI line at 778 nm while the OI line at 844 nm decreased to the level of the background.

The intensity of the ($3p - 2s$) transition of H_α at 656 nm showed a significant increase that paralleled the increase in pressure from 100 mtorr to 500 mtorr, shown in Figure 4.42. The H_α line was seen in all Figures (4.31– 4.34) of the (**Near**) spectra at all pressures and applied power levels. Cvelbar et al.[81] attribute the appearance of H_α to desorption of hydrogen off the walls of the chamber, while Chu et al.[170] mention the rapid incorporation of atomic components of "residual water" in the reactor.

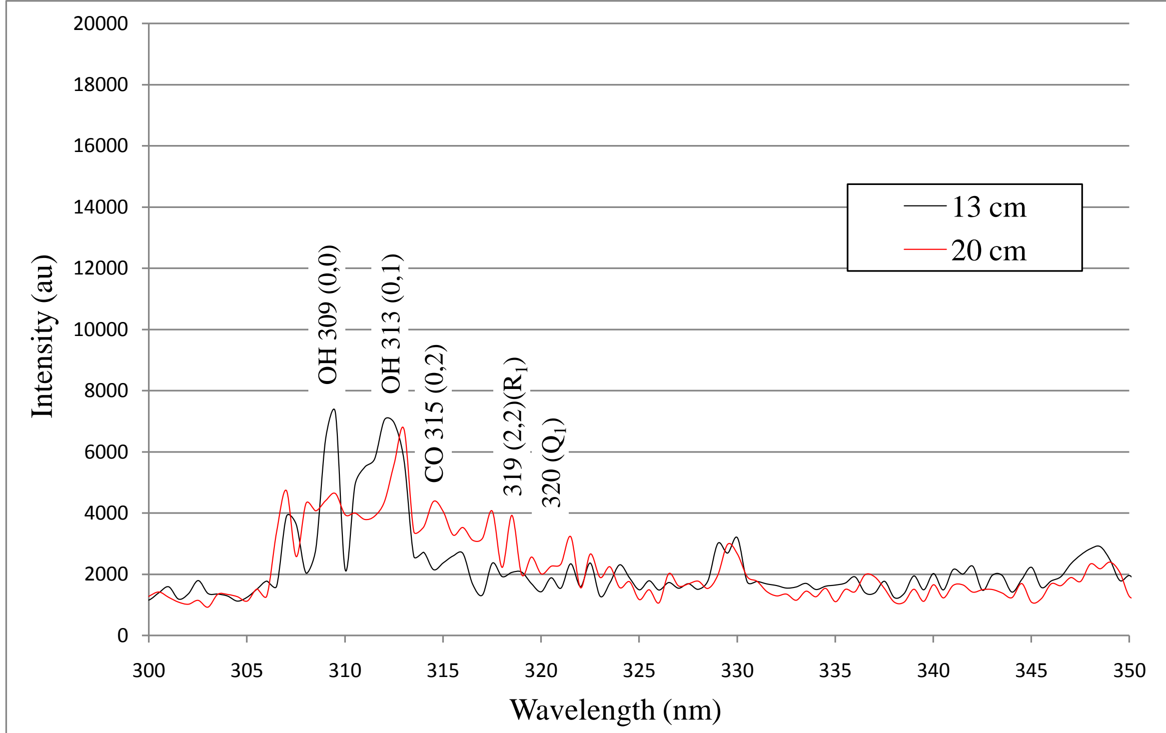

Figure 4.40: Intensity as a function of wavelength for processing discharges at a distance of 20 cm (red) and a distance of 13 cm (black) from the center of the coil at a pressure of 300 mtorr and an applied power of 500 watts.

Krstulović et al.[2] attribute the appearance of H_2 at 616 nm in the Fulcher band to the presence of water vapor in the system. But Ivanov et al.[4] confirm the creation of "stable gaseous products: H_2, H_2O, CO and CO_2...," from an initial process atmosphere containing only oxygen, which could just as easily explain the appearance of H_α, and other molecular species seen in the initial spectra. While the introduction of water into the system is indeed possible for a chamber that is used without a device to minimize exposure of samples to outside atmosphere, the low levels of hydrogen species seen are most likely the result of residue of previous polymerization of samples left behind after ashing of the chamber, not due to water.

The appearance of the continuum running from about 300 to 700 nm with a center at about 500 nm, first shown in Figure 4.39 and enlarged in Figure 4.43, indicated a mechanism at work in the (**Near**) series not seen in the (**Cap**), or (**Far**) series of

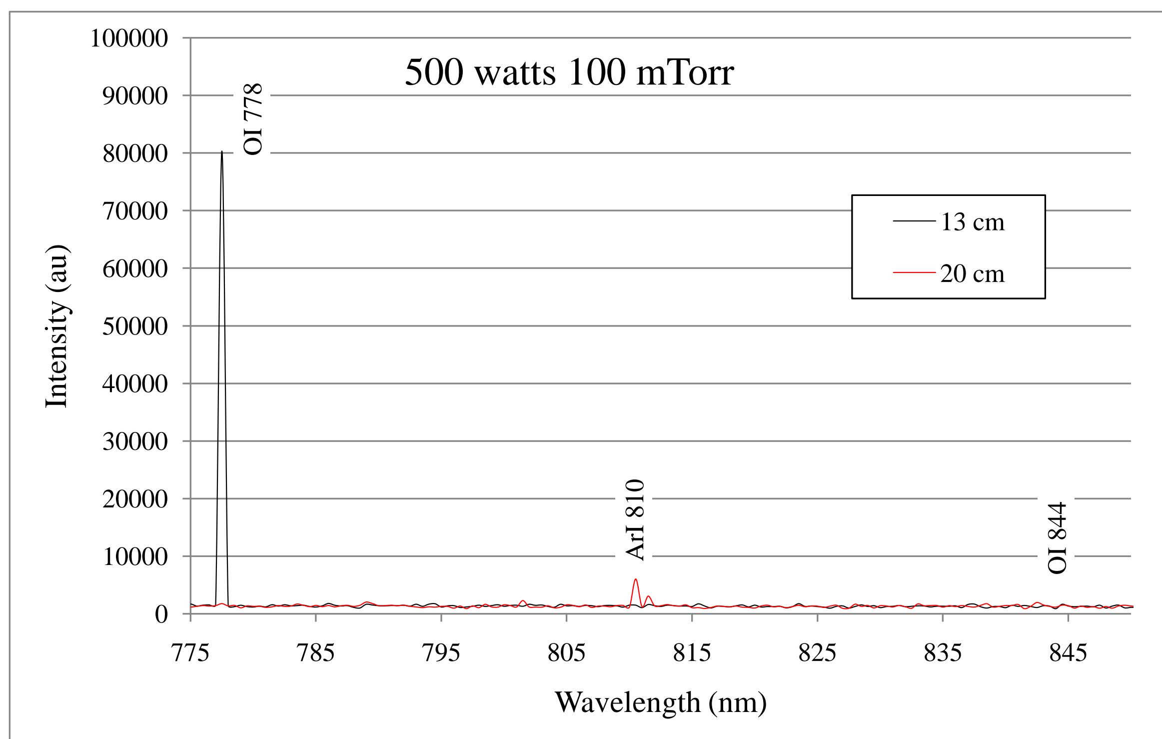

Figure 4.41: Spectra at a distance of 20 cm (black) and 13 cm (red) from the center of the coil at a pressure of 100 mtorr and an applied power of 500 watts.

experiments. Although their primary area of interest was the O_2^+ first negative system, Vassallo et al.[87] reported the appearance of the Ångstrom system bandhead of CO (Table 4.6) at 519 nm that showed an increase in intensity proportional to the increase in applied power that was consistent with the observed spectral data from the (**Near**) series. Rond et al.,[171] in an examination of a CO_2 nonequilibrium inductive discharge, reported a spectrum comparable to that seen in the (**Near**) experimental series in that the lines of oxygen at 778 and 844 nm were seen in addition to a continuum created by multiple overlapping bandheads of molecular CO (Ångstrom, Triplet, and Asundi)[171,172] acquired at a distance of 11 cm from the center of the coil. Rond et al.[171] attributed the appearance of this continuum to the "chemiluminescence effect accompanying the recombination of CO and O", as described by Broida and Gaydon[173] and Gaydon.[174]

Rond et al.[171] discussed the use of the continuum mid point to estimate the temperature of the discharge. That technique, although intriguing, was considered to be

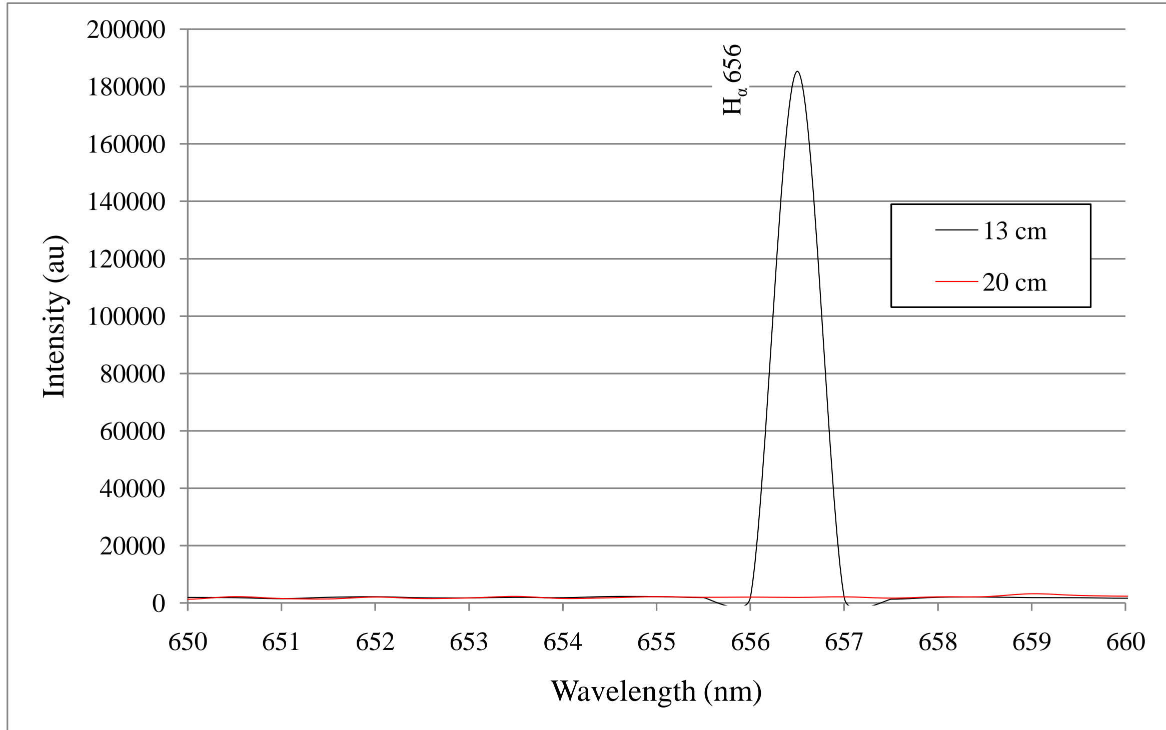

Figure 4.42: Comparison of OES data showing the H_α transition at 656 nm data taken at the (**Near**) sample position (black) and the (**Far**) sample position (red) for an applied power of 500 watts at a pressure of 100 mtorr.

outside the scope of this series of experiments.

4.4 Summary

A discussion of the data acquired during the characterization of a capacitively coupled discharge (**Cap**) processing system and an inductive decoupled plasma system (**DPS**) used for modification of the surface of poly(ethylene terepthalate) (PET) samples in an oxygen process atmosphere was presented in this chapter. The samples were placed at varying distances from the center of the coil generating the plasma discharge with the goal of varying the processing properties within the DPS chamber. Optical emission spectroscopy (OES) was used to monitor the **Cap** and **DPS** systems during processing. OES allowed the non-contact monitoring of changes in intensity of the discharge during processing of the PET samples. Spectra acquired in the DPS system showed an increase

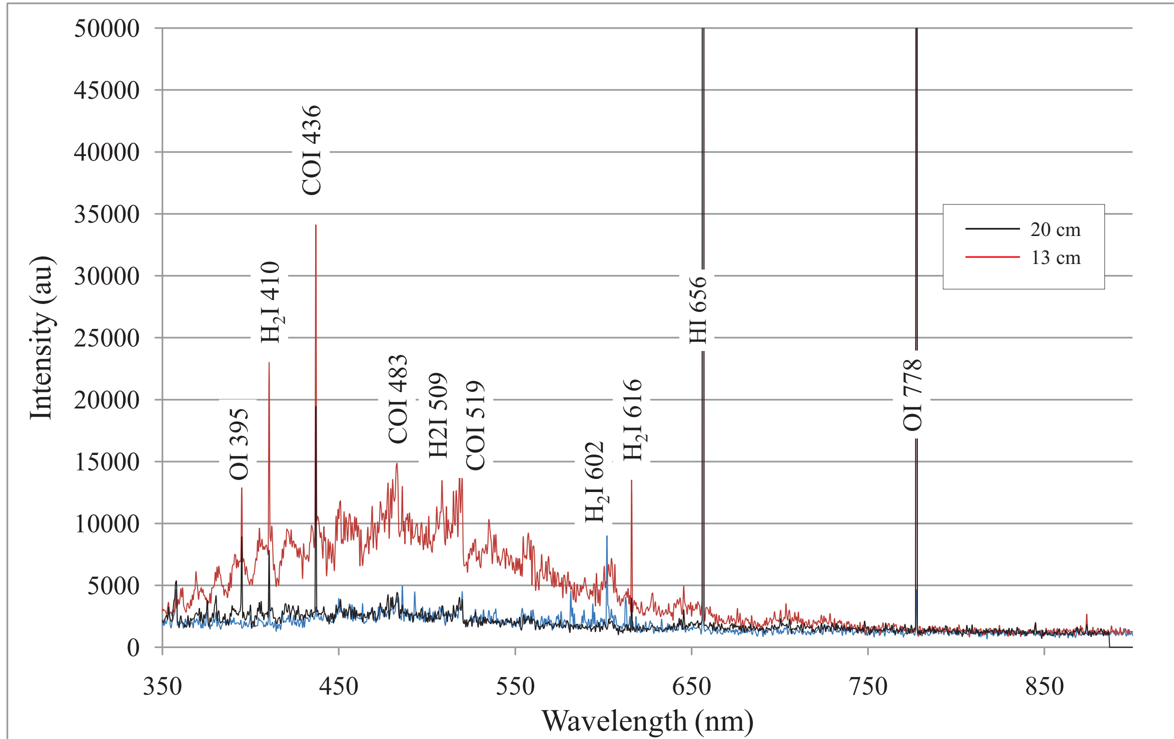

Figure 4.43: Overlapping bandheads of CO and continuum attributed to chemiluminescence during recombination of CO and O showing the (**Near**) sample position (red) and the (**Far**) sample position (black) at a pressure of 100 mtorr and an applied power of 500 watts.

in chemical species activity attributed to the increase in discharge density due to the decrease in distance of the sample to the center of the discharge coil driving the chamber discharge. An increase in the "richness" of the spectra can also be attributed to the increase in applied power, as well as the increase in chamber pressure. Power and pressure showed influence in the experiments as found by other experimenters; however, distance from the driving coil made the most difference in the number and intensity of the atomic and molecular species seen during processing.

Chapter 5

Conclusions

5.1 Conclusions

In this dissertation, three related non-thermal plasma discharges — capacitive (**Cap**), inductive DPS (**Near**), and inductive DPS (**Far**) — were investigated, including a novel application of the inductive DPS discharge used to modify the surface of poly(ethylene terepthalate) (PET) samples. A capacitively coupled discharge processing system was assembled to process PET samples in an oxygen process atmosphere. The system components and matching network were reconfigured as an inductive decoupled plasma system (DPS) and were employed in additional investigations of PET samples. Configurations used during this research were discussed in Chapter 3. Optical emission spectroscopy (OES) was used as an in-process diagnostic. Measurement of the relative degree of processing of each of the experimental systems, when referenced to an increase in spectral intensity of atomic and molecular species, was presented and discussed. Change in contact angle (CA) was used as a comparative process diagnostic. The change in CA of the PET samples after processing in each increasing electron density as compared to initial values obtained using ASTM-2578 test were presented and discussed.

The assembly of three related processing systems allowed comparison of the ability of each system to modify the surface of polymer samples under controlled process conditions. Monitoring of process efficiency at setpoints developed during the prior research, described in Chapter 3, and during the examination of the work of other

researchers, in Chapter 2, allowed the comparison of the ability of the discharge to modify the samples at each increase in power and pressure. The increase in process electron density, seen in each system, was found to directly affect the ability of the process system to modify surface characteristics of the PET samples.

System parts were reassembled into a low electron density ($\approx 10^8\ cm^{-3}$) capacitive discharge system (**Cap**) which included the design and fabrication of equal sized electrodes (13 mm spacing) designed in the style of a traditional capacitive discharge.[27] Following the experiments discussed in Chapter 3, the system was disassembled and reconfigured into the original high electron density ($10^{13}\ cm^{-3}$) inductive DPS configuration (**Far**) and the PET sample placed 20 cm from the center of the discharge coil. Upon restoring the capacitive system to the original coil and dome design, the impedance of the chamber was recalculated and appropriate modifications were made to the matching network in order to enable a unity match between the RF generator and the processing chamber. Additional PET samples were processed in the high electron density inductive DPS configuration (**Near**) at a distance of 13 cm from the center of the discharge coil.

OES spectra acquired during initial characterization of each chamber showed an increase in the overall intensity of spectral emissions indicative of an increase in the electron density generated in each chamber configuration progressing from least dense to most dense ((**Cap**) $\Rightarrow$ (**Far**) $\Rightarrow$ (**Near**)). Comparison of the three system configurations (Chapter 4) indicated an increase in degree of processing available that increased with each of the systems. Comparison of the change in intensity of emissions of both atomic and molecular species after introduction of PET samples, especially the transitions of neutral oxygen at 778 and 844 nm, OH at 309 nm, CO at 456 nm as well as H_α at 656 nm, showed an increase in the intensity of emission that also paralleled the change from the lowest to highest density discharge seen in the initial characterization series.

Characterization of the poly(ethylene terepthalate) material prior to any processing

showed the roll polymer material to be of a slightly hydrophobic condition as indicated by a contact angle of 72°. This value was confirmed during the secondary characterization performed after preparation of the PET samples but prior to processing in the chamber. Contact angle values acquired after processing showed a continuing decrease in measured contact angle progressing from least dense to most dense ((**Cap**) ⇒ (**Far**) ⇒ (**Near**)). Comparison of the results from each of the system configurations (Chapter 4), indicated an increase in degree of processing that paralleled the change from the lowest to highest density discharge seen in the experimental series. The increase in degree of processing was also confirmed by visual examination of the samples before and after processing; degradation of the surface was seen as described in Chapter 4.

5.2 Further Work

The experimental data collected from these experimental series indicated that the increased power and pressure of a non-thermal inductive discharge was able to affect the surface of the poly(ethylene terepthalate) test material; the surface energy of all of the samples tested was increased after exposure to the discharge increasing the wettability of the sample surface. Many researchers have attributed the increase in surface energy of treated polymers to the build up of oxygen and other fragments on the surface of the treated samples. The initial breaking of the carbon-hydrogen bonds of the polymer backbone of the poly(ethylene terepthalate) samples yield the initial increase in the active species of OH and CO described by Chung et al.,[175] Cvelbar et al.,[81] and others.[48,176–178] Investigations of the efficiency of the excited oxygen discharge used to modify the surface of the PET samples were limited to a comparison of surface between succeeding experiments to determine, by examination, an increase in discharge density based upon inspection and determination of the change in surface energy and the estimation of electron density based upon other sources/researchers. The development of a method to measure the electron density of the discharge would add to the diagnostic

ability of this series of experiments. A conventional Langmuir-type probe is generally used in the measurement of electron density in plasma discharges. In this case, however, re-deposition of polymer fragments from the processing atmosphere onto any passive probe inserted into the discharge would immediately insulate the surface, rendering it inoperative. The development of an active diagnostic probe would allow the accurate measurement of electron densities for each of the experimental discharges, allowing for more accurate explanation for the reported increase in surface energy of processed samples.

The experimental data acquired during this series of experiments, ((**Cap**) $\Rightarrow$ (**Far**) $\Rightarrow$ (**Near**)), indicate that an increase in electron density provided by the change from a capacitive processing chamber to an inductive decoupled plasma system (DPS) not only increased the density of the discharge, but exposure of the samples to the denser discharge increased the surface energy of the sample but showed a corresponding change in the degree of modification as samples were moved from the less-dense processing system to the more-dense processing system. The use of a scanning electron microscope (SEM), proposed in an earlier work,[20] as a diagnostic tool for visualization of the physical changes in the surface of the polymer samples viewed at a microscopic level could allow the investigation of the sample surface in order to verify the reports of Beake et al.[179] and Vesel et al.[180] of the actual erosion of the sample surface consistent with the exposure of the sample to the energetic discharges. In addition, this method of characterization is widely used in industry.[1,180–182]

Although the use of optical emission spectroscopy as a diagnostic tool enabled the monitoring of the changes in the process atmosphere during the sample exposure time, the scanning monochromator used in this series of experiments was unable to measure time slices small enough to do more than see a possible trend in the relationship between OH, CO and OI reported by Krstulović et al.[2] Any additional investigation into the relationship between these species as described by Krstulović et al.[2] and other

researchers[81,180] would require the addition of a CCD-based spectrometer able to acquire complete spectra of multiple transitions of interest at millisecond intervals in order to build a time axis of changes in spectral intensities of these atomic and molecular species.

Bibliography

Bibliography

1. Carlotti, S.; Mas, A. *J Appl Polym Sci* **1998**, *69*, 2321–2330.
2. Krstulović, N.; Labazan, I.; Milošević, S.; Cvelbar, U.; Vesel, A.; Mozetič, M. *Journal of Physics D: Applied Physics* **2006**, *39*, 3799–3804.
3. Berins, M. L. *Plastics Engineering Handbook of the Society of the Plastics Industry*; New York:Chapman & Hall, 1991.
4. Ivanov, S. I.; Svirachev, D. M.; Pechenyakova, V. P.; Petrov, C. V.; Dobreva, E. D. *Bulg. J. Phys.* **1987**, *14*, 581–588.
5. Deshmukh, R.; Bhat, N. *Material Research Innovations* **2003**, *7*, 283–290.
6. Glogauer, S. *Rubber & plastics news* **2009**, *38*, 16–19.
7. Bol'shakov, A. A.; Cruden, B. A.; Mogul, R.; Rao, M.; Sharma, S. P.; Khare, B. N.; Meyyappan, M. *AIAA journal* **2004**, *42*, 823–832.
8. Laroussi, M. *Plasma Processes and Polymers* **2005**, *2*, 391–400.
9. Polini, W.; Sorrentino, L. *Applied Surface Science* **2003**, *214*, 232–242.
10. Font, G. I. *American Institute of Aeronautics and Astronautics* **1998**, 1–10.
11. Liu, C.; Xue, B.; Eliasson, B.; He, F.; Li, Y.; Xu, G. *Plasma Chemistry and Plasma Processing* **2001**, *21*, 301–310.

12. Wertheimer, M. R.; Martinu, L.; Liston, E. M. *J. Adhes. Sci. Technol.(The Netherlands)* **1993**, *7*, 1091–1127.

13. Nickerson, R. *Plasma Surface Modification for Cleaning and Adhesion*; TAPPI PRESS, 1998; pp 1101–1108.

14. Shenton, M. J.; Stevens, G. C. *Journal of Physics D: Applied Physics* **2001**, *34*, 2761–2768.

15. Bonizzoni, G.; Vassallo, E. *Vacuum* **2002**, *64*, 327–336.

16. Chen, F. F. *Phys. Plasmas* **1995**, *2*, 2164–2175.

17. Jung, C. K.; Bae, I. S.; Lee, S. B.; Cho, J. H.; Shin, E. S.; Choi, S. C.; Boo, J. H. *Thin Solid Films* **2006**, *506*, 316–322.

18. Kalpakjian, S.; Schmid, S. *Manufacturing Engineering and Technology*, 5th ed.; Upper Saddle River N.J.:Pearson Prentice-Hall., 2006.

19. Vassallo, E.; Cremona, A.; Ghezzi, F.; Ricci, D. *Vacuum* **2010**, *84*, 902–906.

20. Rhoton, R. L. M.Sc. thesis, Eastern Michigan University, 2009.

21. Rhoton, R. L.; Brake, M. Characterization of PET samples processed in an RF oxygen discharge. *Proceedings of the 61st Annual Gaseous Electronics Conference. Dallas, Texas*, 2008.

22. Setsuhara, Y.; Cho, K.; Takenaka, K.; Ebe, A.; Shiratani, M.; Sekine, M.; Hori, M.; Ikenaga, E.; Kondo, H.; Nakatsuka, O.; Zaima, S. *Thin Solid Films* **2009**, *518*, 1006–1011.

23. Tajima, S.; Komvopoulos, K. *J.Phys.Chem.B* **2005**, *109*, 17623–17629.

24. Wertheimer, M. R.; Thomas, H. R.; Perri, M. J.; Klemberg-Sapieha, J. E.; Martinu, L. *Pure and Applied Chemistry* **1996**, *68*, 1047–1054.

25. Quirk, M.; Serda, J. *Semiconductor manufacturing technology*; Prentice Hall Upper Saddle River,NJ, 2000.

26. Keller, J. H. *Plasma Sources Science and Technology* **1996**, *5*, 166–172.

27. Lieberman, M. A.; Lichtenberg, A. J. *Principles of Plasma Discharges andMaterials Processing*, 2nd ed.; John Wiley & Sons, Inc.: Hoboken, NJ, 2005.

28. Hopwood, J. *Plasma Sources Science and Technology* **1992**, *1*, 109–116.

29. Piejak, R. B.; Godyak, V. A.; Alexandrovich, B. M. *Plasma Sources Science and Technology* **1992**, *1*, 179–186.

30. Chen, F. F. *Plasma Physics and Controlled Fusion, Volume 1: Plasma Physics.*; New York: Plenum Press., 1984.

31. Brown, S. *Basic Data of Plasma Physics*; New York: American Institute of Physics., 1994.

32. Chapman, B. *Glow Discharge Processes*; New York: John Wiley & Sons., 1980.

33. Bogaerts, A.; Neyts, E.; Gijbels, R.; van der Mullen, J. *Spectrochimica Acta Part B: Atomic Spectroscopy* **2002**, *57*, 609–658.

34. Chen, F. F.; Chang, J. P. *Lecture notes on principles of plasma processing*; New York: Plenum Press., 2003.

35. Godyak, V. A.; Piejak, R. B.; Alexandrovich, B. M. *Journal of Applied Physics* **1999**, *85*, 703.

36. Ding, Z. F.; Yuan, G. Y.; Gao, W.; Sun, J. C. *Physics of Plasmas* **2008**, *15*, b063506–1–7.

37. Huang, Y.-C.; Buie, M.; Stoehr, B.; Buxbaum, A.; Ruhl, G. *SPIE* **2001**, 1–9.

38. Cunliffe, A. M.; Jones, N.; Williams, P. *Environmental Technology* **2003**, *24*, 653–663.

39. Guddeti, R. R.; Knight, R.; Grossmann, E. D. *Plasma Chemistry and Plasma Processing* **2000**, *20*, 37–64.

40. Surendra, M.; Graves, D. B. *Applied Physics Letters* **1991**, *57*, 20912–2093.

41. Moravej, M.; Hicks, R. F. *Chemical vapor deposition* **2005**, *11*, 469–476.

42. Babaeva, N. Y.; Kushner, M. J. *J. Appl. Phys.* **2007**, *101*, 113307–1–11.

43. Hollander, A.; Behnisch, J. *Surface and Coatings Technology* **2001**, *142-144*, 1074–1077.

44. Cui, N.; Brown, N. M. D. *Applied surface science* **2002**, *189*, 31–38.

45. De Geyter, N.; Morent, R.; Leys, C.; Gengembre, L.; Payen, E. *Surface and Coatings Technology* **2007**, *201*, 7066–7075.

46. Dumitrascu, N.; Borcia, G.; Apetroaei, N.; Popa, G. *Plasma Sources Science and Technology* **2002**, *11*, 127–134.

47. Salge, J. *Le Journal de Physique IV* **1995**, *5*, 5–5.

48. Kogelschatz, U. *Plasma Chemistry and Plasma Processing* **2003**, *23*, 1–46.

49. Selwyn, G. S.; Herrmann, H. W.; Park, J.; Henins, I. *Contributions to Plasma Physics* **2001**, *41*, 610–619.

50. Chiper, A. S.; Chen, W.; Stamate, E. Diagnostics of DBD Plasma Produced Inside a Closed Package. *19th International Symposium on Plasma Chemistry, Bochum, July 26 to 31, 2009*, 2009.

51. Borcia, G.; Anderson, C. A.; Brown, N. M. D. *Plasma Sources Science and Technology* **2003**, *12*, 335–344.

52. Moravej, M.; Yang, X.; Hicks, R. F.; J., P.; Babayan, S. E. *Journal of Applied Physics* **2006**, *99*, 1–6.

53. Morent, R.; De Geyter, N.; Leys, C.; Gengembre, L.; Payen, E. *Surface& Coatings Technology* **2007**, *201*, 7847–7854.

54. Almazn-Almazn, M. C.; Paredes, J. I.; Prez-Mendoza, M.; Domingo-Garca, M.; Fernndez-Morales, I.; Martnez-Alonso, A.; Lopez-Garzn, F. J. *J. Phys. Chem. B* **2006**, *110(23)*, 11327–11333.

55. Wang, H.; Liu, Y.; Li, Z.; Zhang, X.; Zhang, S.; Zhang, Y. *European Polymer Journal* **2009**, *45*, 1535–1544.

56. Kamimura, A.; Yamamoto, S. *Org. Lett* **2007**, *9*, 2533–2535.

57. Adams, B. E. *Characterization of an Oxygen Plasma Process for Cleaning Packaged Semiconductor Devices*; Technical Report KCP-613-5798, 1996.

58. Buckles, S. L. The Use of Argon Plasma for Cleaning Hybrid Circuits Prior to Wire Bonding. *The Proceedings of the 1984 International Symposium on Microelectronics (ISHM)*, Minneapolis, MN, 1987; pp 476–479.

59. Arefi-Khonsari, F.; Tatoulian, M.; Bretagnol, F.; Bouloussa, O.; Rondelez, F. *Surface and Coatings Technology* **2005**, *200*, 14–20.

60. Polak, A. J., 1982, US Patent 4,337,279.

61. Heinecke, R.; Ojha, S.; Llewellyn, I., 1987, US Patent 4,684,535.

62. Keane, J. J.; Lough, J. C., 1969, US Patent 3,431,135.

63. Gleich, H.; Criens, R. M.; Mosle, H. G.; Leute, U. *International Journal of Adhesion and Adhesives* **1989**, *9*, 88–94.

64. Smith, M. D. Practical applications of plasma surface modification. *Conference: International symposium on polymer surface modification: relevance to adhesion,Las Vegas,NV (United States),3-5 Nov 1993*, 1993.

65. Grace, J. M.; Gerenser, L. J. *Journal of Dispersion Science and Technology* **2003**, *24*, 305–341.

66. Eliasson, B.; Kogelschatz, U. *IEEE Transactions on Plasma Science* **1991**, *19*, 1063–1077.

67. Kaplan, S. L.; Rose, P. W. *International Journal of Adhesion and Adhesives* **1991**, *11*, 109–113.

68. Li, Z. F.; Netravali, A. N.; Sachse, W. *Journal of Materials Science* **1992**, *27*, 4625–4632.

69. Bryce, D. M. *Plastic injection molding: Manufacturing process fundamentals*; Society of Manufacturing Engineers: One SME Drive, Dearborn, MI 48121, 1996.

70. Pfender, E. *Plasma Chemistry and Plasma Processing* **1999**, *19*, 1–31.

71. Martinu, L.; Poitras, D. *Journal of Vacuum Science; Technology A: Vacuum,Surfaces,and Films* **2000**, *18*, 2619.

72. Kalpakjian, S.; Schmid, S. *Manufacturing Engineering and Technology*, 6th ed.; Upper Saddle River N.J.:Pearson Prentice-Hall., 2010.

73. Guang-qiu, Z.; Yuan-jing, G.; Zhu-fa, Z.; Zhi-shan, Q.; Yi-min, L. *Plasma Science and Technology* **2001**, *3*, 877–882.

74. Zhang, C.; Fang, K. *Surface & Coatings Technology* **2009**, *203*, 2058–2063.

75. McAlpine, M. C.; Friedman, R. S.; Lieber, C. M. *Nano Letters* **2003**, *3*, 443–446.

76. Chen, T.-H.; Teng, J.; Sheu, H.-L.; Liu, C.-H.; Hsieh, W.-T.; Su, C.-H.; Lin, S. Surface modification for adhesion enhancement of PET/silicone using atmospheric plasma-induced grafting. In *IEEE Int. Conf. Plasma Science - Abstracts ICOPS 2009*; IEEE, 2009; p 1.

77. Carrino, L.; Moroni, G.; Polini, W. *Journal of Materials Processing Tech.* **2002**, *121*, 373–382.

78. Kuhr, M.; Bauer, S.; Rothhaar, U.; Wolff, D. *Thin Solid Films* **2003**, *442*, 107–116.

79. Nowling, G.; Yajima, M.; Babayan, S. E.; Moravej, M.; Yang, X.; Hoffman, W.; Hicks, R. F. *Plasma Sources Science and Technology* **2005**, *14*, 477–484.

80. Mahoney, L. J. Private communication, 2010.

81. Cvelbar, U.; Krstulović, N.; Milovšević, S.; Mozetič, M. *Vacuum* **2007**, *82*, 224–227.

82. Graves, D. B. *IEEE Transactions on Plasma Science* **1994**, *22*, 31–42.

83. Hershkowitz, N. *IEEE Transactions on Plasma Science* **1998**, *26*, 1610–1620.

84. Mozetič, M. *Vacuum* **2003**, *71*, 237–240.

85. Ma, S.; Jain, M.; Chinn, J. D. *Journal of Vacuum Science Technology* **1998**, *16*, 1440–1443.

86. Cunge, G.; Vempaire, D.; Ramos, R.; Touzeau, M.; Joubert, O.; Bodard, P.; Sadeghi, N. *Plasma Sources Sci. Technol.* **2010**, *19*, 1–11.

87. Vassallo, E.; Laguardia, L.; Catellani, M.; Cremona, A.; Dellera, F.; Ghezzi, F. *Unknown* **2007**, *4*, S801–S805.

88. Inagaki, N.; Narushim, K.; Tuchida, N.; Miyazaki, K. *Journal of Polymer Science Part B: Polymer Physics* **2004**, *42*, 3727–3740.

89. Kabajev, M.; Prosycevas, I.; Kazakeviciute, G.; Valiene, V. *Materials Science* **2004**, *10*, 173–176.

90. Svirachev, D. M.; Tabaliov, N. A. *Bulgarian Journal of Physics of Plasmas* **2005**, *32*, 22–33.

91. Vujošević, D.; Mozetič, M.; Cvelbar, U.; Krstulović, N.; Milošević, S. *Journal of Applied Physics* **2007**, *101*, 103–305.

92. Vesel, A.; Junkar, I.; Cvelbar, U.; Kovac, J.; Mozetič, M. *Surface and Interface Analysis* **2008**, *40*, 1444–1453.

93. Ding, G.; Wu, W.-T.; Mak, S.; Yau, W.-F. *Journal of Vacuum Science Technology A* **2003**, *21*, 577–581.

94. Krishnan, S.; Hallet, B.; Schell, J. Plasma damage characterization of the decoupled plasma sources (DPS) reactors. *1996-1st International Symposium on Plasma Process-Induced Damage*, 1996.

95. Tuszewski, M. *Journal of Applied Physics* **2006**, *100*, 053301.

96. Tuszewski, M. *Physics of plasmas* **1998**, *5*, 1198.

97. Tuszewski, M.; Gary, S. P. *Physics of Plasmas* **2003**, *10*, 539–545.

98. Tuszewski, M.; White, R. R. *Journal of Applied Physics* **2003**, *94*, 2858–2863.

99. Tuszewski, M.; White, R. R. *Plasma Sources Sci. Technol.* **2002**, *11*, 338–350.

100. Tuszewski, M.; White, R. R.; Wurden, G. A. *Plasma Sources Sci. Technol.* **2003**, *12*, 396–402.

101. Carazzetti, P.; Renaud, P.; Shea, H. *Sensors and Actuators A: Physical* **2009**, *154*, 275–280.

102. Guo, L. J. *Adv. Mater* **2007**, *19*, 495–513.

103. Chirila, G., V. Marginean; Brandl, W. *Surface & Coatings Technology* **2005**, *200*, 548–551.

104. Borcia, G.; Anderson, C. A.; Brown, N. M. D. *Applied Surface Science* **2004**, *225*, 186–197.

105. Borcia, G.; Anderson, C. A.; Brown, N. M. D. *Plasma Sources Science and Technology* **2005**, *14*, 259–267.

106. MKS Instruments, *GHW Series RF Plasma Generators*; 2008.

107. Ritchey, H. C. *Tuner Topics*; Engineering White Paper 16-270-02, 2007.

108. Mussenbrock, T.; Hemke, T.; Ziegler, D.; Brinkmann, R. P.; Klick, M. *Plasma Sources Science and Technology* **2008**, *17*, 18–25.

109. Orfanidis, S. J. *Electromagnetic Waves and Antennas*; ECE Department Rutgers University: 94 Brett Road, Piscataway, NJ, 2008.

110. Pozar, D. M. *Microwave Engineering*, 3rd ed.; John Wiley & Sons, Inc.: Hoboken, NJ, 2005.

111. Weir, W. J. *Electronic Circuit Fundamentals*; Prentice-Hall, Inc.: Englewood Cliffs, NJ, 1987.

112. Cartwright, K. V. *the Technology Interface* **2008**, *Spring*, 1–19.

113. Ludwig, R.; Bretchko, P. *RF Circuit Design Theory and Applications*; Prentice-Hall, Inc.: Upper Saddle River, NJ 07458, 2000.

114. Turner, R. P.; Gibilisco, S. *Principles and Practice of Impedance*, 2nd ed.; Tab Books:PA, 1987.

115. Norstrom, H. *Vacuum* **1979**, *29*, 341–350.

116. Chung, B. K. *Microelectronics Journal* **2006**, *17*, 1007–1011.

117. Bakker, L. P.; Kroesen, G. M. W.; de Hoog, F. J. *IEEE Transactions on Plasma Science* **1999**, *27*, 759–765.

118. Kieft, I. E.; Laan, E. P.; Stoffels, E. *New Journal of Physics* **2004**, *6*, 149.

119. Sears, F. W.; Zemansky, M. W.; Young, H. D. *University Physics*, 6th ed.; Addison-Wesley, 1982.

120. Advanced Energy, *Impedance Matching*; Engineering White Paper 18-270-02, 2006.

121. Chen, Z. *IEEE Transactions on Plasma Science* **2002**, *30*, 1922–1930.

122. Lascari, L. *LLsmith Smith Chart Software*, [online], 2007. `http://www.rfdude.com`, Software V 0.810.

123. Maxim, *Impedance Matching and the Smith Chart: The Fundamentals*; Application Note 742, 2002.

124. Miller, P. A.; Hebner, G.; Greenberg, K. E.; Pochan, P. D.; Aragon, B. P. *Journal of Research of the National Institute of Standards and Technology* **1995**, *100*, 427–439.

125. Advanced Energy, *Navigator Digital Matching Networks*; Manual, Advanced Energy Industries, Inc.: 1625 Sharp Point Drive Fort Collins, CO 80525 USA, 2000.

126. Selwyn, G. *Optical diagnostic techniques for plasma processing.*; Bellingham, WA: International Society for Optical Engineering., 1989.

127. Lerner, J.; Thevenon, A. *The Optics of Spectroscopy A tutorial*; eBook, Jobin Yvon: 3880 Park Avenue Edison, NJ, 1988.

128. Navrátil, Z.; Trunec, D.; Smíd, R.; Lazar, L. *Czechoslovak Journal of Physics* **2006**, *56*, Suppl. B, B944–951.

129. Ralchenko, Y.; Kramada, A.; Reader, J.; Team, N. *NIST Atomic Spectra Database (version 3.1.5)*, [online], 2008. `http://physics.nist.gov/asd3[2010,April18].`

130. Sainz, M. A.; Coleman, D. M. *Applied Spectroscopy* **1981**, *35*, 564–567.

131. Oriel Instruments, *Booklet of Spectra*; Booklet 6502, Newport: Oriel Instruments 150 Long Beach Blvd. Stratford, CT, 2006.

132. Fantz, U. *Plasma Sources Science and Technology* **2006**, *15*, S137–S147.

133. Yubero, C.; Garcia, M. C.; Calzada, M. D. *Optica Applicata* **2008**, *XXXVIII*, 353–363.

134. Optronics, *High-Accuracy Irradiance Standards*; Bulletin 6, 2007.

135. Bibinov, N. K.; Bolshukhin, D. O.; Kokh, D. B.; Pravilov, A. M.; Vinogradov, I. P.; Wiesemann, K. *Measurement Science and Technology* **1997**, *8*, 773–771.

136. International, A. *Standard Test Method for Wetting Tension of Polyethylene and Polypropylene Films*; Standard D-2578-08, ASTM International: ASTM International 100 Barr Harbor Drive, PO Box C700, West Conshohocken, PA, 2008.

137. Zisman, W. A. Relation of the Equilibrium Contact Angle to Liquid and Solid Constitution. In *Contact Angle, Wettability, and Adhesion*; Fowkes, F., Ed.; American Chemical Society: Washington, DC, 1964; Vol. 43, Chapter 1, pp 1–51.

138. Thurston, R. M.; Clay, J. D.; Schulte, M. D. *Journal of Plastic Film and Sheeting* **2007**, *23*, 63–78.

139. Upadhyay, D. J.; Cui, N. Y.; Anderson, C. A.; Brown, N. M. D. *Applied Surface Science* **2004**, *229*, 352–364.

140. Lai, J.; Sunderland, B.; Xue, J.; Yan, S.; Zhao, W.; Folkard, M.; Michael, B. D.; Wang, Y. *Applied Surface Science* **2006**, *252*, 3375–3379.

141. Woodward, R. P. *Surface Tension Measurements Using the Drop Shape Method*; White Paper, 2000.

142. Herzberg, G. *Molecular Spectra and Molecular Structure: 1. Spectra of Diatomic Molecules.*; New York: Von Nostrand Reinhold Co., 1950.

143. Hata, D. M. *Introduction to Vacuum Technology*; Pearson/Prentice Hall: Upper Saddle River, New Jersey, 2008.

144. Pearse, R. B.; Gaydon, A. G. *The Identification of Molecular Spectra*; London: Chapman and Hall, 1965.

145. Junkar, I.; Vesel, A.; Cvelbar, U.; Mozetič, M.; Strnad, S. *Vacuum* **2010**, *84*, 83–85.

146. Svirachev, D.; Tabaliov, N. *Journal of Physics: Conference Series* **2006**, *44*, 151–154.

147. Greim, D. *Principles of Plasma Spectroscopy*; Cambridge University Press, 1998.

148. Lochte-Holtgreven, W. Plasma Diagnostics. In *Plasma Diagnostics*; Lochte-Holtgreven, W., Ed.; American Vacuum Society Classics; American Institute of Physics, 1995; Chapter Evaluation of Plasma Parameters, pp 135–213.

149. Thorne, A.; Litzen, U.; Johansson, S. *Spectrophysics: principles and applications*; Springer-Verlag Berlin Heidelberg, 1999.

150. Gupta, B.; Hilborn, J.; Hollenstein, C. H.; Plummer, C. J. G.; Houriet, R.; Xanthopoulos, N. *Journal of Applied Polymer Science* **2000**, *78*, 1083–1091.

151. Kumagai, H.; Hiroki, D.; Fujii, N.; Kobayashi, T. *Journal of Vacuum Science and Technology A: Vacuum,Surfaces,and Films* **2004**, *22*, 1.

152. Chan, C. M.; Ko, T. M.; Hiraoka, H. *Surface Science Reports* **1996**, *24*, 1–54.

153. Laskarakis, A.; Logothetidis, S.; Kassavetis, S.; Papaioannou, E. *ThinSolidFilms* **2008**, 1443–1448.

154. Morra, M.; Occhiello, E.; Garbassi, F. *Surface and Interface analysis* **1990**, *16*, 412.

155. Borges, F. O.; Cavalcanti, G. H.; Trigueiros, A. G. *Brazilian Journal of Physics* **2004**, *34*, 1673–1676.

156. Bourg, F.; Pellerin, S.; Morvan, D.; Armouroux, J.; Chapelle, J. *Solar Energy Materials & Solar Cells* **2002**, *72*, 361–371.

157. Calzada, M. D.; Garcia, M. C.; Luque, J. M.; Santiago, I. *Journal of Applied Physics* **2002**, *92*, 2269–2275.

158. Engelhard, C.; Chan, C.-Y.; Gamez, G.; Buscher, W.; Hieftje, G. M. *Specrtochimica Acta Part B* **2008**, *63*, 619–629.

159. Sung, Y.; Lim, H. B. *J. Anal. At. Spectrom.* **2003**, *18*, 897–901.

160. *Handbook of Chemistry and Physics*, 87th ed.; Lide, D. R., Ed.; CRC Presss: Taylor & Francis Group 6000 Broken Sound Parkway NW, Suite 300 Boca Raton, FL 33487-2742, 2006-2007.

161. Madziwa-Nussinov, T.; Arnush, D.; Chen, F. F. *IEEE Transactions on Plasma Science* **2007**, *35*, 1388.

162. Roth, R.; Li, Q.; Tsai, P.; Chen, Z. Polymer Surface Modification with a one atmosphere uniform Glow Discharge Plasma (OAUDGP). *6th International*

Symposium on Polymer Surface Modification at University of Cincinnati, Cincinnati, Ohio., 2007.

163. Papakonstantinou, D.; Amanatides, E.; Mataras, D.; Ioannidis, V.; Nikolopolous, P. *Plasma Process. Polym.* **2007**, *4*, 51057–51062.

164. Pandiyaraj, K. N.; Selvarajan, V.; Deshmukh, R. R.; Bousmina, M. *Surface and Coatings Technology* **2008**, *202*, 4218–4226.

165. Deshmukh, R. R.; Shetty, A. R. *Journal of Applied Polymer Science* **2007**, *104*, 449–457.

166. Kitova, S.; Minchev, M.; Danev, G. *Journal of Optoelectronics and Advanced Materials* **2005**, *7*, 2607–2612.

167. Coates, D.; Kaplan, S. Modification of Polymeric Surfaces with Plasma. In *Plasma Processing of Advanced Materials*; Collins, G. A., Rej, D. J., Eds.; MRS Bulletin, 1996; Chapter 4.

168. Vesel, A.; Mozetič, M. *Journal of Physics:Conference Series* **2009**, *162*, 1–20.

169. McWhirter, R. W. P. Spectral Intensities. In *Plasma Diagnostic Techniques*; Huddlestone, R. H., Ed.; Academic Press: 111 Fifth Avenue, New York, New York 10003, 1965; Chapter 5, pp 525–650.

170. Chu, P. K.; Chen, J. Y.; Wang, L. P.; Huang, N. *Materials Science and Engineering: R: Reports* **2002**, *36*, 143–206.

171. Rond, C.; Bultel, A.; Boubert, P.; Chron, B. G. *Chemical Physics* **2008**, *354*, 16–26.

172. Krupenie, P. H. *The Band Spectrum of Carbon Monoxide*; US Dept. of Commerce, National Bureau of Standards; for sale by the Superintendent of Documents, US Govt. Print. Off., 1966.

173. Broida, H. P.; Gaydon, A. G. *Transactions of the Faraday Society* **1953**, *49*, 1190.

174. Gaydon, A. G. *The Spectroscopy of Flames*; Chapman and Hall, Ltd., 1957.

175. Chung, T. H.; Seo, D. C.; Kim, G. H.; Kim, J. S. *IEEE Transactions on Plasma Science* **2001**, *29*, 970–973.

176. Economou, D. J.; Park, S.-K.; Williams, G. D. *J. Electrochem. Soc.* **1989**, *136*, 188–198.

177. Eliasson, B.; Kogelschatz, U. *Journal of Physics B: Atomic and Molecular Physics* **1986**, *19*, 1241–1247.

178. Panda, S.; Economou, J.; Mayyappan, M. *Journal of Applied Physics* **2000**, *87*, 8323–8333.

179. Beake, B.; Ling, J.; Leggett, G. *J.Mater.Chem.* **1998**, *8*, 1735–1742.

180. Vesel, A.; Mozetič, M.; Hladnik, A.; Dolenc, J.; Zule, J.; Milośevič, S.; Krstulović, N.; Klanjšek-Gunde, M.; Hauptmann, N. *Journal of Physics D: Applied Physics* **2007**, *40*, 3689–3696.

181. Yip, J.; Chan, K.; Sin, K.; Lau, K. *Polymer International* **2004**, *53*, 634–639.

182. Kaless, A.; Schulz, U.; Munzert, P.; Kaiser, N. *Surface and Coatings Technology* **2005**, *200*, 58–61.

Appendices

Appendix A

Contact Angle Plots

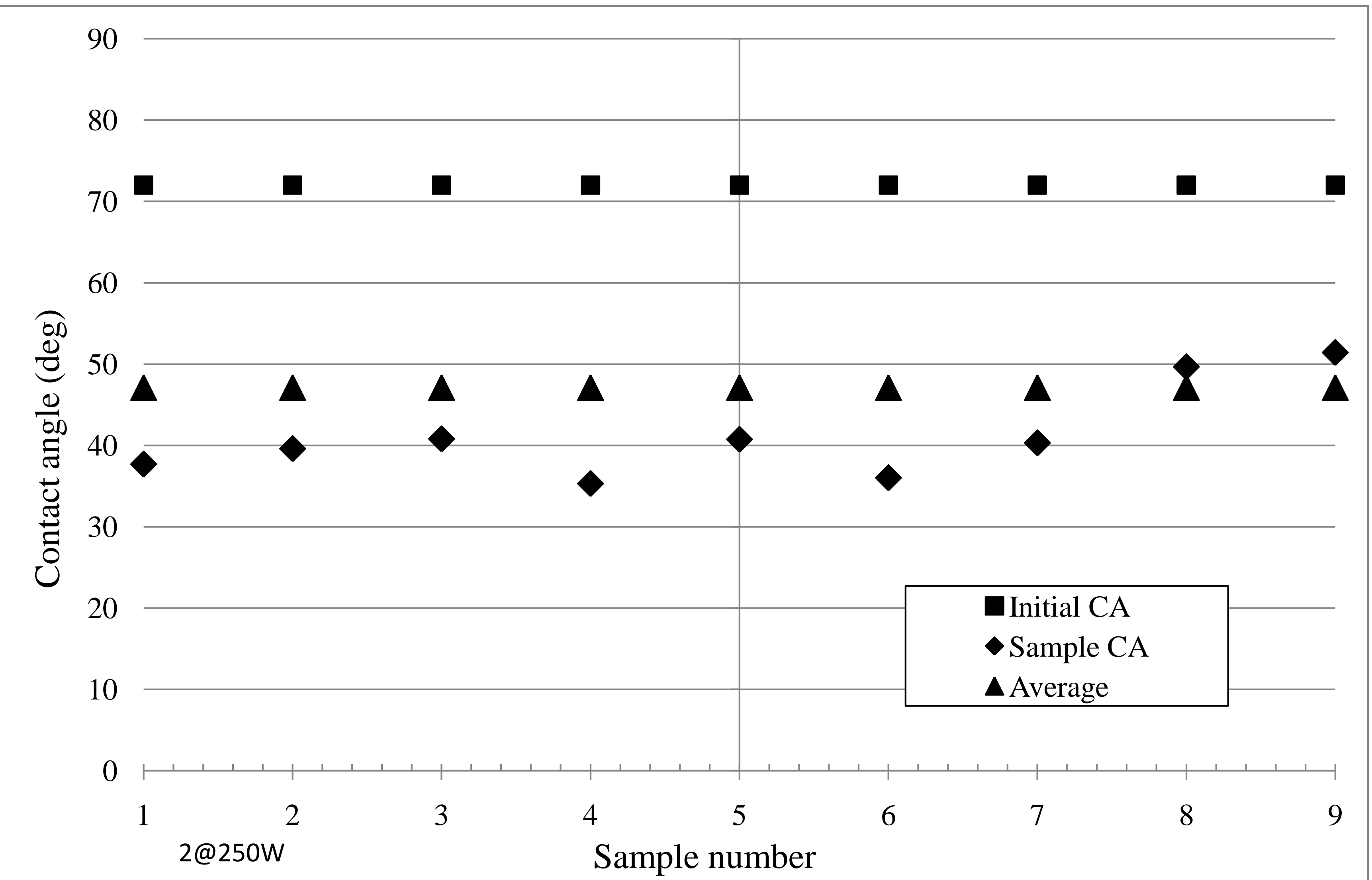

Figure A.1: Contact angle values acquired across the diameter of a sample processed for 2 minutes at 100 mtorr in an $O_2 + Ar$ atmosphere at an applied power of 250 Watts.

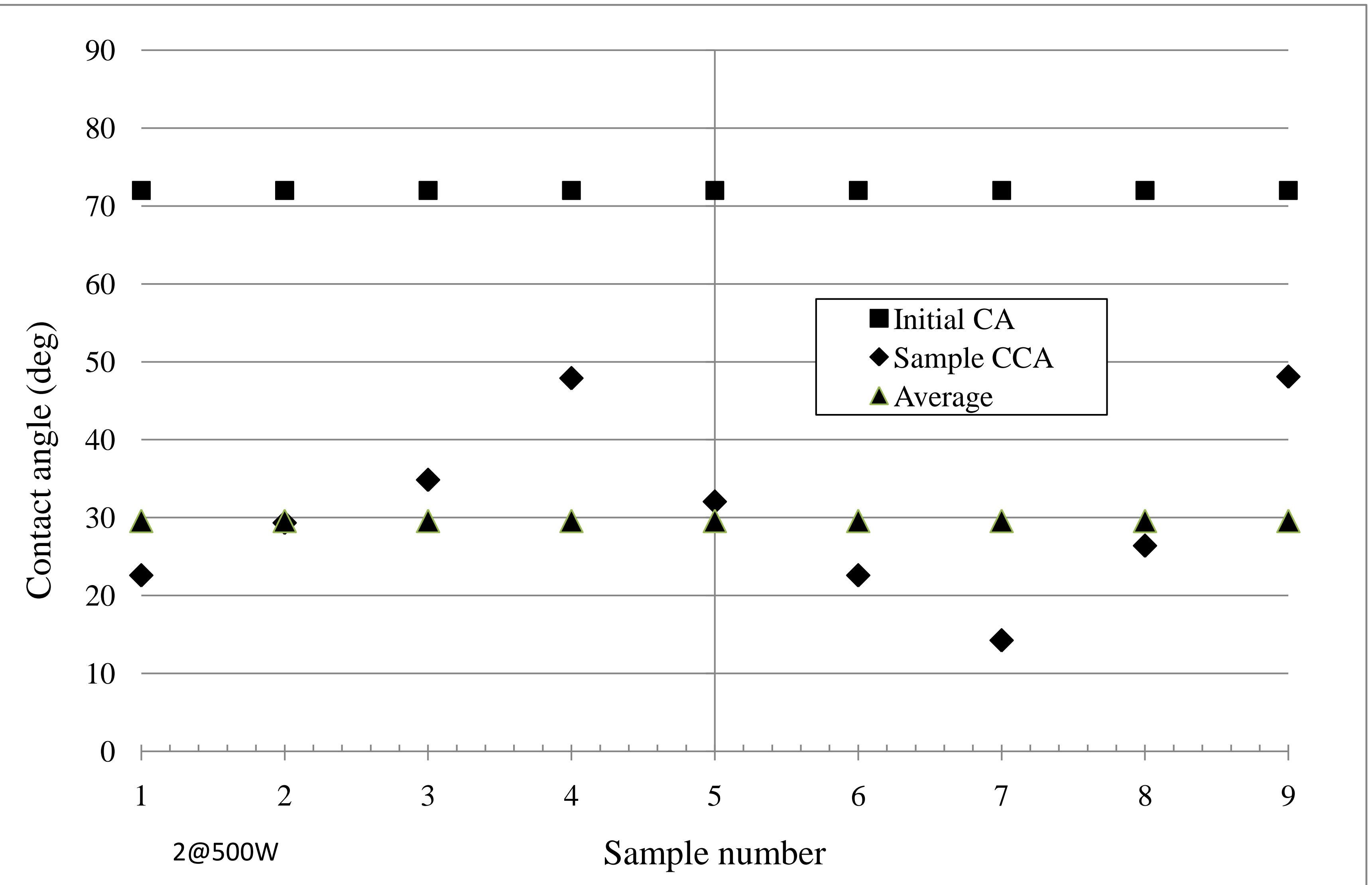

Figure A.2: Contact angle values acquired across the diameter of a sample processed for 2 minutes at 100 mtorr in an $O_2 + Ar$ atmosphere at an applied power of 500 Watts.

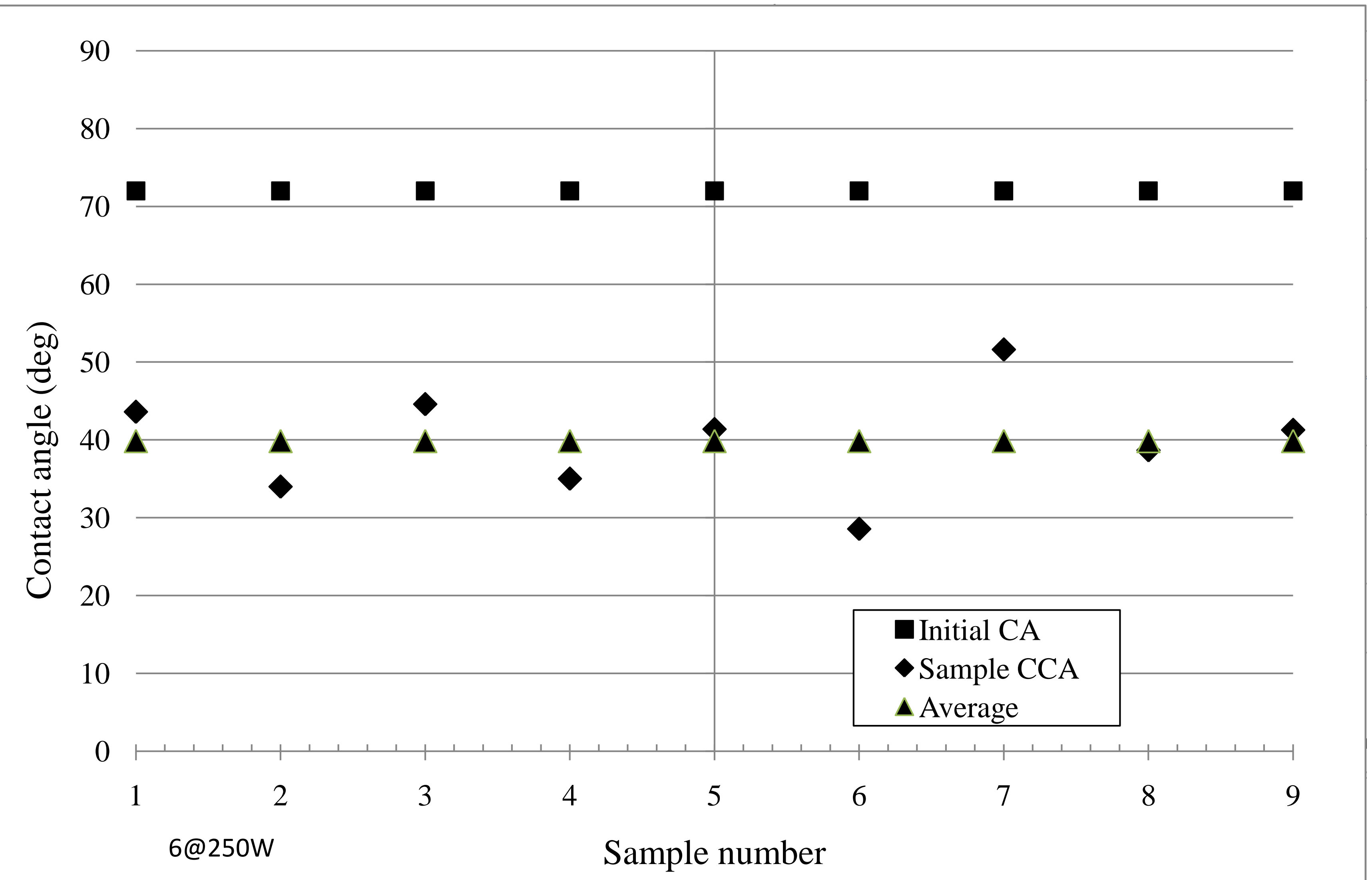

Figure A.3: Contact angle values acquired across the diameter of a sample processed for 6 minutes at 100 mtorr in an $O_2 + Ar$ atmosphere at an applied power of 250 Watts.

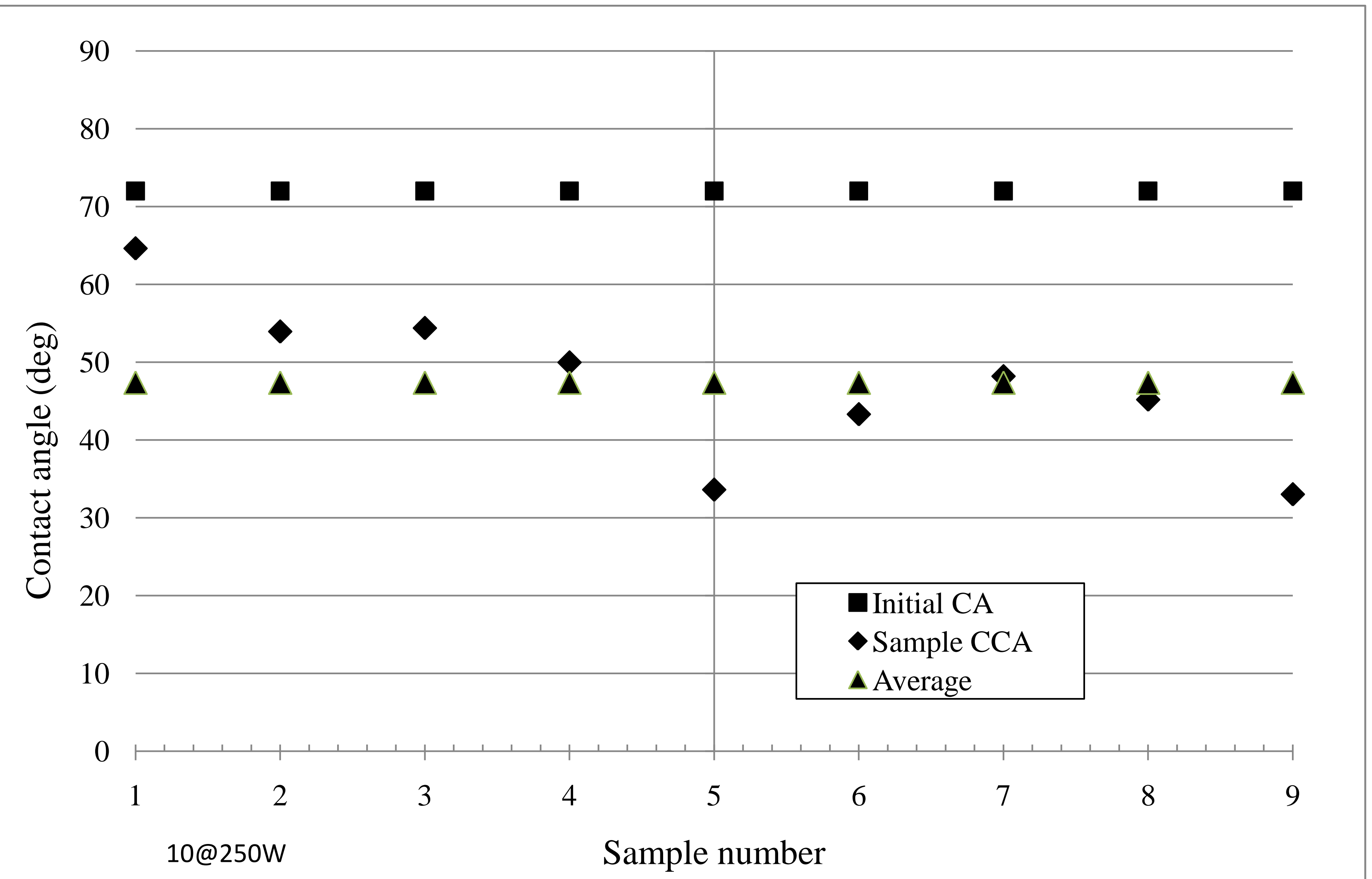

Figure A.4: Contact angle values acquired across the diameter of a sample processed for 10 minutes at 100 mtorr in an $O_2 + Ar$ atmosphere at an applied power of 250 Watts.

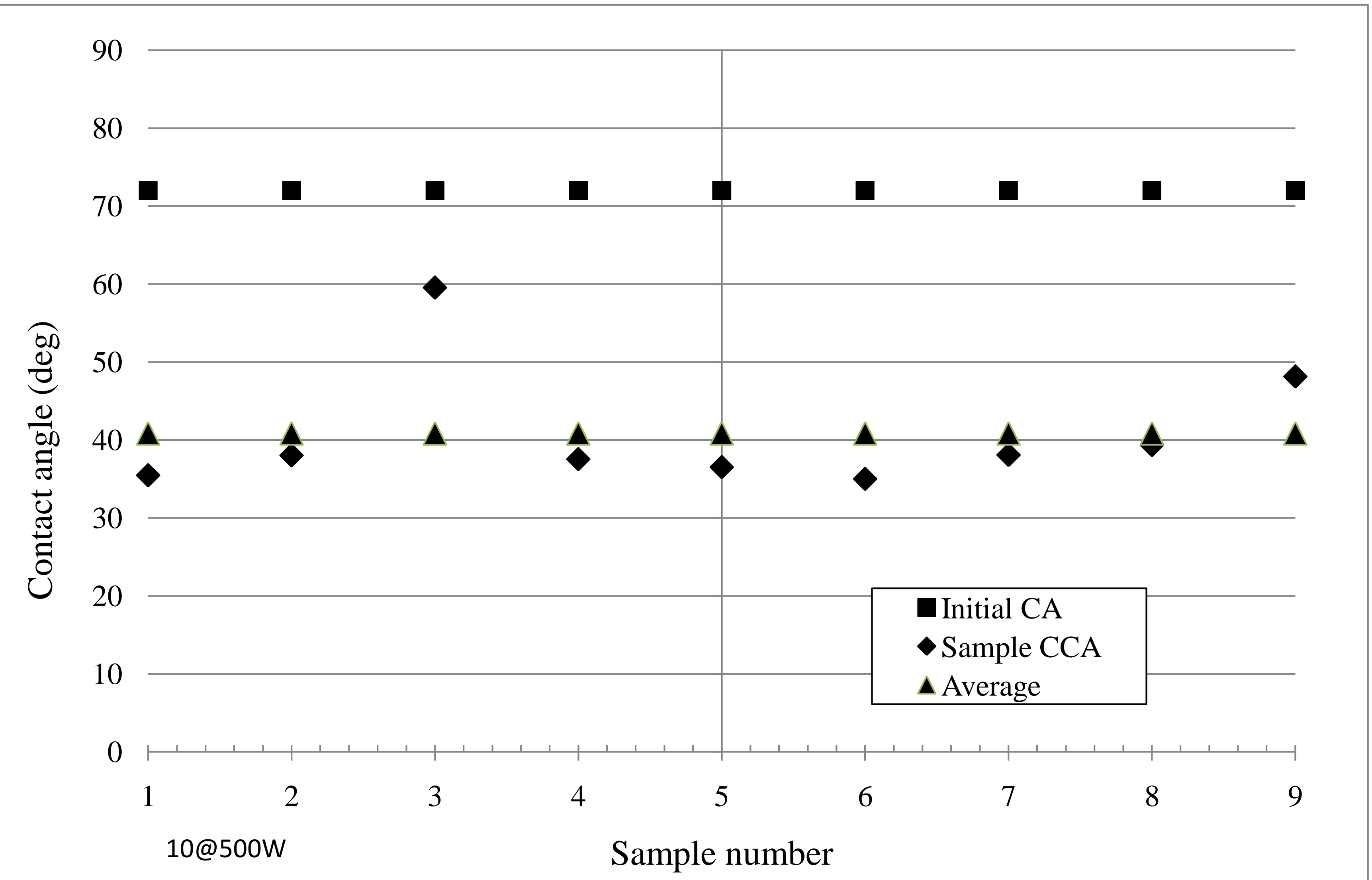

Figure A.5: Contact angle values acquired across the diameter of a sample processed for 10 minutes at 100 mtorr in an $O_2 + Ar$ atmosphere at an applied power of 500 Watts.

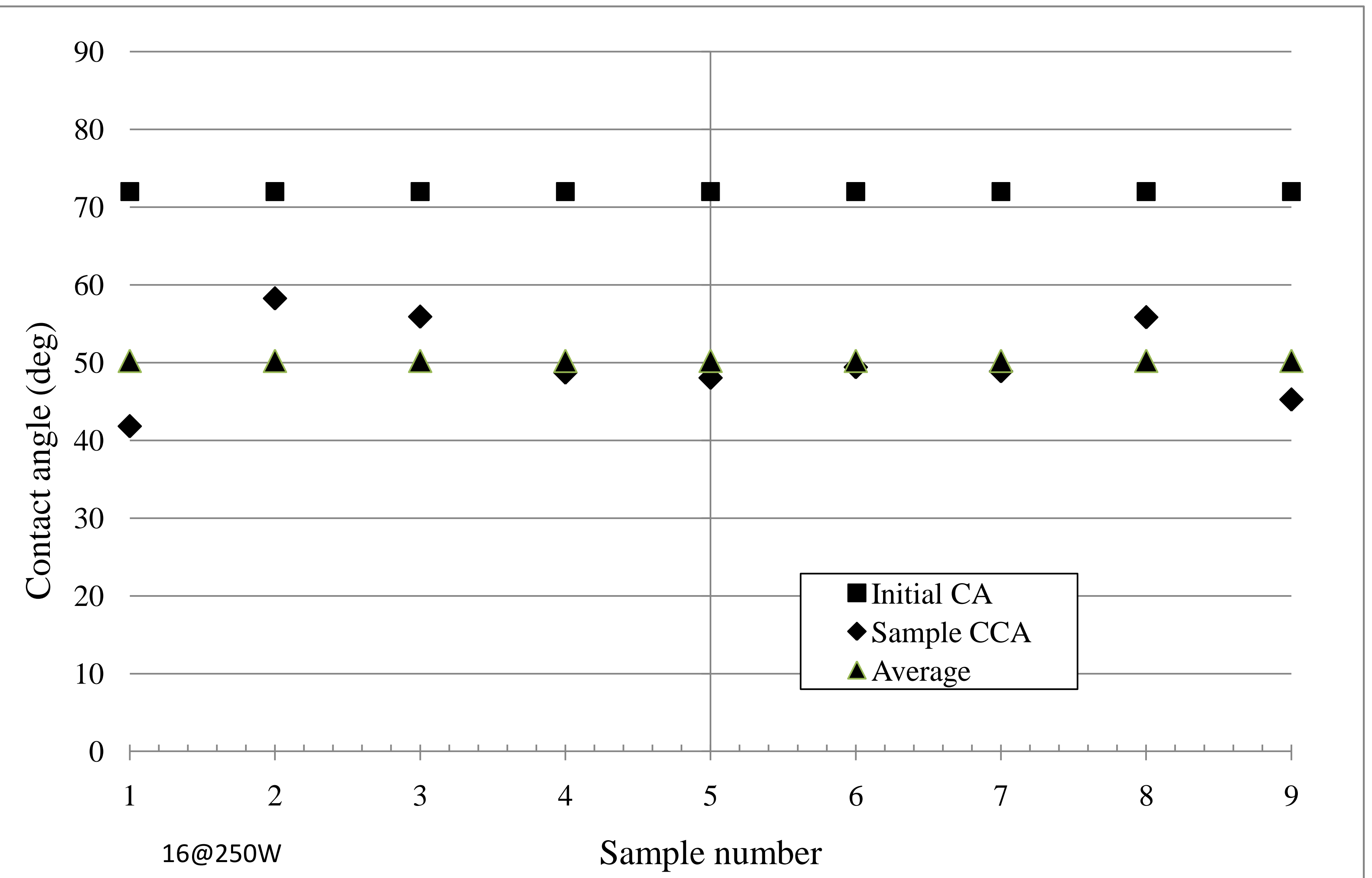

Figure A.6: Contact angle values acquired across the diameter of a sample processed for 16 minutes at 100 mtorr in an $O_2 + Ar$ atmosphere at an applied power of 250 Watts.

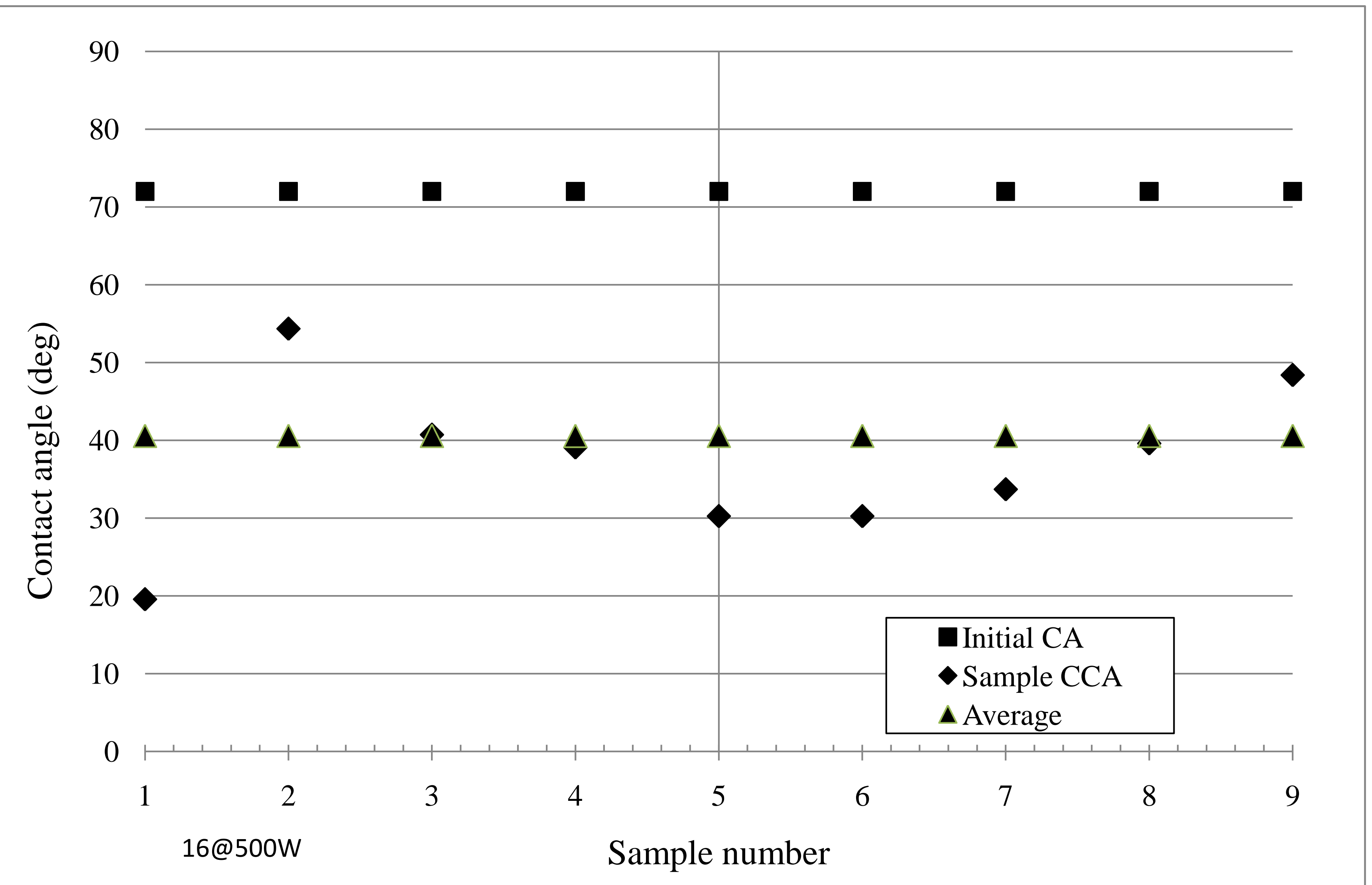

Figure A.7: Contact angle values acquired across the diameter of a sample processed for 16 minutes at 100 mtorr in an $O_2 + Ar$ atmosphere at an applied power of 500 Watts.

Appendix B

Contact Angle Pictures

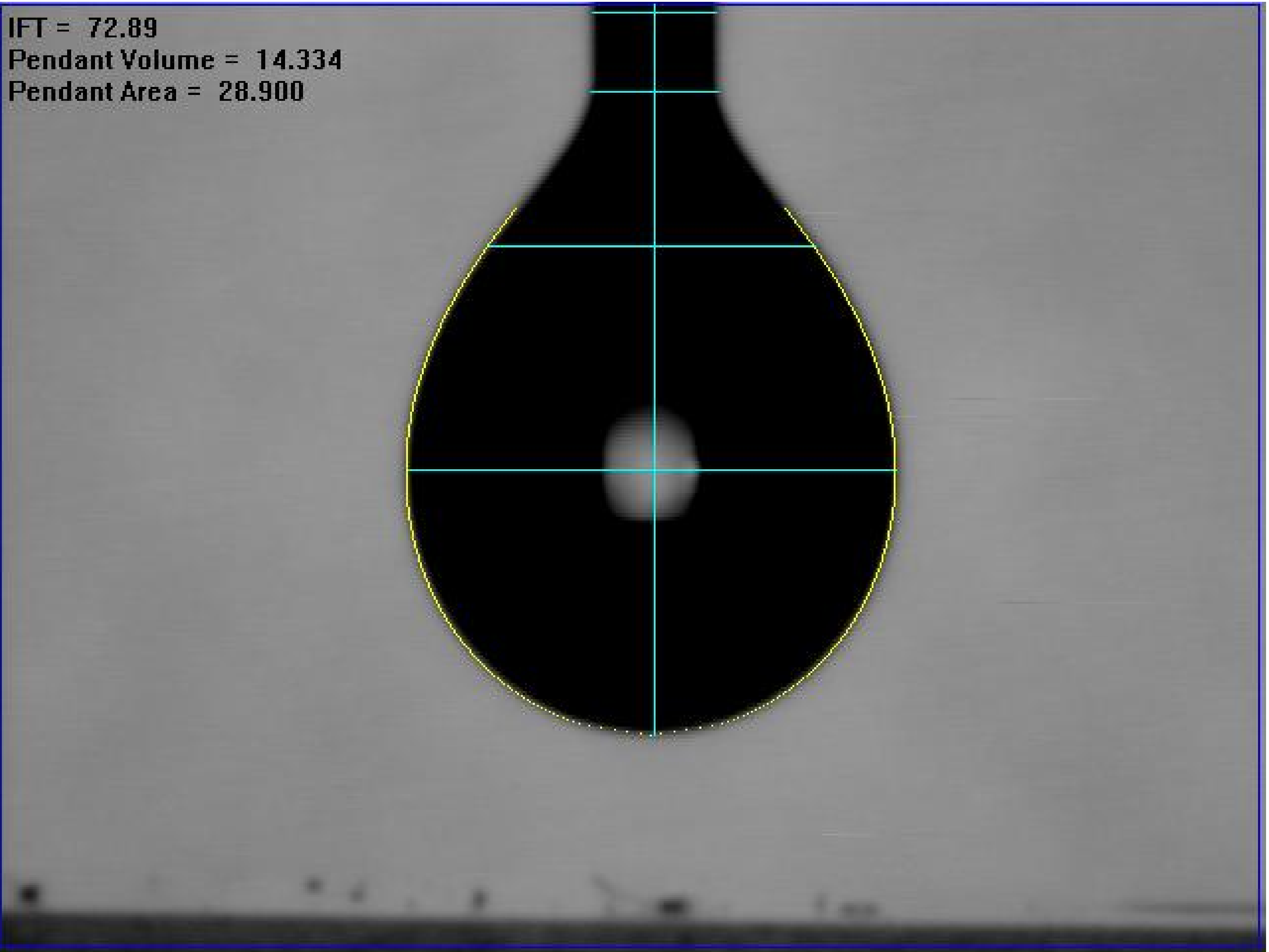

Figure B.1: Initial characterization test liquid (deionized water) shows an interfacial tension of 72.89 dynes/cm. This value is in good agreement with published values.

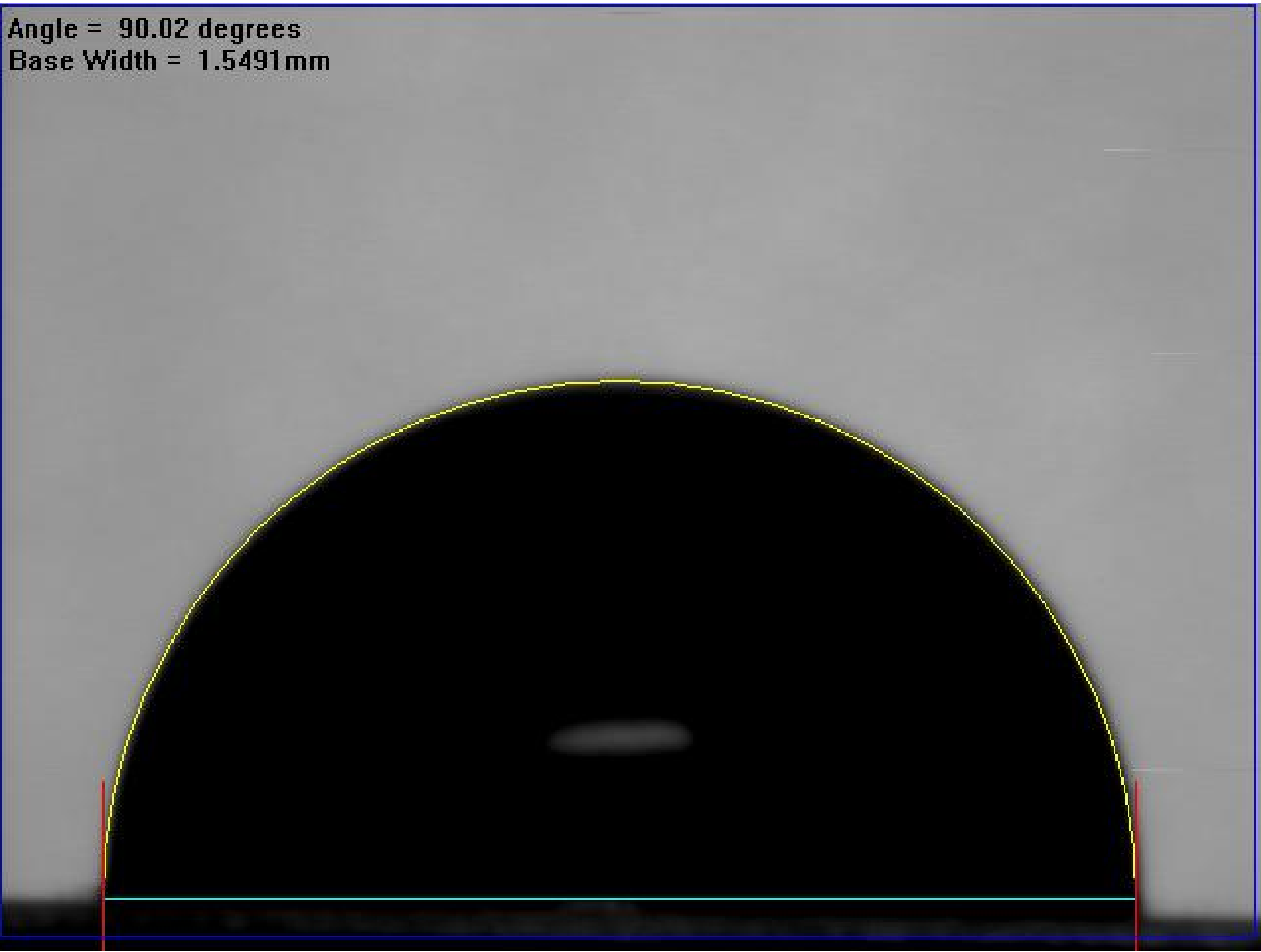

Figure B.2: Initial characterization of video system using vendor-supplied Sapphire calibration standard (90°± 0.10)

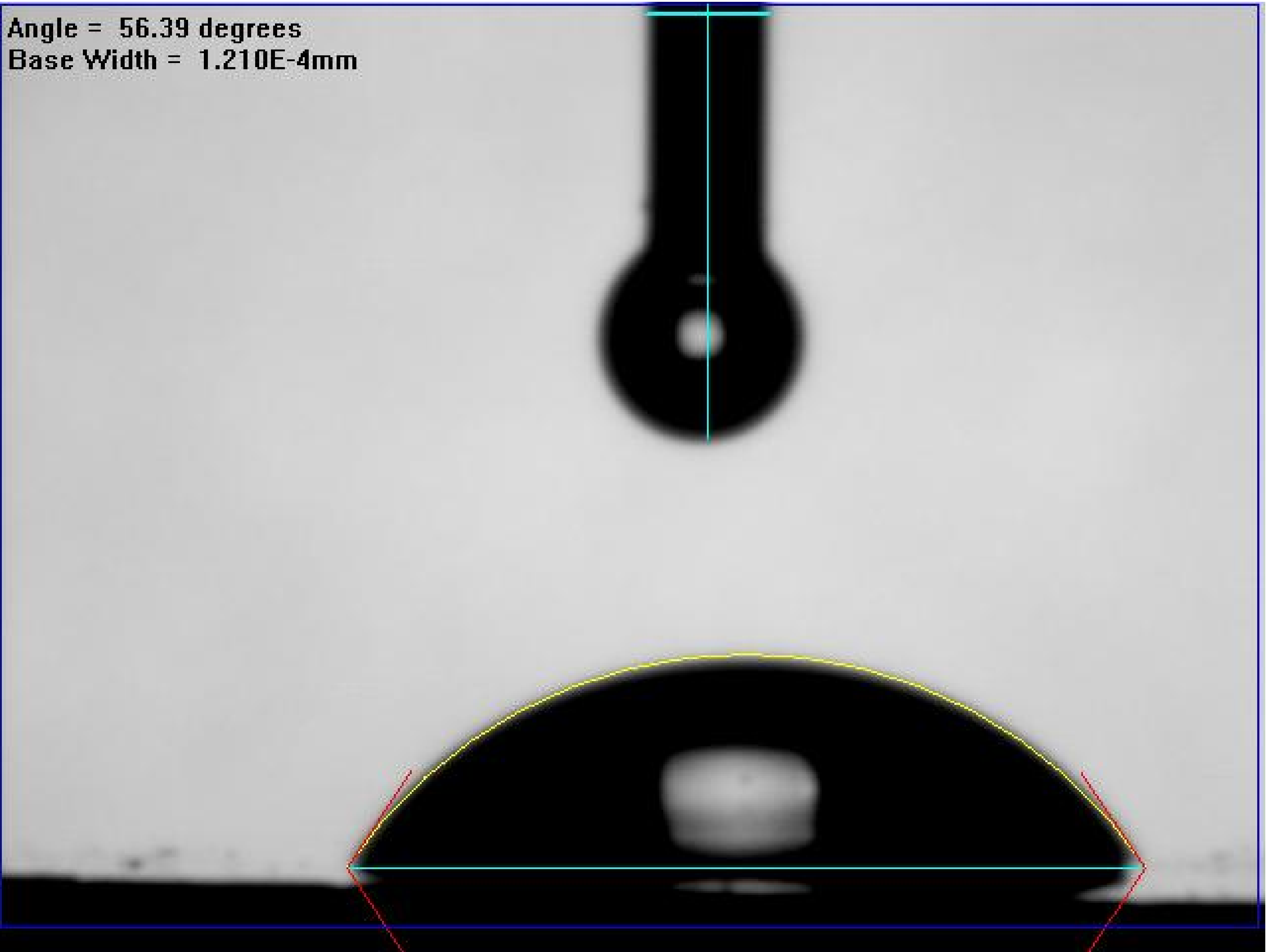

Figure B.3: Contact angle value acquired across the diameter of a sample processed for 2 minutes at 400 mtorr in an $O_2 + Ar$ atmosphere at an applied power of 250 Watts, Sample 1.

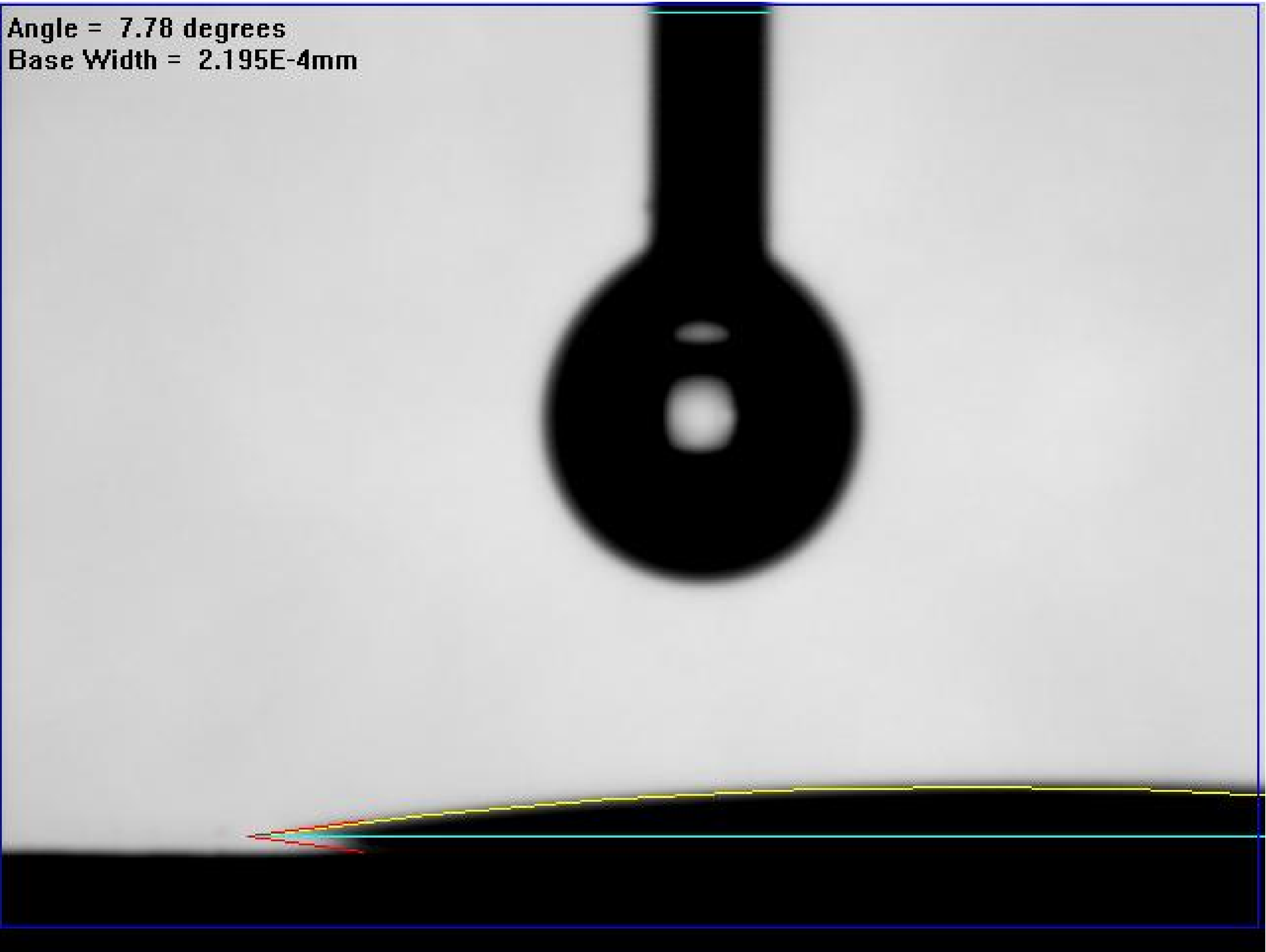

Figure B.4: Contact angle value acquired across the diameter of a sample processed for 2 minutes at 400 mtorr in an $O_2 + Ar$ atmosphere at an applied power of 250 Watts, Sample 2

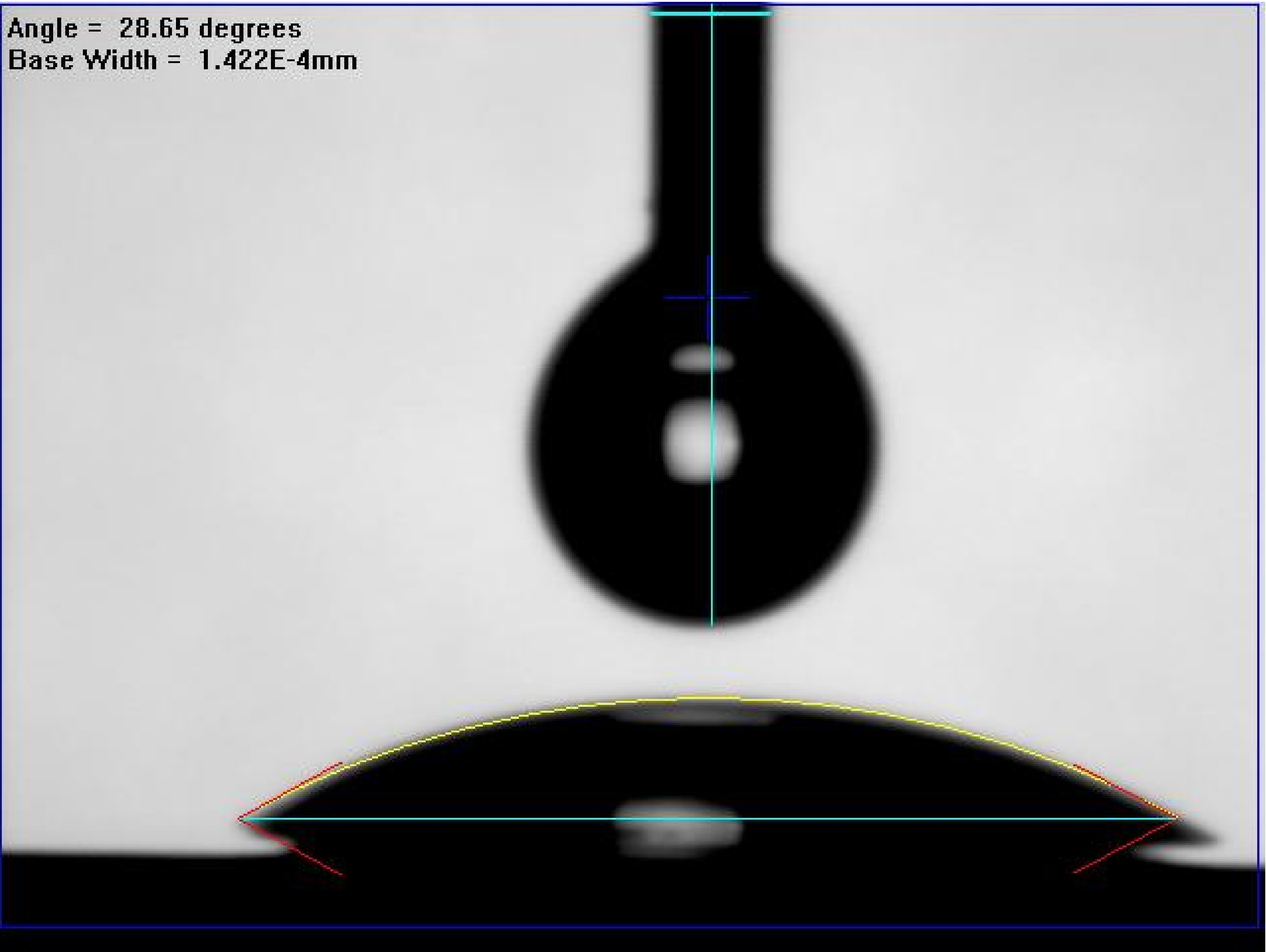

Figure B.5: Contact angle value acquired across the diameter of a sample processed for 2 minutes at 400 mtorr in an $O_2 + Ar$ atmosphere at an applied power of 250 Watts, Sample 3

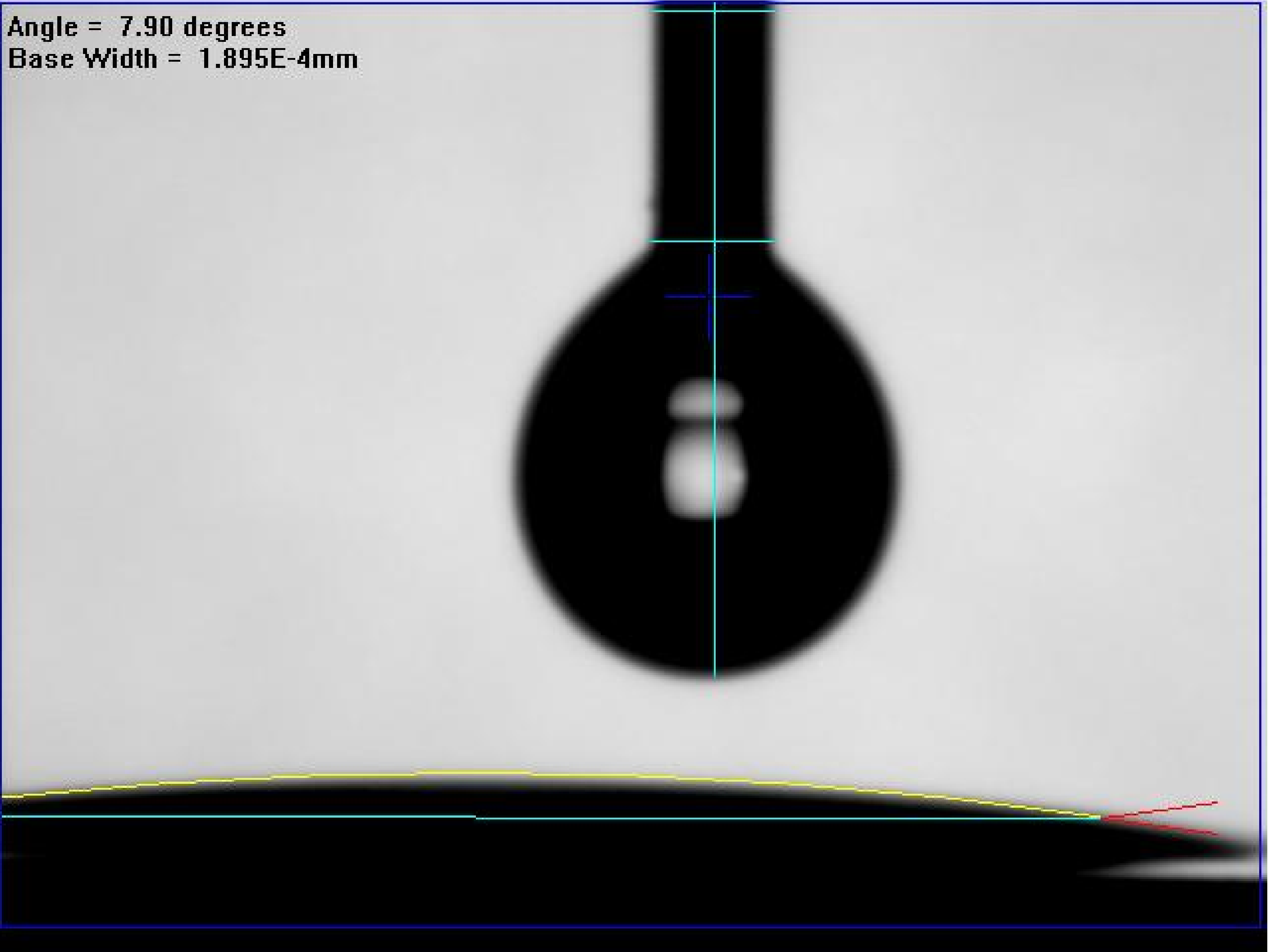

Figure B.6: Contact angle value acquired across the diameter of a sample processed for 2 minutes at 400 mtorr in an $O_2 + Ar$ atmosphere at an applied power of 250 Watts, Sample 4

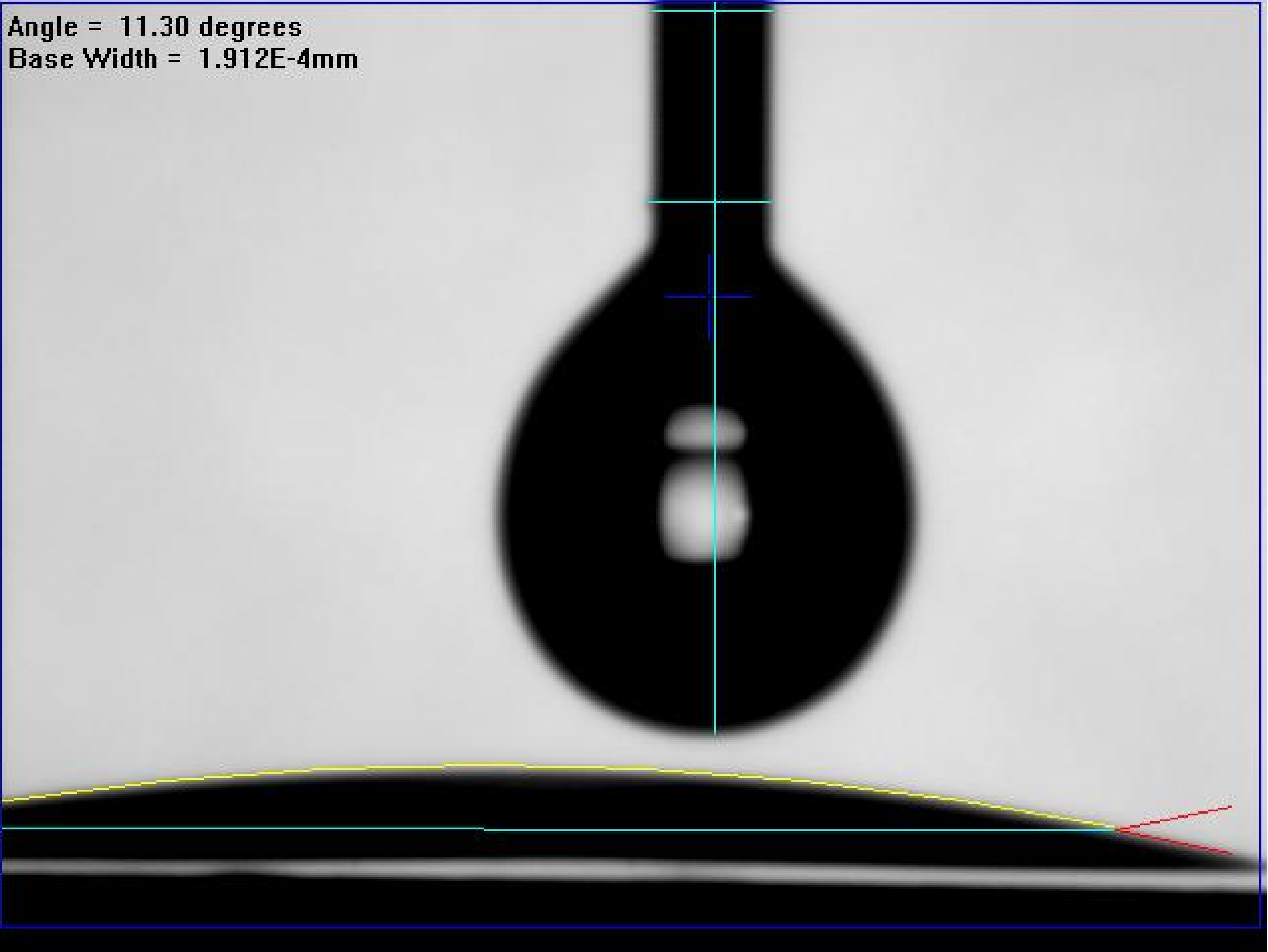

Figure B.7: Contact angle value acquired across the diameter of a sample processed for 2 minutes at 400 mtorr in an $O_2 + Ar$ atmosphere at an applied power of 250 Watts, Sample 5

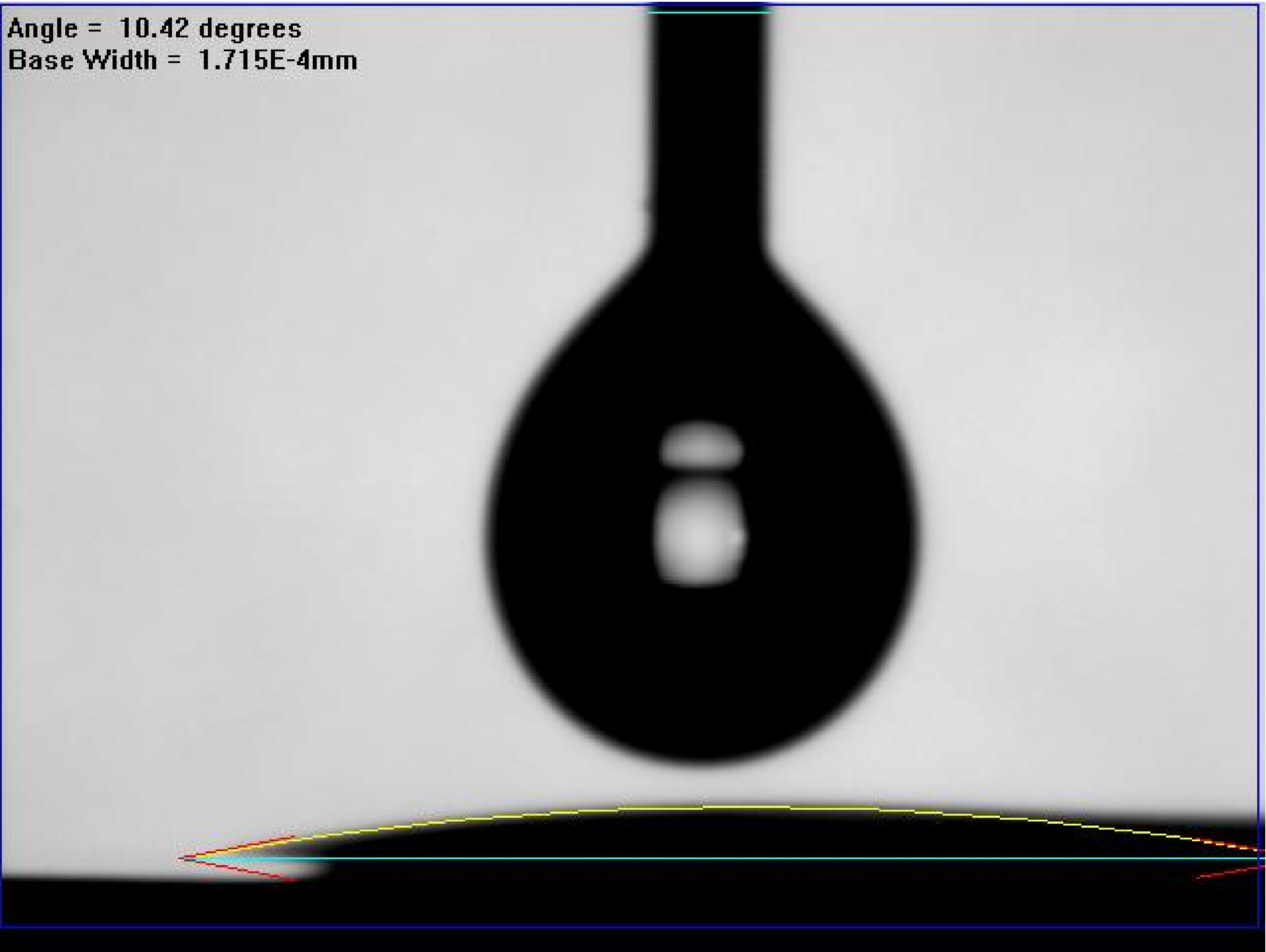

Figure B.8: Contact angle value acquired across the diameter of a sample processed for 2 minutes at 400 mtorr in an $O_2 + Ar$ atmosphere at an applied power of 250 Watts, Sample 6

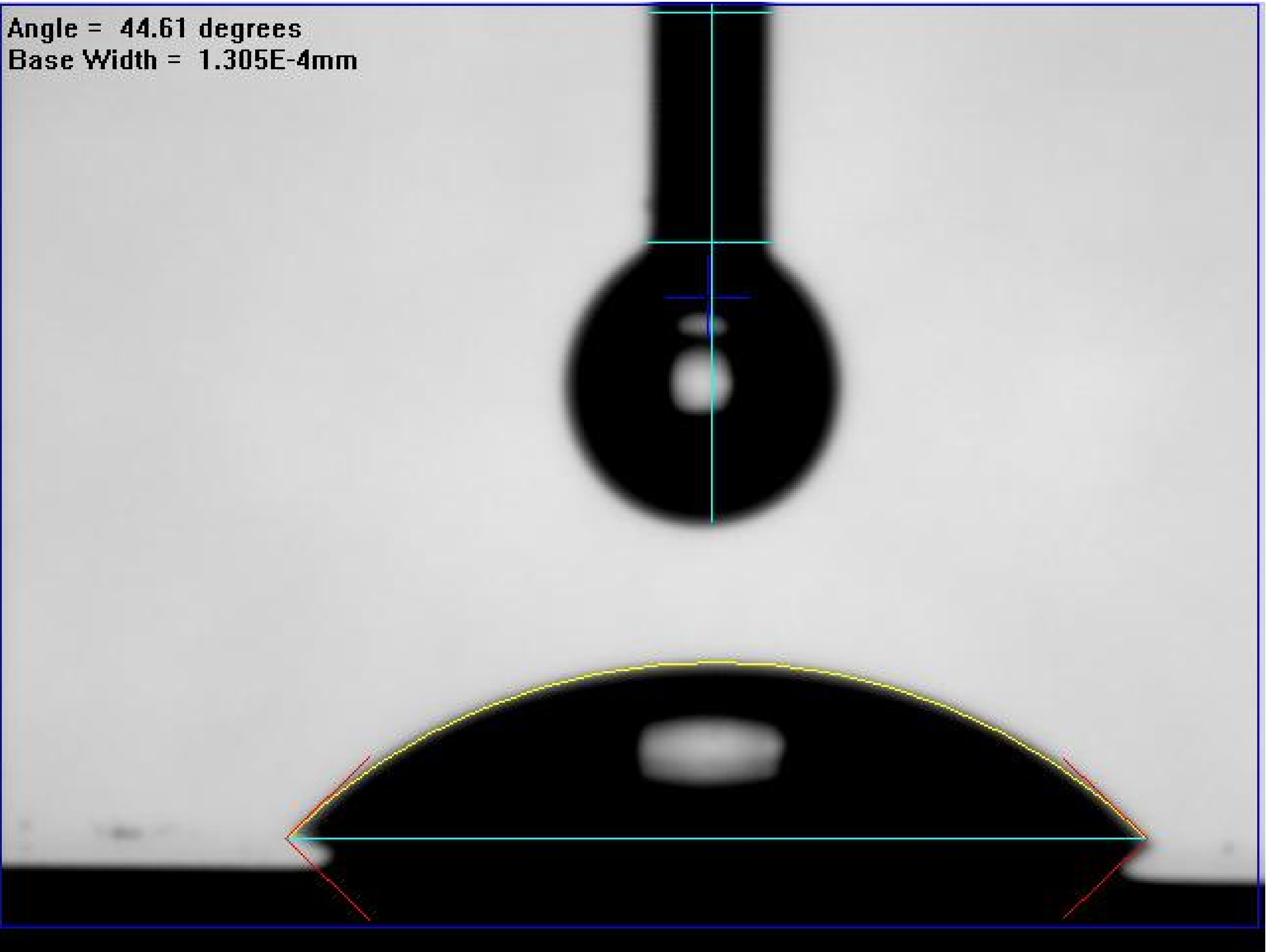

Figure B.9: Contact angle value acquired across the diameter of a sample processed for 2 minutes at 400 mtorr in an $O_2 + Ar$ atmosphere at an applied power of 250 Watts, Sample 7

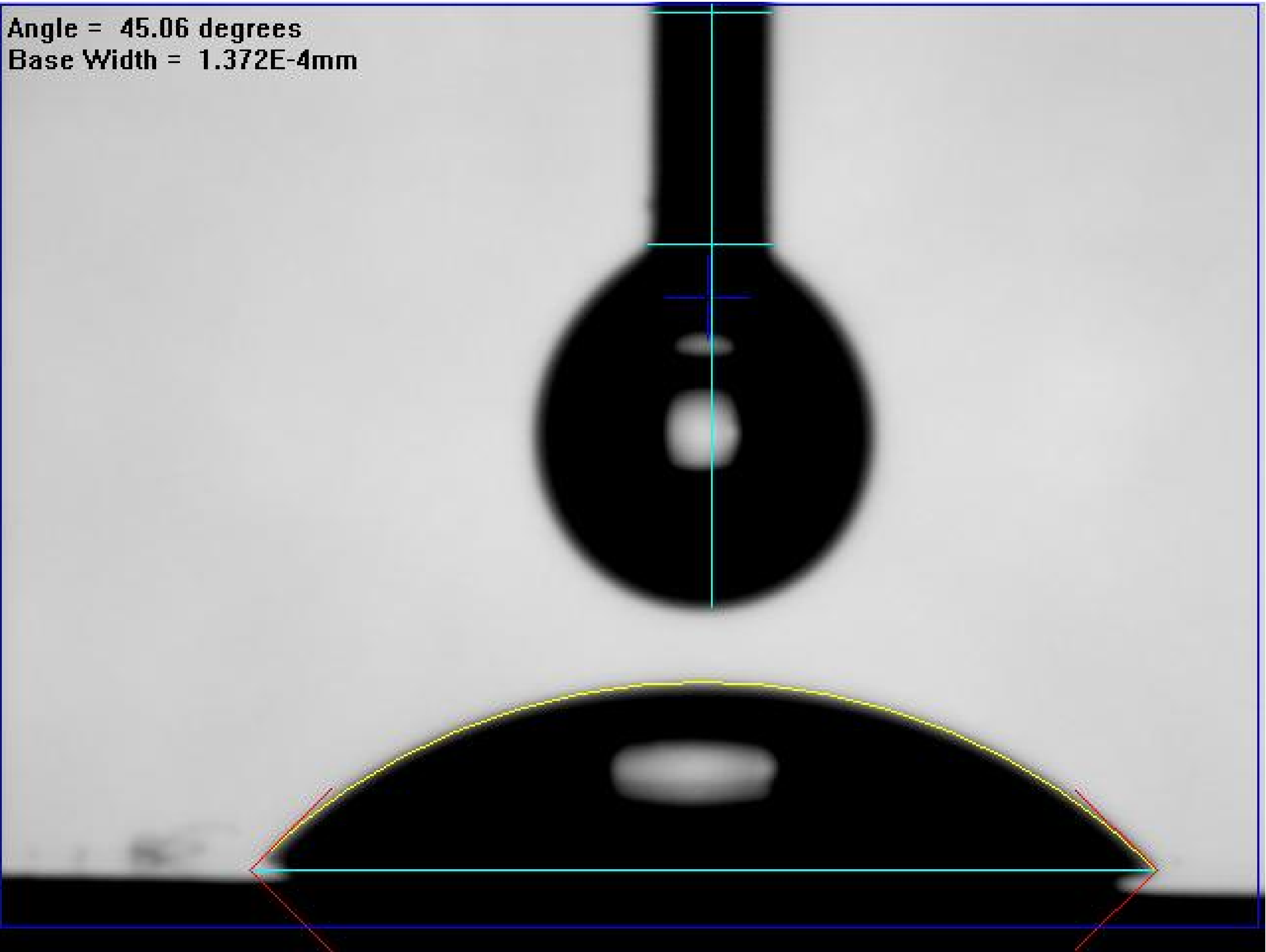

Figure B.10: Contact angle value acquired across the diameter of a sample processed for 2 minutes at 400 mtorr in an $O_2 + Ar$ atmosphere at an applied power of 250 Watts, Sample 8

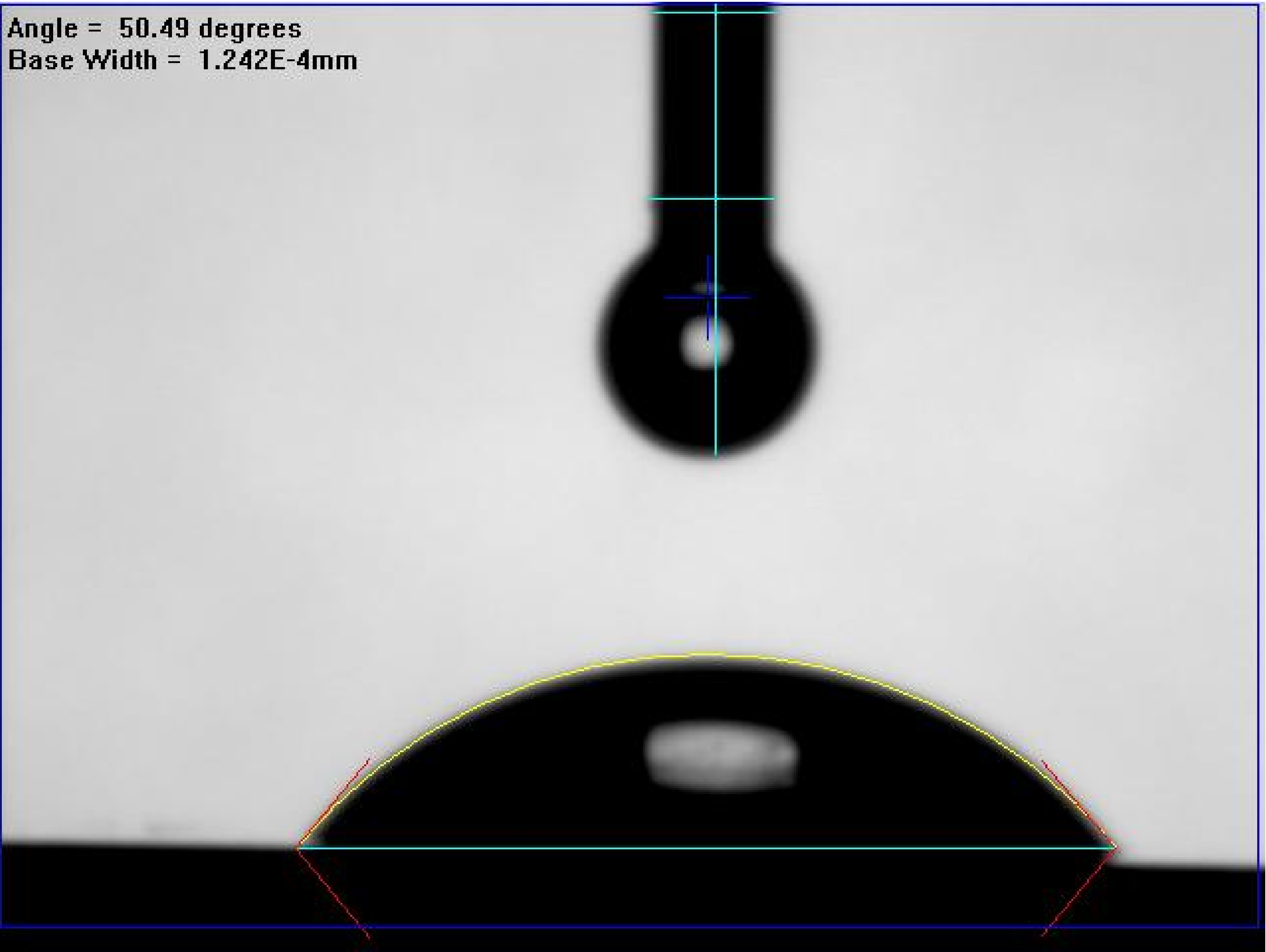

Figure B.11: Contact angle value acquired across the diameter of a sample processed for 2 minutes at 400 mtorr in an $O_2 + Ar$ atmosphere at an applied power of 250 Watts, Sample 9

Appendix C

Spectra of Runs in Inductive Decoupled Plasma System (DPS)(20.0 cm)

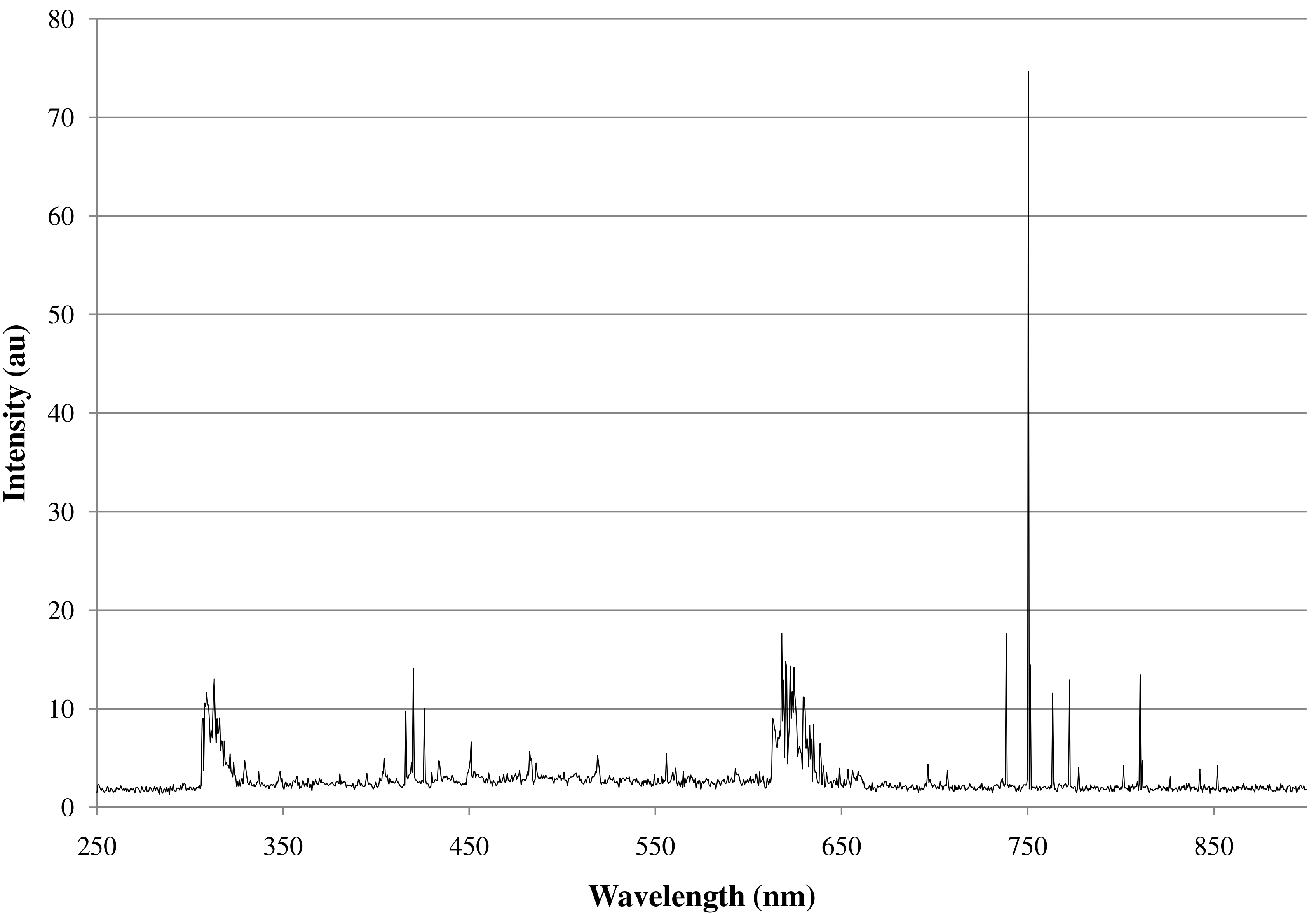

Figure C.1: Intensity as a function of wavelength of a sample processed for 2 minutes at a pressure of 100 mtorr and an applied power of 250 watts.

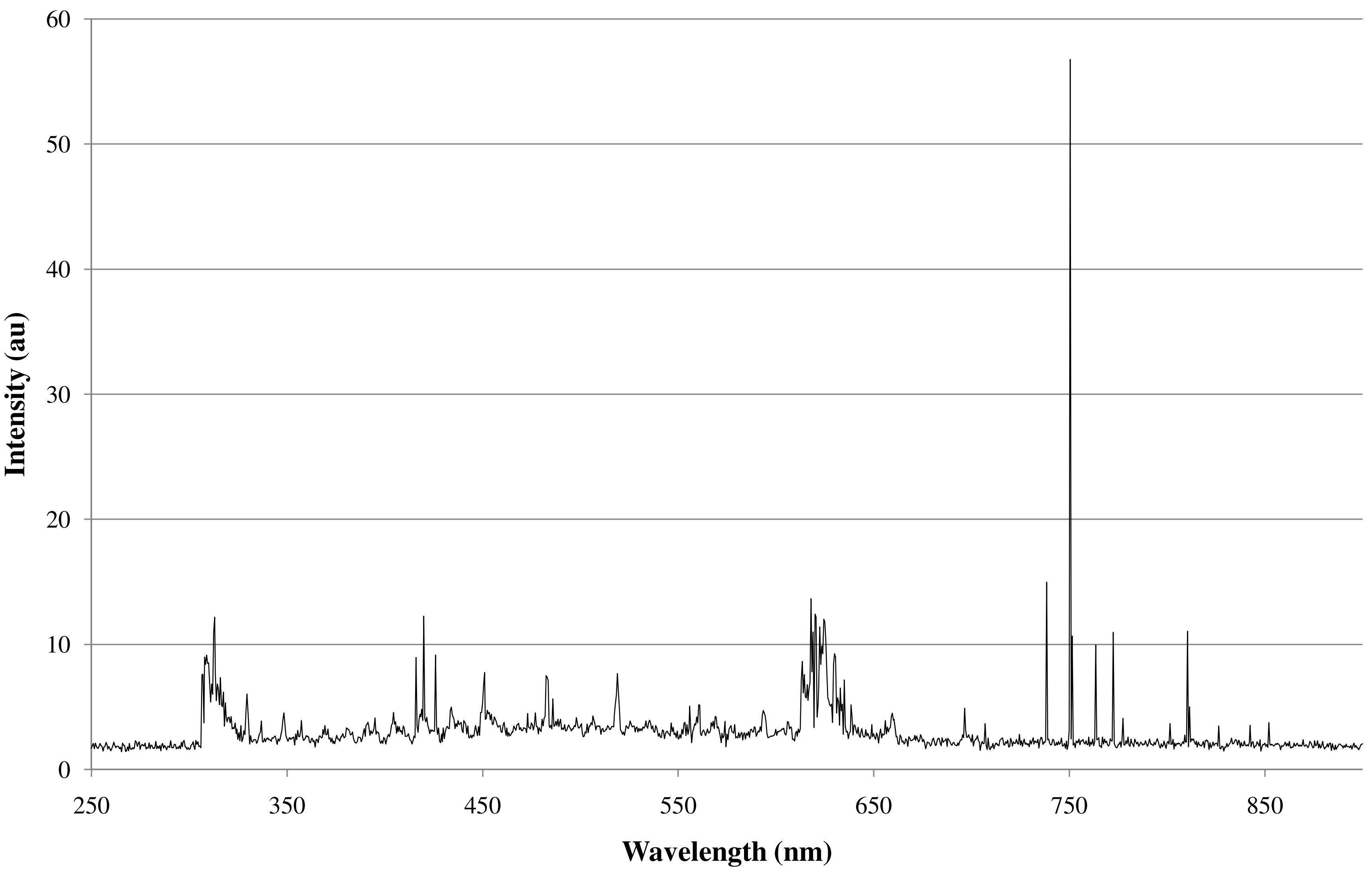

Figure C.2: Intensity as a function of wavelength of a sample processed for 2 minutes at a pressure of 100 mtorr and an applied power of 500 watts.

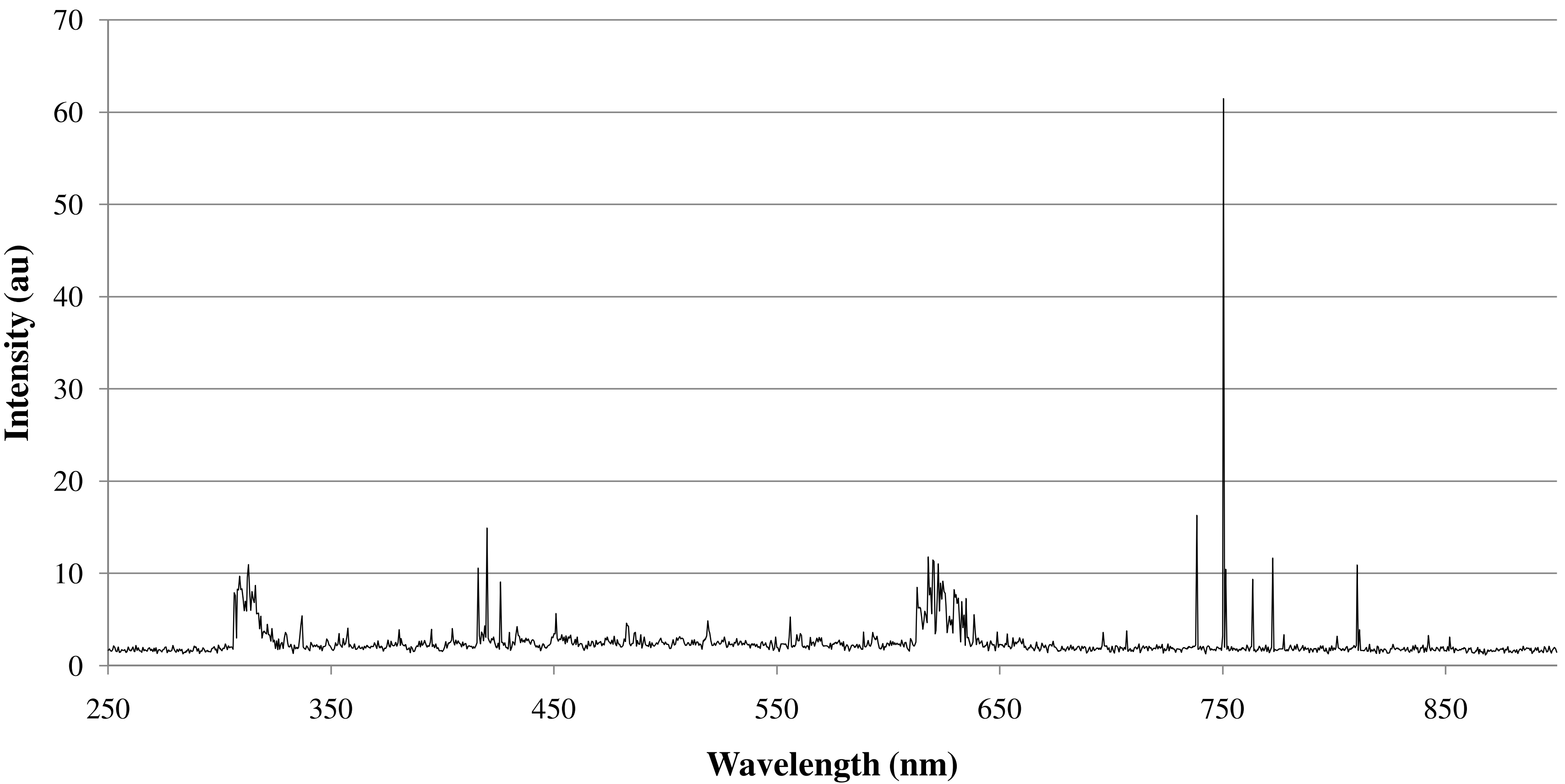

Figure C.3: Intensity as a function of wavelength of a sample processed for 6 minutes at a pressure of 100 mtorr and an applied power of 250 watts.

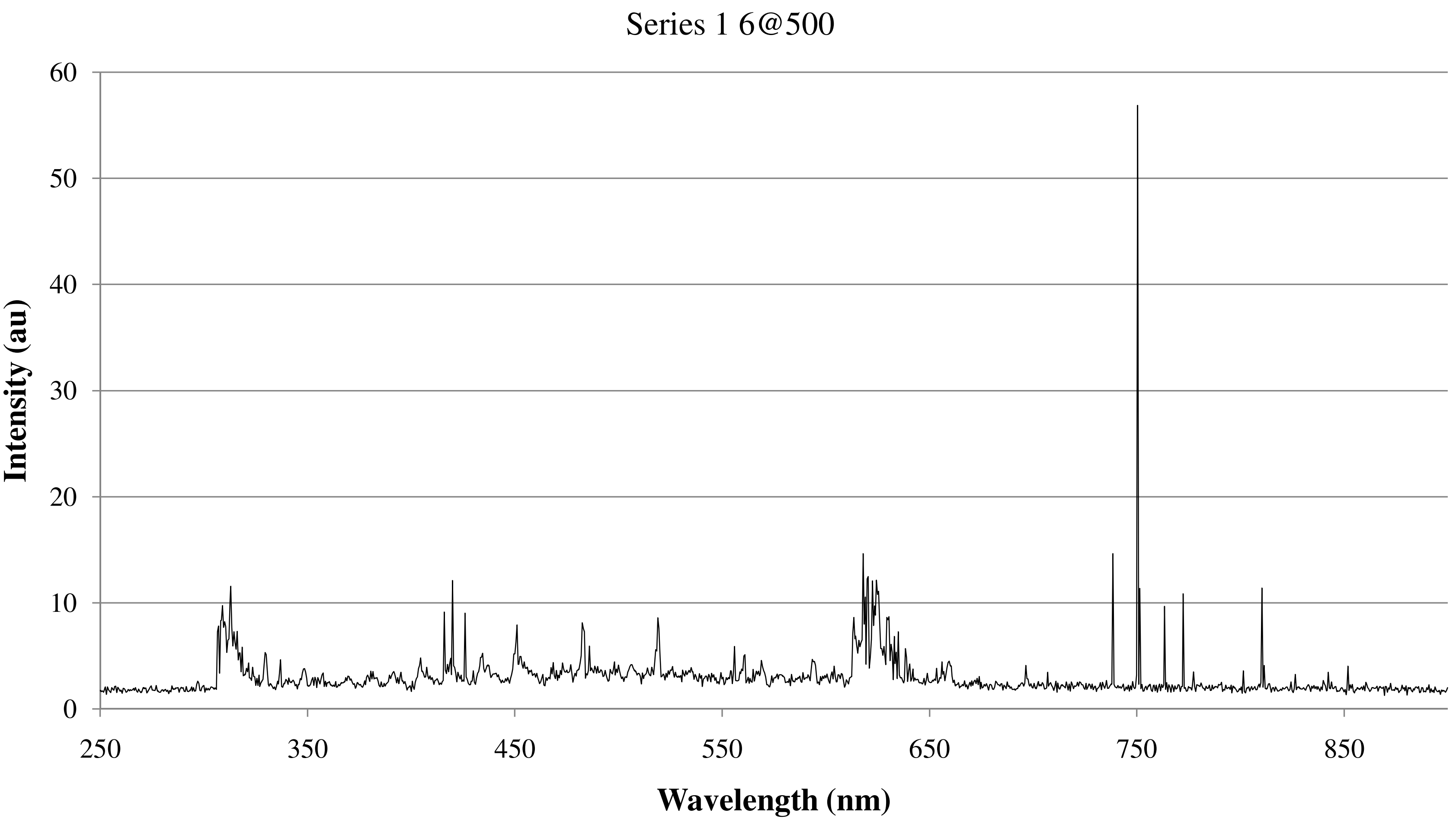

Figure C.4: Intensity as a function of wavelength of a sample processed for 2 minutes at a pressure of 100 mtorr and an applied power of 500 watts.

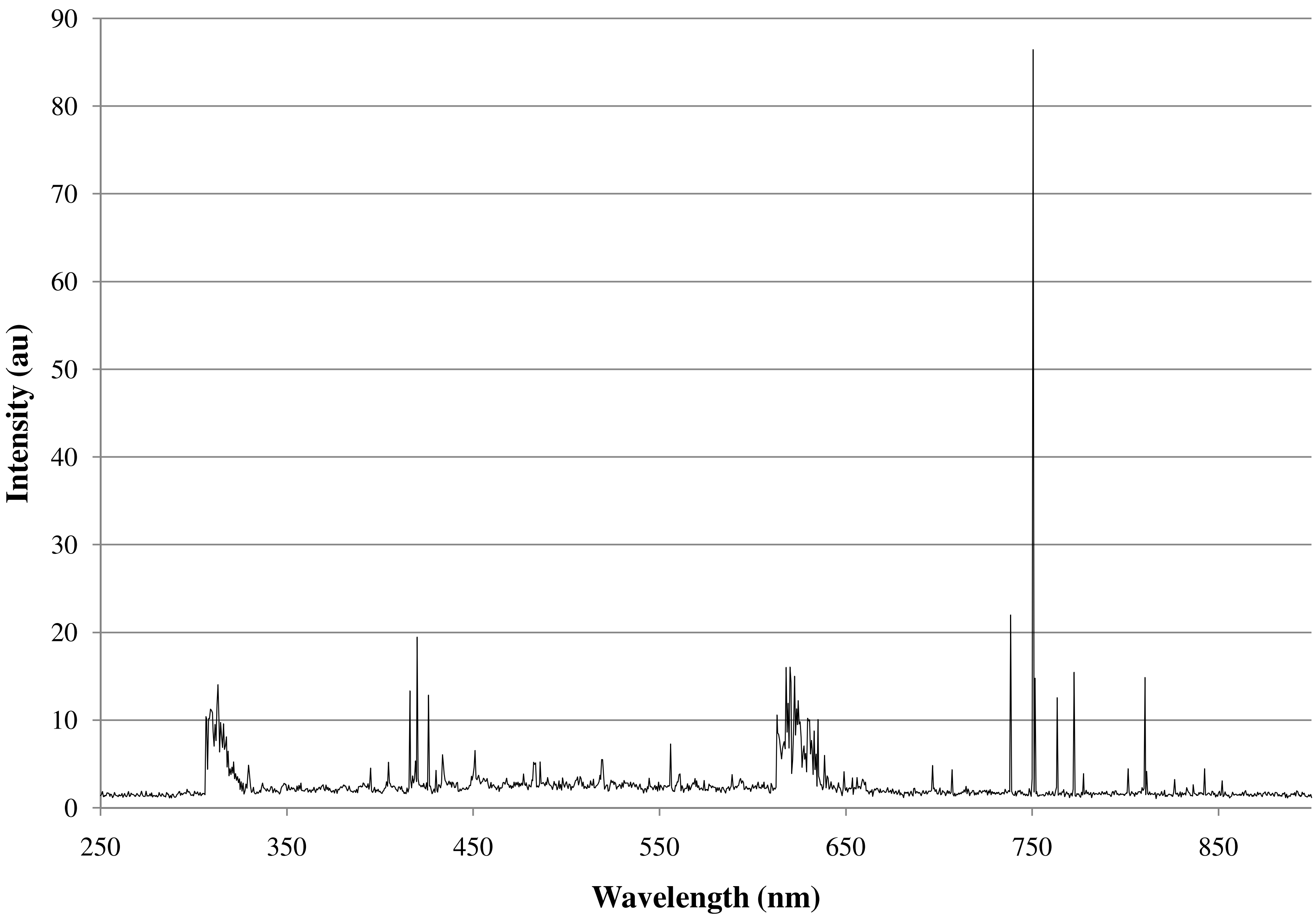

Figure C.5: Intensity as a function of wavelength of a sample processed for 10 minutes at a pressure of 100 mtorr and an applied power of 250 watts.

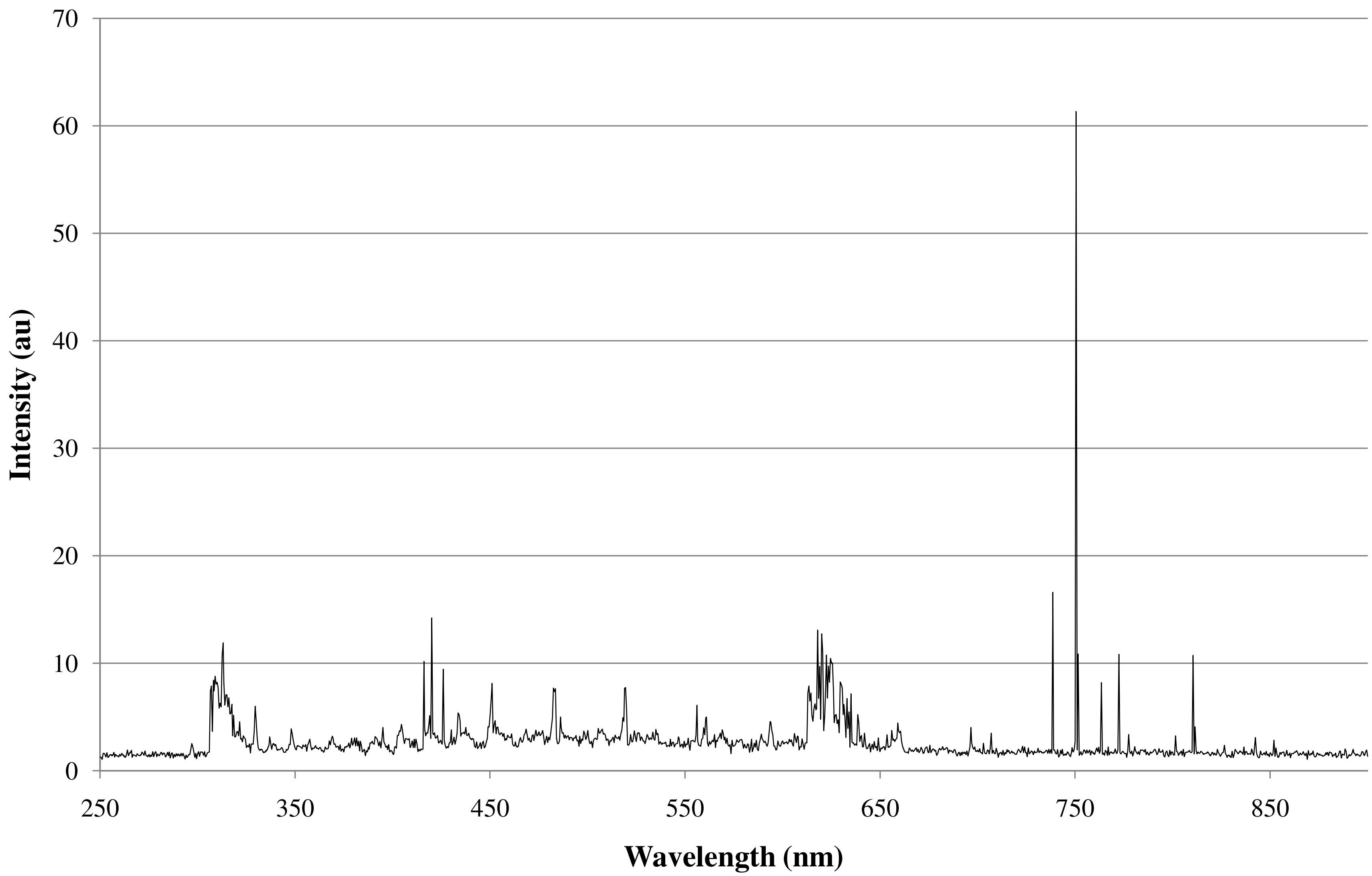

Figure C.6: Intensity as a function of wavelength of a sample processed for 10 minutes at a pressure of 100 mtorr and an applied power of 500 watts.

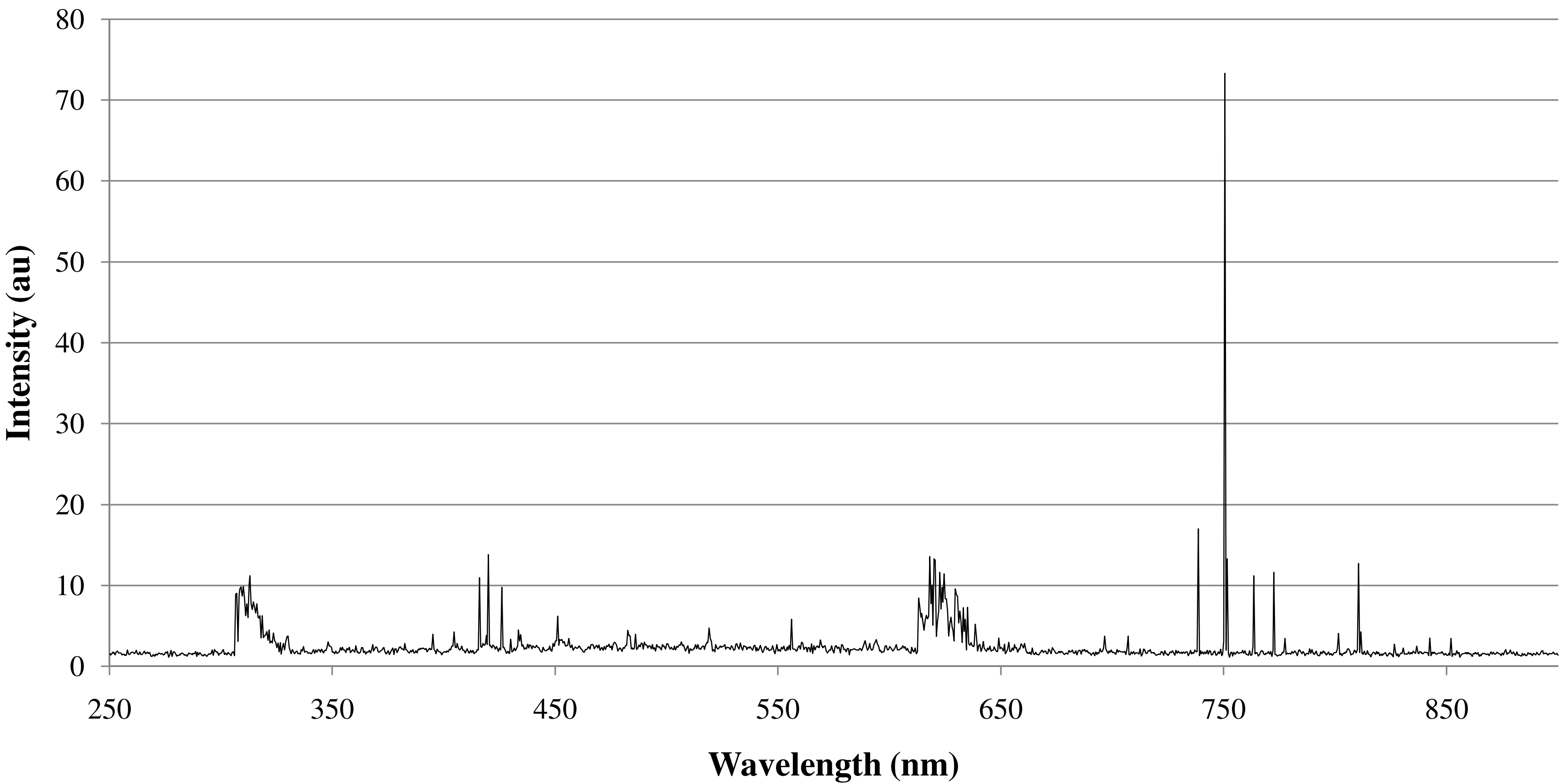

Figure C.7: Intensity as a function of wavelength of a sample processed for 16 minutes at a pressure of 100 mtorr and an applied power of 250 watts.

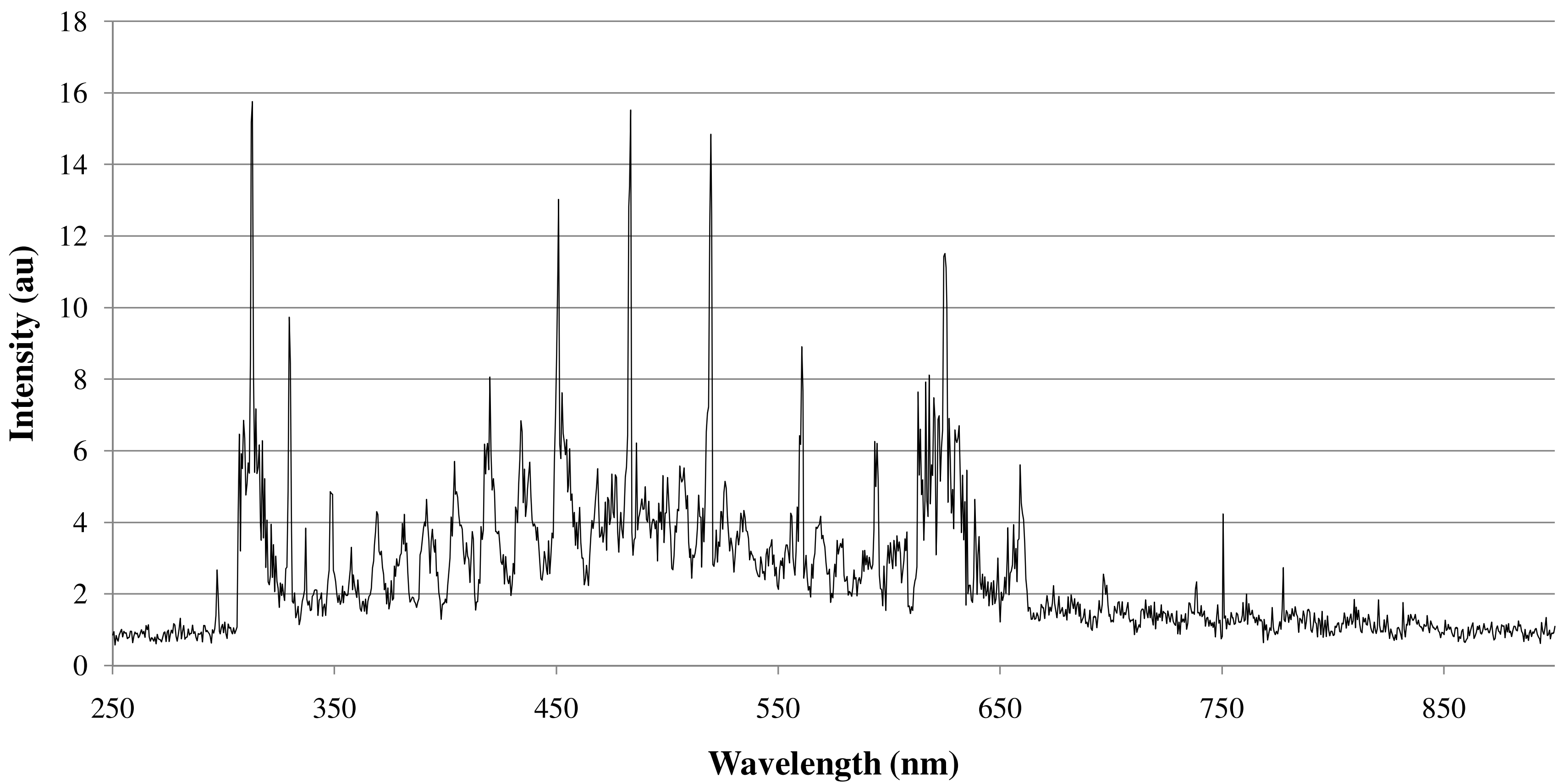

Figure C.8: Intensity as a function of wavelength of a sample processed for 16 minutes at a pressure of 100 mtorr and an applied power of 500 watts.

Appendix D

Spectra of Runs in Inductive Decoupled Plasma System (DPS)(13.0 cm)

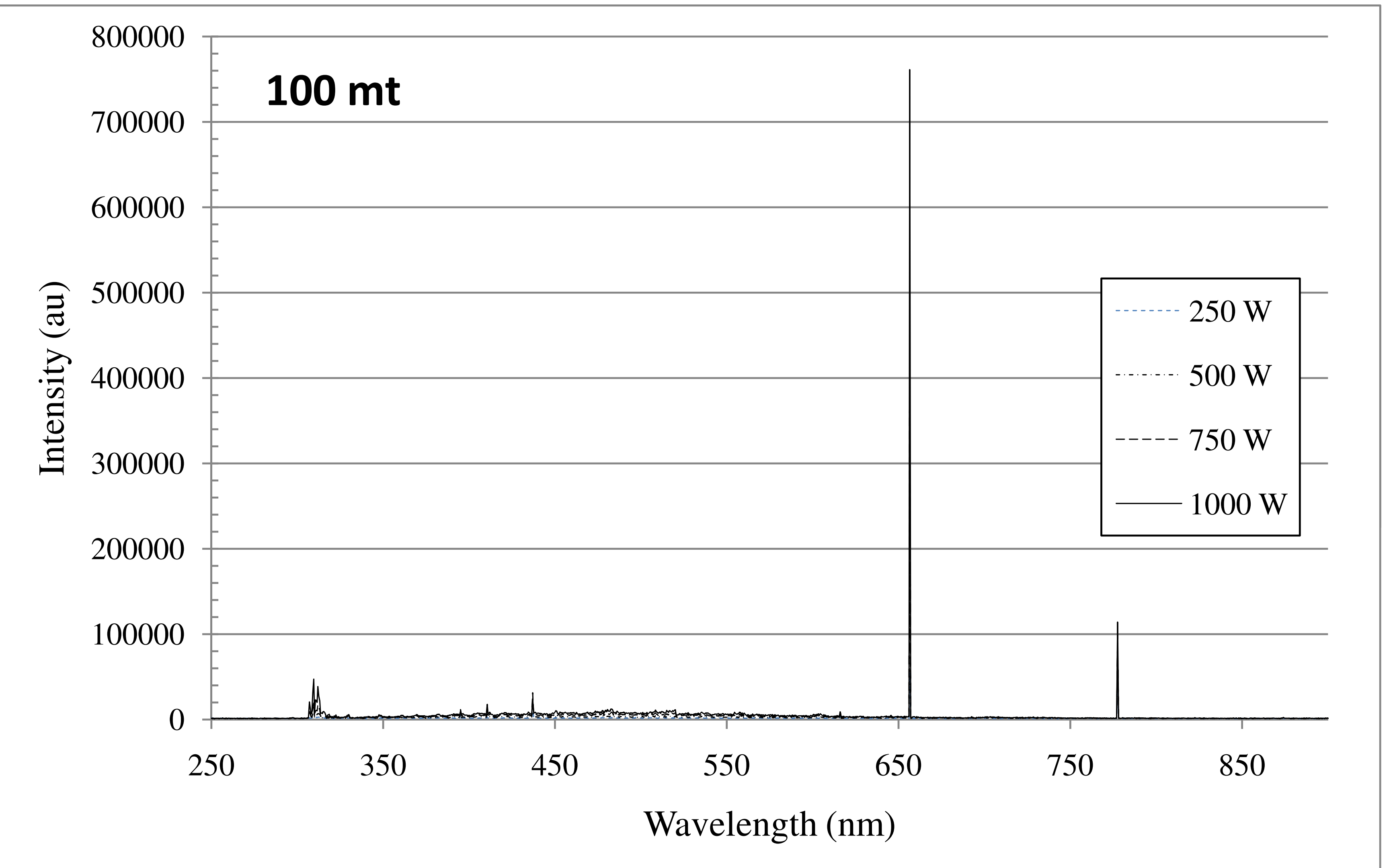

Figure D.1: Intensity as a function of wavelength of samples processed for 2 minutes at a pressure of 100 mtorr and an applied power of 250, 500, 750 1000 Watts as shown.

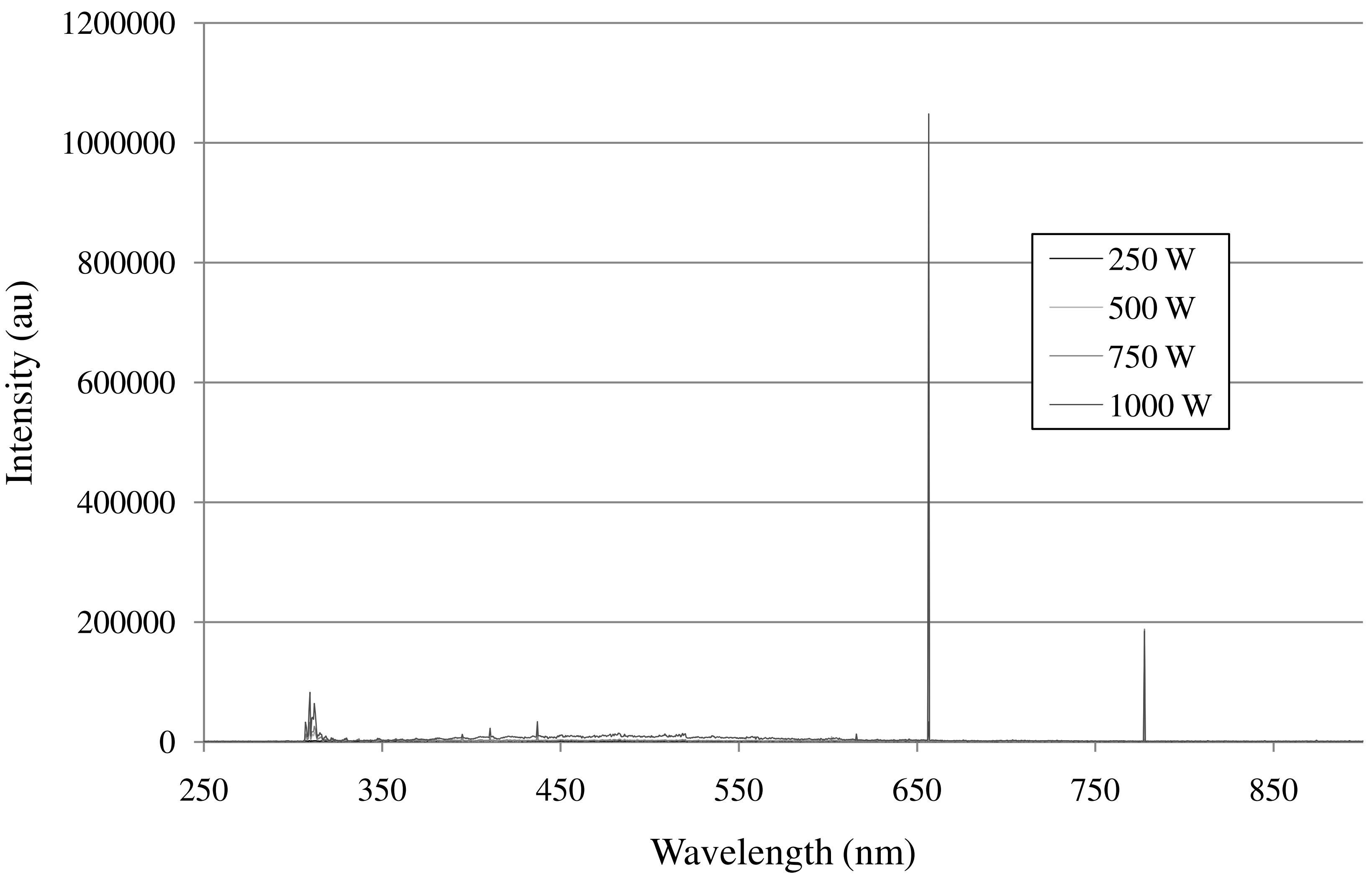

Figure D.2: Intensity as a function of wavelength of samples processed for 2 minutes at a pressure of 300 mtorr and an applied power of 250, 500, 750 1000 Watts as shown.

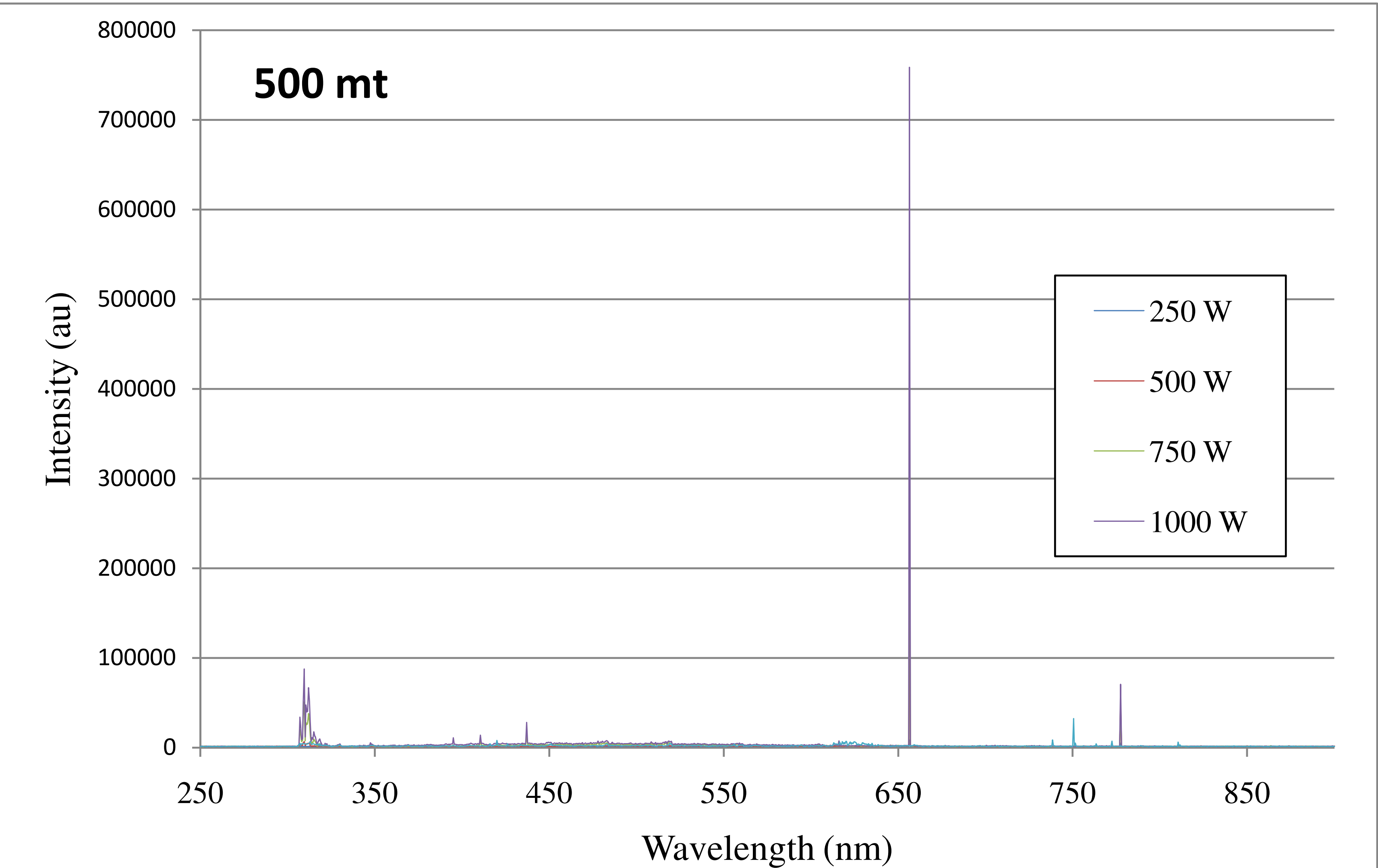

Figure D.3: Intensity as a function of wavelength of samples processed for 2 minutes at a pressure of 500 mtorr and an applied power of 250, 500, 750 1000 Watts as shown.

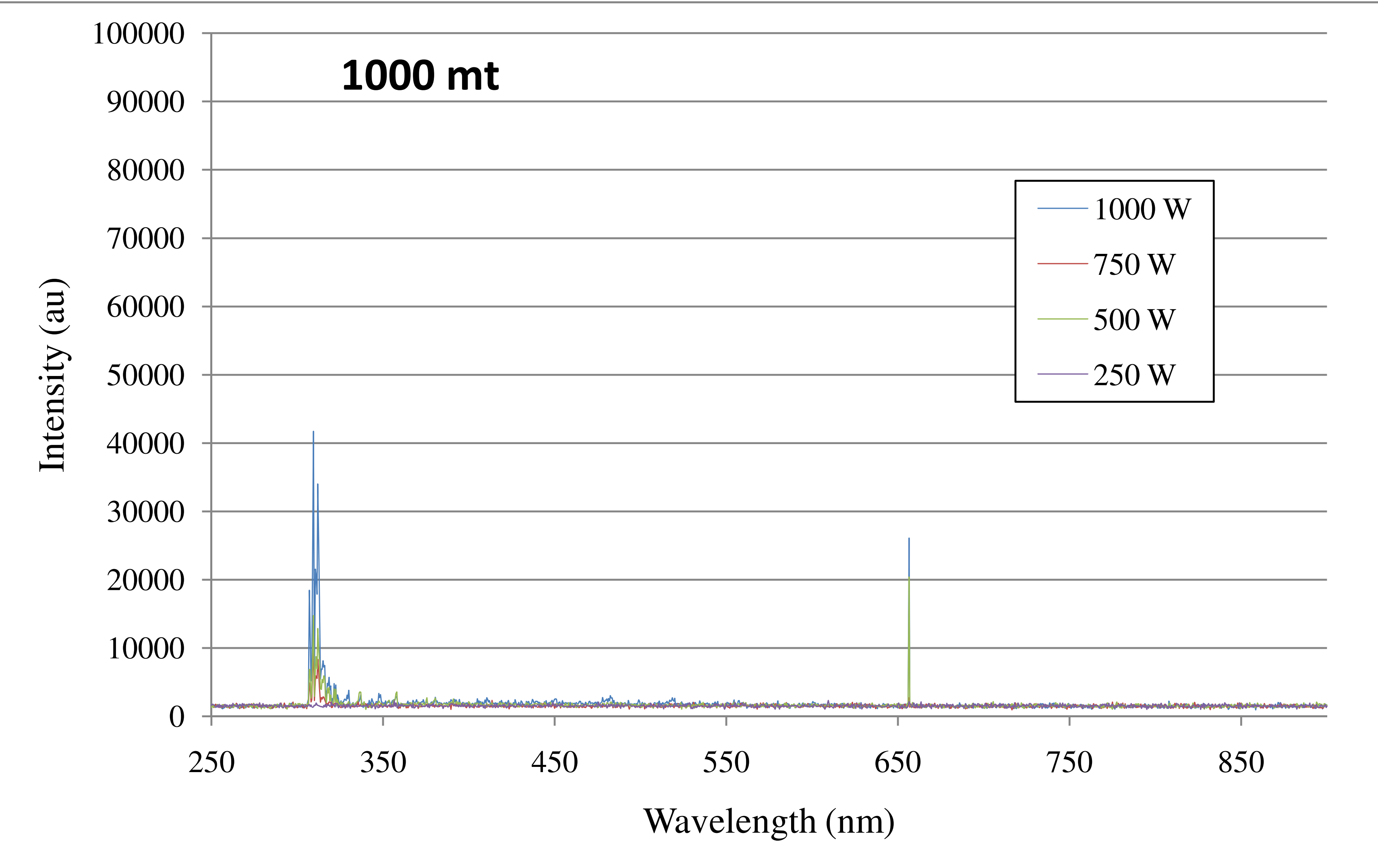

Figure D.4: Intensity as a function of wavelength of samples processed for 2 minutes at a pressure of 1000 mtorr and an applied power of 250, 500, 750 1000 Watts as shown.

Appendix E

ASTM-2855 Test Protocols and Equipment

Designation: D 2578 – 08

Standard Test Method for Wetting Tension of Polyethylene and Polypropylene Films[1]

This standard is issued under the fixed designation D 2578; the number immediately following the designation indicates the year of original adoption or, in the case of revision, the year of last revision. A number in parentheses indicates the year of last reapproval. A superscript epsilon (ε) indicates an editorial change since the last revision or reapproval.

1. Scope*

1.1 This test method covers the measurement of the wetting tension of a polyethylene or polypropylene film surface in contact with drops of specific test solutions in the presence of air.

1.2 The values stated in SI units are to be regarded as standard. The values given in parentheses are mathematical conversions to inch-pound units that are provided for information only and are not considered standard.

1.3 *This standard does not purport to address all of the safety concerns, if any, associated with its use. It is the responsibility of the user of this standard to establish appropriate safety and health practices and determine the applicability of regulatory limitations prior to use. Specific hazards statements are given in Section 8.*

NOTE 1—This test method is equivalent to ISO 8296.

2. Referenced Documents

2.1 *ASTM Standards:*[2]

D 618 Practice for Conditioning Plastics for Testing

E 691 Practice for Conducting an Interlaboratory Study to Determine the Precision of a Test Method

2.2 *ISO Standard:*

ISO 8296 [3]

3. Summary of Test Method

3.1 In this test method drops of a series of mixtures of formamide and ethyl Cellosolve[4] of gradually increasing surface tension are applied to the surface of the polyethylene or polypropylene film until a mixture is found that just wets the film surface. The wetting tension of the polyethylene or polypropylene film surface will be approximated by the surface tension of this particular mixture.

4. Significance and Use

4.1 When a drop of liquid rests on the surface of a solid, and a gas is in contact with both, the forces acting at the interfaces must balance. These forces can be represented by surface energies acting in the direction of the surfaces and it follows that:

$$\gamma GL \cos \theta = \gamma GS - \gamma SL \quad (1)$$

where:

θ = angle of contact of the edge of the drop with the solid surface,
γGL = surface energy of the gas - liquid interface,
γGS = surface energy of the gas - solid interface, and
γSL = surface energy of the solid - liquid interface.

4.1.1 The right side of the above equation (the difference between the surface energies of the gas - solid and solid - liquid interfaces) is defined as the wetting tension of the solid surface. It is not a fundamental property of the surface but depends on interaction between the solid and a particular environment.

4.1.2 When the gas is air saturated with vapors of the liquid, γGL will be the surface tension of the liquid. If the angle of contact is 0° the liquid is said to just wet the surface of the solid, and in this particular case (since $\cos \theta = 1$) the wetting tension of the solid will be equal to the surface tension of the liquid.

4.2 The ability of polyethylene and polypropylene films to retain inks, coatings, adhesives, etc., is primarily dependent upon the character of their surfaces, and can be improved by one of several surface-treating techniques. These same treating techniques have been found to increase the wetting tension of a polyethylene or a polypropylene film surface in contact with mixtures of formamide and ethyl Cellosolve in the presence of air. It is therefore possible to relate the wetting tension of a polyethylene or a polypropylene film surface to its ability to accept and retain inks, coatings, adhesives, etc. The measured wetting tension of a specific film surface can only be related to acceptable ink, coating, or adhesive retention through experience. Wetting tension in itself is not a completely acceptable measure of ink, coating, or adhesive adhesion.

NOTE 2—A wetting tension of 35 dynes/cm or higher has been generally found to reveal a degree of treatment normally regarded as acceptable for tubular film made from Type 1 polyethylene and intended for commercial flexographic printing. It is, however, possible that some other level of wetting tension may be required to indicate the acceptability

---

[1] This test method is under the jurisdiction of ASTM Committee D20 on Plastics and is the direct responsibility of Subcommittee D20.19 on Film and Sheeting.

Current edition approved Nov. 1, 2008. Published November 2008. Originally approved in 1967. Last previous edition approved in 2004 as D 2578 - 04a.

[2] For referenced ASTM standards, visit the ASTM website, www.astm.org, or contact ASTM Customer Service at service@astm.org. For *Annual Book of ASTM Standards* volume information, refer to the standard's Document Summary page on the ASTM website.

[3] Available from American National Standards Institute (ANSI), 25 W. 43rd St., 4th Floor, New York, NY 10036, http://www.ansi.org.

[4] Registered trademark of Union Carbide Corp. for ethylene glycol monoethyl ether.

***A Summary of Changes section appears at the end of this standard.**

Copyright © ASTM International, 100 Barr Harbor Drive, PO Box C700, West Conshohocken, PA 19428-2959, United States.

of polyethylene films made by other processes, or from other types of polyethylene, or intended for other uses.

At the present date, insufficient experience has been gained to state a generally acceptable level of wetting tension for polypropylene films for commercial flexographic printing.

5. Interferences

5.1 Since the wetting tension of a polyethylene or polypropylene film in contact with a drop of liquid in the presence of air is a function of the surface energies of both the air - film and film - liquid interfaces, any trace of surface-active impurities in the liquid reagents or on the film may affect the results. It is, therefore, important that the portion of the film surface to be tested not be touched or rubbed, that all equipment be scrupulously clean, and that reagent purity be carefully guarded. Glass apparatus in particular is likely to be contaminated with detergents having very strong surface tension reducing ability unless specific precautions are taken to ensure their absence such as cleaning with chromic-sulfuric acid and rinsing with distilled water.

6. Apparatus

6.1 *Cotton-Tipped Wooden Applicators*, approximately 150 mm (6 in.) in length.

6.2 *Burets*, two, 50-mL.

6.3 *Bottles*, 100-mL, with caps and labels.

7. Reagents and Materials

7.1 Prepare mixtures of reagent grade formamide ($HCONH_2$) and reagent grade ethyl Cellosolve ($CH_3CH_2OCH_2CH_2OH$) in the proportions shown in Table 1 for the integral values of wetting tension in the range over which measurements are to be made. For extremely precise work, mixtures for determining fractional values of wetting tension may be made up by interpolating between the concentrations shown in Table 1.

NOTE 3—Although the mixtures of ethyl Cellosolve and formamide used in this test method are relatively stable, exposure to extremes of temperature or humidity should be avoided.

7.2 If desired, add to each of the formamide ethyl Cellosolve mixtures a very small amount of dye of high tinctorial value. The dye used should be of such color as to make drops or thin films of the solutions clearly visible on the surface of polyethylene or polypropylene film and must be of such chemical composition that it will not measurably affect the wetting tension of the solutions in the concentration used.[5]

7.3 Fully prepared mixtures of these reagents in varying concentrations are available from a number of commercial sources. Pens containing these mixtures are also commercially available. However, correlations between these options and freshly prepared solutions have not been established.

NOTE 4—Care must be taken when handling pens. Prolonged exposure to the atmosphere, temperature or humidity extremes, exposure to contaminants, or use beyond the stated expiration date will change their characteristics creating a potential for erroneous results.

TABLE 1 Concentration of Ethyl Cellosolve—Formamide Mixtures Used in Measuring Wetting Tension of Polyethylene and Polypropylene Films

Formamide, Volume %	Ethyl Cellosolve,[A] %	Wetting Tension,[B] dynes/cm
0	100.0	30
2.5	97.5	31
10.5	89.5	32
19.0	81.0	33
26.5	73.5	34
35.0	65.0	35
42.5	57.5	36
48.5	51.5	37
54.0	46.0	38
59.0	41.0	39
63.5	36.5	40
67.5	32.5	41
71.5	28.5	42
74.7	25.3	43
78.0	22.0	44
80.3	19.7	45
83.0	17.0	46
87.0	13.0	48
90.7	9.3	50
93.7	6.3	52
96.5	3.5	54
99.0	1.0	56

[A] Cellosolve is the registered trademark of Union Carbide Corp. for ethylene glycol monoethyl ether.

[B] Measured under conditions of 23 ± 2°C and 50 ± 5 % relative humidity.

8. Hazards

8.1 Formamide may cause skin irritation and is particularly dangerous in direct contact with the eyes. Safety goggles should be worn when making up new test mixtures.

8.2 Ethyl Cellosolve is a highly flammable solvent.

8.3 Both ethyl Cellosolve and formamide are toxic and pose exposure risks. Consult the applicable MSDS before use and ensure that the appropriate Personal Protective Equipment (PPE) is used, especially when preparing new solutions.

8.4 All tests should be performed with adequate ventilation.

9. Sampling

9.1 The minimum amount of film required for this test depends upon the skill of the operator. This usually amounts to one sample across the entire width of a roll in order to obtain a representative value.

9.2 Extreme care must be taken to prevent the surface of the film sample from being touched or handled in the areas upon which the test is to be made.

9.3 Usually it will be adequate to make one determination at each location ¼ , ½ , ¾ of the way across the width of the film, to arrive at an average value for the sample or to determine when treatment is uneven.

10. Conditioning

10.1 *Conditioning*—Condition the test specimens at 23 ± 2°C (73.4 ± 3.6°F) and 50 ± 10 % relative humidity for not less than 40 h prior to test in accordance with Procedure A of Practice D 618 unless otherwise specified by agreement or the relevant ASTM material specification. In cases of disagreement, the tolerances shall be ±1°C (±1.8°F) and ±5 % relative humidity.

[5] "DuPont Victoria Pure Blue BO" at a maximum concentration of 0.03 % has been found satisfactory.

10.2 *Test Conditions*—Conduct the tests at 23 ± 2°C (73.4 ± 3.6°F) and 50 ± 10 % relative humidity unless otherwise specified by agreement or the relevant ASTM material specification. In cases of disagreement, the tolerances shall be ±1°C (±1.8°F) and ±5 % relative humidity.

NOTE 5—In specific cases, such as control testing, where the conditioning requirements cannot be met and the data are of direct assistance to the operation, other conditioning procedures can be used and recorded in the report.

11. Procedure

11.1 Wet the very tip of a cotton applicator with one of the mixtures. Use only a minimum amount of liquid as an excess of reagent can affect the end point of the test.

11.2 Spread the liquid lightly over an area of approximately 6.5 cm^2 (1 $in.^2$) of the test specimen. Do not try to cover a larger area lest there be insufficient liquid to give complete coverage.

11.3 Note the time required for the continuous film of liquid formed in 11.2 to break up into droplets. If the continuous film holds for 2 s or more, proceed to the next higher surface tension mixture, but if the continuous film breaks into droplets in less than 2 s, proceed to the next lower surface mixture. A clean, new cotton applicator must be used each time to avoid contamination of the solutions (even for successive dips into the same solution).

NOTE 6—The solution is considered as wetting the test specimen when it remains intact as a continuous film of liquid for at least 2 s. The "reading" of the liquid film behavior should be made in the center of the liquid film. Shrinking of the liquid film about its periphery does not indicate lack of wetting. Breaking of the liquid film into droplets within 2 s indicates lack of wetting. Severe peripheral shrinkage may be caused by too much liquid being placed upon the film surface. Experience with the test will give excellent insight into "reading" the liquid film behavior.

11.4 Proceeding in the direction indicated by the results of 11.3, continue repeating 11.1 through 11.3 until it is possible to select the ethyl Cellosolve-formamide mixture that comes nearest to wetting the film surface for exactly 2 s. The surface tension of this mixture in dynes per centimetre is called the wetting tension of the polyethylene or polypropylene film specimen.

NOTE 7—Since the surface tension of the formamide/ethyl cellosolve solutions can change, for example, through evaporation of one or both components, or through contamination, and is dependent upon temperature, the actual surface tension of the solution that wet the film for exactly 2 s should be measured. This can be accomplished very simply with a surface tensiometer.[6]

11.5 Experience with this test has shown that on occasion erroneous wetting tension results can be obtained when the final wetting tension is determined by working progressively to lower surface tension mixtures when practicing 11.1-11.4. It is recommended that the test analyst should check the reported wetting tension of the film by working progressively to higher surface tension mixtures.

12. Report

12.1 Report the average value of the wetting tension of each sample to the nearest 0.5 dynes/cm.

12.2 If the polyethylene or polypropylene film has been unevenly treated, it may not be possible to arrive at a single value of wetting tension. In this case, report the individual values whenever the largest value exceeds the smallest by more than 1 dyne/cm.

13. Precision and Bias [7]

13.1 *Precision*:

13.1.1 Table 2 is based on an interlaboratory study conducted in 1995 in accordance with Practice E 691 involving three materials and thirteen laboratories. Each test result was the average of three individual determinations. Each laboratory obtained three test results for each material on two days.

13.1.2 The values of the repeatability standard deviation S_r, reproducibility standard deviation S_R, the 95 % repeatability and reproducibility limits on the difference between two test results, r and R, respectively, for different treatment levels have been determined and are shown in Table 2. The results demonstrate that the precision of the results depends on the treatment level (wetting tension) of the film, the higher the treatment level, the higher the variability between single test results obtained in different laboratories, or the lower the precision.

13.1.3 *Definitions*:

Warning—The following explanations of r and R are only intended to present a meaningful way of considering the approximate precision of this test method. The data in Table 1 should not be rigorously applied to the acceptance or rejection of material, as those data are specific to the interlaboratory study and may not be representative of other lots, conditions, materials, or laboratories. Users of this test method should apply the principles outlined in Practice E 691 to generate data specific to their laboratory and materials, or between specific laboratories. The principles 13.1.3-13.2 would then be valid for such data.

[6] The Fisher Surface Tensiometer, Model 20, has been found satisfactory for this application.

[7] Supporting data are available from ASTM Headquarters, Request RR:D20-1236.

TABLE 2 Interlaboratory Study Results.

Material	Treatment Power, W/ft^2 /min	Average Wetting Tension, dyne/cm	Repeatability Standard Deviation, S_r	Reproducibility Standard Deviation, S_R	r	R
PP film	20	39.45	0.74	1.97	2.06	5.52
PP film	1.6	36.27	0.32	1.85	0.90	5.19
PP film	0.5	33.07	0.38	0.87	1.06	2.43

13.1.3.1 S_r = the within laboratory standard deviation for the individual material. It is obtained by pooling the within-laboratory standard deviations of the test results from all of the participating laboratories.

13.1.3.2 S_R = the between-laboratories reproducibility, expressed as standard deviation.

13.1.3.3 r = the within-laboratory critical interval between two results = 2.8 × S_r. The two test results should be judged not equivalent if they differ by more than the r dyne/cm for that treatment level.

13.1.3.4 R = the between-laboratories critical interval between two results = 2.8 × S_R. The two test results should be judged not equivalent if they differ by more than the R dyne/cm for that treatment level.

13.1.3.5 Any judgment in accordance with 13.1.3.1 and 13.1.3.2 would have an approximate 95 % (0.95) probability of being correct.

13.2 *Bias*—No statement can be made about the bias of this test method because wetting tension is defined in terms of the test method.

SUMMARY OF CHANGES

Committee D20 has identified the location of selected changes to this standard since the last issue (D 2578 - 04a) that may impact the use of this standard. (November 1, 2008)

(*1*) Revised Section 10.

ASTM International takes no position respecting the validity of any patent rights asserted in connection with any item mentioned in this standard. Users of this standard are expressly advised that determination of the validity of any such patent rights, and the risk of infringement of such rights, are entirely their own responsibility.

This standard is subject to revision at any time by the responsible technical committee and must be reviewed every five years and if not revised, either reapproved or withdrawn. Your comments are invited either for revision of this standard or for additional standards and should be addressed to ASTM International Headquarters. Your comments will receive careful consideration at a meeting of the responsible technical committee, which you may attend. If you feel that your comments have not received a fair hearing you should make your views known to the ASTM Committee on Standards, at the address shown below.

This standard is copyrighted by ASTM International, 100 Barr Harbor Drive, PO Box C700, West Conshohocken, PA 19428-2959, United States. Individual reprints (single or multiple copies) of this standard may be obtained by contacting ASTM at the above address or at 610-832-9585 (phone), 610-832-9555 (fax), or service@astm.org (e-mail); or through the ASTM website (www.astm.org).

UV PROCESS SUPPLY, INC.

CON-TROL-CURE© DYNE PENS

PART # N001-010 (Levels 36-48)

INSTRUCTION FOR USE

For maximum accuracy when testing, an ink from the middle of the range should first be applied. (e.g. 40 dynes/cm) If the ink wets the surface within two seconds without forming globules, the treatment level of the film is either higher than, or exactly that of the liquid.

A second test using the ink of the next higher value, in this case 42 dynes/cm., should then be performed and the process repeated using inks of increased values until the ink forms globules within the first two seconds of application.

However, should the first application of ink have formed globules within two seconds, then the same ink test should be repeated, but using the next lower value.

In this way, one is able to pinpoint the treatment level measurement through two tests. For example, it can be established that the level of treatment of the tested film is between the levels of two inks – 36 to 38 dynes/cm. With a certain amount of practice it can be accurately estimated whether the level lies closer to 36 or 38 dynes/cm.

This test is a suitable test carried out by the machine operator and gives a trained person an easy and effective means of determining the treatment levels achieved on film samples.

Since the inks are made up of liquids with various surface tensions and are also hydroscopic, it is imperative that the caps be firmly replaced immediately after use.

The surface tension is a definite criteria for the adhesion of ink onto PE and PP. There are, however, other factors such as migration of slip additives that influence the adhesion of inks quite negatively, that in turn do not necessarily register on surface tension testing. Consequently, even though good surface tension results were found, the ink adhesion can result negatively. It is also possible that polymer plastics with the same surface tension can give varying degrees of print adhesion.

In most cases, however, one can disregard these exceptions and get the best possible results of ink adhesion with the surface tension of between 38 and 41 dynes/cm. Too low of a surface tension value, approximately 35 dynes/cm., almost always result in poor adhesion.

UV Process Supply, Inc.
1229 W. Cortland St.
Chicago, IL 60614-4805
Copyright © 2004 UV Process Supply, Inc.
773-248-0099 • 800-621-1296 • 888-UVLAMPS
FAX 773-880-6647 • 800-99FAXUV
email: info@uvps.com • www.uvprocess.com

UV PROCESS SUPPLY, INC.

CON-TROL-CURE© DYNE PENS

PART # N001-010 (Levels 36-48)

This document provides information about a product distributed by UV Process Supply, Inc ("the Seller"). The information provided in this document is offered in good faith and is believed to be reliable, but is made WITHOUT WARRANTY, EXPRESS OR IMPLIED, AS TO MERCHANTABILITY, FITNESS FOR A PARTICULAR PURPOSE, OR ANY OTHER MATTER.

This document is not intended to provide advice (technical, legal or otherwise) for a particular set of facts, but is of a general nature. Users of this document should consult with their own advisors and appropriate sources. The Seller and its employees do not assume any responsibility for the user's compliance with any applicable instructions, laws or regulations, nor for any persons relying on the information contained in this document.

All risk arising out of the performance of this product and/or the understanding of its usage remains solely with the Buyer. In no event shall the Seller be held liable for lost profits, lost savings, incidental or direct damages or other economic consequential damages regardless of any statement, expressed or implied, of such liability by the Seller's employees or any of its authorized agents. In addition, the Seller and its suppliers will be held harmless for any damages claimed on behalf of any third party.

The Buyer of this product accepts full responsibility and understanding for the terms and specifications set forth herein.

UV Process Supply, Inc.
1229 W. Cortland St.
Chicago, IL 60614-4805
Copyright © 2004 UV Process Supply, Inc.

773-248-0099 • 800-621-1296 • 888-UVLAMPS
FAX 773-880-6647 • 800-99FAXUV
email: info@uvps.com • www.uvprocess.com